UNIVERSITY OF LONDON THESIS

Degree PhD Year 2007 Name of Author DOUGLAS CHARLES ALEXANDER MARSHALL

Structural and Functional Studies of Respiratory Chain Proteins Using InfraRed Spectroscopy

Douglas Charles Alexander Marshall

Glynn Laboratory of Bioenergetics

Department of Biology

University College London

Submitted for the Degree of Doctor of Philosophy

2007

Primary supervisor: Prof. Peter R. Rich

Secondary supervisor: Prof. Conrad W. Mullineaux

Internal Examiner: Prof. Peter J. Nixon

External Examiner: Prof. Steve K. Chapman

ProQuest LLC
789 East Eisenhower Parkway
P.O. Box 1346
Ann Arbor, MI 48106-1346

Declaration:

The work presented in this thesis is my own except where stated otherwise.

Signed:

Dated: 22nd March 07

Abstract:

Attenuated total reflection Fourier transform infrared (FTIR) spectroscopy in the 4000-800 cm^{-1} range was applied to NADH:ubiquinone oxidoreductase (complex I) and cytochrome bc_1 complex of the respiratory electron transfer chain. High signal:noise redox difference spectra were acquired using novel electrochemical and perfusion techniques to reversibly adjust protein redox state which, where appropriate, was monitored by simultaneous UV/visible spectroscopy. Interpretation of spectra was assisted by hydrogen-deuterium exchange, ^{15}N labelling and redox titration. Model compound data, including protonation state/redox difference spectra of histidine, flavin mononucleotide and ferredoxins, were recorded and are presented as a comprehensive 'toolkit' for assisting in acquisition and interpretation of protein IR data in general.

Electrochemically-induced difference spectra of bovine and *Rhodobacter capsulatus* cytochrome bc_1 complex are comparable to published perfusion data but are at significantly higher signal:noise demonstrating the functionality of the electrochemical technique. Comparison of wild-type and E295V *Rba. capsulatus* difference spectra resulting from haem b_L reduction/oxidation definitively rules out Glu-295 as the principal carboxylic acid residue responsive to haem b_L redox change.

Full redox difference spectra of *Yarrowia lipolytica* and bovine complex I are similar to published *E. coli* transmission FTIR spectra where signals in the amide I and II region were interpreted as indictors of large scale conformational change. Comparison of complex I and ferredoxin difference spectra rules out this interpretation. Signals in the presented spectra are tentatively assigned to reduced flavin and to protonation state change of one or more histidine residues. In iron-sulphur centre N2 redox difference spectra, measured in intact complex I for the first time, signals from substrate ubiquinone/ubiquinol formation are clear; a putative histidine protonation change signal is also present. Perfusion induced-difference spectra, using NADH as reductant, indicate that NADH does not reduce the full complement of iron-sulphur centres and no signals indicative of large scale conformational change were present.

Table of Contents:

Acknowledgments:

I would like to thank Prof. Peter R. Rich for excellent supervision. I would also like to thank Prof. Conrad W. Mullineaux.

I am grateful to my parents for support during the preparation of this manuscript, to my brothers George and Ed and to my Uncle John for words of wisdom and endless encouragement.

Words cannot sufficiently express my gratitude to Sheridan for the help and support that she has given me over the last six months. I only hope I can return the favour over the coming months.

In addition I would like to thank the other members of the Glynn Laboratory of Bioenergetics: Dr Masayo Iwaki, Mrs Vasanti Amin; Mr Santiago Garcia for manufacture of the electrochemical cells; and the postgraduate students of the Biology and Biochemistry departments.

Publications (included in Appendix I)

1. Iwaki, M., Yakovlev, G., Hirst, J., Osyczka, A., Dutton, P. L., Marshall, D., and Rich, P. R. (2005) Direct observation of redox-linked histidine protonation changes in the iron-sulfur protein of cytochrome bc_1 complex by ATR-FTIR spectroscopy, *Biochemistry 44*, 4230-4237.

2. Marshall, D., Fisher, N., Grigic, L., Zickermann, V., Brandt, U., Shannon, R. J., Hirst, J., Lawrence, R., and Rich, P. R. (2006) ATR-FTIR redox difference spectroscopy of *Yarrowia lipolytica* and bovine complex I, *Biochemistry 45*, 5458-5467.

Abbreviations and Nomenclature

A	Absorbance
Acetyl CoA	Acetyl coenzyme A
ADP	Adenosine diphosphate
APP	Applied PhotoPhysics
ATP	Adenosine triphosphate
ATR	Attenuated total reflection
c	Speed of light (2.997925×10^8 m.s^{-1})
cm^{-1}	Reciprocal wave length (also known as Wavenumber)
Da	Dalton
DDM	n-dodecyl-β-D-maltoside
DFT	Density functional theory
EDTA	Ethylenediamine tetra-acetic acid
EM	Electron microscopy
EPR	Electron paramagnetic resonance

F	Faraday constant (0.0965 $kJ.mol^{-1}.mV^{-1}$)
FAD	Flavin adenine dinucleotide
Fe-S	Iron-sulphur (centre)
FMN	Flavin mononucleotide
FT	Fourier tranform
g_{av}	Average acceleration due to gravity
h	Planck's constant (4.135667×10^{-15} eV.s)
H-D	Hydrogen-Deuteron
IR	Infrared
IRE	Internal reflecting element
ISP	Iron sulphur protein
KH	Keilin-Hartree
LDAO	*N*,*N*-dimethyldodecylamine *N*-oxide
MCT	Mercury Cadmium Telluride
NAD^+	Nicotinamide adenine dinucleotide (oxidised form)
NADH	Nicotinamide adenine dinucleotide (reduced form)
NMR	Nuclear magnetic resonance
PDB	Protein Database
PMF	Protonmotive force
Q	Quinone (in either reduced or oxidised form)
QH_2	Quinone (reduced form)
Q-site	Quinone-binding site
R	The gas constant (8.3 $J.mol^{-1}.K^{-1}$)
ROS	Reactive oxygen species
rpm	Revolutions per minute
SHE	Standard hydrogen electrode

SQ	Semiquinone
TCA	Tricarboxylic acid
TMH	Transmembrane Helices
UV	Ultraviolet
ν	Frequency
ΔpH	Chemical component of protonmotive force
$\Delta\mu_{H^+}$	Protonmotive force
$\Delta\psi$	Electrical component of protonmotive force
ε	Extinction coefficient
λ	Wavelength

Figure list

Table list

Chapter 1: Introduction

1.1 The electron transfer chain and cellular respiration

1.1.1 Overview

Electron transfer chains are an integral part of the mechanisms of cellular respiration and photosynthesis and are therefore essential for almost all forms of life. The role of the electron transfer chain in eukaryotic respiration is to couple a series of exergonic redox reactions to the translocation of protons across the inner mitochondrial membrane into the inter-membrane space. Energy stored in the resulting electrochemical gradient across the inner membrane is used to drive various endergonic processes including the phosphorylation of ADP to produce ATP by ATP synthases. The nature of this energetic coupling was first described in 1961 by Peter Mitchell in his chemiosmotic hypothesis (*1*), for which he was awarded the Nobel Prize in 1978.

1.1.2 Krebs cycle

Hans Krebs was awarded the Nobel Prize in 1953 for discovering the pathway that now bears his name. The Krebs cycle (see Figure 1.1), also known as the tricarboxylic acid (TCA) cycle or citric acid cycle (CAC), provides precursors for, and is directly linked to, the respiratory electron transfer chain and takes

place within the mitochondrial matrix. In addition to generating many biosynthetic precursors, the Krebs cycle accounts for the major fraction of carbohydrate, fatty acid and amino acid oxidation within the cell. Cytoplasmic metabolic pathways, in particular glycolysis and fatty acid oxidation, result in the generation of acetyl coenzyme A (acetyl CoA), the main substrate of the pathway. Oxidation of the acetyl group of acetyl CoA via the Krebs cycle results in the reduction of three NAD^+ to NADH and the formation of reduced FAD during the oxidation of succinate to fumarate. It is the reoxidation of these molecules that provides the energy to drive the proton pumps of the respiratory electron transfer chain.

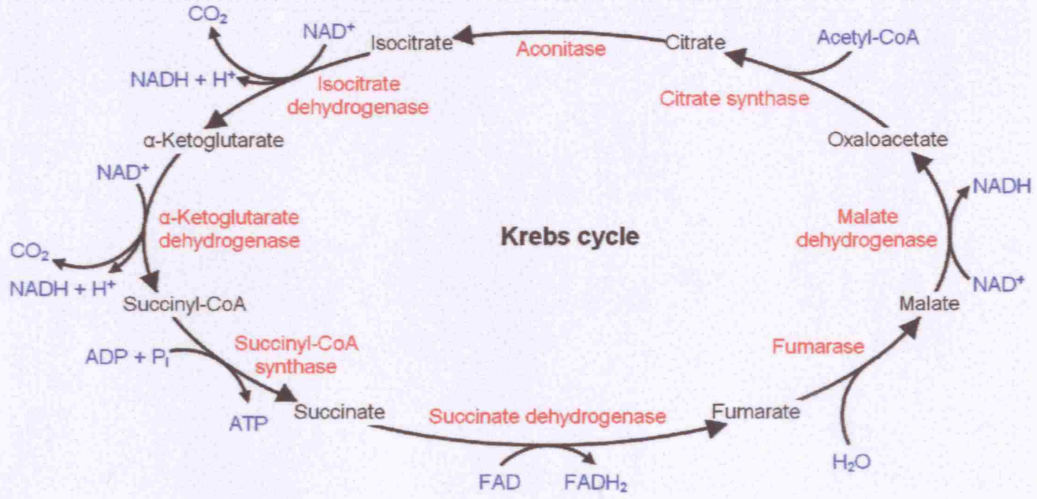

Figure 1.1 Summary of the Krebs cycle. Carbon compounds and enzymes catalysing each step are shown in black and red respectively; the substrates and products of each step are shown in blue. Adapted from (*2*).

1.1.3 The mammalian respiratory electron transfer chain

The mammalian respiratory electron transfer chain includes four large multisubunit protein complexes which mediate the transfer of electrons from the products of glycolysis and the Krebs cycle to molecular oxygen (see Figure 1.2). NADH:ubiquinone oxidoreductase (complex I), ubiquinol:cytochrome *c* oxidoreductase (complex III) and cytochrome *c* oxidase (complex IV) couple electron transfer reactions to proton translocation; succinate:ubiquinone oxidoreductase (complex II) does not. Although there is evidence that the protein complexes are, to various extents, associated with one another forming

supercomplexes (see (*3*) for a review), for the purpose of this thesis they will be discussed as single entities that do not interact directly. The complexes, each of which are embedded in and span the inner mitochondrial membrane, are linked by the freely diffusible electron carriers: - ubiquinone and cytochrome *c*. Ubiquinone, a small lipophilic molecule, transports pairs of hydrogen atoms (i.e. two electrons + two protons) from complexes I and II to complex III. Cytochrome *c*, a small hydrophilic haemoprotein located in the inter-membrane space, transports electrons singly from complex III to complex IV. The overall redox span of the respiratory chain, from the NAD^+/NADH couple to the $O_2/2H_2O$ couple, is 1.1 V (*4*).

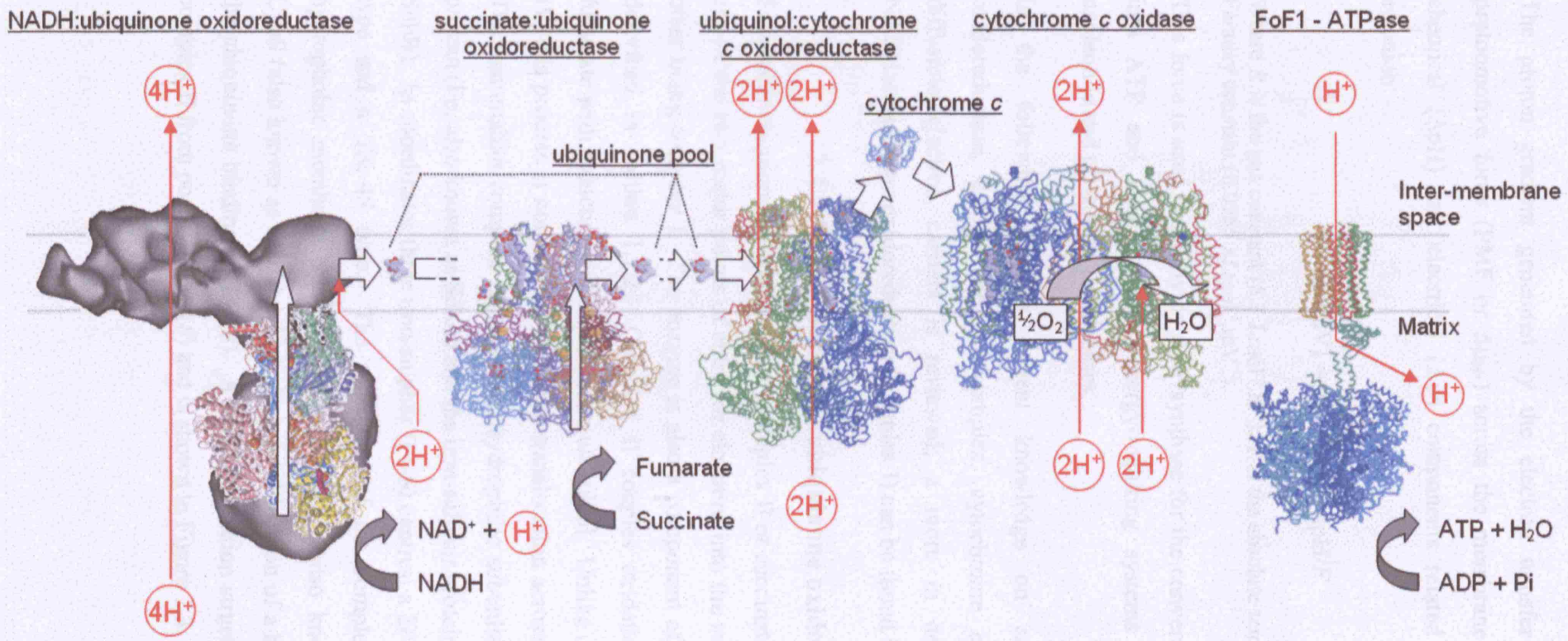

Figure 1.2 Overview of structure and function of the respiratory chain and ATP synthase. Adapted/extended from (*5*), structures were drawn using Protein Explorer - PDB files: 1NEK (succinate:ubiquinone oxidoreductase at 2.6 Å), 1BGY (ubiquinone:cytochrome *c* oxidoreductase at 3 Å), 2OCC (cytochrome *c* oxidase at 2.3 Å), 1QO1 (ATP synthase at 3.9 Å), 1HRC (cytochrome *c* at 1.9 Å), 2FUG (peripheral domain of NADH:ubiquinone oxidoreductase at 3.3 Å), also includes reconstructed image of NADH:ubiquinone oxidoreductase at 22 Å from (*6*). White and red arrows indicate electron transfer and proton translocation respectively (number of protons translocated per electron pair is indicated in red; not applicable to ATPase); grey arrows indicate conversion of substrate into products.

The proton gradient generated by the electron transfer chain leads to a protonmotive force (PMF or $\Delta\mu_{H^+}$) across the membrane which consists of chemical (ΔpH) and electrical ($\Delta\psi$) components related as shown by the equation: -

$$\Delta p \text{ (mV)} = \Delta\psi - 2.3RT\,\Delta\text{pH}/F$$

Where R is the gas constant (8.3 $J.mol^{-1}.K^{-1}$), T is the absolute temperature and F is the Faraday constant (0.0965 $kJ.mol^{-1}.mV^{-1}$).

This force is used primarily by ATP synthase for the conversion of ADP and Pi into ATP and also by other energy-requiring systems including adenine nucleotide and phosphate translocases.

In the following sections current knowledge on succinate:ubiquinone oxidoreductase, cytochrome bc_1 complex, cytochrome *c* oxidase and the diffusible electron carriers is reviewed; a more in depth discussion of NADH:ubiquinone oxidoreductase (complex I) can be found in section 1.3.

1.1.3.1 Succinate:ubiquinone oxidoreductase

Succinate:ubiquinone oxidoreductase (complex II or succinate dehydrogenase) is one of the two major points of entry for electrons into the respiratory chain; the other being complex I. The enzyme is also a component of the Krebs cycle as described in section 1.1.2. Complex II couples oxidation of succinate to fumarate with reduction of ubiquinone to ubiquinol. Unlike complexes I, III and IV, this process is not coupled to proton translocation across the membrane (*7*). The mammalian complex includes two hydrophilic subunits: the FAD binding protein (Fp, also known as SdhA) and the iron-sulphur protein (Ip, also known as SdhB). Ip coordinates three iron-sulphur (Fe-S) centres: a 2Fe-2S type, a 4Fe-4S type and a 3Fe-4S type. The remainder of the complex consists of two hydrophobic membrane spanning subunits, CybL (also known as SdhC) and CybS (also known as SdhD), which share axial ligation of a haem B and provide the ubiquinone binding site(s) (*8*). A 2.4 Å resolution structure is available for complex II from porcine heart (*8*) and is shown in Figure 1.3.

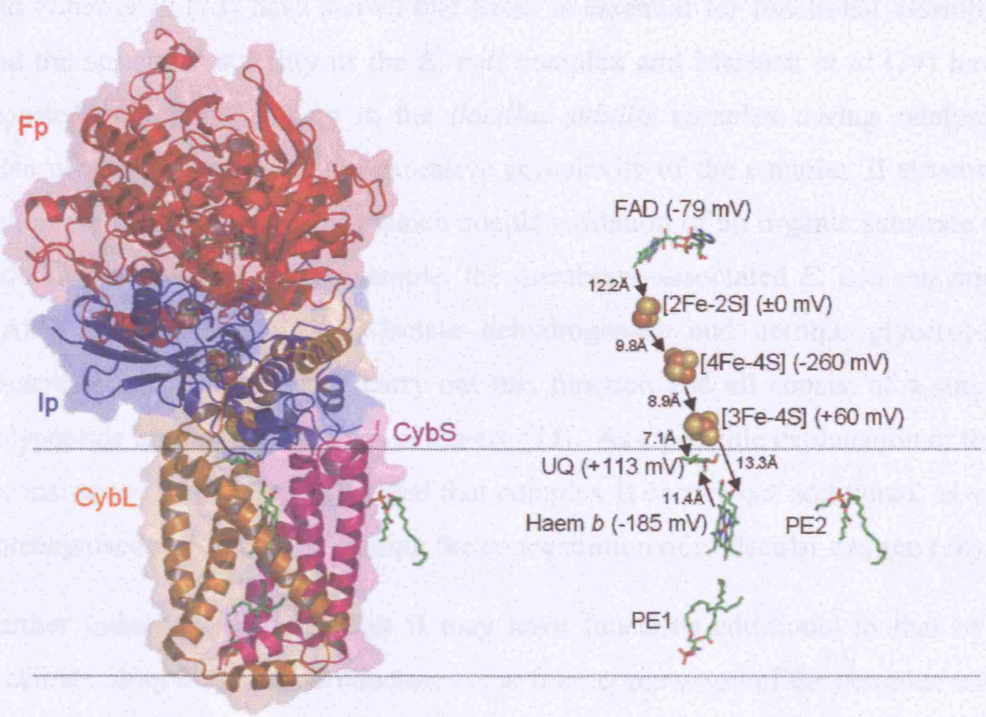

Figure 1.3 Structure and function of Complex II from porcine heart. On the left side, a ribbon diagram of the complex is superimposed on the semitransparent molecular surface. FAD binding protein (Fp) is shown in red; iron-sulphur protein (Ip) is shown in blue; the transmembrane proteins CybL and CybS are shown in orange and magenta respectively. The putative membrane region is indicated by horizontal dotted lines (orientation is such that the matrix is at the top of the page). On the right side, the prosthetic groups constituting the electron transfer pathway (FAD, [2Fe-2S], [4Fe-4S], [3Fe-4S] and haem *b*) are shown together with ubiquinone (UQ); edge-to-edge distances (*8*) and E_{m7} values (for bovine) (*9*) and the proposed electron transfer route (*8*) are indicated. The locations of two structural phosphatidylethanolamine lipids (PE1 and PE2) are also shown. Figure drawn using PyMOL™ (DeLano Scientific LLC) from PDB file 1ZOY.

The porcine and similar *Escherichia coli* (*10*) structures reveal a pathway, consisting of FAD, 2Fe-2S, 4Fe-4S and 3Fe-4S centres, which connects the substrate- and ubiquinone- binding sites and with no single step exceeding 14 Å. 14 Å has been proposed to be the maximum distance for physiological electron transfer by Dutton *et al* (*11*) based on a survey of proteins with known atomic structure whose function involves electron transfer. They found that electrons travel up to 14 Å between redox centres through the protein medium and that transfer over longer distances always involves a chain of cofactors. The role of the haem B, which is located some 11.4 Å beyond ubiquinone with respect to FMN and within electron transfer range of both the 3Fe-4S centre and ubiquinone in the porcine structure, is not known. However, Nakamura *et al* (*12*)

and Nihei *et al* (*13*) have shown that haem is essential for functional assembly and the structural stability of the *E. coli* complex and Matsson *et al* (*14*) have reported reduction of haem in the *Bacillus subtilis* complex during catalysis. Also of note is the seemingly excessive complexity of the complex II structure compared with other enzymes which couple oxidation of an organic substrate to reduction of quinone. For example, the membrane-associated *E. coli* enzymes NADH dehydrogenase II, D-lactate dehydrogenase and aerobic glycerol-3-phosphate dehydrogenase all carry out this function and all consist of a single polypeptide binding a single flavin moiety (*15*). As a possible explanation of this inconsistency it has been suggested that complex II carries out additional, as yet unrecognised, tasks such as sensing the concentration of molecular oxygen (*16*).

Further indicators that complex II may have functions additional to that of a succinate:ubiquinone oxidoreductase come from comparison of the complex with the closely related and functionally-opposite fumarate reductase, of which structures are available from *E. coli* and *Wolinella succinogenes* (*17;18*). The extracellular domains of both fumarate reductase structures are similar to each other and to the extracellular domain of complex II. However, the membrane domains differ between the two fumarate reductase structures and the complex II structure in the type and number of prosthetic groups that they bind. The membrane domain of fumarate reductase from *W. succinogenes* binds two B-type haems: b_P and b_D. In approximately equivalent positions to these two haems the *E. coli* fumarate reductase, which binds no haems, binds two menaquinones: Q_P and Q_D. Curiously haem b_P and menaquinone Q_P are in approximately equivalent positions to the haem *b* of porcine complex II where the equivalent position of b_D and Q_D is occupied by the two sidechains of a structural phosphatidylethanolamine lipid (PE1) (or cardiolipin in the *E. coli* structure) (*19*). Furthermore, in complex II from Archaea and most Gram-positive bacteria each of these two positions is occupied by a B-type haem. Parallels between the arrangement of co-factors found within the membrane domains of the complex II superfamily and the arrangement of haem b_L and b_H in cytochrome bc_1 complex (see section 1.1.3.2) have prompted suggestions that complex II from some species may pump protons by a similar mechanism to cytochrome bc_1 complex

(*20*). However, there is currently no experimental evidence to support generation of PMF by complex II.

Also of relevance to the mechanism of complex II, in particular to the oxidation of succinate via hydride transfer to FAD, is a recent study on the soluble fumarate reductase from *Shewanella frigidimarina* by Chapman *et al* (*21*). This study defines a proton pathway, consisting of Arg-381, Glu-378 and Arg-402 (*S. frigidimarina* numbering), which delivers a single proton per catalytic cycle to FAD and is preserved throughout the fumarate reductase/succinate dehydrogenase family of enzymes. Although the primary sequences of the soluble fumarate reductase and the Fp subunit of porcine complex II differ considerably, analysis of the available high resolution structures reveal that much of the secondary structure has been retained. Closer inspection of the architecture surrounding the succinate/fumarate binding site suggests that a proton pathway equivalent to that described by Chapman *et al* may be formed by Arg-270, Glu-267 and Arg-298 (porcine numbering) in the Fp subunit of complex II (see Figure 1.4). This pathway would function to supply a proton to FAD (from the matrix) accompanying its reduction and remove a proton accompanying its reoxidation.

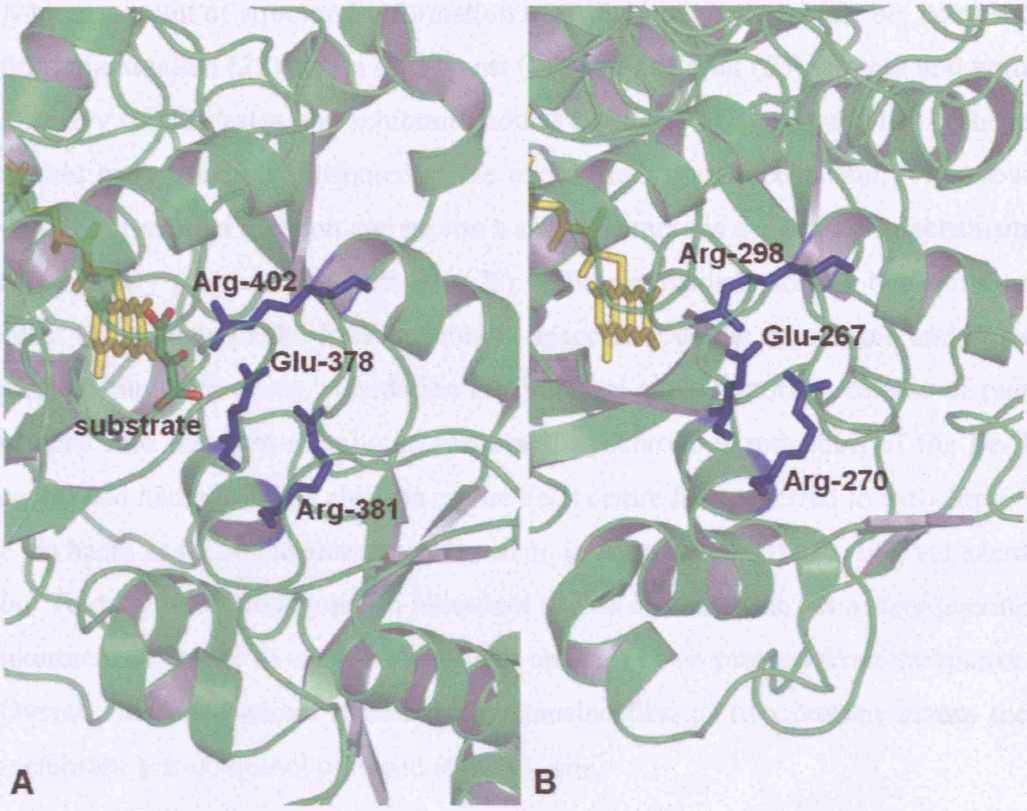

Figure 1.4 Proton delivery pathway complex II. A. Active site and proton delivery pathway in soluble fumarate reductase from *S. frigidimarina* and B. Succinate binding site and putative proton delivery pathway in Fp subunit of porcine complex II. FAD is drawn in yellow and sidechains forming the (putative) proton pathway are drawn in blue. The difference in the position of Arg-402/409 is likely to result from the presence of substrate in A. and its absence in B. Figure drawn using PyMOL™ from PDB files 1QJD and 1ZOY.

1.1.3.2 Cytochrome bc_1 complex

Electrons are transferred from ubiquinol to cytochrome *c* by cytochrome bc_1 complex. For each ubiquinol oxidised two protons are translocated across the membrane (*5*). Bovine cytochrome bc_1 complex consists of 11 subunits; however, only three of these contain redox active prosthetic groups: - "Rieske" iron-sulphur protein contains a 2Fe-2S Rieske-type Fe-S centre, cytochrome c_1 contains a C-type haem and cytochrome *b* contains two B-type haems. Extraction of fully functional *Rhodobacter capsulatus* cytochrome bc_1 complex consisting solely of three subunits homologous to the redox centre-containing bovine subunits suggests that the non-redox centre-containing subunits do not play a role in the core function of the complex (*5*). This conclusion is further supported by the fact that there are no homologues of the bovine non-redox centre containing subunits encoded in the *Rba. capsulatus* genome.

A large amount of structural information is available on cytochrome bc_1 complex from mammalian (*22*), avian (*23*), yeast (*24*) and bacterial (*25*) sources and with a variety of substrates and inhibitors bound (*22;26;27*) (see Figure 1.5). These studies have greatly contributed to the understanding of mechanism. It is now widely agreed that electron and proton transfer occurs via a 'Q-cycle' mechanism as originally proposed by Mitchell (*28*). The mechanism utilises two quinone sites: Q_o is close to the inter-membrane space side of the membrane and Q_i is close to the matrix side. Oxidation of ubiquinol at Q_o results in release of two protons into the inter-membrane space and synchronous reduction of the Fe-S centre and haem b_L. The electron on the Fe-S centre is transferred to cytochrome *c* via haem c_1 while the electron on haem b_L is transferred to the Q_i-site, via haem b_H. Reduction of ubiquinone to ubiquinol occurs in two steps, via a semiquinone intermediate, at the Q_i-site and results in uptake of two protons from the matrix. Overall, this mechanism results in the translocation of two protons across the membrane per ubiquinol oxidised at the Q_o-site.

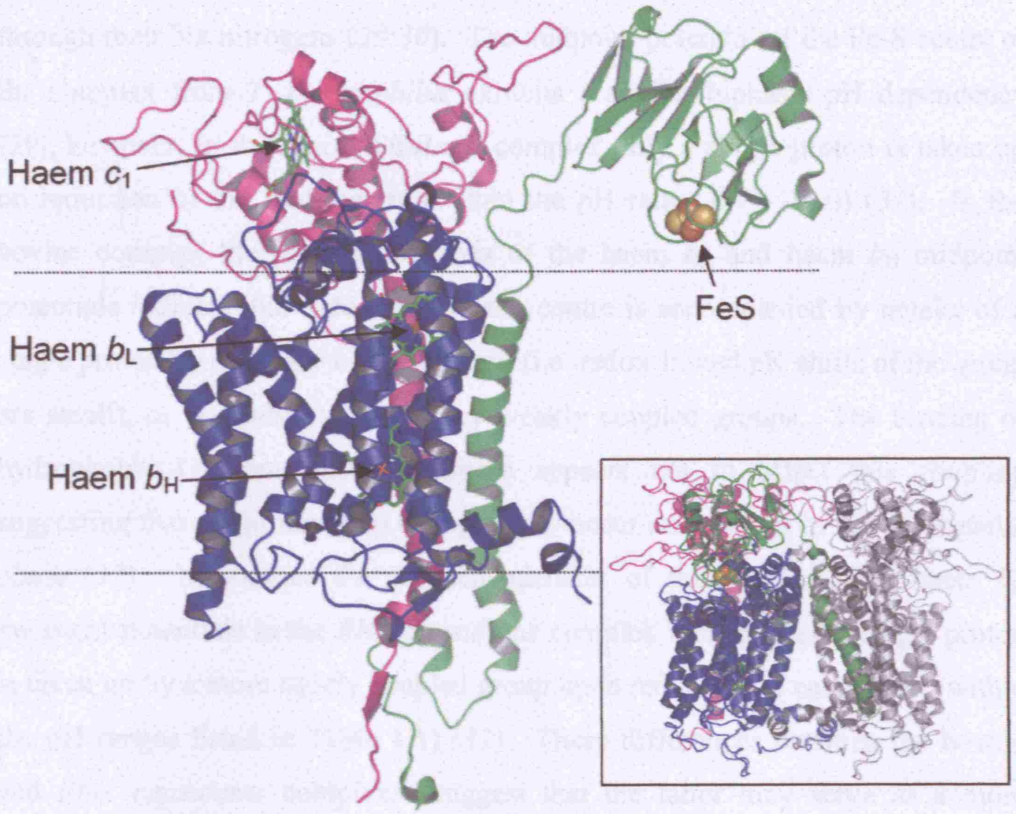

Figure 1.5 Structure of core subunits of bovine cytochrome bc_1 complex. Cytochrome *b*, cytochrome c_1 and Rieske iron-sulphur protein are shown in blue, magenta and green respectively. B-type and C-type haems are drawn as 'stick' structures; the iron and sulphur atoms of the Rieske-type 2Fe-2S centre are shown in red and orange respectively. Approximate position of membrane is indicated by dotted lines (orientation is such that the inter-membrane space is at the top of the page). In the dimer structure (see inset structure of *Rba. capsulatus* dimer) the Fe-S centre of one monomer is located close to the haem c_1 and haem b_L of the other monomer; this interaction is necessary to form the active homodimeric structure. Figure drawn using PyMOL™ from PDB files 1NTM and 1ZRT.

The midpoint potentials, and their pH dependencies (see Table 1.1), of the redox centres of cytochrome bc_1 complex support a Q-cycle mechanism with high potential (Fe-S and haem c_1) and low potential (haem b_L and haem b_H) chains. Midpoint potentials with pH dependency indicate that redox change of the group is accompanied by a protonation state change of either the redox group itself or a separate group with a redox-dependent pK (for example, a protonatable amino acid sidechain). The pH dependency of the Fe-S centre midpoint potential in the bovine complex indicates that reduction of the centre is accompanied by uptake of a single proton within the pH range 7.6 - 9.2 and two protons within the pH

range 9.2 - 10.0 (*29*). The two protonatable groups are the Nτ nitrogens of each of the two histidine sidechains that coordinate the Rieske-type 2Fe-2S centre through their Nπ nitrogens (*29;30*). The midpoint potential of the Fe-S centre of the complex from *T. thermophilus* exhibits a similar biphasic pH dependency (*29*), however, in the *Rba. capsulatus* complex only a single proton is taken up on reduction of the Fe-S centre (within the pH range 6.7 - 10.0) (*31*). In the bovine complex the pH dependencies of the haem b_L and haem b_H midpoint potentials indicate that reduction of each centre is accompanied by uptake of a single proton by a weakly coupled group (i.e. redox-linked pK shifts of the group are small), or possibly by many very weakly coupled groups. The binding of hydrophobic Q_o- or Q_i-site inhibitors appears not to affect this coupling suggesting that the protonation changes may occur on residues in the hydrophilic phase (*32*). In contrast the pH dependencies of the haem b_L and haem b_H midpoint potentials in the *Rba. capsulatus* complex indicate that a single proton is taken up by a more tightly coupled group upon reduction of each haem (within the pH ranges listed in Table 1.1) (*31*). These differences between the bovine and *Rba. capsulatus* complexes suggest that the latter may serve as a more convenient system for investigating the currently unknown protonatable groups redox-linked to the B-type haems.

Component	E_{m7} (mV)*		pH dependency (mV per pH unit, approximate range pH range of dependency quoted as pK_{red} to pK_{ox})	
	Bovine	*Rba. capsulatus*	Bovine	*Rba. capsulatus*
Fe-S	305 [a]	320 [d]	0 (≤5.5 to 7.6) -60 (7.6 to 9.2) -120 (9.2 to ≥10.0) [a]	0 (≤5.0 to 6.7) -60 (6.7 to ≥10.0) [d]
Haem c_1	242 [b](*33*)	320 [d]	0 [e]	0 [d]
Haem b_L	-25 [c]	-140 [d]	0 (≤5.0 to 5.9) -60 (5.9 to 7.9) 0 (7.9 to ≥9.0) [c]	-60 (5.0 to 9.0) 0 (9.0 to ≥10.0) [d]
Haem b_H	90 [c]	40 [d]	0 (≤5.0 to 5.7) -60 (5.7 to 7.7) 0 (7.7 to ≥9.0) [c]	0 (≤5.0 to 6.4) -60 (6.4 to 9.2) 0 (9.2 to ≥10.0) [d]

Table 1.1 Midpoint potentials of redox components of cytochrome bc_1 complex. * Potentials are quoted versus standard hydrogen electrode (SHE). References: [a] (*34*), [b] (*33*), [c] (*32*), [d] (*31*), [e] (*35*).

Despite this detailed information, several key features of the electron-/proton-transfer mechanism of cytochrome bc_1 complex remain unclear. For example, the physical and chemical factors that cause the strictly bifurcated electron transfer from ubiquinol at the Q_o-site to haem b_L and the Fe-S centre while preventing the energetically favourable 'short circuit' reduction of the Fe-S centre by haem b_L are not known. Although structures are available with Q_o-site inhibitors bound there are no structures available with ubiquinone bound and the identities of the amino acid sidechains that interact with quinone during redox catalysis are under debate (see below). Our understanding of the Q_o-site is further complicated by data from electron paramagnetic resonance (EPR) (*36*), nuclear magnetic resonance (NMR) (*37*) and inhibitor binding titration (*38*) studies which have led to suggestions that the Q_o-site either binds two ubiquinones simultaneously or that two sequential binding positions may be in operation (*5*). It has been suggested by Crofts *et al* (*39;40*) that movement of substrate ubiquinol/semiquinone in the Q_o-site may be required for bifurcated

electron transfer. However, it has been argued by Rich *et al* (*41*) that strict bifurcation upon formation of the iron-sulphur-ubiquinone-haem b_L ternary complex occurs simply as a result of the thermodynamics and that relative rate constants of the complex and multiple binding positions (or formation of a semiquinone intermediate) are not required. In addition, some variation in the position of the Fe-S centre-containing domain of the iron-sulphur protein has been found in the available structures. In the static structures the distances are such that rotational displacement of this domain must occur in order to allow interaction of the Fe-S with both the ubiquinol-haem b_L complex and cytochrome c_1 (*5;42*). The movement may also play a role in the prevention of 'short circuit' reduction of the Fe-S centre by haem b_L. These complications have led to a range of mechanistic models (*41-49*). However, a recent detailed quantitative assessment based upon predicted electron transfer rates by Osyczka *et al* (*31*) has led to the conclusion that none can satisfactorily account for the rapid reversibility and low rates of unwanted short-circuit reactions. It was concluded that this could be achieved only by a 'true' concerted n = 2 oxidation of quinol or by addition of further complicating gating mechanisms (*31*).

As mentioned above cytochrome bc_1 complex has not yet been co-crystallised with bound ubiquinone. However, other studies have yielded valuable insight into the organisation of the Q_o-site (shown in detail from *Rba. capsulatus* with stigmatellin bound, in Figure 1.6). For example, a recent study of the iron-sulphur protein in isolation and in the intact complex by IR spectroscopy supports the suggestion that the Nτ nitrogen of one of the histidine sidechains that coordinate the Fe-S centre (His-161 in bovine and His-156 in *Rba. capsulatus* of the iron-sulphur protein) forms a hydrogen bond acceptor for substrate quinol (*30*). Also implicated in the Q_o-site mechanism is the glutamic acid residue (Glu-271 in bovine and Glu-295 in *Rba. capsulatus*) of the highly conserved PEWY loop of cytochrome *b*; in addition to being one of few protonatable amino acids near the Q_o-site, the sidechain of Glu-295 adopts different orientations depending on the presence and type of Q_o-site inhibitor (*50-53*). The role of Glu-295 is further discussed alongside new data from infrared spectroscopy in Chapter 4; existing IR data on cytochrome bc_1 complex

is also discussed in Chapter 4 (in order to allow for the technique to first be introduced in section 1.2).

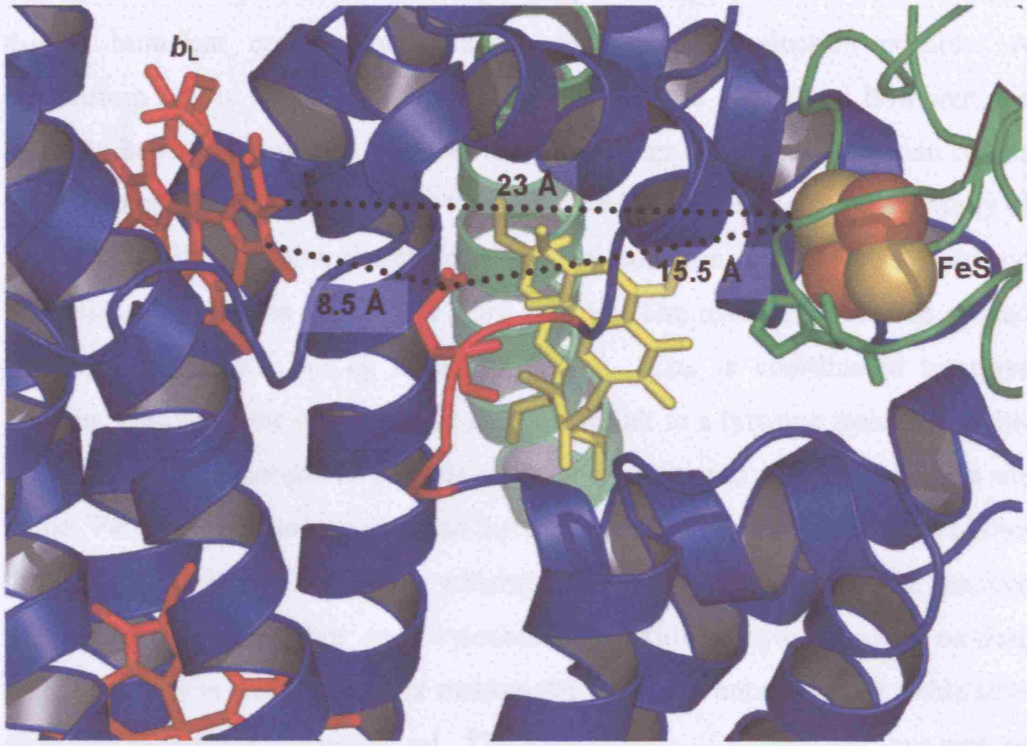

Figure 1.6 Detail of the Q_o-site of *Rba. capsulatus* cytochrome bc_1 complex. Cytochrome *b* and Rieske iron-sulphur protein are shown in blue and green respectively. The conserved PEWY motif of cytochrome *b* is shown in red with Glu-295 shown as sticks. Stigmatellin (shown in yellow) is within hydrogen bonding distance of Glu-295 and His-156 of the iron-sulphur protein (green sticks) (*25*). Distances shown are edge to edge and are taken from (*53*). Figure drawn using PyMOL™ from PDB file 1ZRT.

1.1.3.3 Cytochrome *c* oxidase

Cytochrome *c* oxidase catalyses the oxidation of cytochrome *c* and reduction of O_2 to H_2O. Electron transfer is coupled to proton translocation across the membrane according to the equation: -

$$4 \text{ cytochrome } c^{2+} + O_2 + 8\ H^+n \rightarrow 4 \text{ cytochrome } c^{3+} + 2\ H_2O + 4\ H^+p$$

Where H^+n and H^+p refer to the protons translocated from the negative side to the positive side of the membrane, respectively.

As with succinate:ubiquinone oxidoreductase and cytochrome bc_1 complex, atomic resolution structures are available for both mammalian and bacterial forms of cytochrome *c* oxidase (*54-57*). Mitochondrial cytochrome *c* oxidase is a dimer with each monomer consisting of 13 subunits. Three subunits make up

the catalytic core (see Figure 1.7) which contains a bimetallic Cu^{2+}-Cu^{+} centre termed Cu_A, haem *a* and haem a_3-Cu_B binuclear centre (*5*). Electrons are transferred from cytochrome *c*, through Cu_A, to haem *a* and then onto the haem a_3-Cu_B binuclear centre where oxygen binding and reduction occurs. A magnesium ion is also present in bovine cytochrome *c* oxidase; however, the complex has been shown to retain 40% activity after up to 75% depletion of this ion (*58*) therefore it is not thought to be involved in the catalytic cycle. Many of the details of the complex chemistry of oxygen reduction to water are known and a simplified scheme is shown in Figure 1.8 (*5*). The reaction is centred around the high spin haem a_3-Cu_B binuclear centre. Cu_B is coordinated by three histidine residues, one of which has a covalent link to a tyrosine residue and this his-tyr doublet is thought to provide a transient additional electron donation site at the 'Peroxy' intermediate stage of the catalytic cycle (see below). This allows the four electron reduction of O_2 without release of potentially-harmful reactive oxygen species (*59*). For each cytochrome *c* oxidised cytochrome *c* oxidase takes up a proton from the matrix making the transition between each stable state shown in Figure 1.8 electroneutral. The translocation of an addition four protons from the matrix to the inter-membrane space is coupled to the reduction of each O_2. However, the mechanism of coupling is not well understood and the pathways for transfer of protons through the protein structure are controversial (*5*). The available structures show several arrays of relatively hydrophilic amino acids and water molecules that may act as proton channels. Channels D and K, named after conserved aspartic and lysine residues, are likely to allow protons to move from the matrix to the binuclear site. The four protons required for reduction of O_2 are likely to be transferred through the D channel. The route(s) by which protons are released into the inter-membrane space remains unknown (*5*).

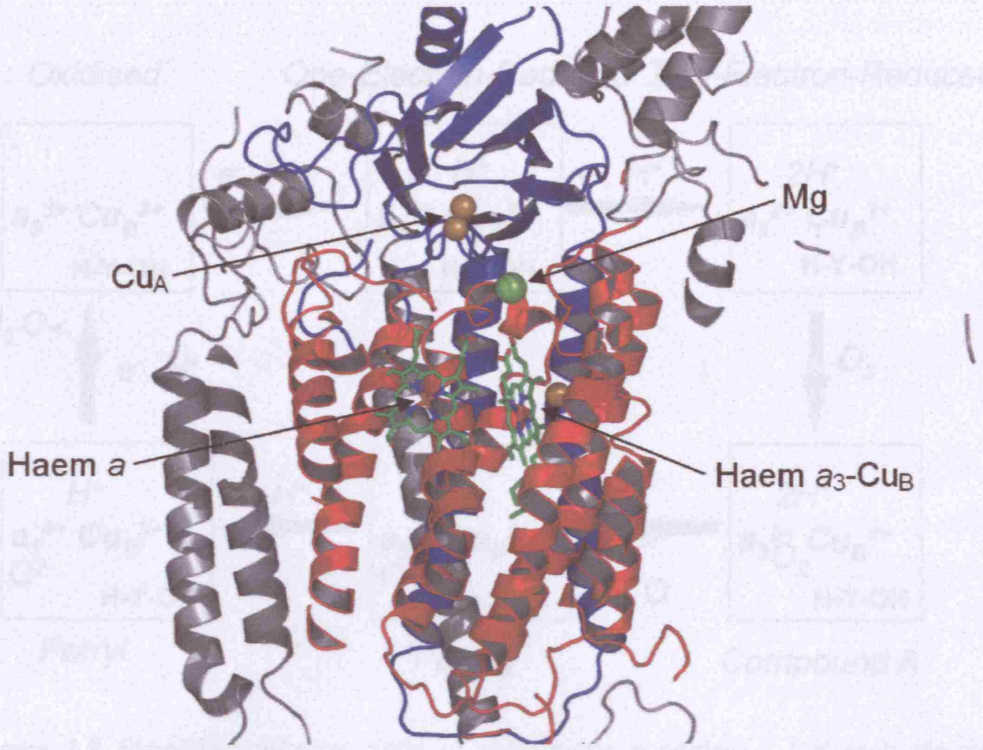

Figure 1.7 Section through cytochrome *c* oxidase structure from bovine heart. The bimetallic Cu^{2+}-Cu^{+} centre Cu_A, haem *a* and the haem a_3-Cu_B binuclear centre are labelled. Subunits I and II are coloured red and blue respectively; all other (visible) subunits are coloured grey. Orientation is such that the plane of the membrane would be approximately perpendicular to the page and the inter-membrane space would be located towards the top of the page. Figure drawn using PyMOL™ from PDB file 2OCC.

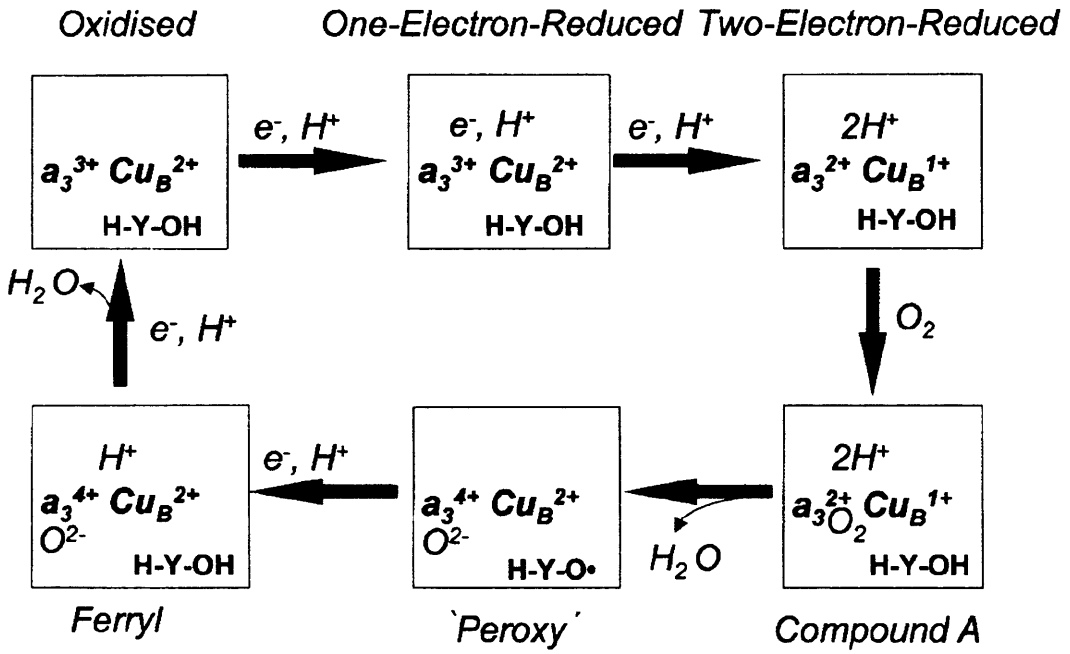

Figure 1.8 Simplified reaction cycle of cytochrome *c* oxidase. For each electron supplied by cytochrome *c* a proton is taken up from the matrix. Cytochrome *c* donates an electron to oxidised cytochrome *c* oxidase forming the one-electron-reduced state where the electron, transferred via Cu_A, is shared by haem *a* and the haem a_3-Cu_B binuclear centre. Subsequent reduction by another reduced cytochrome *c* results in the two-electron-reduced state which binds molecular oxygen to form an unstable oxygen-ferrous species that is similar to oxyhaemoglobin and termed compound A. This converts to the 'Peroxy' state by a four electron reduction of O_2 with two electrons from ferrous haem a_3, one from cuprous Cu_B and one, most probably from the his-tyr doublet. This results in formation of the ferryl form of haem a_3, cupric Cu_B and a radical on his-tyr, together with one molecule of H_2O. A third cytochrome *c* reduces the his-tyr radical back to its ground state to produce the so-called 'Ferryl' intermediate. The final reduction converts ferryl haem a_3 back into its ferric state and results in release of the second molecule of H_2O and reversion of the complex to the oxidised state. In addition, the translocation of four protons from the matrix to the inter-membrane space is coupled to this cycle (see text). Figure adapted from (*5*).

1.1.3.4 Ubiquinone and cytochrome *c*

Ubiquinone, also known as coenzyme Q, consists of a 2,3-dimethoxy-5-methyl-para-benzoquinone ring with a long poly-isoprenoid tail in the 6th position (see Figure 1.9) (*60*). The isoprenoid tail contributes to the hydrophobic nature of the molecule and the benzoquinone ring is redox active existing in quinone, semiquinone and quinol forms. Ubiquinone transfers electrons within the membrane environment from complexes I and II to cytochrome bc_1 complex. Crucial to the mechanism of cytochrome bc_1 complex (see section 1.1.3.2), ubiquinone/ubiquinol in the membrane gains/loses two protons in its two electron

reduction/oxidation step. The semiquinone pK is around 6 in solution (*61*); however, this is often changed when bound so that ubiquinone can be reduced to semiquinone with or without uptake of a proton. The stability of the semiquinone form is very low and it is not able to exist as a freely diffusing species within the membrane environment. However, it is a key intermediate in the mechanisms of complexes I, II and III where its stability can be greatly enhanced by protein interactions through quinone-binding sites during interconversion between ubiquinone and ubiquinol.

Ubiquinone interacts with proteins through quinone-binding sites (Q-sites). These are widespread amongst membrane bound redox proteins and more than 50 distinct Q-sites associated with respiratory and photosynthetic electron transfer complexes are already known. The diverse origins of these proteins probably contribute to the diversity of Q-sites and to the challenge in identifying common structural motifs that they present (*62*). Analysis of available high-resolution structures and sequence alignments has shown the presence of a weak motif in a number of known quinone-binding proteins, supported by analysis of available high-resolution structures. This weak sequence motif suggests a triad of residues of the form aliphatic-(X)3-H-(X)2/3-(L/T/S) form the Q-site and interact with the quinone (*62*). However, it is already clear that Q-site structures are very diverse with no single common structural motif. In addition, Q-sites must be accessible to ubiquinone and therefore require access pathways that allow rapid equilibration with ubiquinone species that are located in the membrane domain. The sites are hydrophobic in nature with aliphatic and aromatic residues flanking the head group of the bound quinone. Common features of Q-sites also include the ability to form hydrogen bonds with the carbonyl/hydroxyl groups for stabilising bound quinone/quinol and facilitating protonation/deprotonation (*62*). For those deeply-buried Q-sites that utilise the QH_2/Q couple, it is also necessary for the protein to provide a channel or other link to allow protons to move between the Q-site and an aqueous phase.

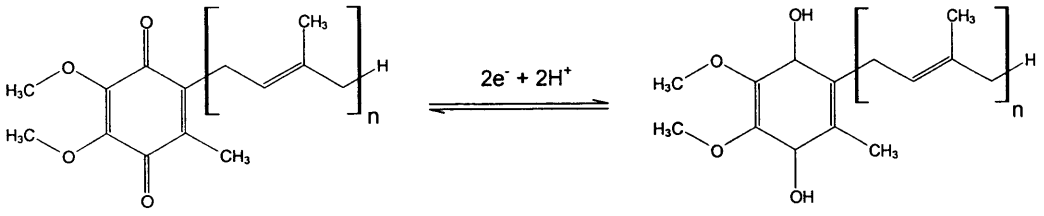

Ubiquinone Ubiquinol

Figure 1.9 Structure of oxidised and fully-reduced forms of ubiquinone (coenzyme Q). n is generally between 8 and 10.

Cytochrome *c* transfers single electrons between cytochrome bc_1 complex and cytochrome *c* oxidase. It is a small (mass of equine cytochrome *c* = 12,384 Da) soluble protein found loosely associated with the inter-membrane space surface of the inner membrane of mitochondria (*63*). The single polypeptide chain coordinates a low spin haem C. The C haem porphyrin ring is covalently bound to cysteine 14 and 17 while the haem iron is axially coordinated by the Nτ nitrogen of the imidazole sidechain of histidine-18 and the sulphur atom of methionine 80 (see Figure 1.10) (*63*). One edge of the haem porphyrin ring is accessible to the exterior via a cleft which is surrounded by a cluster of lysine sidechains. This array of positive charges on the surface of cytochrome *c* is necessary for its strong electrostatic interactions with its negatively-charged docking sites on complexes III and IV (*2*). In addition to its role in the respiratory electron transfer chain, cytochrome *c* has been shown to be an important intermediate in apoptosis, programmed cell death, where release of cytochrome *c* (and other inter-membrane factors) into the cytoplasm appears to trigger the apoptopic caspase cascade (*64*).

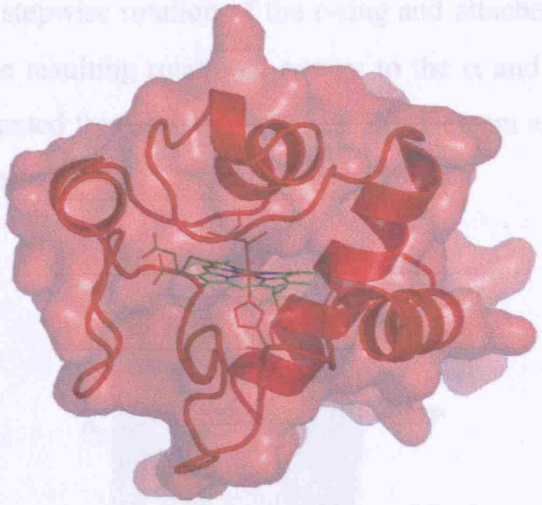

Figure 1.10 Structure of equine cytochrome *c*. Ribbon diagram of equine cytochrome *c* structure at 1.9 Å superimposed on semitransparent molecular surface. The porphyrin ring of haem *c* (shown as sticks coloured by element) is covalently bound to cysteine-14 and -17 (red sticks); axial coordination of the haem *c* iron is provided by histidine-18 and methionine-80 (also shown as red sticks) (see text for details). Orientation is such that the haem is most accessible from the surface which is facing the viewer. Figure drawn using PyMOL™ from PDB file 1HRC.

1.1.3.5 ATP synthase

Complexes I to IV catalyse the oxidation of NADH and succinate to NAD^+ and fumarate respectively and the reduction of molecular oxygen to water. Coupled to this highly exergonic electron transfer is the translocation of protons from the matrix to the inter-membrane space creating the PMF. By allowing the passage of protons from the *p*-side to the *n*-side of the membrane the F_1F_0 ATP synthase is able to use the PMF to drive the highly endergonic generation of ATP from ADP and inorganic phosphate. The F_1F_0 ATP synthase consists of two large subcomplexes: F_1 located on the matrix side of the membrane and F_0 which spans the membrane (see Figure 1.11). The complex functions via a rotary catalytic mechanism where a central region (F_1-$\gamma\varepsilon F_0 c_{10}$) rotates relative to the surrounding region ($F_1\alpha_3\beta_3\delta$-$F_0 ab_2$). Central to this mechanism is a multimeric ring of *c* subunits within the rotating central region. Channels connect this ring to both the *p*- and *n*- sides of the membrane. These allow protons to enter and leave the ring, however, to pass the ring they must protonate a *c* subunit at asparagine 61, drive rotation of the ring, then deprotonate close to the channel leading to the *n*-side of the membrane. It is proposed that passage of protons in this manner, causing repeated protonation then deprotonation of the subunits of

the *c*-ring, causes a stepwise rotation of the *c*-ring and attached subunits. The γ subunit transmits the resulting rotational energy to the α and β subunits which are themselves prevented from rotating by the stator element and use this energy to drive ATP synthesis (*65*).

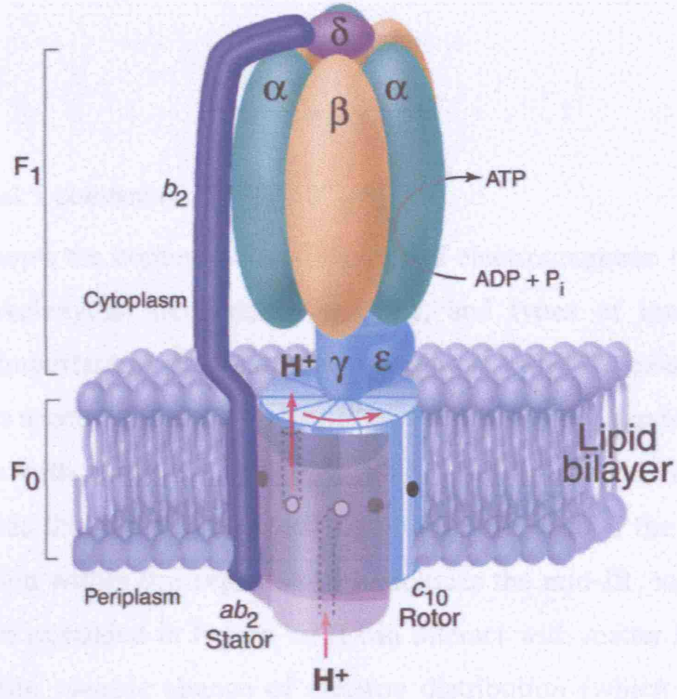

Figure 1.11 Schematic showing proposed mechanism for the *E. coli* F_1F_0 ATP synthase. Proton entry from the periplasm through a channel in the F_0 subcomplex results in protonation of a *c* subunit on asparagine 61 (open/closed circles) and stepwise rotation of the c_{10} rotor or *c*-ring. Protons exit the F_0 subcomplex into the cytoplasm after the rotor has completed its 10 step rotation. Rotational energy is passed to the α and β subunits which are themselves prevented from rotating by the stator and used for ATP synthesis from ADP and inorganic phosphate. Figure reproduced from (*65*).

1.2 Spectroscopy

The work of this thesis has employed two major types of spectroscopy, namely ultraviolet (UV)/visible and mid-range Fourier Transform Infrared (FTIR), the basic principles of which are outlined below. However before discussing spectroscopy, it is useful briefly to describe the nature of electromagnetic radiation.

According to Maxwell's classical theory of electro- and magnetodynamics electromagnetic radiation consists of two mutually perpendicular electric and magnetic fields oscillating in single plans at right angles to each other. These fields are in phase and propagate as a sine wave at a constant velocity of

2.997925×10^{8} m.s^{-1}, the speed of light (c). The frequency (ν) of electromagnetic radiation is therefore related to wavelength (λ) as shown below:

$$\nu = c/\lambda$$

The energy (E) associated with an electromagnetic wave is related to its wavelength:

$$E = hc/\lambda$$

Where h = Planck's constant (4.135667×10^{-15} eV.s)

Figure 1.12 shows the common classifications of electromagnetic radiation with associated wavelengths, frequencies, energies, and types of interaction with matter. It is important to note that electromagnetic radiation exists as a broad and continuous spectrum: "common name" classifications overlap as do the types of interactions with matter which are possible. The interactions of matter and radiation outside the 10^{-3}-10^{-7} m wavelength range are beyond the scope of this study. Radiation within this region, which includes the mid-IR, visible and UV regions (shown expanded in Figure 1.12) can interact with matter in one of two ways: absorption causing change of electron distribution (which can result in structural changes) and absorption causing change of rotational/vibrational state. The former occurs via excitation of electron(s) in certain chemical groups from lower to higher energy states and requires the energy of the radiation to be equal to the electronic transition energy. The energies involved typically correspond to radiation in the near-infrared, visible and UV regions and, in this work, absorption is studied by UV/visible spectroscopy (see section 1.2.1). Electromagnetic radiation can also be absorbed by causing change of configuration. This occurs when the frequency of the radiation matches that of a molecular vibration and is caused by coupling of the electric field vector of the electromagnetic wave with the dipole moment of the molecular vibration. The energies involved in this type of interaction are lower than those required to cause a change of electron distribution and typically correspond to radiation in the mid-range and far infrared regions; absorption is studied by IR spectroscopy (see section 2.4).

Conventionally, IR spectroscopic data are plotted in reciprocal wavelength units (wavenumber (cm^{-1})). The use of wavenumber to describe wavelength/frequency is useful because the wavenumber scale is linearly proportional to energy (see Figure 1.12). In contrast, UV/visible spectroscopic data are usually plotted on a wavelength scale in nm. The interrelation between these scales, and their conversion into energy units, is summarised in Figure 1.12.

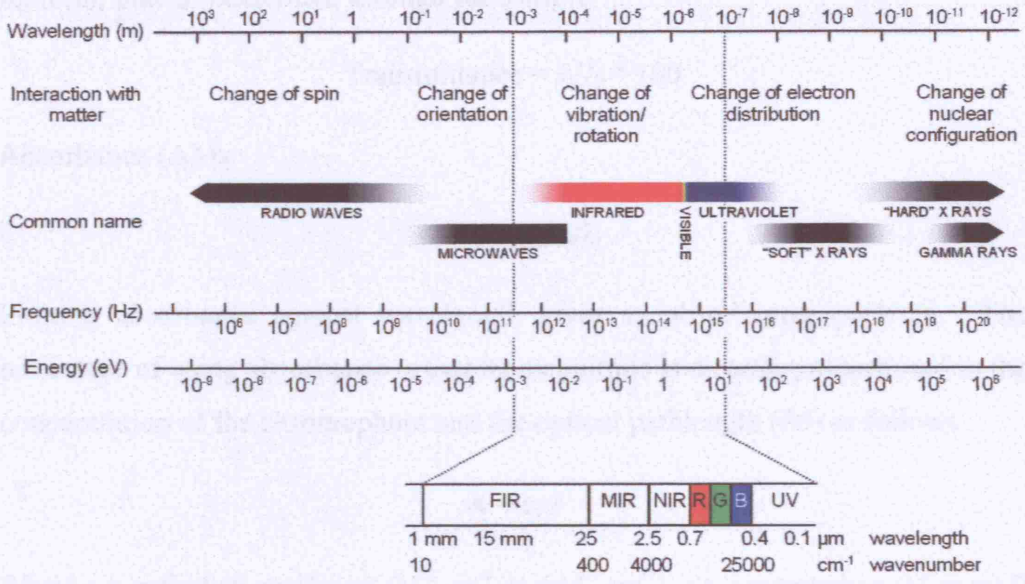

Figure 1.12 The electromagnetic spectrum. Expanded region shows far infrared (FIR), mid-range infrared (MIR), near infrared (NIR), visible (shown in colour) and ultraviolet (UV) regions (see text).

1.2.1 UV/Visible spectroscopy

Many chemical groups contain electrons that can be promoted to higher energy orbitals by absorption of electromagnetic radiation with energy that matches the electronic transition energy. In such chromophores, the energies necessary for excitation/absorption correspond to electromagnetic radiation in the 200-2000 nm range encompassing the UV, Visible and near-infrared.

For redox-active chromophores, many of these electronic transitions are dependent upon redox state; hence, absorption spectra in the UV/visible/near-IR regions can be very informative regarding redox changes. Furthermore, each chemically-distinct chromophore has a distinct signature and so can be used to quantitatively deconvolute multiple redox groups.

Typically a UV/visible spectrum is measured by preparing a sample in a transparent cuvette then passing a beam of UV/visible radiation through the sample (see Figure 1.13). In a step-scanning spectrometer, use of a monochromator allows the wavelength of the incident radiation to be stepped through an appropriate range. The intensity of the transmitted radiation (I_I) is recorded for each step. Transmittance is defined as the percentage of incident light (I_0) that is transmitted through the sample:

$$\text{Transmittance} = I_I/I_0 * 100$$

Absorbance (A) is:

$$A = \log_{10} I_0/I_1$$

Plotting absorbance against wavelength gives an absorbance spectrum. The advantage of using absorbance is that its magnitude is directly proportional to the concentration of the chromophore and the optical pathlength (*66*) as follows:

$$A = \varepsilon cl$$

Where ε = extinction coefficient ($M^{-1}.cm^{-1}$ or $mM^{-1}.cm^{-1}$), c = concentration (M or mM) and l = path length (cm)

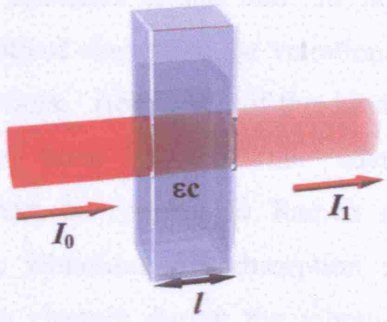

Figure 1.13 Interaction of UV/visible radiation and sample. Incident radiation (I_0) enters cuvette of path length (l) containing sample of concentration (c) and extinction coefficient (ε); sample absorbs a portion of the radiation and attenuated radiation (I_I) exits cuvette.

The concepts of transmittance, absorbance and extinction coefficient are equally applicable to IR spectroscopy in transmission mode since measurements are made with a frequency-independent pathlength. They can also apply to IR spectroscopy in attenuated total reflection (ATR) mode provided that the

frequency-dependent effective pathlength can be determined (see section 1.2.2.2 for description of IR spectroscopy in ATR mode).

UV/Visible spectroscopy has played a major role in the detection and kinetic characterisation of many of the electron transfer prosthetic groups of the respiratory electron transfer chain because many contain chromophores with characteristic UV/visible/near-IR features (*67;68*). For example, the reduced and oxidised forms of A-, B-, and C-type haem groups (*68*), FMN and FAD (*69*) all have characteristic and well-documented UV/visible absorption bands that can be used to quantitate their levels and follow the kinetics of their redox changes during catalysis. Exceptions, however, are Fe-S centres: they do have very broad redox-dependent absorbance bands over the UV/visible range but these have small extinction coefficients, are rather featureless and generally do not allow different Fe-S centres to be distinguished. Hence, for complex I UV/visible spectroscopy has been useful primarily for FMN studies and other spectroscopies are required for analyses of the Fe-S centres.

1.2.2 Infrared spectroscopy

Distinct from absorption via the excitation of electrons to orbitals of higher energy, electromagnetic radiation in the mid- to far-IR range can also be absorbed by causing quantised changes in the vibrational (and rotational) modes of chemical bonds and groups. Absorption of this kind occurs when the energy of the electromagnetic wave matches the energy gap between the vibrational/rotational states; in contrast to Raman spectroscopy which has different selection rules, vibrational IR absorption requires that the dipole moment of the molecule changes during the vibration. The probability of absorption, and therefore the extinction coefficient, increases with increasing bond polarity (*70;71*). The energies associated with molecular vibrations are lower than those required for electronic transitions and are most commonly studied in the mid-IR region (typically over the 4000-800 cm^{-1} range that is most easily accessed from a technical point of view). However, there are many further vibrational modes below 800 cm^{-1} in the far-IR region and more recent technical developments are beginning to allow application of far-IR spectroscopy to biological problems.

1.2.2.1 Fourier transform spectroscopy

In section 1.2.1 the principle of step-scanning spectroscopy in the UV/visible range using a monochromator was described; this technique is also applicable to IR spectroscopy. A convenient alternative to step-scanning, which has become standard in mid- and near-IR ranges and is sometimes used in the UV/visible range, is Fourier transform spectroscopy. In this method a beam of broad frequency radiation is passed through a Michelson interferometer prior to interacting with the sample. The interferometer consists of a beam splitter and two mirrors, one of which is suspended on an air-bearing and able to move. The beam first strikes the beam splitter, ½ passes through and ½ is reflected at 90°. Both of the resulting beams are subsequently reflected 180° back towards the beam splitter, one by the fixed mirror and one by the movable mirror. Upon striking the beam splitter for a second time the beams recombine to yield two beams each of half the original intensity, one is directed toward the sample and one is lost in the direction of the radiation source. The variation of position of the movable mirror introduces a varying pathlength difference into the recombined beams causing constructive and destructive interference of specific frequencies to varying extents dependent on the pathlength difference. For each frequency the intensity versus mirror position varies as a sine wave, the peak separation of which is dependent on frequency. These sine waves of intensities of all frequencies combine to produce an interferogram of intensity versus mirror position that is detected by the measuring device. Provided that the position of the mirror is known accurately (which is achieved with a fixed frequency laser that is passed through the same interferometer), the interferogram can be Fourier-transformed with a standard algorithm to produce into a plot of intensity versus frequency and this can be used to derive plots of absorbance or transmittance as in conventional spectra. Typically many interferograms are averaged prior to Fourier transformation in order to increase signal:noise. Typically, acquisition of 1000 interferograms at 4 cm^{-1} resolution, averaging and Fourier transformation requires approximately 2 minutes (for the 4000-400 cm^{-1} mid-IR range). This is significantly less time than would be required to obtain an equivalent spectrum using a step-scanning technique and because of this the introduction of interferometers and Fourier transformation algorithms has widened the biological

applications of mid-/near-IR and UV/visible spectroscopy. The practical limit of the use of the method occurs when the wavelength becomes small in comparison to the accuracy of the mirror position detection system - in devices such as the Bruker IFS66/S, the practical limit of the FT method is around 500 nm (20,000 cm^{-1}).

1.2.2.2 Transmission versus attenuated total reflection modes

FTIR spectroscopy is commonly performed in transmission mode in which the sample to be analysed is placed in an IR-transmitting material or between a pair of IR-transmitting windows. This method is applicable to a wide range of sample types and, because it is relatively simple to set up a sample of defined pathlength, is convenient for determining extinction coefficients. However, transmission mode does have some limitations when analysing samples in aqueous media. H_2O absorbs IR radiation strongly at 1640 cm^{-1} and high sample concentrations are required if IR absorbances of the sample are to be distinguished from those of the solvent. This can be particularly problematic for the study of proteins which may not be stable in solution at the required concentrations (> 20 mg/ml) or may not be available in the quantities required. The strong H_2O absorption at 1640 cm^{-1} generally dictates a maximum sample thickness of approximately 10 μm in order to avoid complete attenuation of the beam at 1640 cm^{-1} and associated loss of signal:noise and introduction of artefacts. Preparation of such thin samples can be time consuming and difficult to achieve reproducibility. In addition, when placing a transmission sample into the IR beam path it is practically impossible to avoid introducing water vapour which, if not purged, masks the sample spectrum in the 2100-1200 cm^{-1} region. A delay between placing the sample in the beam path and collecting data during which time water vapour is purged is necessary, the length of which depends on the sizes of the signals under investigation and on the efficiency of the mechanism by which the water vapour is purged. In the case of vacuum purge instruments this delay is minimal but when a compressed dry nitrogen or air system is used this delay can become problematic particularly for acquiring spectra of unstable samples. In addition, and of great importance for the study of protein by difference spectroscopy, the means by which the sample can be

manipulated *in situ* are limited in transmission mode compared to ATR mode; this point is discussed in detail below and in section 1.2.2.3. Despite these limitations transmission mode spectroscopy has been applied successfully to a number of proteins (see below) and is invaluable as a tool for determining extinction coefficients.

ATR FTIR spectroscopy is an alternative to the transmission technique described above. In ATR FTIR spectroscopy the IR beam is directed from the interferometer through an ATR accessory, principally consisting of a focusing element and an internal reflecting element (IRE), and then onto the detector. The IRE, which is transparent for the IR frequency range of interest, is a prism with geometry such that the IR beam undergoes total internal reflection at a surface onto which the sample is placed. The physics of internal reflection is explained in detail in reference (*72*) and will only be discussed briefly here. Total internal reflection occurs when radiation strikes the IRE/sample interface at an angle greater than θ_c (the critical angle):

$$\theta_c = \sin^{-1} (n_1 / n_2)$$

Where n_1 = refractive index of Sample and n_2 = refractive index of IRE (*72*).

The IR beam produces an evanescent field that extends a short distance into the sample at the point of internal reflection. This distance, typically of the order of a few microns, is dependent on frequency of radiation, incident angle and the ratio of refractive indices of the IRE and sample:

$$d_P = (\lambda/n_1)/(2\pi\,[\sin\theta-(n_1/n_2)^2]^{0.5})$$

Where d_P = depth of penetration, λ = wavelength, n_1 = refractive index of sample, n_2 = refractive index of IRE and θ = angle of incident radiation (*73*).

The evanescent field interacts with the sample in the same way as IR radiation in transmission mode, i.e. the sample absorbs radiation of specific frequencies/energies. Generally the IRE is shaped in such a way that internal reflection occurs several times, each resulting in additional attenuation of the IR beam leading to amplification of the signal. The attenuated beam then exits the IRE and is directed to a detector (see Figure 1.14). The dependence of depth of penetration of the evanescent field - and therefore effective path length - on

frequency leads to an increase in sensitivity of the ATR method that is linearly inversely proportional to frequency. This effect manifests itself as a linear ramp of intensity increase as frequency is lowered that can be clearly seen when comparing ATR FTIR difference spectra with equivalents recorded in transmission mode.

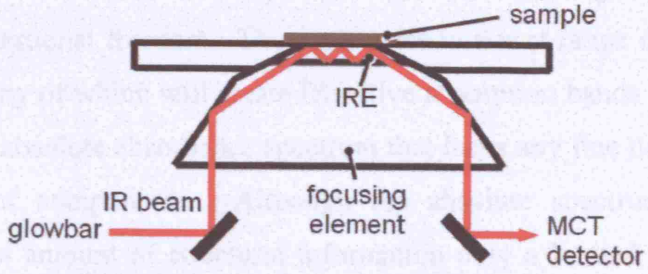

Figure 1.14 Schematic of the ATR accessory used in this study (not to scale). IR radiation (red line) is emitted from a glow bar and (after passing through an interferometer (not shown)) is directed into the IRE via a focusing element. Total internal reflection occurs three times at the sample (shown in brown)/IRE interface. The attenuated radiation is then directed to an MCT detector.

Use of ATR FTIR spectroscopy overcomes many of the disadvantages associated with working in transmission mode, particularly when working with proteins. In recent studies (*30;53;74-76*) protein films have been adhered directly to the IRE by drying. Upon rehydration the protein layer remains adhered to the IRE, presumably by hydrophobic interaction between the protein film and the IRE. In studies done to date, this interaction has been shown not to affect significantly the IR characteristics of the protein or its functionality although this does require confirmation in each case. This technique greatly increases the concentration of the protein within the region of the evanescent field, in comparison to that of a sample in solution, and also decreases the water band contributions. Most importantly, the sample is more accessible than the sealed samples used in transmission mode. This has been exploited by our laboratory's development of devices that allow synchronous acquisition of UV/visible and infrared spectra (see sections 2.4.5 and 2.4.6) and with which redox and ligand changes can be cyclically induced in the protein films. This accessibility is also vital for manipulation of samples *in situ*, the great importance of which will be made clear in section 1.2.2.3.

1.2.2.3 The study of proteins by infrared spectroscopy

The IR absorbance characteristics even of a small protein are complex on account of the great number of vibrational modes present. As an example, a protein of 200 amino acids will consist of approximately 3000 atoms, each of which will have three degrees of vibrational freedom, leading to a total of 9000 degrees of vibrational freedom. These give rise to a vast range of normal mode vibrations, many of which will create IR-active absorption bands. These overlap to produce an absolute absorbance spectrum that lacks any fine detail because of the number of components. Although the absolute spectrum theoretically contains a vast amount of structural information only a limited amount can be easily deconvoluted and interpreted, for example, types of secondary structure content and lipid content. Because of the large number of peptide bonds, common to all amino acids, their normal modes in the 1700-1590 cm^{-1} and 1570-1490 cm^{-1} regions, termed amide I and amide II respectively, dominate protein absolute absorbance spectra. Amide I signals arise primarily from the peptide C=O stretching modes (~80%) with contributions from peptide C-N stretching and N-H bending modes (~10% each) (*73*); they are little affected by the amino acid sidechains (*77*) but their frequencies are governed by their secondary structures. Deconvolution of the broad amide I band (and, to a lesser extent, the other amide bands) has yielded secondary structural information, such as α-helix, β-sheet and β-turn content, that is in good agreement with known high resolution protein structures for proteins both in solution (*78*) and in rehydrated layers adhered to an IRE (*79*). Absolute absorbance spectra are also useful for rapid and accurate determination of the protein/lipid ratio. The carbonyl group of lipids has a characteristic absorbance at 1736 cm^{-1} and the absorbance of protein at this frequency is minor (*79*). Therefore, integrals of the 1736 cm^{-1} lipid band and the protein amide I band can be used to determine the lipid/protein concentration accurately if a calibration curve is prepared. Goormaghtigh *et al* have also derived a quantitative relation using dimyristoylphosphatidylcholine of:

$$S_{\text{amide I}}/S_{\nu(\text{C=O}) \text{ lipid}} = [\text{Protein}]/5.[\text{Lipid}]$$

Where $S_{amide\ I}$ is the integrated area of amide I and $/Sv_{(C=O)\ lipid}$ is the integrated area of the band at 1736 cm^{-1} (*79*)

For protein studies, however, far more informative structural and mechanistic information can be obtained from analyses of difference spectra. Subtraction of a spectrum recorded after induction of a change in the protein sample from a spectrum recorded before the change yields a difference spectrum consisting solely of signals arising from vibrational modes affected by the change. Signals in difference spectra arise from chemical changes within the protein structure, including protonation state changes of individual amino acid sidechains, and from changes in bond strength, polarity and hydrogen-bonding. Even very small changes, for example hydrogen-bonding-distance changes of less than 0.1 Å, can produce frequency changes that are easily detected (*80*).

Because the amplitude of the features that make up a difference spectrum can be several orders of magnitude less than those of an absolute spectrum, any such changes must be induced with minimal additional disturbance to the sample and it is highly desirable that the induced change be reversible so that many difference spectra for the same transition of the same sample can be averaged to achieve acceptable signal:noise. In practice it is almost impossible to induce the desired change without introduction of some additional signals due to protein concentration changes or from changes of other reagents in the mixture and it is routine to acquire high quality model spectra of added compounds or representing artefactual protein changes for use as subtractors (this process is explained in detail in Chapter 3). Available methods for reliably inducing changes include buffer exchange and electrochemistry. Perfusion-induced difference spectroscopy can currently only be carried out in ATR mode. A buffer is continuously perfused over the protein film surface and the protein state can be changed by switching reagents in the perfusant using an electronic valve. This method has been used to monitor changes induced by redox state changes (*74*), pH jumps (*81*), ligand binding (*82*), and interconversions between reaction intermediates (*83*). Electrochemically-induced difference spectroscopy can be performed in either transmission (*84*) or ATR mode (*30*). In both cases suitable redox mediators are required in order to allow electrical communication between the working electrode and the protein. Potential is controlled using a

conventional three electrode potentiostat. The systems developed within our laboratory for perfusion- and electrochemically-induced ATR FTIR difference spectroscopy allow synchronous UV/visible spectroscopy. The IR and UV/visible spectrophotometers and the electronic valve (for perfusion experiments) or potentiostat (for electrochemical experiments) are interfaced to the same computer allowing multiple experimental cycles to be performed for signal averaging purposes without the presence of an operator. These systems are described in detail in section 2.4.

1.2.2.4 Interpretation of protein difference spectra

The complexity of protein difference spectra is dependent on the degree of localisation of the induced change and its chemical nature. Even seemingly small changes induced in small proteins can produce difference spectra that are challenging to interpret. This challenge is by no means insurmountable and there are several strategies for assigning the features of such spectra. Tentative assignments can be made simply by comparison of the position, amplitude and bandwidth of features with those of a range of model compound spectra. Use of D_2O media to replace exchangeable protons with deuterons results in characteristic H-D exchange effects for those groups that involve exchangeable protons. Comparison of the H-D exchange effects on a protein signal and on a signal in a model compound spectrum to which the protein signal has been tentatively assigned can allow the assignment to be further established. A range of model compound spectra in H_2O and, where available and appropriate, D_2O media (obtained either from the literature or by experimental measurement) that have assisted the interpretation of the difference spectra obtained from cytochrome bc_1 complex and complex I are detailed in Chapter 3. Further support for assignments can be obtained from the use of isotopically-labelled material to label the protein globally, to label just one specific type of amino acid or cofactor or, in its most elegant and technically challenging form, to label just one specific amino acid (*85*). In addition site-directed mutagenesis of individual residues, selected by study of X-ray crystallographic or nuclear magnetic resonance structures, can be used to confirm assignments. Finally, *ab initio* calculations of normal mode frequencies and intensities using density functional theory (DFT) can be performed serving as a parallel means of making

assignments and, potentially, represent an important means of assigning signals to chemical structures which are not easily represented by model compounds (for example, the covalently linked histidine/tyrosine structure of cytochrome *c* oxidase (*86*)). Currently these methods are limited to relatively small molecules in simple environments by the time taken for calculations to be performed. With the continual introduction of ever faster microprocessors the value of the computation approach is likely to increase rapidly.

In summary, the mechanism by which IR radiation is absorbed by proteins leads to availability of very fine scale structural/mechanistic information, such as hydrogen bond strength changes and protonation state changes, that cannot be obtained by techniques such as NMR or X-ray crystallography. However, interpretation of information provided by the IR spectra of proteins is greatly aided by the structural data that these techniques provide. Model compound data also play a vital role and such data are continuing to accumulate. As each protein study is published, in addition to a contribution toward the understanding of that protein, a series of more widely applicable model compound measurements are usually included (for example, Iwaki *et al* (*30*)). In this way, as time progresses, the interpretation of protein difference spectra will become less challenging and the need for the time consuming acquisition of model compound spectra will be reduced.

1.3 NADH:ubiquinone oxidoreductase

1.3.1 Overview

Much of the work presented in this thesis is directed towards the analysis of NADH:ubiquinone oxidoreductase (Complex I): the largest and most complex component of the respiratory electron transfer chain. Complex I serves as the main entry point for electrons into the respiratory chain. It catalyses the oxidation of NADH and reduction of ubiquinone coupled to the translocation of protons across the inner membrane of mitochondria, or the plasma membrane in prokaryotes, as detailed below:

$$NADH + Q + 5H^{+}n \rightarrow NAD^{+} + QH_2 + 4H^{+}p$$

Where Q refers to ubiquinone and H^+n and H^+p to the protons translocated from the negative side to the positive side of the membrane (*87*)

Recent advances in the study of complex I have greatly increased our understanding of electron transfer within the complex. However, knowledge of how protons are pumped and by what means this is coupled to electron transfer is limited. This lack of understanding is largely due to the great number of subunits and prosthetic groups, to the difficulty in monitoring the internal reaction kinetics of the component Fe-S centres and to limited availability of structural information.

1.3.2 Subunit composition and prosthetic groups

Complex I extracted from bovine heart mitochondria consists of at least 46 different subunits with a combined mass of ~ 980 kDa (*88;89*). Bacterial complex I (~ 500 kDa) typically consists of 14 subunits (See Table 1.2). Notable exceptions are *E. coli* and *Thermus thermophilus* complexes; the former consisting of 13 subunits due to gene fusion (*87*) and the latter including an additional non-homologous 15th subunit with a possible function connected to its unusual habitat (*90*). Homologues of all 14 of the common bacterial subunits are present throughout the superfamily and bind all known prosthetic groups. Therefore these 14 subunits are thought to represent a common minimal functional core for complex I from all sources.

Eukaryotes			Prokaryotes			
B. taurus	*Y. lipolytica*	Gene location[#]	*T. thermophilus*	*E. coli*	Location	Properties
ND1	ND1	Mitochondrial	NQO8	NuoH	Membrane arm	8 (8) TMH, ubiquinone binding?
ND2	ND2	Mitochondrial	NQO14	NuoN	Membrane arm	12 (8) TMH
ND3	ND3	Mitochondrial	NQO7	NuoA	Membrane arm	3 (3) TMH, proton channel?
ND4	ND4	Mitochondrial	NQO13	NuoM	Membrane arm	10 (12) TMH
ND4L	ND4L	Mitochondrial	NQO11	NuoK	Membrane arm	3 (3) TMH, proton channel?
ND5	ND5	Mitochondrial	NQO12	NuoL	Membrane arm	13 (11) TMH
ND6	ND6	Mitochondrial	NQO10	NuoJ	Membrane arm	5 (5) TMH
75 kDa	NUAM	Nuclear	NQO3	NuoG	Peripheral arm	N1b, N4, N5, N7
51 kDa	NUBM	Nuclear	NQO1	NuoF	Peripheral arm	NADH binding site, FMN, N3
49 kDa	NUCM	Nuclear	NQO4	NuoD*	Peripheral arm	
30 kDa	NUGM	Nuclear	NQO5	NuoC*	Peripheral arm	
24 kDa	NUHM	Nuclear	NQO2	NuoE	Peripheral arm	N1a
PSST	NUKM	Nuclear	NQO6	NuoB	Peripheral arm	N2
TYKY	NUIM	Nuclear	NQO9	NuoI	Peripheral arm	N6a, N6b
			NQO15		Peripheral arm	Unique to *T. thermophilus* and close relatives

Table 1.2 Core subunits from *Bos taurus*, *Yarrowia lipolytica*, *T. thermophilus* and *E. coli* complex I. Transmembrane Helices (TMH) prediction for *E. coli* and, in parentheses, bovine from (*91*). Prosthetic group locations from (*90*). [#]Typical gene location in eukarya. *Subunits NuoC and NuoD are fused in *E. coli* (*87*).

The 14 core subunits can be divided into a hydrophobic group and a hydrophilic group. Using bovine nomenclature, ND1, ND2, ND3, ND4, ND5, ND6 and ND4L are hydrophobic subunits predicted to fold into approximately 50 α-helices across the membrane (*91*). These subunits, which are usually mitochondrially encoded in Eucarya, do not contain any known cofactor-binding motifs nor have any redox active prosthetic groups been reliably associated with them, though they may provide part of the substrate ubiquinone binding site. Weak homology of ND2, ND4 and ND5 with components of the Na^+/H^+ antiporter in *Bacillus subtilis* (see section 1.3.3) and the transmembrane position of the hydrophobic subunits has led to the suggestion that they are involved in proton translocation.

The 75 kDa, 51 kDa, 49 kDa, 30 kDa, 24 kDa, PSST and TYKY subunits are hydrophilic and bind all known prosthetic groups, namely a non-covalently bound flavin mononucleotide (FMN), two binuclear Fe-S centres and, typically, six tetranuclear Fe-S centres (See Table 1.2 for details of their coordination within the complex). Binuclear centres N1a and N1b and tetranuclear centres N2, N3, N4 and N5 are detectable by EPR allowing their midpoint potentials (E_{m7}) to be measured (See Table 1.3). E_{m7} values for tetranuclear centres N6a and N6b, which are not detectable by EPR, have been measured by UV/visible spectroscopy (*92*) (See Table 1.3). The midpoint potential of N2 is higher than this group (bovine and *Y. lipolytica* complex I) and is pH dependent (*93*) indicating that upon reduction a proton is taken up or released either from the centre itself or from a nearby amino acid residue. Complex I from *E. coli*, *T. thermophilus* and various other bacteria contains an additional tetranuclear centre N7 (*94*). The location and function of the prosthetic groups will be discussed in section 1.3.6.

Component	E_{m7} (mV)					pH dependency
	B.t	*T.t* [4]	*E.c* [5]	*Y.l* [6]	*N.c* [7]	(mV/pH)
FMN $2e^- \rightarrow 1e^-$	-336# [1]					-30 above pH 8 (measured for $2e^-$ reduction) [1]
FMN $1e^- \rightarrow 0e^-$	-414# [1]					
[2Fe-2S] N1a	-370 [2]	<-350	-330			-60 [2]
[2Fe-2S] N1b	-245 [2]	-270	-230			0 [2]
[4Fe-4S] N2	-50 to -150 [3]	-300	-220	-140	-168	-60 [2] to -36 [9]
[4Fe-4S] N3	-245 [2]	-440	-270		-265	0 [2]
[4Fe-4S] N4	-245 [2]	-290	-270		-268	0 [2]
[4Fe-4S] N5	-270 [2]					0 [2]
[4Fe-4S] N6a					-270	0 [7]
[4Fe-4S] N6b					-270	0 [7]
[4Fe-4S] N7*			-250			0 [5]
NADH	-320 ($2e^-$) (in solution) [8]					
Ubiquinone	110 ($2e^-$) (in solution) [8]					

Table 1.3 Midpoint potentials for redox active groups of complex I. Substrates and prosthetic groups of Complex I from bovine (*B.t*), *T. thermophilus* (*T.t*), *E. coli* (*E.c*), *Y. lipolytica* (*Y.l*) and *Neurospora crassa* (*N.c*); E_{m7} values, where known, and pH dependencies are indicated. *N7 is only present in some bacteria, for example *E. coli* (*94*). #Measured at pH 7.5. [1] (*95*) [2] (*93*) [3] (*96*) [4] (*97*) [5] (*98*) [6] (*99*) [7](*92*) [8] (*100*) [9] (*101*)

The roles of the additional non-core subunits of eukaryotic complex I, of which there are 32 in the bovine complex, are in general unknown. With the exception of the 10.6 kDa subunit the sequences of all of the bovine non-core subunits are known (see (*88*) for review). These subunits are not thought to be directly involved with the electron transfer/proton pumping functions of complex I. Instead, it has been proposed that they function to allow assembly, to provide additional stability (*90;102*), to allow regulation (*88*), or to provide protection against detrimental effects resulting from reactive oxygen species (ROS) (*103*).

Some of the bovine non-core subunits show homology to proteins of unrelated function, the consequences of which are not known. Examples of subunits showing such homology and for which there is experimental evidence suggesting

that the homologue's function may be retained in complex I are detailed in Table 1.4.

Subunit*	Details	References
39 kDa	Nucleotide binding motif (residues 19-49), may bind either NADH or NADPH. Disruption of the 39 kDa homologue in *Neurospora crassa* resulted in the absence of a tightly bound NADPH observed in the wild-type enzyme. In addition, sequence comparisons suggest the 39 kDa subunit is related to short-chain dehydrogenase/reductases.	(*88;104;105*)
SDAP	Closely related to acyl-carrier proteins involved in fatty acid biosynthesis in bacteria and chloroplasts. Disruption of the SDAP homologue in *N. crassa* resulted in incorrect assembly of complex I and a 4-fold increase of the lysophospholipid content of the mitochondrial membranes.	(*88;106*)
B16.6	B16.6 is a homologue of human GRIM-19, thought to be part of the interferon-β (IFN-β) and all-trans-retinoic acid (RA) pathway of cell-death induction. Treatment of MCF-7 cells with IFN-β and RA has been shown to result in upregulation of the homologues of the B16.6, 30 kDa and 15 kDa complex I subunits.	(*107;108*)

Table 1.4 Subunits of complex I which show homology to proteins of alternative function. Only examples for which there is experimental evidence to support alternative function associated with complex I are included. **B. taurus* nomenclature.

1.3.3 Modular structure

Based on its size, complexity and sequence analysis it is generally accepted that complex I evolution involved the recruitment of pre-existing functional modules (*103;109;110*). In addition to complex I, several other proteins sharing one or more of these ancestral modules have been identified. These proteins fall primarily into a class of enzymes called hydrogenases and catalyse the inter-conversion of molecular hydrogen and two protons plus two electrons (*110*). The study of their structure and function has yielded useful information on the organisation of the subunits in complex I and their function (*111*). In addition, the availability of high resolution structures for some complex I homologues has enabled the construction of homology models (see below).

The proposed electron input, or N, module of complex I consists of the 24 kDa, 51 kDa and 75 kDa subunits and transfers electrons from NADH via FMN onto a

chain of Fe-S centres. This module shares a common ancestor with the α subunit (encoded by *hoxF*) and, in part, the γ subunit (encoded by *hoxU*) of NAD^+-reducing hydrogenases of the type in *Alcaligenes eutrophus* (*111;112*). These subunits contain a non-covalently bound FMN and motifs for two Fe-S centres; it is expected that electrons are transferred through 2 4Fe-4S Fe-S centres onto FMN where NAD^+ reduction occurs (*112*). It is proposed that this reaction is reversed in the N module. Complex I equivalents found in chloroplasts, cyanobacteria, and the archaeon *Archaeoglobus fulgidus* use alternative electron input modules (*110*). The seeming interchangeability implies that the module's function is distinct from energy coupling and proton pumping.

The connecting, or Q, module consists of the 49 kDa, 30 kDa, TYKY and PSST subunits (*111*) and, catalysing electron transfer from the N module to ubiquinone, is the likely location for at least part of the energy coupling site(s) of complex I. The 49 kDa subunit (which is fused to the 30 kDa subunit in *E. coli*) and part of the PSST subunit are homologous to the large and small subunits, respectively, of water soluble [NiFe] hydrogenases (*113;114*). The small subunit homologue in the membrane bound type-3 hydrogenase from *E. coli* is shortened accommodating only the NiFe proximal Fe-S centre of the three Fe-S centres present in the soluble hydrogenase. The missing Fe-S centre binding domain is replaced in the membrane bound hydrogenase by an additional ferredoxin-like subunit with homology to TYKY. The structures of the 49 kDa and PSST subunits of *Y. lipolytica* complex I have been modelled based on the 2.7 Å resolution structure of the two subunit water soluble [NiFe] hydrogenase from *Desulfovibrio fructosovorans* (PDB file 1FRF) in combination with sequence alignments and secondary structure predications from other hydrogenases. This model, and site-directed mutagenesis work based on this model, suggests that during the evolution of complex I the hydrogenase NiFe centre was replaced by a ubiquinone binding site (*102;115;116*) (see Figure 1.15). This model will be further discussed in section 1.3.7.

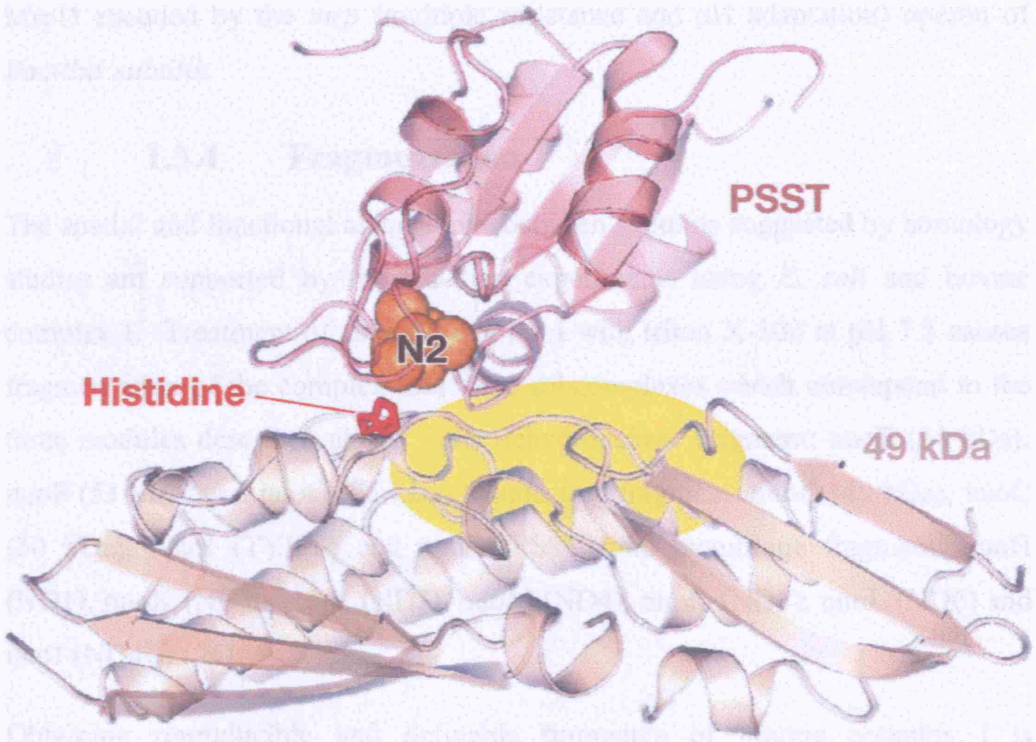

Figure 1.15 Homology model of 49 kDa and PSST subunits. Model was constructed using structural elements conserved from the large and small subunits of water-soluble [NiFe] hydrogenase (1FRF). Fe-S centre N2 is shown as a space filled model. The area highlighted in yellow corresponds to the location of the [NiFe] site in hydrogenases and to a region of complex I where residues effecting quinone-homologue-inhibitor sensitivity have been identified. The labelled histidine residue (His-226, *Y. lipolytica* numbering) is the proposed centre N2 redox-Bohr group (See section 1.3.7). Reproduced from (*111*).

The N and Q modules account for the hydrophilic subunits of the complex, NADH oxidation, electron transfer to ubiquinone, and at least part of the quinone binding site (*111*). The remaining hydrophobic subunits: - ND1, ND2, ND3, ND4, ND5, ND6 and ND4L are known as the P module and most likely play a major role in proton translocation across the membrane. A homologue of ND1 forms a component of the membrane bound type-3 hydrogenase from *E. coli* as do homologues of subunits ND2, ND4 and ND5 which are also homologues of each other and of subunits of the type-3 hydrogenase from the archaeon *Methanosarcina barkeri*. The hydrogenase part of the formate hydrogen lyase (FHL)-2 complex from *E. coli* contains further homologues of the ND2/ND4/ND5 family and a homologue of ND4L. Subunits ND2, ND4 and ND5 also show weak homology to the Na^+/H^+ antiporter proteins MrpA and

MrpD encoded by the *mrp* (multiple resistance and pH adaptation) operon of *Bacillus subtilis*.

1.3.4 Fragmentation

The spatial and functional associations between subunits suggested by homology studies are supported by fractionation experiments using *E. coli* and bovine complex I. Treatment of *E. coli* complex I with triton X-100 at pH 7.5 causes fragmentation of the complex into three subcomplexes which correspond to the three modules described above: - the dehydrogenase fragment: nuoE (24 kDa), nuoF (51 kDa) and nuoG (75 kDa), connecting fragment: nuoD (49 kDa), nuoC (30 kDa), NuoI (TYKY) and nuoB (PSST) and membrane fragment: nuoH (ND1), nuoN (ND2), nuoA (ND3), nuoM (ND4), nuoK (ND5), nuoL (ND6) and nuoJ (ND4L) (*98*).

Obtaining reproducible and definable fragments of bovine complex I is complicated by the great number of subunits present. The composition of subcomplexes published to date is summarised in Table 1.5. Fragmentation of bovine complex I initially results in one fragment which includes the seven hydrophilic core subunits, which coordinate all of the known prosthetic groups, and two fragments which each include a portion of the hydrophobic core subunits. The distribution of the hydrophobic subunits in these fragments suggests that ND4 and 5 are close to each other as are ND1, ND2, ND3 and ND4L (*117*).

FP	Iα	Iλ	Iβ	Iβs	Iβl	Iγ
51 kDa	24 kDa	24 kDa	ND4	(10*)	ND4	ND1
24 kDa	51 kDa	51 kDa	ND5		ND5	ND2
(1)	75 kDa	75 kDa	(~ 11)		(2*)	ND3
	49 kDa	49 kDa				ND4L
	30 kDa	30 kDa				(~ 4)
	TYKY	TYKY				
	PSST	PSST				
	(~ 16)	(8)				

Table 1.5 Composition of each of the defined bovine complex I fragments. Core subunits are listed by name with number of non-core subunits in parentheses (* non-core subunits PDSW and B17 are found in both Iβs and Iβl (*117*)). Treatment of bovine complex I with perchlorate releases fragment FP (flavoprotein) which is water soluble and able to transfer electrons from NADH to ferricyanide (*118;119*). Treatment with the non-denaturing detergent *N,N*-dimethyldodecylamine *N*-oxide (LDAO) results in three subcomplexes termed Iα, Iβ and Iγ. Iα consists of approximately 23 subunits, includes all prosthetic groups and is equivalent to the electron input and connecting (N and Q) modules discussed above (*120*); fragments Iβ and Iγ combined are equivalent to the P module. Under slightly different conditions subcomplex Iα further fragments and Iλ is obtained. Further treatment of subcomplex Iβ with LDAO results in fragmentation into Iβs and Iβl providing insight into the organisation of the hydrophobic subunits (*117*). Subunit ND6 has not yet been identified in any of the bovine fragments.

1.3.5 Structure

With the exception of two recent publications resulting from X-ray crystallographic studies of the peripheral arm of *T. thermophilus* (*90;121*), structural information has been derived primarily from indirect homology modelling and more direct fragmentation, cross linking and electron microscopy (EM) studies.

Single particle image reconstruction EM studies have allowed the gross structure of complex I from *E. coli* (*122-125*), *Aquifex aeolicus* (*126*), *Neurospora crassa* (*127*), *Y. lipolytica* (*111;128-130*), *Arabidopsis thaliana* (*131*) and *B. Taurus* (*6;119*) to be visualised ((*132-134*) for review) (see Figure 1.16). The earliest study, published by Leonard et al (*135*), shows the structure of *N. crassa* complex I to be shaped like a Stone Age axe head (*134*), however the same group

later published alternative L-shaped structures which are in good accordance with the structures obtained from other organisms. In 2002 Böttcher *et al* proposed that the active form of *E. coli* complex I assumes a horseshoe-like structure and that the L-shaped structure is actually an inactive form (*123*). However, these findings could not be reproduced by other groups (*124*) and therefore their significance is uncertain. At this time the consensus view is that complex I from all sources examined has an L-shaped structure with a peripheral or matrix-located arm and a membrane-located arm. In addition Sazanov *et al* obtained 2D images of bovine complex I lacking ND5 and, by comparison with images of the intake complex I, were able to conclude that ND5 is located at the distal end of the membrane arm (*119*).

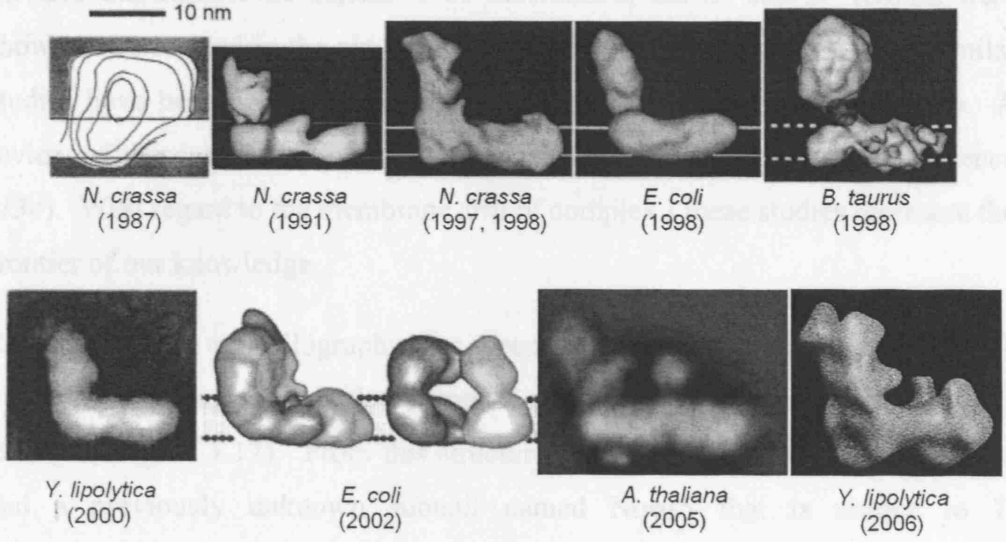

Figure 1.16 Complex I 3D models/2D images obtained from EM analysis. From top left to bottom right (in order of publication): *N. crassa* in 1987 (*135*); *N. crassa* in 1991 (*136*); *N. crassa* in 1997 (*127*); *E. coli* in 1998 (*122*); *B. taurus* in 1998 (*6*); *Y. lipolytica* in 2000 (*128*); *E. coli* inactive and active form in 2002 (*123*); *A. thaliana* in 2005 (*131*); *Y. lipolytica* in 2006 (*111;130*). The *A. thaliana* structure's unusual form is accounted for by its additional carboanhydrase module which protrudes into the mitochondrial matrix near the middle of the membrane arm (*131*).

Data described in previous sections and studies utilising chemical cross-linking agents and methods analysing the conditions necessary to extract or disassociate subunits from the membrane environment have contributed to the "pre-high resolution structure" understanding of how the subunits fit into the presented EM structures. The use of cross-linkers, for example disuccinimidyl tartrate - a lysine specific cross-linker - followed by identification of products by Western blotting with monospecific antisera has shown subunit-subunit interactions

between the 51 kDa, 24 kDa and 75 kDa subunits and between the 30 kDa and 49 kDa subunits (*137;138*). Treatment of *Paracoccus denitrificans* complex I containing membranes with sodium iodide and alkali pH extracted only the subunits making up the peripheral or matrix located arm. Identification of these subunits shows that the peripheral arm consists of 75 kDa, 51 kDa, 49 kDa, 30 kDa, 24 kDa, PSST and TYKY subunits and the membrane arm must therefore consist of ND1, ND2, ND3, ND4, ND5, ND6 and ND4L (*139*). Transmembrane helix predictions also support this conclusion (*91*) (see Table 1.2), as do topology studies using immunochemical methods in conjunction with cysteine-scanning mutagenesis and chemical modification to analyse the ND6 homologue of *P. denitrificans*. This study enabled the orientation within the membrane of each of the five transmembrane helices to be determined; the C- and N- termini were shown to be located in the cytoplasm and periplasm respectively (*140*). Similar studies have been performed for ND3 (*139*), ND4L (*141*), and ND1 (*142*). A review of these and additional biochemical analyses can be found in reference (*134*). With regard to the membrane arm of complex I these studies represent the frontier of our knowledge.

Recently X-ray crystallography has been used to obtain a structure of the hydrophilic domain of complex I from *T. thermophilus* at a resolution of 3.3 Å (*90*) (See Figure 1.17). From this structure the seven hydrophilic core subunits and a previously unknown subunit named Nqo15 that is unique to *T. thermophilus* and close relatives can be resolved along with the cofactors they coordinate. Nqo15 has a similar fold to frataxin, a mitochondrial iron chaperone, and a role in Fe-S centre regeneration with possible connection to the extreme habitat of *T. thermophilus* has been suggested (*90*). The peripheral arm structure accounts for 280 kDa of the total mass of the complex, 520 kDa. Out of the 2510 residues predicted from the sequences, 2333 have been modelled. They form a Y-shaped structure approximately 140 Å in height. The orientation was determined by fit within an unpublished *E. coli* low resolution EM structure produced by the same group (presumably equivalent to that presented above (*122*)) and by qualities of the N-terminal α–helix of the PSST homologue (labelled H1 in Figure 1.17). The electron density map from which the structure is derived suggests that this helix is rigid, protruding some 25 Å from the body of

the peripheral arm. It has a relatively polar upper surface and a hydrophobic lower surface and is proposed to extend into the surface region of the membrane domain. Therefore it is proposed that the membrane domain extends below and to the right of the structure as orientated in Figure 1.17.

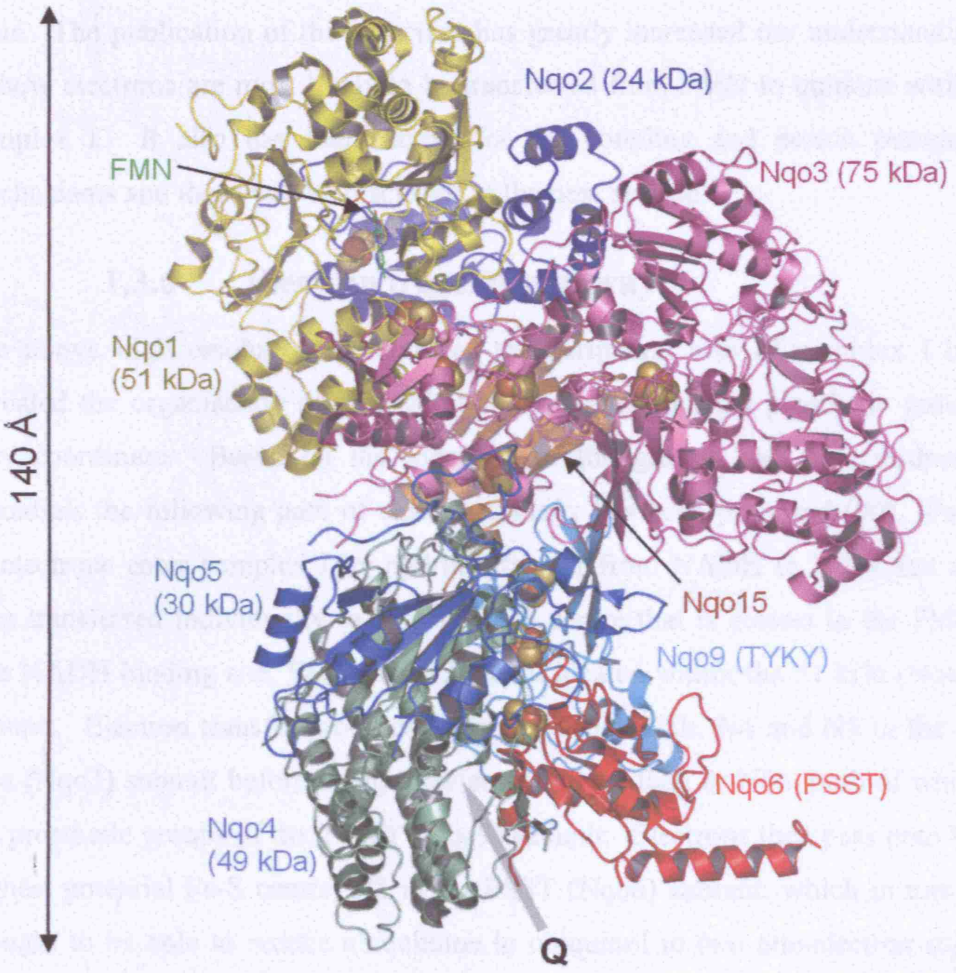

Figure 1.17 Architecture of the hydrophilic domain of *T. thermophilus* complex I at 3.3 Å. Side view with membrane arm likely to be below extending to the right. Colour is by subunit, which are labelled using *T. thermophilus* nomenclature (bovine nomenclature in parentheses). Atoms of FMN are shown as a stick model and labelled; those of iron and sulphur from the Fe-S centres are shown in red and yellow respectively. A possible quinone-binding site (Q) is indicated by an arrow (*90*). See text for significance of helix H1 of Nqo6 (PSST). Figure drawn using PyMol™ from PDB file 2FUG.

A solvent exposed cavity is proposed for the NADH binding site in the 51 kDa homologue that is sufficiently close to FMN to permit hydride transfer. Fe-S centres N3 and N1a are within 14 Å of FMN, the maximum distance for physiological electron transfer (*11*). From N3, Fe-S centres N1b, N4, N5, N6a and N6b form a linear chain to N2 without any individual transfer step exceeding

an edge to edge distance of 14 Å. Fe-S centre N2 is coordinated entirely in the PSST homologue and, uniquely, by two consecutive cysteine residues. The poorly conserved centre N7 is 20.5 Å from this chain; the roles of N1a and N7 will be discussed in section 1.3.6. A quinone binding site is proposed to be located close to N2 and at the interface between the peripheral and membrane arms. The publication of this structure has greatly increased our understanding of how electrons are most likely to be transferred from FMN to quinone within complex I. It also has implications for the coupling and proton pumping mechanisms and these will be discussed in the next section.

1.3.6 Electron transfer pathway

The above high resolution structure of the peripheral arm of complex I has revealed the organisation of the hydrophilic subunits and the prosthetic groups they coordinate. Based on the locations of the groups and their midpoint potentials the following path of electron transfer has been proposed (*90*). Pairs of electrons enter complex I by hydride transfer from NADH to FMN and are then transferred individually to N3, the Fe-S centre that is closest to the FMN. The NADH binding site, FMN and N3 are all located within the 51 kDa (Nqo1) subunit. Electron transfer proceeds linearly through N1b, N4 and N5 in the 75 kDa (Nqo3) subunit before being transferred to N6a then to N6b, both of which are prosthetic groups of the TYKY (Nqo9) subunit. Electrons then pass onto the highest potential Fe-S centre, N2 in the PSST (Nqo6) subunit, which in turn is thought to be able to reduce ubiquinone to ubiquinol in two one-electron steps (via semiquinone) (*90*). This electron transfer chain may be summarised as: NADH-FMN-N3-N1b-N4-N5-N6a-N6b-N2-ubiquinone and its topography and energetics are illustrated in Figure 1.18.

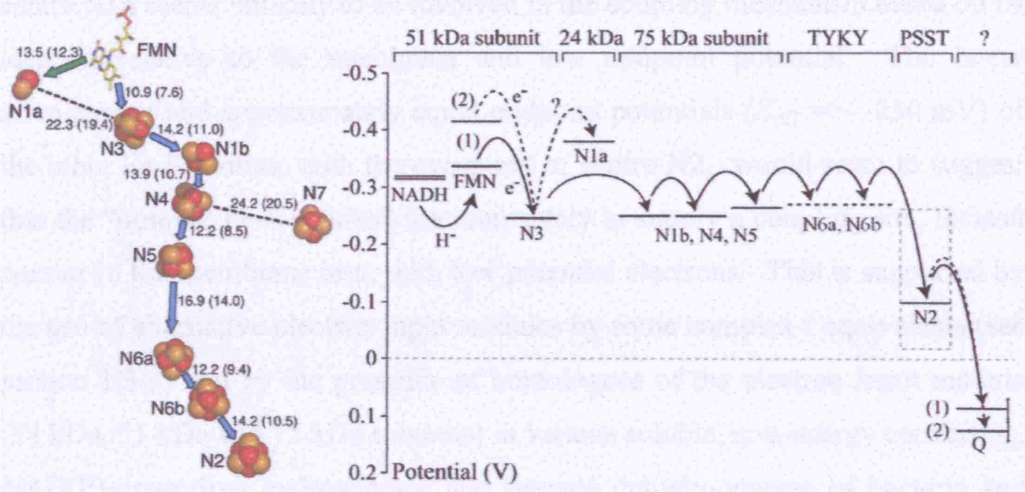

Figure 1.18 Organisation and energetics of the complex I electron transfer chain. Left: Organisation of Fe-S centres of *T. thermophilus* complex I showing proposed route of electron transfer and centre-centre transfer distances (edge to edge distances are given in parentheses) in Å (see text). Reproduced from (*90*). Right: Schematic for electron transfer. Midpoint potentials (E_{m7} V) are indicated by horizontal bars. Fe-S centre N1a is not likely to be involved in direct electron transfer from FMN to Q (see text). Adapted from (*143*).

Support for direct electron transfer from N2 to Q is provided by EPR data which shows a magnetic interaction between N2 and semiquinone that indicates a 12 Å distance between the centres (*144;145*) (see later discussion in this section and section 1.3.8.1). The edge-to-edge separation of centre N7 from the proposed electron transfer chain is 20 Å (~ 6 Å greater than the proposed maximum distance for physiological electron transfer (*11*)). This, combined with the poor conservation of N7, suggests it to be an evolutionary remnant without an important role in complex I function (*90*). The involvement of N1a is more perplexing. It is possible that $FMNH_2$ transfers electrons almost synchronously to N3 and N1a, minimising time spent in the semiquinone form. Upon oxidation of N3 the electron at N1a could be transferred via FMN to re-reduce N3. The proposed advantage for this would be to minimise ROS formation from the semiquinone form of FMN (*90*).

1.3.7 Coupling mechanism

Complex I pumps four protons across the membrane per pair of electrons transferred from NADH to ubiquinone (*146;147*). Neither the mechanism by which protons are pumped nor the means by which proton pumping is coupled to the relatively well understood process of electron transfer are known. Fe-S

centre N1a seems unlikely to be involved in the coupling mechanism based on its location relative to the membrane and low midpoint potential. The linear arrangement and approximately equal midpoint potentials (E_{m7} = ~ -250 mV) of the other Fe-S centres, with the exception of centre N2, would seem to suggest that the "non-N2 Fe-S centres" function solely to supply a coupling site, located near or in the membrane arm, with low potential electrons. This is supported by the use of alternative electron input modules by some complex I equivalents (see section 1.3.3) and by the presence of homologues of the electron input module (24 kDa, 51 kDa and 75 kDa subunits) in various soluble, non-energy converting, NAD(P)-depending hydrogenases and formate dehydrogenases of bacteria and archaea (*110*).

In *Y. lipolytica* site-directed mutagenesis experiments have shown that the E_{m7} of Fe-S centre N2 can be lowered from -140 to -220 mV by replacing a single residue (an H226M substitution in subunit NUCM). This also resulted in elimination of the N2 pH dependence and, unexpectedly, did not affect the function of the complex (*101*). This would seem to render N2 equivalent to the six isopotential centres and would suggest that all the Fe-S centres function solely to transport electrons from FMN to an unknown coupling site. Alternative functions for the 85 Å long electron transfer chain formed by the Fe-S centres may include minimising generation of ROS or minimising damage caused by ROS.

Highly active complex I preparations from bovine and *Y. lipolytica* have been shown to retain only substoichiometric amounts of ubiquinone (*148*) which would seem to rule out the presence of any tightly bound quinone moieties. This conclusion and those of the discussion above put great emphasis on the role of the Q-site(s) in the coupling and proton translocation mechanisms. The location and number of Q-site(s) in complex I is not known. Studies of bovine complex I by EPR spectroscopy (see section 1.3.8.1) have identified three distinct semiquinone signals, termed SQ_{Nf}, SQ_{Ns}, and SQ_{Nx}, with differing physicochemical properties (*144;145*). SQ_{Nf} has a rapid spin relaxation time, is dependent on the presence of a membrane potential and, in conjunction with analysis of the Fe-S centre N2 signal, has been shown to indicate a paramagnetic interaction between the semiquinone from which it arises and N2 (*144;145*).

Analysis of this interaction indicates that the distance between N2 and the source of SQ_{Nf} is ~12 Å (*145*). Currently it is not known whether the three EPR signals arise from three semiquinones in three distinct binding sites or from a combination of a lesser number of bound semiquinones in differing states (i.e. effects of changes in the protein are transmitted to the semiquinone via the Q-site in which the semiquinone is bound and affect its EPR characteristics). The application of EPR spectroscopy to complex I is discussed in greater detail in section 1.3.8.1.

Mutations in subunit ND1 have been found that result in altered quinone reduction kinetics (*149*) suggesting that ND1 may form part of the Q-site(s), a conclusion that is further supported by photolabelling experiments using a rotenone analogue (*150*) and from the study of Q-site inhibitor resistant mutants (*151*). The homology, fragmentation and structural data discussed above do not rule out the possibility that there is a large Q-site formed from residues of the 49 kDa, PSST and ND1 subunits. A possible Q-site binding motif has been identified in ND4 and ND5 by bioinformatic analysis of known Q-sites (*62*). The possibility of the involvement of ND4 is further supported by a study in which the ND4 subunit homologue in *E. coli* was directly photoaffinity labelled by an azido-Q analogue (*152*). In addition, several mutations that are linked to human mitochondrial diseases map very close to the identified motifs indicating that this region is functionally important (*62;153*). Structural studies suggest that ND4 and ND5 are located at the distal end of the membrane arm to N2 (see sections 1.3.4 and 1.3.5) which would suggest that the coupling mechanism involves the full length of the membrane arm.

Studies demonstrating the binding and reduction of compounds ranging from the relatively hydrophilic ubiquinone-0 to ubiquinone derivatives especially synthesised with large bulky sidechains (*154*) have suggested that the Q-site(s) is either large or flexible. This notion is further supported by the plethora of hydrophobic complex I inhibitors with widely differing structures (*155*), a great number of which have been shown to occupy the same binding pocket by equilibrium binding studies (*156*).

Also relevant to the complex I coupling mechanism are studies suggesting complex I from *Klebsiella pneumoniae* (*157*) and *E. coli* (*158*) are able to pump sodium ions in place of protons. This is a controversial issue at present: a recent review by Brandt (*111*) argues compellingly against this, suggesting, amongst other things, that the observed activity could be due to NQR-type NADH dehydrogenase in *K. pneumoniae* and H^+/Na^+ antiporter activity in *E. coli*.

In 1998 Dutton *et al* proposed that coupling and proton translocation may be accomplished using a reverse Q-cycle mechanism similar but functionally opposite to that of cytochrome bc_1 complex (see section 1.1.3.2) (*159*). The first step of the proposed mechanism is reduction of a ubiquinone, bound at a Q-site within the membrane arm close to the matrix side (Q_{nz}), by Fe-S centre N2 forming a reactive semiquinone. This semiquinone subsequently oxidises a ubiquinol also bound within the membrane arm but at a Q-site near the inter-membrane space side (Q_{nx}). Redox changes are accompanied by uptake of 2 protons from the matrix during the formation of ubiquinol at Q_{nz} and release of a single proton into the inter-membrane space during the formation of a semiquinone at Q_{nx}. The ubiquinol bound at Q_{nz} is then released and a ubiquinone binds in its place. A second electron from Fe-S centre N2 reduces this ubiquinone forming a second reactive semiquinone which oxidises the semiquinone bound at Q_{nx} to ubiquinone. As with the first stage 2 protons are taken up from the matrix and one is released into the inter-membrane space. Exchange of ubiquinol for ubiquinone at Q_{nz} and ubiquinone or ubiquinol at Q_{nx} marks the end of the cycle. This mechanism accounts for translocation of 2 protons per NADH oxidised. Dutton *et al* propose that an additional tightly or covalently bound quinone or quinone-like moiety (Q_{ny}), located between Q_{nx} and Q_{nz}, couples the transfer of electrons between the Q-sites to proton translocation using a conformation gated mechanism. They speculate Q_{nz} may account for UV/visible data assigned to a possible quinone-like structure in the membrane arm of complex I by Friedrich *et al* (*160*) (discussed in section 1.3.8.2). Other Q cycle based mechanisms have also been proposed (*161*), but they are less obviously related to known mechanisms of other enzymes and remain speculative (*162*).

Proposed mechanisms (or components of mechanisms, see above) that do not utilise a reverse Q cycle fall into two classes: directly-coupled and indirectly coupled (*125;134;163;164*). In directly-coupled mechanisms proton transfer across a hydrophobic barrier is controlled directly by a gating reaction, such as a coupled electron-transfer reaction, positioned at (or close to) the barrier. Cytochrome *c* oxidase is an example of a directly-coupled proton-pump (see section 1.1.3.3). In indirectly-coupled mechanisms the driving reaction is spatially separated from proton transfer across the hydrophobic barrier, and the two are coupled indirectly by interactions with the protein structure. The rotary catalysis of F-type ATPases (see section 1.1.3.5) is an example of an indirectly-coupled mechanism.

Hirst (*162*) discusses two mechanisms that are broadly in accord with the experimental evidence described in this section and could each occur with direct- or indirect-coupling. In the first, proton transfer is coupled to a reduction of Fe-S centre N2. An electron is transferred to N2 forming a high energy state, perhaps by altering the conformation of the surrounding protein, conserving the potential energy. Relaxation of the reduced centre N2 from this high energy state to a lower energy state could be coupled to the transfer of two protons across a barrier. Reduced centre N2 in the lower energy state would still be capable of reducing bound (semi)quinone. In the second mechanism described, proton transfer is coupled to substrate binding or product dissociation. This would require the translocation of 4 protons using energy liberated from the binding of ubiquinone or the release of ubiquinol.

From the currently available experimental data it is not possible to tell whether the coupling mechanism is direct or indirect. Centre N2 has been particularly implicated in directly-coupled mechanisms because of its midpoint pH-dependency, which means that a proton is bound on reduction and released again on reoxidation. Combining this with a gating mechanism that only allows protonation from the *n*-side of the membrane and deprotonation to the *p*-side would create a coupled proton transfer mechanism. The unique ligation of N2 by two consecutive cysteine residues may allow the 4Fe-4S centre to be directly protonated (*90*) which would favour a direct redox driven model. However, the fact that the redox Bohr group of N2 can be removed without adverse

consequence to function disfavours a direct redox driven model of this kind (*101*).

More recently, a number of groups have emphasised indirectly-coupled mechanisms involving conformational changes operating over a distance. For example, Sazanov *et al* have suggested that elements within the high resolution structure may be able to transmit redox state-dependent signals from the Fe-S centres to the membrane domain (*90*). Brandt *et al* have suggested that the high levels of variability within their EM particle analysis data sets are indicative of unusual flexibility in the complex I structure. They also suggest features in the structure may represent a transient structural connection between the peripheral domain and the middle of the membrane domain (*130*). Occurrence of such large scale structural changes may also account for the 'horseshoe' shaped EM image obtained by Böttcher *et al* (see section 1.3.5). However, it is clear that further data are required before the nature of coupling/proton-pumping mechanism of complex I can be determined.

1.3.8 Spectroscopic studies of complex I

1.3.8.1 Electron paramagnetic resonance spectroscopy

EPR spectroscopy allows detection and characterisation of species that have unpaired electrons including the Fe-S centres (when reduced), FMN (when in the semiquinone form) and substrate ubiquinone (when in the semiquinone form) of complex I. Sled *et al* used a combination of potentiometry and X-band EPR spectroscopy to redox titrate the g = 2.005 flavosemiquinone signal in bovine complex I (*95*). Relative flavosemiquinone concentration ($[Fl^{1}]/[Fl_{tot}]$), calculated from the relative peak to peak amplitude of the g = 2.005 signal and the total FMN concentration, was plotted against ambient potential (E_h). At 25 °C $[Fl^{1}]/[Fl_{tot}]$ is related to E_h by the following equation:

$$[Fl^{1}]/[Fl_{tot}] = \frac{1}{1+10^{(E_h - E_m^{1/0})/59} + 10^{(E_m^{2/1} - E_h)/59}}$$

Where $E_m^{1/0}$ and $E_m^{2/1}$ are midpoint potentials for the first and second reductive steps of FMN (*165*).

Sled *et al* found values of -414 mV and -336 mV for $E_m^{1/0}$ and $E_m^{2/1}$ respectively (see Table 1.3) to be optimal for simulation of their data obtained at pH 7.5 (*95*). Additional data obtained at a range of pH values enabled the pH dependency of the midpoint potential of the 2 e^- reduction of FMN in complex I to be determined (see Table 1.3). The data also allowed pK values of the flavosemiquinone ($Fl^{\bullet -}/FlH^{\bullet}$) and reduced flavin ($FlH^-/FlH_2$) forms to be estimated as 7.7 and 7.1 respectively (*95*).

Ohnishi *et al* have reviewed the large body of EPR data on the Fe-S centres of complex I (*96*). This work details the resolution of six distinct Fe-S centres: 2Fe-2S centres N1a and N1b and 4Fe-4S centres N2, N3, N4 and N5 using reductive titrations, potentiometric titrations and spectral computer simulations. Beinert *et al* originally identified four Fe-S centres in the isolated bovine complex. The signal of the first centre (N1b in modern nomenclature) at $g_{z,\,y,\,x}$ = 2.022, 1.938, 1.923 was measured at 77 K and was characteristic of a binuclear centre. The second centre (N2) produced a well resolved signal characteristic of a tetranuclear centre at g_z = 2.054, $g_{x=y}$ = 1.922 at temperatures above 20 K. The third and forth centres (N3 and N4) could not be resolved in this study; in combination they produced an EPR signal at g_z = 2.100 and g_x = 1.886 and 1.862 (*166*). Ohnishi *et al* later resolved the third and forth centres potentiometrically in pigeon heart submitochondrial particles where they exhibited different $E_{m7.2}$ values (-240 and -410 mV, respectively). The N3 and N4 signals were suggested to be at $g_{z,\,y,\,x}$ = 2.10, ~1.93, 1.87 and $g_{z,\,y,\,x}$ = 2.11, ~1.93, 1.88 respectively (*167*). Albracht suggested a value of 2.037 for the N3 g_z signal obtained from computer fit for equi-spin content of centres N3 and N4 from the bovine heart complex I (*168*). This finding was confirmed by experiment by Ohnishi and the g value of centre N3 in pigeon heart submitochondrial particles was revised: $g_{z,y,x}$ = 2.04, 1.93, 1.87 (*96*). At lower temperatures EPR signals from species with more rapid spin relaxation rates are more readily detectable. Low temperature (<7 K) measurements of the Nqo3 subunit of *P. denitrificans* complex I (homologue of the bovine 75 kDa subunit) have allowed detection of the centre N5 signal at $g_{z,y,x}$ = 2.07, 1.92, 1.90 (*169*). An EPR signal at $g_{z,y,x}$ = 2.00, 1.95, 1.92 measured in the flavoprotein fragment of *P. denitrificans* has been tentatively assigned to centre N1a (*170*). The additional Fe-S centre found

in *T. thermophilus*, *E. coli* and some other bacteria was originally thought to be a third 2Fe-2S type centre. EPR data from Ohnishi *et al* later proved that the additional centre is tetranuclear prompting its name to be changed from centre N1c to N7 (*94*). Investigation of complex I fragments with EPR spectroscopy allowed the locations of all EPR-detectable Fe-S centres to be tentatively assigned prior to publication of the high resolution structure of the *T. thermophilus* hydrophobic domain (*90*) (which confirmed the earlier findings) (see Table 1.2). EPR experiments in conjunction with potentiometry and pH titration have enabled midpoint potentials and their pH dependencies to be determined (see Table 1.3). Fe-S centres N6a and N6b have not yet been detected by EPR spectroscopy, although they have been detected by UV/visible spectroscopy as described in section 1.3.8.2.

As briefly described in section 1.3.7, EPR spectroscopy has also been applied to ubisemiquinone species associated with complex I (*144;145;171*). Three distinct signals have been resolved in the complex I segment of the mitochondrial respiratory chain during steady-state NADH oxidation in tightly coupled bovine heart submitochondrial particles. These signals are distinguishable by their spin relaxation properties. SQ_{Nf} has a fast spin relaxation rate and is only observable in the presence of a membrane potential. SQ_{Ns} and SQ_{Nx} are both insensitive to membrane potential and have slow and very slow spin relaxation rates respectively. Because semiquinones have their spin densities distributed over several atoms paramagnetic interactions with nearby spin systems are the strongest determinates of spin relaxation rate (*145*). The differences in spin relaxation rates of the observed semiquinone signals therefore indicate that the semiquinone species from which they originate are located at differing locations within the enzyme complex or that the redox centres close to the Q-site(s) are in differing states (*145*). The enhanced spin relaxation time of SQ_{Nf} is an indication of interaction between the semiquinone and a tetranuclear Fe-S centre (*145*). Based on a close correlation between a line shape alteration of the $g_z = 2.054$ signal of centre N2 and quenching of the SQ_{Nf} signal, either by changing membrane potential or through use of inhibitors, it was proposed that SQ_{Nf} interacts with centre N2 (*144*). This proposal was confirmed through identification of additional indicators for interaction between the N2 and SQ_{Nf}

signals and, through computer simulation of the interactions, a centre-to-centre distance of 12 Å has been proposed (*145*).

Although the studies outlined above have provided information on complex I of great value the technique of EPR spectroscopy is not without limitations. Relatively large volumes and high concentrations of protein are required for analysis. Also, options for *in situ* manipulation of the sample during acquisition of spectra are limited because of the inaccessibility of the sample chamber and the necessity for very low temperatures for detection of signals with fast spin relaxation rates. Finally, EPR is unable directly to detect non-paramagnetic species.

1.3.8.2 UV/Visible spectroscopy

Complex I is not well suited to investigation by UV/visible spectroscopy on account of the poor UV/visible signatures of the Fe-S centres. Although flavin and flavoproteins are in general amenable to investigation by UV/visible spectroscopy (oxidised flavin has well characterised absorptions at 450 and 370 nm) (*172*), most data on FMN in complex I have been obtained by EPR (see section 1.3.8.1). This is because the broad signals from the Fe-S centres obscure the more informative contributions from FMN (*95*).

UV/Visible spectroscopy has been used to characterise the EPR-silent tetranuclear Fe-S centres N6a and N6b by Friedrich *et al.* Signals at 325 and 425 nm appearing as troughs in oxidised *minus* reduced difference spectra were resolved from those of FMN and the EPR detectable Fe-S centres kinetically during the oxidation of NADH-reduced *N. crassa* complex I by oxygen. The midpoint potential of this signal was determined to be -270 mV by redox titration and found to be pH-independent between pH 7.0 and 8.2. Equivalent signals at 330 and 425 nm were detected in *E. coli* complex I, although they could not be completely resolved from other components (*92;160*). Equivalent signals were detected in an *E. coli* fragment consisting of subunits NuoB, NuoCD and NuoI and in the related Ech hydrogenase from *M. barkeri*, a membrane-bound multisubunit [NiFe] hydrogenase which contains homologues of all subunits in the *E. coli* fragment plus homologues of two of the membrane subunits. The absence of similar signals in an equivalent spectrum from the soluble NAD^+-

reducing hydrogenase from *Ralstonia eutropha*, which contains homologues of all subunits of the *E. coli* fragment with the exception of NuoI (TYKY) supported tentative assignment of the novel redox centre to the NuoI subunit (*160*). Subsequent comparison of the connecting fragment spectrum with an equivalent spectrum of the *Clostridium pasteurianum* 8 Fe-ferredoxin supported the assignment of the novel signal to two tetranuclear Fe-S centres located on subunit NuoI (*92;160*). These findings have subsequently been confirmed with the publication of the high resolution structure of the *T. thermophilus* hydrophobic domain (*90*).

Hellwig *et al* recorded electrochemically induced UV/visible redox difference spectra of *E. coli* complex I and a fragment of that complex to accompany FTIR measurements (see section 1.3.8.3). They reported several broad and featureless signals resulting from overlapping contributions from FMN and the Fe-S centres which were monitored in order to confirm the reversibility of induced redox changes (*84*).

Friedrich *et al* have reported UV/visible signals in a reduced *minus* oxidised difference spectrum of *E. coli* complex I which they tentatively assign to an additional redox group of unknown chemistry possibly located in the membrane arm (*160*). With continuous acquisition of UV/visible spectra, oxidised complex I was reduced with a 5-fold excess of NADH in anaerobic conditions; complete reduction was confirmed by removing a small aliquot for analysis by EPR. The NADH:NAD^+ ratio was then adjusted by adding lactate dehydrogenase and pyruvate to give a final redox potential of -150 mV (calculated from the applied pyruvate/lactate ratio). Oxidation of NADH to NAD^+ occurred in seconds and oxidation of complex I occurred in minutes. At equilibrium a small aliquot was removed for analysis by EPR, this indicated that all EPR detectable components had been re-oxidised. However, the UV/visible spectrum obtained at -150 mV differed from the initial fully oxidised spectrum. The plot of the reduced *minus* oxidised difference consisted of a positive absorbance at approximately 300 nm and a very broad negative feature around 450 nm. Redox titration in an ultra-thin layer spectroelectrochemical cell allowed a midpoint potential for the cause of these unusual signals to be estimated at -80 mV. Based on this midpoint value Friedrich *et al* suggest that the putative redox centre lies in the membrane arm

where it is involved in electron transfer from Fe-S centre N2 to quinone. The origin of the signals was further investigated by acquisition of an oxidised *minus* reduced FTIR difference spectrum for the 0 mV to -130 mV transition. The presented spectrum consists of peaks at 1656, 1638, 1165 cm^{-1} and a trough at 1100 cm^{-1}. The peaks at 1656 and 1638 cm^{-1} are tentatively assigned to C=O and C=C modes, respectively, or to perturbations of the peptide backbone. Friedrich *et al* go on to speculate that these signals may arise from an unknown quinoid structure. It is important to note that since these findings were published in 2000 no further supporting evidence for such a structure, with the exception of the EPR findings discussed above, has been found. Also, our group has applied redox difference FTIR spectroscopy to the membrane arm of bovine complex I and found no supporting evidence (work of Fisher, N., unpublished).

1.3.8.3 FTIR spectroscopy

In Chapter 5 a thorough FTIR characterisation of complex I from *Y. lipolytica* and *B. taurus* is described. Prior to this study several FTIR studies on complex I from *E. coli* were published by Hellwig *et al*, these are summarised below. The data presented in Chapter 5 are broadly consistent with the *E. coli* data however the presented interpretations and conclusions differ radically from those of Hellwig *et al.* It is therefore appropriate to describe the available IR data on complex I only briefly here prior to discussing it fully in light of the findings of this work (and the additional high resolution structural data now available) in Chapter 5.

The first FTIR spectroscopic characterisation of complex I was performed by Hellwig *et al* in 2000 (*84*). In this study electrochemically induced difference spectra were recorded in transmission mode for critical potential steps of complex I from *E. coli* and of the soluble NADH dehydrogenase fragment, which consists of subunits NuoE, NuoF and NuoG, of the same complex. Redox difference spectra of all components were recorded using oxidising and reducing potentials of 200 and -700 mV versus Ag/AgCl (corresponding to 404 and -496 mV SHE) respectively. In order to investigate signals arising from changes associated with FMN, the midpoint of which they determined to be -530 mV versus Ag/AgCl (-326 mV SHE) in *E. coli* complex I (as unpublished data),

difference spectra were obtained for the potential step between -500 and -700 mV versus Ag/AgCl (-296 and -496 mV SHE). Additional difference spectra for the potential step between -300 and -500 mV versus Ag/AgCl (-96 and -296 mV SHE) were recorded in order to investigate signals arising from changes associated with the isopotential Fe-S centres and, in the case of the whole complex, Fe-S centre N2. The results of this study are discussed in detail in Chapter 5. Briefly, obtained spectra are interpreted to indicate that strong reorganisations on the polypeptide backbone occur with redox changes of both FMN and Fe-S centres based on amplitude of amide I signals. A signal at 1548 cm^{-1} and an indistinct signal at 1710 cm^{-1} in the spectra obtained for the -296 to -496 mV potential step were tentatively assigned to FMN based on comparisons with difference spectra obtained for FMN and FAD in solution. Contributions from FMN were noted to be smaller than expected. Differences between spectra obtained from the whole complex and from the NADH dehydrogenase fragment were interpreted as arising primarily from changes associated with reduction/oxidation of Fe-S centre N2, which is not present in the fragment, and associated protonation state changes. Also absent from the fragment and therefore likely to contribute are Fe-S centres N6a and N6b. Although these centres were characterised and tentatively assigned to subunit NuoI of *E. coli* complex I in a manuscript by the same authors submitted within the same month (*160*), their contributions are not discussed. Differences in the amplitude of signals between 1710 and 1720 cm^{-1} in the spectra obtained for the -96 to -296 mV SHE potential step of the fragment and of the whole complex were interpreted as indicating either a possible deprotonation of an aspartic or glutamic acid sidechain or a change in the environment of a protonated aspartic/glutamic acid upon reduction of N2.

In a second study by Hellwig *et al* (*173*) electrochemically induced redox difference spectra for the 0 mV to -500 mV potential step were recorded in transmission mode for both *E. coli* complex I and its NADH dehydrogenase fragment. They calculated double difference spectra and observed, in addition to signals that they previously tentatively assigned to aspartic or glutamic acid residues (*84*) (see above), signals at 1515 and 1498 cm^{-1} that they tentatively assigned to protonation and deprotonation of one or more tyrosine sidechains

respectively based on comparison with model compound data (see section 3.5.5). These signals were assigned to tyrosine 114 and tyrosine 139 of subunit NuoB by FTIR analysis of site directed mutants. The putative tyrosine signals were found at half the wild-type intensity in double difference spectra obtained from Y114C and Y139C mutants and at negligible intensity in a Y114C/Y139C double mutant suggesting that they originate from protonation of both tyrosine 114 and tyrosine 139 upon reduction of Fe-S centre N2. The authors speculate that tyrosine 114 and 139 may be involved in the proton pumping mechanism of complex I and draw attention to the reduced amplitude of amide I signals in the double mutant redox difference spectrum which may indicate that a conformational change is involved in this mechanism. In a later publication (*174*) the authors state that this data shows that the reaction of N2 is coupled to a major conformation change of the enzyme. These results are discussed more fully in Chapter 5.

In a further study by Hellwig *et al* (*174*) electrochemically induced difference spectra of *E. coli* complex I are presented for the potential step from -50 to -650 mV versus Ag/AgCl (154 to -446 mV SHE) at pH 5.5, 6.5 and 7.5. A peak at 1732 cm^{-1} in the (oxidised *minus* reduced) pH 5.5 difference spectrum that is absent at pH 6.5 was tentatively assigned to protonation of an aspartic or glutamic acid sidechain which occurred at the lower pH but not at the higher. Concomitant variations at approximately 1585 and 1408 cm^{-1} were tentatively assigned to loss of the deprotonated form, and supported this assignment (assignments were based on IR studies of model compounds (*175*), see section 3.5.5). The complex I preparation used for these studies included 0.5 molecules of quinone per complex. Differences in the amplitude of signals arising from redox changes of ubiquinone between the spectra at different pH values was supposed to reflect an effect of pH on the quinone binding affinity of the complex. The authors made tentative assignments to quinone, including signals at 1264 and 1610 cm^{-1}, and noted their increased amplitude at low pH. They interpreted these findings as possible indicators that the protonation of sidechains, possibly including the glutamic/aspartic acid mentioned above, may promote quinone binding and therefore may be used as markers for identification of the Q-site(s). These results are further discussed in Chapter 5.

1.4 Aims and objectives

This thesis describes the application of FTIR spectroscopy to cytochrome bc_1 complex and complex I. The aims of the present study were: i. to obtain redox difference spectra of cytochrome bc_1 complex, using the novel technique of electrochemically-induced ATR FTIR redox difference spectroscopy, that were comparable to previously published spectra obtained using different approaches (see Chapter 4); ii. to gain new insight into the mechanism of quinone oxidation at the Q_o-site of cytochrome bc_1 complex (see Chapter 4); iii. to obtain redox difference IR spectra of all components of complex I and to resolve signals arising from changes associated with reduction/oxidation of Fe-S centre N2 in order to gain new insight into the structure and mechanism of complex I (see Chapter 5); and iv. to collate IR data on and make new FTIR measurements of a wide range of model compounds to aid acquisition of and interpretation of the respiratory complex spectra (see Chapter 3).

Chapter 2: Materials and Methods

2.1 Protein purification

2.1.1 Mitochondrial cytochrome bc_1 complex

Mitochondrial cytochrome bc_1 complex was isolated from bovine heart muscle by the method described in reference (*74*). All steps were performed at 0-4 °C. First, Keilin-Hartree (KH) particles (*176*) were prepared: 660 g fresh lean beef heart muscle was diced and washed with water to remove haemoglobin prior to placing in a Waring Blender (model 34BL23) with 2 l of 50 mM sodium bicine pH 8.0. 20 ml of 2 M sodium bicine pH 9.0 was added prior to blending for 30 seconds at low speed, 30 seconds at medium speed then 45 seconds at high speed with the blender vessel briefly cooled by plunging into ice between each step. The pH was then adjusted to 8.0 with 2 M sodium bicine pH 9.0 and the sample pressed through a layer of muslin prior to centrifugation at 3000 g_{av} (2500 rpm in Sorvall SLC-6000 rotor) for 40 minutes. The supernatant was passed through 2 layers of muslin then centrifuged at 20,000 g_{av} (13,000 rpm in GSE rotor or 14,500 rpm in Sorvall SS-34 rotor) for 1 hour. The resulting pellet was resuspended with a Dounce homogeniser to 100 ml with 0.1 M sodium borate (orthoborate, BO_3^{3-}), 0.1 M sodium phosphate at pH 8.5. Two beef hearts provided sufficient material for two batches to be processed in a single day. The

two resulting 100 ml suspensions were combined, diluted to 1 l in 0.1 M sodium borate, 0.1 M sodium phosphate pH 8.5 and centrifuged at 20,000 g_{av} for 1 hour. The supernatant was discarded to leave a pellet of KH particles that were resuspended in approximately 100 ml 0.1 M sodium borate, 0.1 M sodium phosphate pH 8.5. The total concentration of protein was estimated from cytochrome *c* oxidase concentration, determined spectrophotometrically from a sodium dithionite-reduced *minus* potassium ferricyanide-oxidised difference spectrum ($\varepsilon_{606\text{-}630\ nm}$ = 25.7 $mM^{-1}.cm^{-1}$ (*177*)). Mitochondrial protein concentration was estimated from this value using a figure of 0.4 nmoles cytochrome *c* oxidase/mg mitochondrial protein (*178*). Typically, a two batch preparation, processed in a single day, yielded around 100 ml of ~ 45 mg of protein/ml resuspended KH particles. These were stored at -80 °C until required.

Both cytochrome bc_1 complex and cytochrome *c* oxidase can be purified from KH particles by cholate solubilisation followed by ammonium sulphate fractionation. KH particles were diluted to 20 mg of protein/ml in 0.1 M sodium borate, 0.1 M sodium phosphate pH 8.5. A 5 ml aliquot was removed and used to determine optimum sodium cholate concentration for solubilisation of cytochrome bc_1 complex and precipitation of contaminants at 40% $(NH_4)_2SO_4$ saturation. This was assessed by incrementally increasing sodium cholate concentration in the presence of 40% $(NH_4)_2SO_4$ and clearing any precipitate using a benchtop microfuge. At each increment the cytochrome *c* oxidase and cytochrome bc_1 complex content of the supernatant was determined spectrophotometrically from reduced *minus* oxidised difference spectra (cytochrome *b* of cytochrome bc_1 complex $\varepsilon_{562\text{-}575\ nm}$ = 28.6 $mM^{-1}.cm^{-1}$ (*177*)). Typically, addition of 46 μl 20% (w/v) sodium cholate per ml was found to be optimal, resulting in a supernatant containing 16% and 63% of the original concentration of cytochrome *c* oxidase and cytochrome bc_1 complex respectively. These conditions were used for the bulk: sodium cholate was added to the diluted KH preparation drop wise, followed by $(NH_4)_2SO_4$ to 40% saturation. After 30 minutes the preparation was centrifuged at 35,000 g_{av} (20,000 rpm in SS-34 rotor) for 20 minutes and the pellet discarded. The supernatant was allowed to stand for 1 hour prior to centrifuging at 35,000 g_{av} for 1 hour. 12 g/100 ml $(NH_4)_2SO_4$ was added to the supernatant to give a final

saturation of 55%. The preparation was allowed to stand for 20 minutes, during which time cytochrome bc_1 complex precipitated, prior to centrifuging at 35,000 g_{av} for 20 minutes. The supernatant, containing primarily haemoglobin and cytochrome *c*, was discarded and the cytochrome bc_1 complex containing pellet was resuspended to 30 ml with 0.1 M sodium phosphate, 0.5% (w/v) sodium cholate pH 7.4. The preparation was left overnight, during which time further contaminants precipitated, prior to centrifuging at 35,000 g_{av} for 20 minutes. The resulting supernatant was brought to 25% $(NH_4)_2SO_4$ saturation prior to centrifuging at 35,000 g_{av} for 15 minutes. The supernatant was treated with additional $(NH_4)_2SO_4$ such that percentage saturation was increased in 3% increments up to 50% with precipitates removed at each increment by centrifugation at 35,000 g_{av} for 15 minutes. Each of the resulting pellets was resuspended in 0.1 ml 0.1 M sodium phosphate pH 8.0; cytochrome *c* oxidase and cytochrome bc_1 complex content were determined spectrophotometrically as before. One typical cytochrome bc_1 complex preparation yielded 150, 312 and 114 nmoles at 38, 41 and 44% $(NH_4)_2SO_4$ saturation respectively; no cytochrome *c* oxidase was detectable in these samples. Finally, fractions with no detectable oxidase were pooled and dialysed against 0.1 M sodium phosphate at pH 8.0; it was not found to be necessary to add additional sodium cholate to prevent precipitation. Typical preparations yielded around 0.7 ml of 100 μM cytochrome bc_1 complex. Samples were stored in small aliquots at -80 °C.

2.1.2 *Rhodobacter capsulatus* cytochrome bc_1 complex (wild-type and E295V mutant)

Bacterial cytochrome bc_1 complex was supplied by P. L. Dutton from the University of Pennsylvania, U.S.A. It was purified from a genetically engineered strain of *Rba. capsulatus* in which the chromosomal copy of the *pet* operon had been deleted and into which a plasmid, encoding the *pet* operon, had been introduced. Because the plasmid was present in multiple copies, cytochrome bc_1 complex was over produced (*179*). Proteins were solubilised with n-dodecyl-β-D-maltoside (DDM) from chromatophores obtained from French-pressure cell extracts. Cytochrome bc_1 complex was subsequently purified with successive

diethylaminoethanol column chromatography steps (*179-181*). The supplied 39 μM aliquots were stored at -80 °C.

Cytochrome bc_1 complex with a glutamic acid to valine substitution at position 295 in cytochrome *b* was also supplied by P. L. Dutton. The site-directed mutation was introduced using the Quikchange system from Stratagene. This system involved the copying of an engineered template plasmid which contained a wild-type copy of *petABC*, using a suitable DNA polymerase and primers designed to incorporate the E295V substitution into the product. Resulting DNA fragments were sequenced and those which encoded only the single amino acid change were inserted into an expression vector and introduced into a *Rba. capsulatus* strain from which the *petABC* gene had been deleted (*182*). Success of the procedure was confirmed by sequencing plasmid DNA from the mutated strains. Cytochrome bc_1 complex was then purified in a similar manner to the wild-type complex (*182;183*). The supplied 40 μM aliquot was stored at -80 °C.

2.1.3 Bovine complex I

Mitochondrial complex I, purified from bovine heart muscle as described in reference (*184*) was supplied by Judy Hirst, Cambridge, U.K. Mitochondrial membranes were prepared from isolated mitochondria by disruption with a Waring blender in the presence of 150 mM potassium chloride (*185*) and resuspended in 20 mM Tris-HCl, 10% (v/v) glycerol and 1 mM ethylenediamine tetra-acetic acid (EDTA) at pH 7.4. Membrane proteins were solubilised by addition of 1% DDM and complex I was purified by anion exchange chromatography followed by size exclusion chromatography then concentrated to ~ 2 mg/ml using a centrifugal concentrator (*184*). The concentration of the supplied samples was 129 mg/ml; samples were stored at -80 °C in 25 μl aliquots.

2.1.4 *Yarrowia lipolytica* complex I (wild-type and H226M mutant)

Wild-type complex I was prepared from a recombinant strain of *Y. lipolytica* which produced complex I with a His-tag incorporated onto the C-terminus of subunit NUGM (the homologue of the bovine 30 kDa subunit). The gene *NUGM*

was deleted from *Y. lipolytica* strain GB1 (*186*), and replaced by a plasmid copy which included a C-terminal extension consisting of six histidine residues. Introduction of the His-tag into complex I was shown not significantly to affect assembly or function of the complex (*186*). Cells in 400 mM sucrose, 1 mM EDTA, 20 mM sodium MOPS at pH 7.2 were broken using a bead beater (*187*). Membrane proteins were made soluble by adding 1 g DDM per g of protein; in the presence of 1 mM phenylmethylsulfonyl fluoride, a protease inhibitor. The His-tagged Complex I was then isolated using a nickel nitrilotriacetic fast flow Sepharose column (Pharmacia) and fast protein liquid chromatography. The combined peak fractions containing complex I activity were pooled, concentrated to 73 mg/ml using a centrifugal concentrator and stored at -80 °C (*186*).

Complex I in which His-226 of the NUCM subunit (homologue of the bovine 49 kDa subunit) was replaced by a methionine residue was prepared from strain Δnucm L1 (*188*), in which the *NUCM* gene had been deleted. The H226M point mutation was generated by the QuikChange method (Stratagene) using a polymerase chain reaction product containing the *NUCM* gene as a template, a suitable DNA polymerase and primers designed to incorporate the substitution into the product. Resulting fragments were sub-cloned into pUB4 and introduced into strain Δ*NUCM* L1 (*188*). *Y. lipolytica* H226M complex I was then purified by essentially the same method as described for the wild-type complex (*186;188*). The concentration of the supplied sample was 9 mg/ml; the sample was stored at -80 °C.

2.1.5 Complex I activity assay

Complex I activity was determined by monitoring oxidation of substrate NADH spectrophotometrically (*148*). NADH absorbs in the near UV at 260 and 340 nm; oxidation to NAD^+ results in a small downshift of the 260 nm absorption and abolition of the 340 nm band, the extinction coefficient ($\varepsilon_{340\ nm}$) of which is 6.2 $mM^{-1}.cm^{-1}$ (*189*). Initial rates for NADH oxidation by complex I were determined from $\Delta A_{340\text{-}400\ nm}$, measured with a Sigma ZWSII dual-wavelength spectrophotometer, versus time and using an $\varepsilon_{340\text{-}400\ nm}$ of 6.1 $mM^{-1}.cm^{-1}$. Reactions were carried out in a 1 cm pathlength cuvette in 3 ml buffer (20 mM Hepes, 250 mM Sucrose, 2 mM EDTA, 2 mM sodium azide pH 8.0) with 2 mM

hexaammineruthenium chloride as an electron acceptor. A baseline absorbance was measured prior to addition of 3 μl 100 mM NADH. After a short delay to determine background rate, 6.8 μg *Y. lipolytica* complex I in a 3 μl volume was added and $\Delta A_{340\text{-}400\ nm}$ was monitored over several minutes. To determine the effect on activity of additional lipid, complex I was incubated on ice for 1 hour with L-α-phosphatidyl choline type IV-S (Sigma P3644) at a lipid to protein ratio of 500:1 prior to the activity assay. For this purpose a 5.4 mM stock solution of L-α-phosphatidyl choline was purified by washing the lipid solid in chloroform, followed by acetone and thorough drying onto the surface of a round bottomed flask. The lipid was then dissolved into 20 mM potassium Hepes, 50 mM potassium chloride, 1.6% w/v n-octyl β-D-glucopyranoside pH 7.2 with vigorous vortex mixing.

2.2 Model compounds and reagents

To aid interpretation of the complex FTIR difference spectra obtained from cytochrome bc_1 complex and complex I a number of simple chemicals and proteins were analysed. The model compounds described below were either components of, or related to components of, the proteins under investigation or were chemicals used to buffer or induce changes in the proteins.

2.2.1 Ferredoxins

Ferredoxins are low molecular weight, soluble proteins that contain one or more iron-sulphur (Fe-S) centres. In some instances, structural data are available for both oxidised and reduced forms, for example *Desulfovibrio africanus* 4Fe-4S ferredoxin (*190;191*), allowing the effect of Fe-S centre redox changes on the peptide backbone to be visualised (*192*) (see section 5.3.1). The IR absorption properties of ferredoxins were analysed to assist in the interpretation of IR spectra of complex I, the bovine and yeast form of which contain two 2Fe-2S type- and six 4Fe-4S type- Fe-S centres. All ferredoxins were supplied by Prof. Richard Cammack, Kings College London with the exception of the 2Fe-2S type ferredoxin from parsley which had been prepared by a standard method (*193*) by P. Rich. Ferredoxins containing a single 4Fe-4S type Fe-S centre or ferredoxin containing two 4Fe-4S type Fe-S centres were purified from *D. africanus* (*194*)

and *Clostridium sporogenes* (*195*) respectively. All samples were stored at -80 °C.

2.2.2 Flavin mononucleotide

Flavin mononucleotide (FMN), supplied by Sigma (F6750), is a non-covalently bound component of complex I. 2 mM FMN solutions in 20 mM potassium phosphate and 200 mM potassium chloride at pH 6.0 and 8.0 were analysed by electrochemically-induced ATR FTIR redox difference spectroscopy (see section 2.4.6) in order to identify marker bands that would be expected to contribute to complex I spectra. FMN exists in reduced ($FMNH_2$), semiquinone ($FMNH^{\bullet}$) and oxidised (FMN) forms. In solution the semiquinone form is unstable and the midpoint potential (E_{m7}) for $2e^-$ reduction/oxidation is -219 mV (*100*). The pK_a values of $FMNH_2$ / $FMNH^-$ and $FMNH^{\bullet}$ / $FMN^{\bullet -}$ are 6.7 and 8.5 respectively in aqueous media (*165;196*); pK_a values and midpoint potentials of FMN in complex I are detailed in section 1.3.2.

2.2.3 Histidine

The imidazole sidechain of histidine is able to ligate metals and exist in four different protonation states (see section 3.5.4). This amino acid therefore has the potential to play a direct role in protonation transfer mechanisms. Imidazole *minus* imidazolate and imidazolium *minus* imidazole FTIR difference spectra were recorded in order to determine IR markers useful for the detection of histidine protonation state changes in proteins. Solubility changes occurring with protonation state changes complicated this process and necessitated the use of monomeric L-histidine solutions and of thin layers of poly-L-histidine (n = 112) for acquiring a full dataset of imidazole *minus* imidazolate and imidazolium *minus* imidazole spectra respectively (see section 3.5.4). pH titration of a solution of 50 mM L-histidine (monomeric) and 10 mM potassium ferrocyanide ($\varepsilon_{2038\ cm^{-1}} = 4140\ M^{-1}.cm^{-1}$) and the measured effective pathlength of the ATR evanescent wave (see section 2.4.2) enabled the extinction coefficient of an IR marker band at 1450 cm^{-1} for the imidazole-imidazolate protonation state change difference spectrum to be determined (see section 3.5.4).

2.2.4 Electrochemical mediators

Potassium ferricyanide (E_{m7} = 420 mV), hexaammineruthenium chloride (E_{m7} = 70 mV), gallocyanine (E_{m7} = 20 mV), anthraquinone-2,6-disulfonate (E_{m7} = -185 mV), benzyl viologen dichloride, (E_{m7} = -311 mV) and methyl viologen, (E_{m7} = -449 mV) were used in appropriate combinations for redox mediation during electrochemically-induced FTIR difference spectroscopy (see section 2.4.6). Redox difference spectra for each of these compounds were measured in order to identify any contribution from these compounds to the redox difference spectra of the proteins under investigation. Such contributions could be removed by subtraction of the appropriate pure mediator spectrum (see section 3.4.2).

2.2.5 Potassium phosphate buffer

Proteins, including ferredoxins, were buffered in potassium phosphate at an appropriate pH during ATR FTIR analyses. Dihydrogen phosphate ions ($H_2PO_4^-$) (hydrogen-ion donor (acid)) and hydrogen phosphate ions (HPO_4^{2-}) (hydrogen-ion acceptor (base)) have different IR absorption characteristics. Variation in the ratio of the concentrations of buffer components is detectable by FTIR for even slight changes in pH. In order to identify buffer contributions to protein FTIR difference spectra and to remove them when necessary absolute FTIR spectra were recorded for 0.5 M potassium phosphate solution at pH values from 5.5 to 8.5 at 0.1 pH unit increments (see section 3.4.1).

2.3 UV/Visible spectroscopy

UV/Visible spectra were recorded in an appropriate wavelength range either using a cuvette or using a fibre optic probe (Avantes, The Netherlands); the latter enabled measurement of samples mounted on the IRE allowing simultaneous UV/visible and ATR FTIR spectroscopy. In both cases similar in-house-assembled spectrophotometers were used. The light source consisted of a 12 V 100 W tungsten lamp in an Applied PhotoPhysics (APP) housing powered by a Bentham 505 current-stabilised filament lamp power supply. UV/Visible radiation was passed through a f/3.4 scanning monochromator (APP) and delivered to the sample either directly, when using a cuvette, or by a fibre optic reflecting probe, when making simultaneous UV/visible and ATR FTIR measurements. Transmitted radiation was detected by a high voltage

photomultiplier tube. The resulting signal was amplified appropriately by a Keithley 428 current amplifier, with 1 ms filter enabled, then digitised by a Microlink analogue to digital converter. Equipment was interfaced to a control computer that could be synchronised to the computer controlling the IR spectrophotometer so that both UV/visible and IR data acquisition could be automatically synchronised. Absorbance values were computed as log I_0/I_1, where I_1 is the sample intensity and I_0 is an appropriate background value. More specific details on how this technique was used are included in the relevant results chapters.

2.4 Infrared spectroscopy

FTIR spectra of cytochrome bc_1 complex, complex I and model compounds were recorded with a Bruker IFS 66/S spectrophotometer, fitted with a liquid nitrogen-cooled MCT-A- or -B-type detector. With the exception of transmission mode measurements performed to determine the effective pathlength of the ATR evanescent wave (see below) all measurements were performed in ATR mode.

2.4.1 Attenuated total reflection FTIR spectroscopy

All measurements in ATR mode were taken at room temperature with a 1.5 mm aperture and a resolution of 4 cm^{-1}. The ATR accessory (DuraSamplIR, SensIR Technologies, Europe) was formed from a 3 mm surface diameter 3 reflection silicon internal reflective element (IRE), mounted on a ZnSe focusing element and surrounded by a stainless steel plate. Prior to sample deposition the IRE was polished with a paste of 0.03 mm alumina powder, and cleaned with water and ethanol; this resulted in the removal of a thin layer (estimated to be in the order of microns) of the uppermost surface of the IRE and with it any contaminants. This configuration allowed the 4000 cm^{-1} to 900 cm^{-1} region to be measured.

2.4.2 Effective ATR path length

In order to interpret ATR FTIR spectra quantitatively it was necessary to determine the path length of the evanescent wave established at the IRE surface. Path length can be calculated from the measured IR absorbance of a sample with known extinction coefficient and concentration (see introduction, section 1.2.1). The extinction coefficient of ferricyanide at 420 nm is 1.0 $mM^{-1}.cm^{-1}$ (*197*);

ferricyanide also has a characteristic absorption in the mid-IR region at 2115 cm^{-1} for which the extinction coefficient is not known. In order to determine this extinction coefficient for use in calculating the ATR evanescent wave pathlength, potassium ferricyanide solutions at 25 mM, 50 mM and 100 mM were prepared in 0.1 M potassium phosphate at pH 7.0. The ferricyanide concentration of these solutions was confirmed using UV/visible spectroscopy and a cuvette of known pathlength with appropriately diluted samples. Each solution was then loaded into a cell consisting of two calcium fluoride windows that are transparent to both UV/visible and IR radiation, and separated by a spacer of approximately 30 μm thickness (Graseby SpecAc). UV/Visible spectroscopy at 420 nm was used to determine the pathlength of this cell prior to recording the intensity of the absorbance at 2115 cm^{-1} by transmission FTIR spectroscopy. From these data, an average value of 1.1 $mM^{-1}.cm^{-1}$ was calculated for the extinction coefficient of the 2115 cm^{-1} absorbance band of ferricyanide (see Table 2.1). The ATR apparatus was then mounted in the IR spectrophotometer and intensities of the 2115 cm^{-1} peaks of the three ferricyanide solutions measured. The pathlength of the evanescent wave at 2115 cm^{-1} was calculated to be 2.6 μm from the ferricyanide extinction coefficient and known concentrations (see Table 2.2). Since the depth of penetration of the evanescent wave is linearly inversely proportional to frequency (*72*), the pathlength (in μm) at any other frequency x cm^{-1} is 2.6 × (2115/x). In addition to wavelength (λ), the depth of penetration (d_P) of the evanescent wave is also affected by the refractive indexes of the sample (n_1) and IRE (n_2) and by the angle (θ) at which incident radiation strikes the reflecting surface; see equation below (*72*) and section 1.2.2.2:

$$d_P = (\lambda / n_1) / (2\pi [\sin \theta - (n_1 / n_2)^2]^{0.5})$$

Therefore extrapolation of an effective pathlength for a protein sample from this data requires the assumption that n_1 is constant.

Ferricyanide conc. (mM)	$\Delta A_{420\text{-}500\ nm}$	Pathlength of cell (μm)	$\Delta A_{2115\text{-}2080\ cm^{-1}}$ (transmission)	$\varepsilon_{2115\ cm^{-1}}$ ($mM^{-1}.cm^{-1}$)
25	0.082	31.5	8.88×10^{-2}	1.07
50	0.166	31.3	1.78×10^{-1}	1.08
100	0.330	31.4	3.58×10^{-1}	1.08
Average		31.4		1.08

Table 2.1 UV/Visible data used for determining pathlength of cell and transmission mode FTIR data used for determining $\varepsilon_{2115\ cm^{-1}}$; see text.

Ferricyanide conc. (mM)	$\Delta A_{2115\text{-}2080\ cm^{-1}}$ (ATR)	$\varepsilon_{2115\ cm^{-1}}$ ($mM^{-1}.cm^{-1}$)	Path length of evanescent wave (μm)
25	6.92×10^{-3}	1.08	2.56
50	1.37×10^{-2}	1.08	2.54
100	2.79×10^{-2}	1.08	2.58
Average			2.56

Table 2.2 ATR FTIR data used for determining effective pathlength of evanescent wave; see text.

2.4.3 Preparation of protein for ATR FTIR spectroscopy

ATR FTIR spectroscopy can be applied to both hydrophilic and hydrophobic proteins. Hydrophilic soluble proteins (e.g. ferredoxins) required less preparation, although it was necessary for proteins to be prepared at sufficient concentration (ideally, $\geq$ 2 mM) and volume (~ 25 μl) for difference spectroscopy.

ATR FTIR difference spectra of poly-L-histidine (in the insoluble imidazole form - see section 3.5.4), cytochrome bc_1 complex and complex I were obtained from rehydrated protein films adhered directly to the IRE through hydrophobic interactions. This procedure required less protein than was necessary for the study of soluble proteins. For example, a single layer of complex I of optimal thickness could be formed from ~ 0.01 mg protein. In order to promote the

hydrophobic forces necessary to create a stable protein layer detergent and excess salt were removed from the samples immediately prior to adhering them to the prism (see Chapter 3). For preparation of a single poly-L-histidine layer 20 μl of 25 mg/ml poly-L-histidine (n = 112) in 0.3 M hydrochloric acid was diluted to 2.5 ml with 1 mM potassium phosphate and the pH adjusted to 8.0 with 0.3 M potassium hydroxide. After centrifuging at 375,000 g_{av} for 5 minutes the resulting pellet was resuspended in 10 μl distilled water and dried onto the IRE prior to rehydration with 1 mM potassium phosphate, 100 mM potassium chloride at pH 8.0. For the cytochrome bc_1 complex and complex I, ATR-ready aliquots consisting of the minimal amount of detergent depleted protein required for a single layer suspended in 1-2 μl water were prepared as follows:

10 μl bovine cytochrome bc_1 complex was diluted into 2 ml 1 mM potassium phosphate, 0.02% sodium cholate pH 7.0 then centrifuged at 414,000 g_{av} (100,000 rpm in Sorvall S100-AT4 rotor) for 90 minutes at 4 °C. The resulting pellet was washed by resuspending in buffer (1 mM potassium phosphate pH 7.0) and centrifuged at 414,000 g_{av} for 60 minutes at 4 °C after which time the supernatant was discarded. The pellet was washed in buffer for a second time by centrifuging as above for 45 minutes and the final pellet was resuspended in 10 μl water then split into 2 μl aliquots that were either diluted and applied to the prism or stored at -80 °C for later use. ATR-ready *Rba. capsulatus* cytochrome bc_1 complex aliquots (wild-type and E295V) were prepared in an identical procedure except the initial material was 40 μl protein diluted into 2 ml buffer.

For bovine and *Y. lipolytica* (wild-type and H226M) complex I, 0.1 mg protein was diluted into 2 ml 20 mM potassium phosphate, 0.0075% (w/v) sodium cholate, 0.0075% (w/v) n-octyl β-D-glucopyranoside at pH 8.0 and pelleted by centrifugation at 390,000 g_{av} (95,000 rpm in S100-AT4 rotor) for 30 minutes at 4 °C. The resulting pellet was washed twice, by resuspending in 20 mM potassium phosphate pH 8.0 and centrifuging at 300,000 g_{av} (85,000 rpm in S100-AT4 rotor) for twenty minutes and then by resuspending in 1 mM potassium phosphate pH 8.0 and centrifuging at 300,000 g_{av} for 20 minutes. The final pellet was resuspended in 10 μl water and split into 1 μl aliquots that were either diluted then applied to the prism or stored at -80 °C.

Prior to preparation of rehydrated protein films the IRE was cleaned as described in section 2.4.1. An ATR-ready aliquot was diluted to a volume of 6 μl with water, which thawed the sample if necessary, and then deposited directly onto the IRE. The sample was then dried under a gentle stream of air. In later experiments a stream of nitrogen was used due to concerns about the purity and reliability of the compressed air supply; this change was not found to have any detectable effect on the experiment. Cytochrome bc_1 complex films were rehydrated with 50 μl 100 mM potassium phosphate, 200 mM potassium chloride at pH 7.0 and Complex I films were rehydrated with 10 μl of 20 mM potassium phosphate, 200 mM potassium chloride at pH 6.0 or 8.0. Drying and rehydration were monitored from absolute ATR FTIR absorption spectra measured at different stages during preparation of a rehydrated protein film (see Chapters 4 and 5). Cytochrome bc_1 complex and complex I protein films were sufficiently stable for ATR FTIR difference spectroscopy after approximately 60 and 30 minutes respectively.

2.4.4 H-D exchange

For deuterium oxide exchange, sample preparation and ATR measurements were performed throughout by substitution of D_2O buffers at appropriate pD (assuming pD is equal to the pH meter reading + 0.4 (*198*)). Preincubation of samples in D_2O overnight at 4 °C before dilution and washing as described above increased the amount of H/D exchange, the final extent of which was estimated to be >90% using the methods described in (*199*). Briefly, extent H-D exchange of the peptide groups was calculated from the change in the ratio w ($A_{amide\ II}/A_{amide\ I}$), where $A_{amide\ II}$ and $A_{amide\ I}$ are the integrated intensity of the amide II and amide I bands, respectively. The total fraction of unexchanged peptide groups in the protein (f) was estimated from the relation $f = w'/w$, where w' is the amide I and II intensity ratio measured for samples exposed to D_2O and w the intensity ratio before exposure (*199*).

2.4.5 Perfusion-induced ATR FTIR difference spectroscopy

For measurement of perfusion-induced difference spectra an in-house constructed stainless steel 75 μl internal volume chamber with inlet and outlet

tubes was placed over the IRE and rehydrated protein layer (see Figure 2.1A). The chamber was sealed to the stainless steal IRE surround by a gasket consisting of parafilm which was cut to shape and onto both sides of which a small quantity of high vacuum grease had been applied. An electronically controlled three-way valve and peristaltic pump allowed continuous flow (approximately 1 ml per minute) of alternating buffers over the rehydrated protein film. ATR FTIR difference spectra were recorded as either protonation state or redox changes were induced by the perfusant. Buffer solutions were freshly prepared and mechanically degassed using a hand vacuum pump (Mityvac 04010) prior to the ATR FTIR measurements. Buffers containing sodium dithionite were maintained under an argon atmosphere and, in experiments using sodium dithionite, the electronic three-way valve was replaced with a manual valve and tubing lengths kept minimal. Details of timings required for redox/protonation state changes are included in the relevant results chapters.

2.4.6 Electrochemically-induced difference spectroscopy

Electrochemically-induced redox difference spectra were measured using an in-house constructed electrochemical cell which was attached to the ATR apparatus in the same way as the perfusion cell (described above). The assembled cell formed a chamber of approximately 20 μl internal volume, the roof of which consisted of a 9 mm diameter circular glassy carbon working electrode, over the rehydrated protein film or containing protein in solution. An auxiliary electrode consisting of a platinum sheet (40 mm^2 surface area) was connected to the sample by a porous glass frit, and a Ag/AgCl reference electrode provided the reference voltage (204 mV) (see Figure 2.1B). A version of this device fitted with a fibre optic probe enabled simultaneous acquisition of UV/visible and FTIR spectra (see Figure 2.1C). Redox mediation between glassy carbon and protein film was provided by an appropriate mediator solution the composition of which is detailed in Chapters 3, 4 and 5, as are the applied potentials and redox equilibration times.

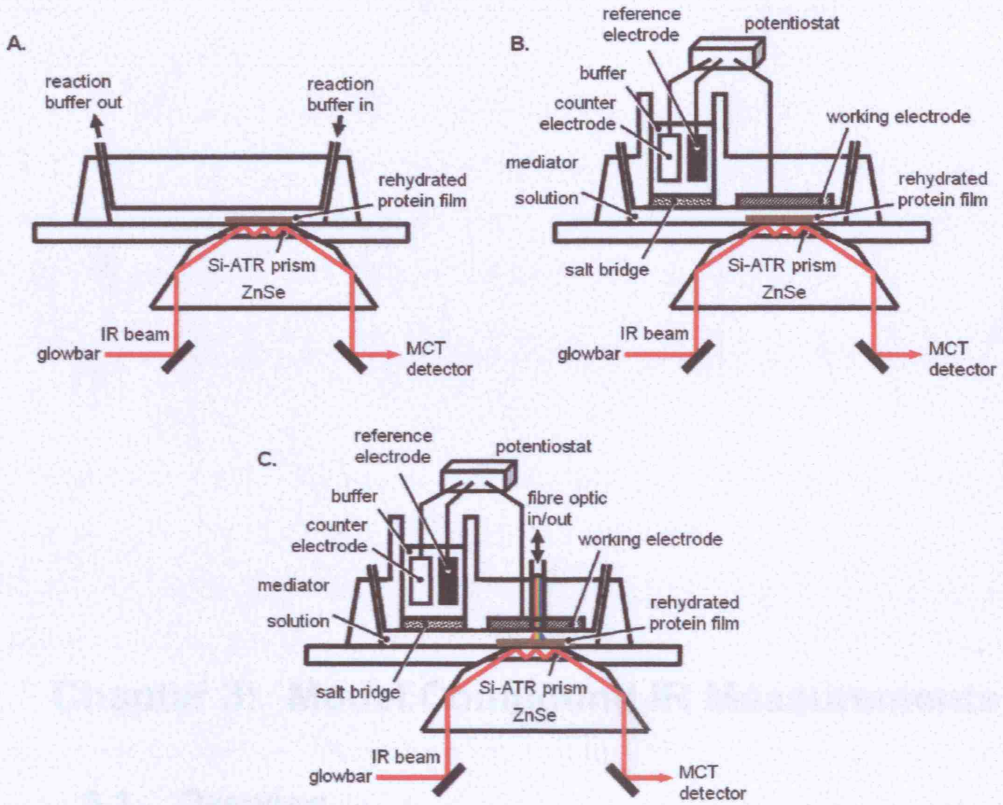

Figure 2.1 Schematics of perfusion and electrochemical cells. The perfusion cell (A) formed a sealed chamber over the rehydrated protein film and IRE. In/outlets allowed buffer, the composition of which was controlled using computer controlled valves, to be continuously perfused through the chamber. The electrochemical cell (B) was used to induce changes in rehydrated protein films and protein in solution. It formed a chamber, the ceiling of which was composed of a circular glassy carbon working electrode, over the sample and IRE. A porous glass frit connected the sample chamber to a platinum auxiliary electrode and a Ag/AgCl reference electrode. Use of appropriate electrochemical mediators allowed redox equilibration between the working electrode and protein sample and potential was controlled using a potentiostat and a computer controlled offset device. A version of the electrochemical cell fitted with a fibre optic probe (C) enabled simultaneous acquisition of UV/visible and FTIR spectra. Drawings are not to scale; see text for further details. Adapted from figures of M. Iwaki.

Chapter 3: Model Compound IR Measurements

3.1 Overview

In order to assist in the acquisition and interpretation of IR difference spectra of cytochrome bc_1 complex and complex I (see Chapters 4 and 5 respectively), the IR absorbance characteristics of a number of more simple proteins/compounds were measured or, where possible, derived from the literature (see also Introduction section 1.2.2.3). The spectra presented below were measured either to allow detection and quantitation of contaminants (sodium cholate, n-octyl β-$_D$-glucopyranoside, polycarbonate and high vacuum grease (see section 3.3)), detection and removal of unavoidable overlapping signals of added reagents (e.g. phosphate, electrochemical mediators, NAD^+, NADH and sodium dithionite (see section 3.4)) or to assist in interpretation of respiratory complex difference spectra (ferredoxins, FMN, ubiquinone and histidine (see section 3.5)). In order to use a model compound spectrum to identify and quantify/remove contributions from contaminants/reagents from respiratory complex difference spectra a full assignment of bands is unnecessary. However, if a model compound spectrum is to assist in interpretation it must be well understood and, where possible, specific features should be assigned to specific vibrational modes. Therefore, a greater level of interpretation is included for the model compound spectra presented in

section 3.5 than for those presented in sections 3.3 and 3.4. Section 3.5 also includes a description of the IR absorbance characteristics of ubiquinone, lysine, tyrosine, aspartic acid and glutamic acid that were taken from available literature (*75;80*). Water vapour, condensed water and deuterium oxide are also addressed (section 3.2) because both model compound spectra and spectra from the respiratory complexes were routinely adjusted to remove their contributions.

3.2 Water vapour, condensed water and deuterium oxide

IR signals from water vapour can contribute to IR spectra when the amount of water vapour in the IR beam path, within the spectrometer and ATR accessory, differs between background and sample measurements. The IR spectrometers used were purged with dry air in order to minimise the amount of water vapour in the beam path. However, some residual water vapour remained in the purge gas and some leakage of atmospheric air was inevitable. Furthermore, the water content of air varied with temperature, atmospheric conditions and other factors. However, since the amount of water vapour fluctuates around an approximately constant value, averaging of many spectra frequently eliminated or greatly reduced the magnitude of the water vapour signals. A high quality absolute absorbance spectrum of water vapour was recorded to identify and remove (where necessary) any remaining contributions (see Figure 3.1, trace A). It consists of a complex and highly reproducible series of bands in the 2100-1200 cm^{-1} region. This spectrum was acquired in conjunction with routine maintenance of the purge system. When the system was shutdown the water vapour concentration within the spectrometer rapidly equilibrated with that of the environment. Immediately after reactivating the purge system a background measurement was made. After several hours the water vapour concentration inside the spectrometer had minimised and a sample measurement was made; the resulting spectrum was inverted to give the presented absolute absorbance spectrum.

Absolute absorbance ATR FTIR spectra of condensed water and deuterium oxide were obtained by measuring the difference between a spectrum obtained from the clean prism surface and one with a 50 μl droplet of water or deuterium oxide

deposited on the prism respectively (see Figure 3.1, traces B and C). In the case of deuterium oxide a volatiles cover was used to prevent H_2O/D_2O exchange with the surrounding atmosphere. These spectra, which are both dominated by O-H/D scissoring mode at 1638/1205 cm^{-1}, were used as subtractors to compensate for changes in H_2O or D_2O concentrations caused by expansion/contraction of protein films and also to remove solvent signals from model compound spectra.

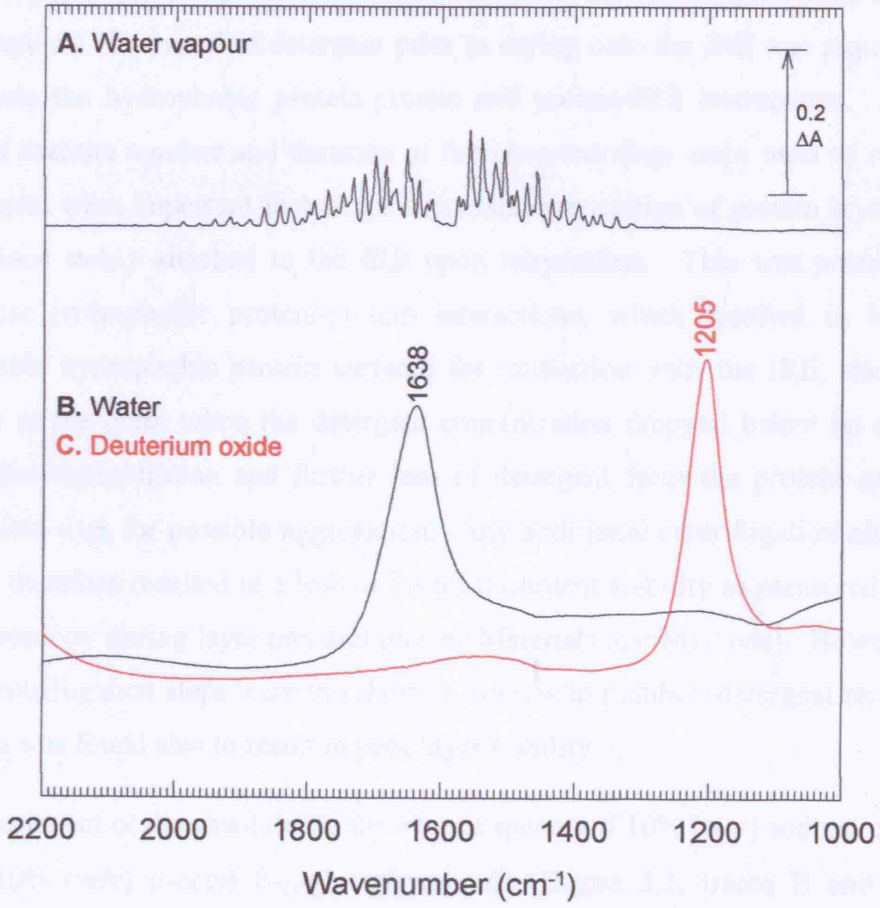

Figure 3.1 FTIR absolute absorbance spectra of water vapour, condensed water and deuterium oxide. Trace A is the inverse of a spectrum recorded during removal of water vapour from the IR beam path after completion of routine maintenance of the system used to purge water vapour from the spectrometer (see text). The sample spectrum at low water vapour (an average of 8000 interferograms at 4 cm^{-1} resolution) was recorded several hours after a background (1000 interferogram average) had been recorded at ambient water vapour content. Traces B and C are absolute absorbance spectra of condensed water and deuterium oxide respectively. Each is the average of 1000 interferograms at 4 cm^{-1} resolution.

3.3 Model compound measurements for detection of contaminants

3.3.1 Detergent

During preparation of ATR-ready aliquots (for adhesion to the IRE), cytochrome bc_1 complex and complex I were made soluble in a solution of 0.02% (w/v) sodium cholate or a solution of 0.0075% sodium cholate and 0.0075% n-octyl β-$_D$-glucopyranoside, respectively (see Materials and Methods section 2.4.3 for full description). Removal of detergent prior to drying onto the IRE was required to promote the hydrophobic protein-protein and protein-IRE interactions. It was found that the number and duration of the ultracentrifuge steps used to remove detergent were important factors for successful preparation of protein layers that remained stably attached to the IRE upon rehydration. This was presumably because hydrophobic protein-protein interactions, which resulted in loss of available hydrophobic protein surfaces for interaction with the IRE, started to occur at the point when the detergent concentration dropped below its critical micellar concentration and further loss of detergent from the protein surfaces provided sites for possible aggregation. Any additional centrifugation after this point therefore resulted in a loss of layer attachment stability as measured by IR spectroscopy during layer preparation (see Materials and Methods). However, if the centrifugation steps were too short or too few in number, detergent remained which was found also to result in poor layer stability.

Measurement of the absolute IR absorbance spectra of 10% (w/v) sodium cholate and 10% (w/v) n-octyl β-$_D$-glucopyranoside (Figure 3.2, traces B and C) in water, with solvent contributions (trace A) subtracted, enabled detergent signals in the spectra acquired during drying of protein layers to be identified when present. The sodium cholate spectrum is simple in the range of interest consisting of a broad peak at 967 cm^{-1} with a shoulder at 929 cm^{-1}; these signals most likely arise from the combination of the numerous C-H out-of-plane bending modes of the ring structures (*73*). The n-octyl β-$_D$-glucopyranoside spectrum is more complex with peaks at 1458, 1376, 1161, 1103, 1097, 1036 and 995 cm^{-1}. The peaks at 1458 and 1376 cm^{-1} are likely to contain contributions from C-H deformation modes of CH_2 and CH_3 groups respectively (*73*). The

overlapping signals between 1161 and 995 cm^{-1} most likely include contributions from C-O stretching modes and C-H bending (both in- and out-of-plane) associated with the ring structure (*73*). The presence of detergent signals in the spectra recorded during layer preparation, which always coincided with complete loss of the layer from the IRE upon rehydration, indicated that layer instability resulted from the ultracentrifugation washes being too mild rather than too harsh. This information was of great use when establishing a procedure to remove sufficient detergent without compromising the quantity of hydrophobic protein surfaces available for interaction with IRE.

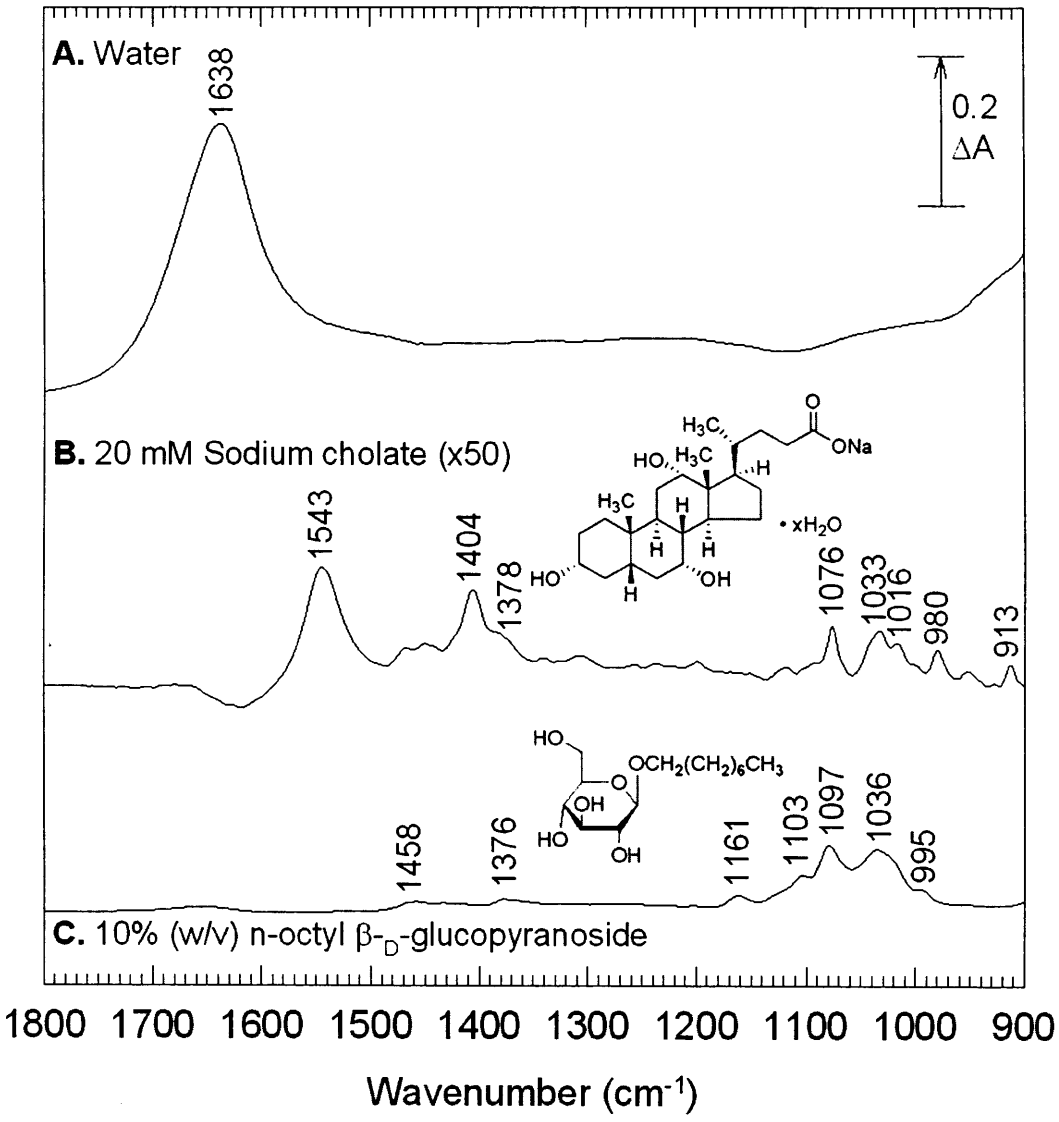

Figure 3.2 Absolute absorbance ATR FTIR spectra of distilled water, sodium cholate, n-octyl β-D-glucopyranoside. Trace A, distilled water; trace B, 10% (w/v) sodium cholate *minus* trace A; and trace C, 10% (w/v) n-octyl β-D-glucopyranoside *minus* trace A. Each spectrum is the average of 1000 interferograms at 4 cm^{-1} resolution.

3.3.2 Polycarbonate and vacuum grease

During preparation of ATR-ready aliquots detergent was removed by a series of ultracentrifugation wash steps (see Materials and Methods and above) using polycarbonate ultracentrifuge tubes. Occasionally aliquots were found to be contaminated with polycarbonate; this presumably occurred while resuspending protein pellets in the polycarbonate tubes using a glass rod. An absolute absorbance spectrum of polycarbonate was measured by pressing the base of a centrifuge tube against the IRE. The resulting spectrum (Figure 3.3, trace A) consists of peaks at 1771, 1504, 1220, 1188, 1158, 1102, 1080 and 1013 cm^{-1}. The absorbance at 1771 cm^{-1}, likely to arise from C=O stretching modes (*73*), was particularly useful for detection of polycarbonate contamination in protein samples because it lies outside the envelope in which biological materials conventionally absorb. Signals between 1220 and 1013 cm^{-1} may arise from C-O stretching modes, however this is speculative because the nature of the polycarbonate polymer used is not known. The presence of polycarbonate signals in the absolute absorbance IR spectra recorded during protein drying (see Materials and Methods) did not coincide with poor layer stability. However, contaminated layers were not used for data collection.

Perfusion and electrochemistry cells were mounted onto the stainless steel surround of the IRE using a parafilm gasket and a small amount of high vacuum grease (see Materials and Methods). In order to address concerns that the vacuum grease might contaminate the protein layer an absolute absorbance spectrum of vacuum grease was recorded. Absolute absorbance spectra measured by directly applying vacuum grease to the IRE consisted solely of signals with ΔA greater than 1; this results from absolute or near absolute attenuation of the IR beam at those frequencies and leads to distortions of the spectra in regions of very high absorption. In order to obtain a thinner (sub-penetration distance of the evanescent wave (see Introduction)) film of vacuum grease, 10 μl of vacuum grease-saturated water was dried onto the IRE and an absorbance spectrum recorded (Figure 3.3, trace B). The resulting vacuum grease spectrum consists of a very sharp peak at 1260 cm^{-1} and two broader overlapping peaks at 1091 and 1021 cm^{-1} all with ΔAs of less than 0.06. This spectrum indicates that the vacuum grease is soluble to a small extent and that its

IR absorbances are very strong. The exact composition of the vacuum grease used is not known other than it being silicone based. Siloxane- (Si-O-Si) forming polymers containing eight or more silicon atoms have characteristic strong absorbances close to 1090 and 1020 cm^{-1} due to the antisymmetric Si-O-Si stretching modes (*200*) and it therefore seems highly probable that vacuum grease contains such polymers. Data were not collected from protein layers in which vacuum grease was detected, either during layer preparation or during the course of an experiment. In practice, vacuum grease contamination occurred very infrequently.

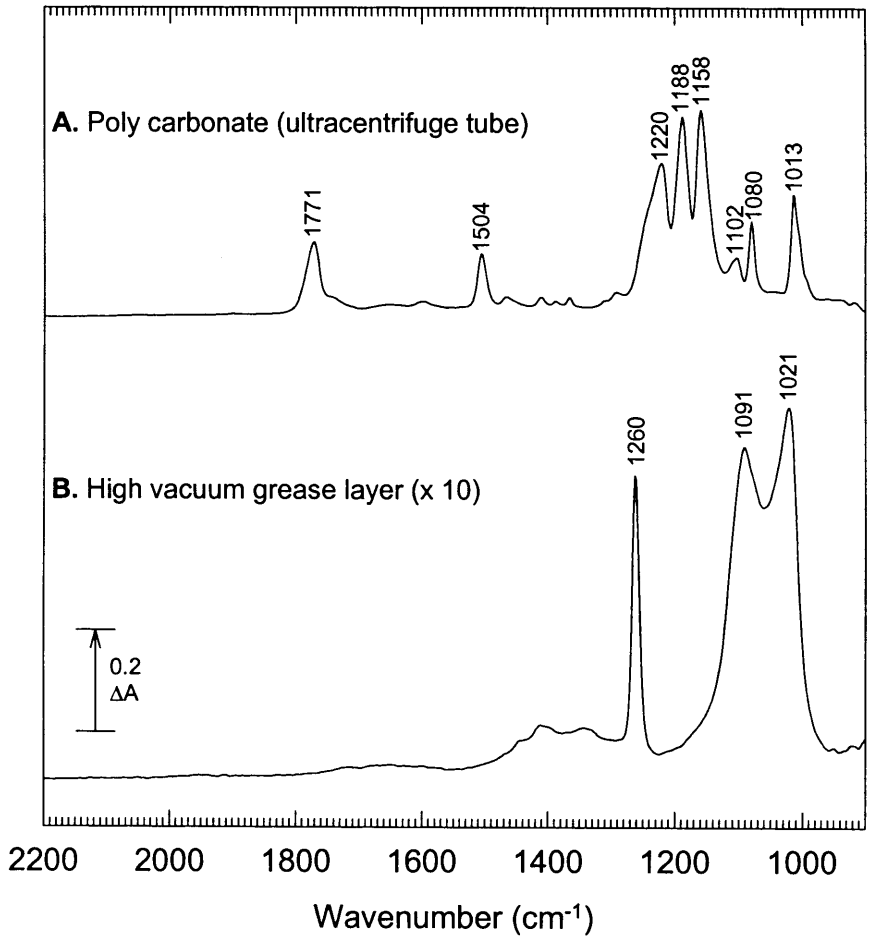

Figure 3.3 ATR FTIR absolute absorbance spectra of polycarbonate (trace A) and high vacuum grease (trace B). Trace A was recorded by pushing the base of an ultracentrifuge against the IRE. Trace B, which is expanded ×10, was recorded by drying 10 μl vacuum grease-saturated H_2O onto the IRE. It was not possible to acquire a spectrum by placing vacuum grease directly onto the IRE because the absorptions at 1260, 1091 and 1021 cm^{-1} were too great (see text). Each spectrum is the average of 1000 interferograms recorded at 4 cm^{-1} resolution.

3.4 Model compound measurements for removal of artefacts

3.4.1 Phosphate

Phosphate was generally used to buffer rehydrated protein films during both perfusion and electrochemistry experiments. Dihydrogen phosphate ($H_2PO_4^-$) ions serve as the major proton donor species and hydrogen phosphate ions (HPO_4^{2-}) as the major proton acceptor species for buffering in the pH 5.0 - 8.0 range. The dihydrogen phosphate and hydrogen phosphate ions have differing IR absorbance characteristics and therefore any pH change of the buffer will contribute a phosphate difference spectrum to electrochemically- and perfusion-induced IR difference spectra of cytochrome bc_1 complex and complex I.

In order to identify and remove (where necessary) phosphate buffer contributions in the IR difference spectra of proteins, absolute absorbance spectra were recorded for an 0.5 M potassium phosphate solution through a pH range of 5.5 to 8.5 in 0.1 pH unit increments (see Figure 3.4 A). The hydrogen phosphate ion (the dominant form at pH 8.5, trace i) absorbs strongly at 1075 and 989 cm^{-1}. The dihydrogen phosphate ion (dominant at pH 5.5, trace iii) absorbs at 1156, 1075, 935 cm^{-1}, however, the absorption at 1075 cm^{-1} is approximately half the intensity of that of the hydrogen phosphate ion. All spectra are dominated by the 1638 cm^{-1} scissoring mode of water. This water contribution was removed by generating phosphate pH difference spectra (see Figure 3.4 B) which were 'interactively' subtracted from protein difference spectra in order to remove any phosphate contributions. Subsequent to these experiments Klähn *et al* published FTIR spectra of 100 mM potassium phosphate solutions at pH 9.2 and 5.2 that are in good agreement with the pH 5.5 and 8.5 spectra presented in Figure 3.4 A and, based on density functional theory (DFT) calculations, made the following assignments: for the $H_2PO_4^-$ ion (the dominant form at low pH) peaks at 1156, 1075 and 935 cm^{-1} arise from a P-O stretching mode, an in-phase P-O stretching mode and a P-OH stretching mode, respectively. For the HPO_4^{2-} ion (the dominant form at high pH) the superposition of two P-O stretching modes results in the peak at 1075 cm^{-1} and the peak at 989 cm^{-1} arises from an in phase P-O stretching mode (*201*).

In order to investigate further the IR signals arising from the different forms of phosphate involved in buffering around pH 7.0, the ΔA of each of the four signals was plotted against pH (see Figure 3.5). Nernst curves were then fitted and pK values for each signal determined, the average of which matches the literature value of 6.8 (*100*) for the $H_2PO_4^-/HPO_4^{2-}$ couple.

It might be noted that any redox or ligand reactions that involve a net protonation change will result in the release/uptake of a buffer proton. Hence, monitoring of the IR changes due to phosphate can be exploited to quantitate net proton change as has been done in, for example, cytochrome bc_1 complex (*202*).

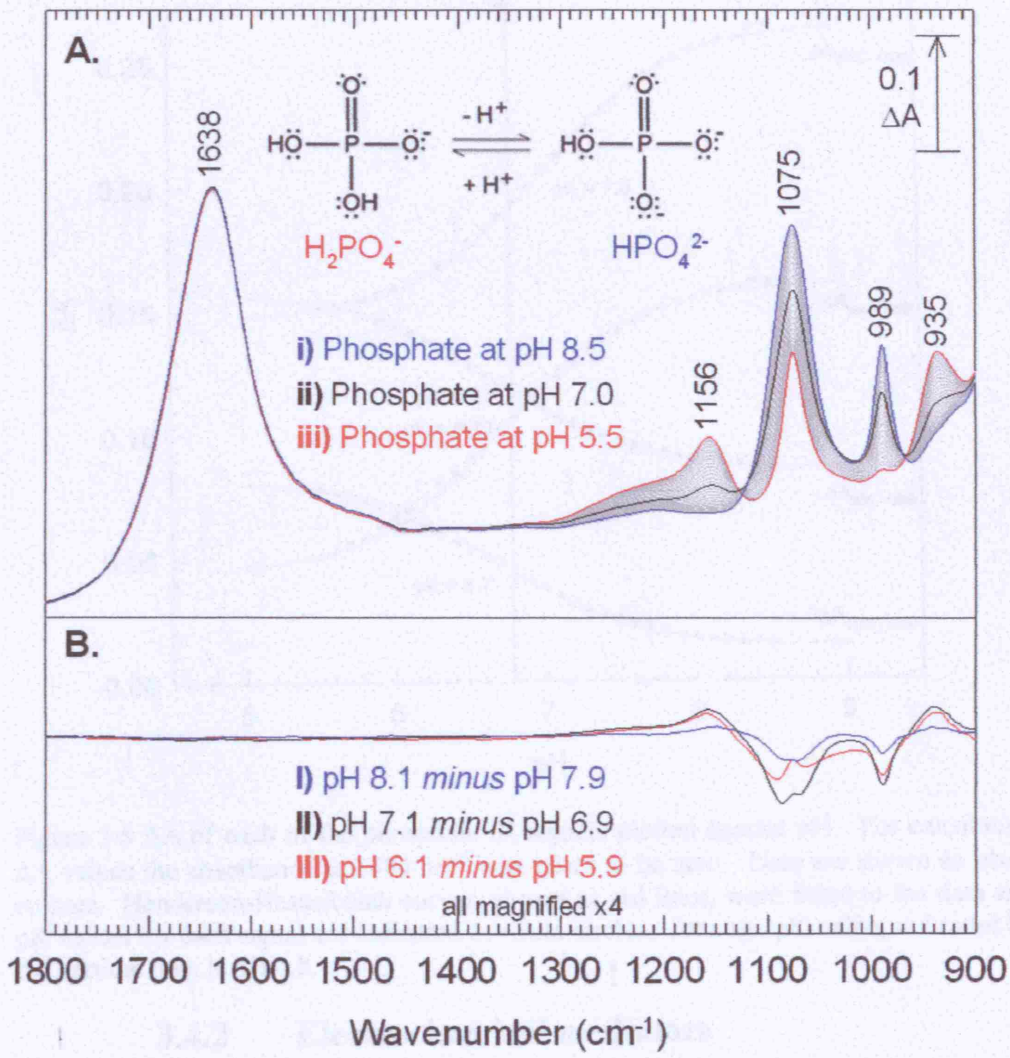

Figure 3.4 Absolute absorbance spectra (A) and difference spectra (B) of 0.5 M potassium phosphate at pH values ranging from 5.5 to 8.5 in 0.1 pH unit increments. In (A) phosphate at pH 8.5, 7.0 and 5.5 is shown in blue, black and red respectively; phosphate at all other pH values is shown in grey. In (B) pH 8.1 *minus* pH 7.9, pH 7.1 *minus* pH 6.9 and pH 6.1 *minus* pH 5.9 difference spectra are shown in blue, black and red respectively; each is expanded ×4. Each spectrum, in both (A) and (B), is the average of 1000 interferograms at 4 cm^{-1}.

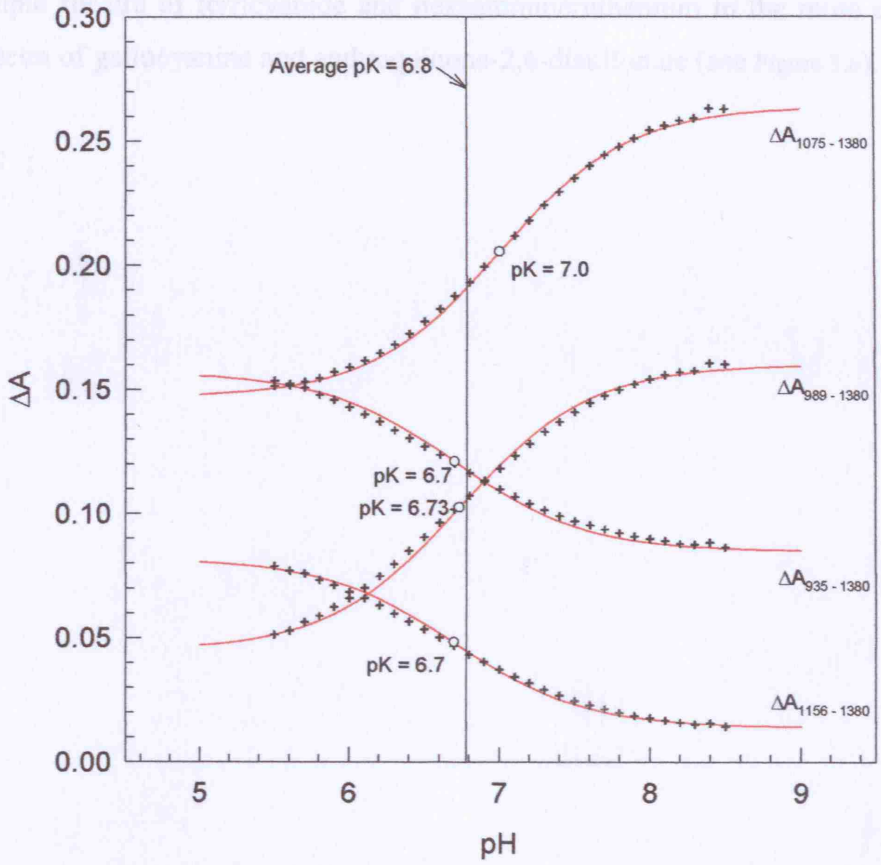

Figure 3.5 ΔA of each of the phosphate IR signals plotted against pH. For calculating ΔA values the absorbance at 1380 cm^{-1} was taken to be zero. Data are shown as black crosses. Henderson-Hasselbalch curves, shown as red lines, were fitted to the data and pK values for each signal are indicated as white circles. Average pK value, indicated by the vertical line, is pH 6.8.

3.4.2 Electrochemical mediators

For acquisition of electrochemically-induced difference spectra, redox mediation between the glassy carbon working electrode and the protein film (or solution) was provided by an appropriate phosphate-buffered mediator solution (see Materials and Methods). The six mediators used were potassium ferricyanide (E_{m7} = 420 mV), hexaammineruthenium chloride (E_{m7} = 70 mV), gallocyanine (E_{m7} = 20 mV), anthraquinone-2,6-disulfonate (E_{m7} = -185 mV), benzyl viologen dichloride (E_{m7} = -311 mV), and methyl viologen (E_{m7} = -449 mV). Electrochemically-induced reduced *minus* oxidised difference spectra of each mediator were measured separately (see Materials and Methods) in order to identify and remove (where necessary) any contributions to the difference spectra of proteins. The redox difference spectra of these compounds vary in complexity, reflecting the complexity of their structures, from the relatively

simple spectra of ferricyanide and hexaammineruthenium to the more complex spectra of gallocyanine and anthraquinone-2,6-disulfonate (see Figure 3.6).

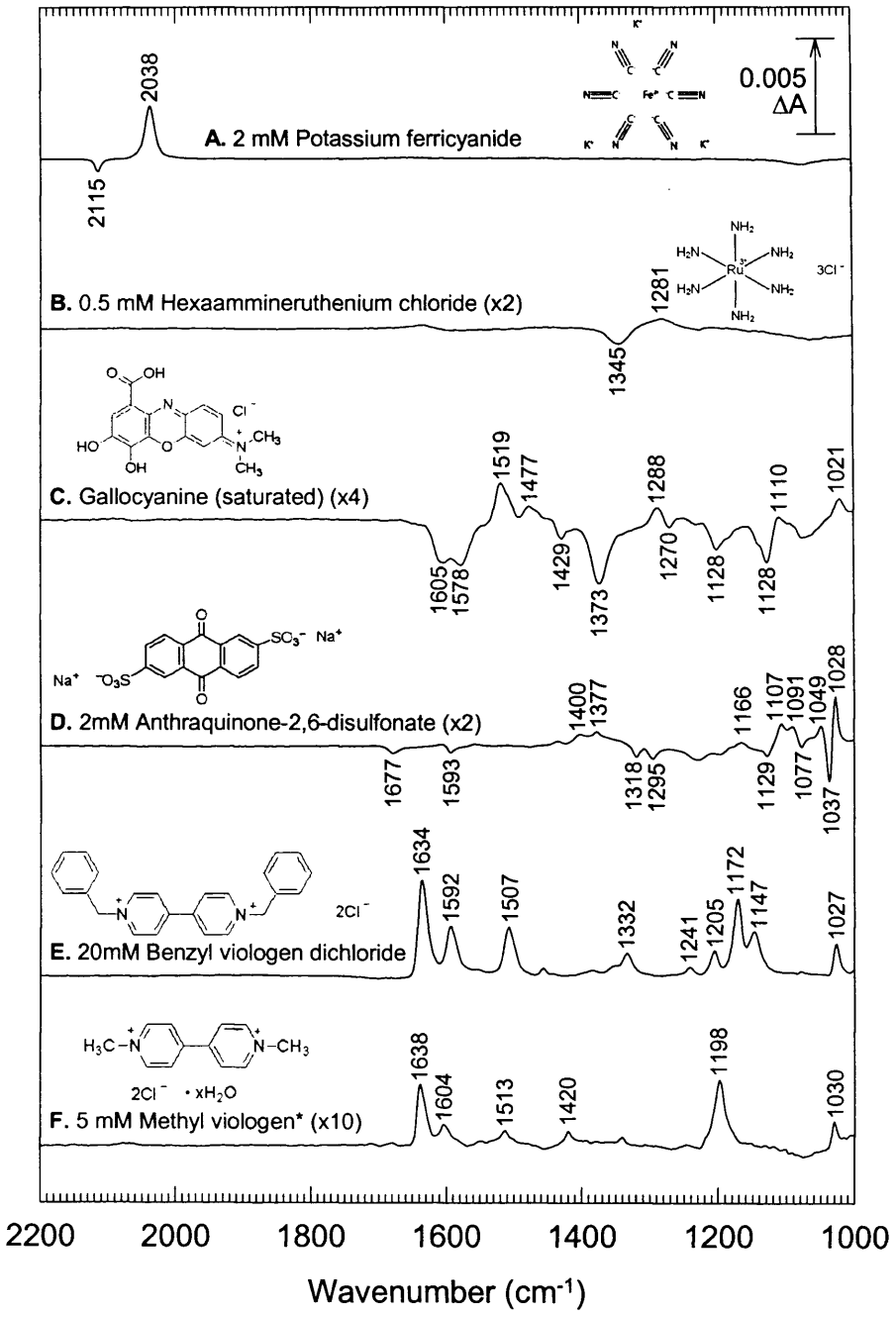

Figure 3.6 Structures and electrochemically-induced reduced *minus* oxidised difference spectra of mediator compounds used to allow redox equilibration between working electrode and protein solutions/layers. Mediator compounds were in 20 mM potassium phosphate, 200 mM potassium chloride at pH 7.0. Reducing/oxidising potentials were 200 mV above/below the E_{m7} value of the mediator compound respectively except for benzyl viologen and methyl viologen where reducing potentials of -400 and -425 mV were used respectively; these potentials were chosen to prevent 2 e^- reduction and formation of the uncharged insoluble doubly-reduced compounds. 10 minutes was allowed for redox equilibration. Reduced *minus* oxidised and oxidised *minus* reduced spectra (each the average of 1000 interferograms at 4 cm^{-1} resolution) were averaged to produce the spectra shown. Spectra are: 2 mM potassium ferricyanide (trace A, average of 80 spectra), 0.5 mM hexaammineruthenium chloride (expanded ×2, trace B, average of 21 spectra), a saturated solution of gallocyanine (×4, trace C, average of 16 spectra), 2 mM anthraquinone-2,6-disulfonate (×2, trace D, average of 264 spectra), 20 mM benzyl viologen dichloride (trace E, average of 20 spectra) and 5 mM methyl viologen (×10, trace F, average of 96 spectra).

3.4.3 NADH, NAD^+ and sodium dithionite

Perfusion-induced reduced *minus* oxidised difference spectra of complex I were recorded using buffer containing 50 μM NADH or 5 mM sodium dithionite for reduction and 50 μM NAD^+ for oxidation (see Materials and Methods and Chapter 5). In order to ascertain whether signals from NADH and NAD^+ contributed to these spectra, absolute absorbance spectra of 40 mM NADH and NAD^+ were reproduced from (*203*) and a NADH *minus* NAD^+ difference spectrum calculated (see Figure 3.7, traces A, B and C respectively). Major features of the NADH *minus* NAD^+ difference spectrum are at 1700(-), 1687(+), 1649(+), 1545(+), 1420(+), 1408(-), 1396(+), 1308(+), 1230(+), 1183(+), 1144(-), 1115(+), 1081(-), 1021(+) and 938(-) cm^{-1} where (+) and (-) indicate peaks and troughs respectively. Scaling the NADH *minus* NAD^+ spectrum to be equivalent to a spectrum produced from 50 μM NADH/NAD^+ gave a maximum ΔA of approximately 0.00001. This value is 20-fold smaller than the perfusion-induced redox difference spectra of complex I (maximum ΔA of approximately 0.0002) (see Chapter 5) and therefore, contributions from NADH and NAD^+ would be indicative of NADH/NAD^+ being retained in the binding site of complex I. The sodium dithionite absolute absorbance spectrum (see Figure 3.7, trace D) was measured by recording a background spectrum of 50 μl water then adding a grain of sodium dithionite, mixing rapidly prior to covering with a volatiles cover, then recording a sample spectrum. This rapid but non-quantitative approach was used because sodium dithionite was observed to decompose rapidly in aqueous solution. The main features of the spectrum are a broad peak at 1055 cm^{-1} and a sharper peak at 920 cm^{-1}.

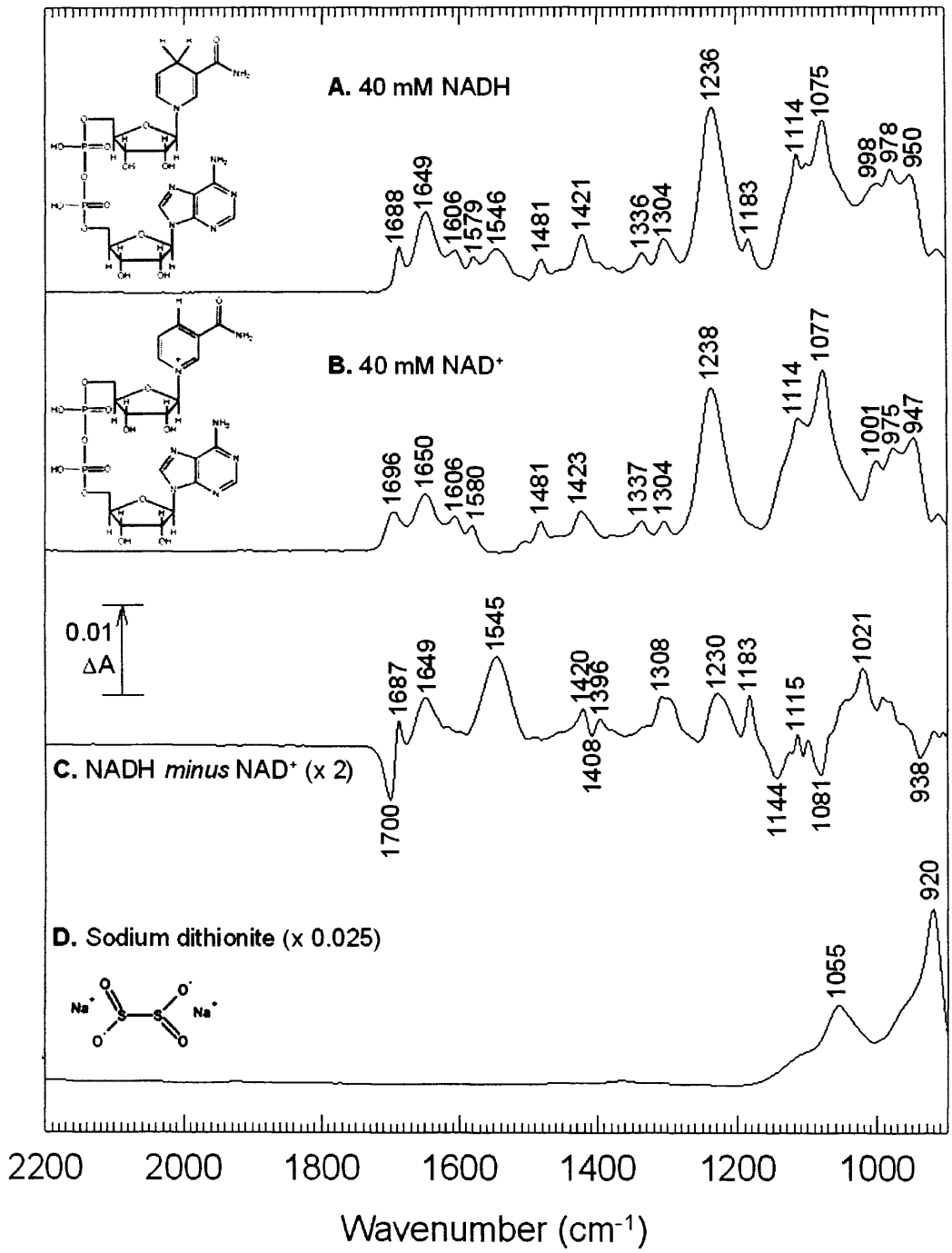

Figure 3.7 ATR FTIR absolute absorbance spectra of 40 mM NADH and NAD^+ in 0.1 M potassium phosphate, 2 mM $MgCl_2$ at pH 7.2 with buffer contributions removed were reproduced from (*203*) (traces A and B respectively); NADH *minus* NAD^+ difference spectrum (expanded ×2, trace C (trace A *minus* trace B)). Absolute absorbance spectrum of sodium dithionite (trace D) was obtained by recording a background spectrum of a droplet of 50 μl of water then adding a grain of sodium dithionite, mixing rapidly prior to covering with a volatiles cover, then recording a sample spectrum. All spectra are the average of 500 interferograms recorded at 4 cm^{-1}.

3.5 Model compound measurements for interpretation of cytochrome bc_1 complex and complex I difference spectra

3.5.1 Ferredoxins

Ferredoxins are small proteins which contain one or more iron-sulphur centres and generally function in electron transfer. Electrochemically-induced redox difference spectra of ferredoxins were recorded to aid in the interpretation of the amide I and II signals in redox difference spectra of complex I (see Chapter 5). Redox difference spectra were recorded in H_2O and D_2O media for the 2Fe-2S parsley ferredoxin and the 2[4Fe-4S] ferredoxin from *C. sporogenes*; a redox difference spectrum was recorded in H_2O media for the 4Fe-4S *D. africanus* ferredoxin (see Materials and Methods) (see Figure 3.8). The 2Fe-2S parsley ferredoxin redox difference spectrum recorded in H_2O media (trace A.) has major features at 1700(-), 1669(-), 1650(+), 1638(+), 1553(+), 1523(+) and 1501(-) cm^{-1}. The redox difference spectra (in H_2O media) of the 2[4Fe-4S] *C. sporogenes* and the 4Fe-4S *D. africanus* ferredoxins are very similar with major features at 1675(-), 1638(+), 1597(+), 1552(+), 1519(-) and 1494(-) cm^{-1}. These spectra and their use in the interpretation of the amide I and II regions of redox difference spectra of complex are discussed in full in Chapter 5.

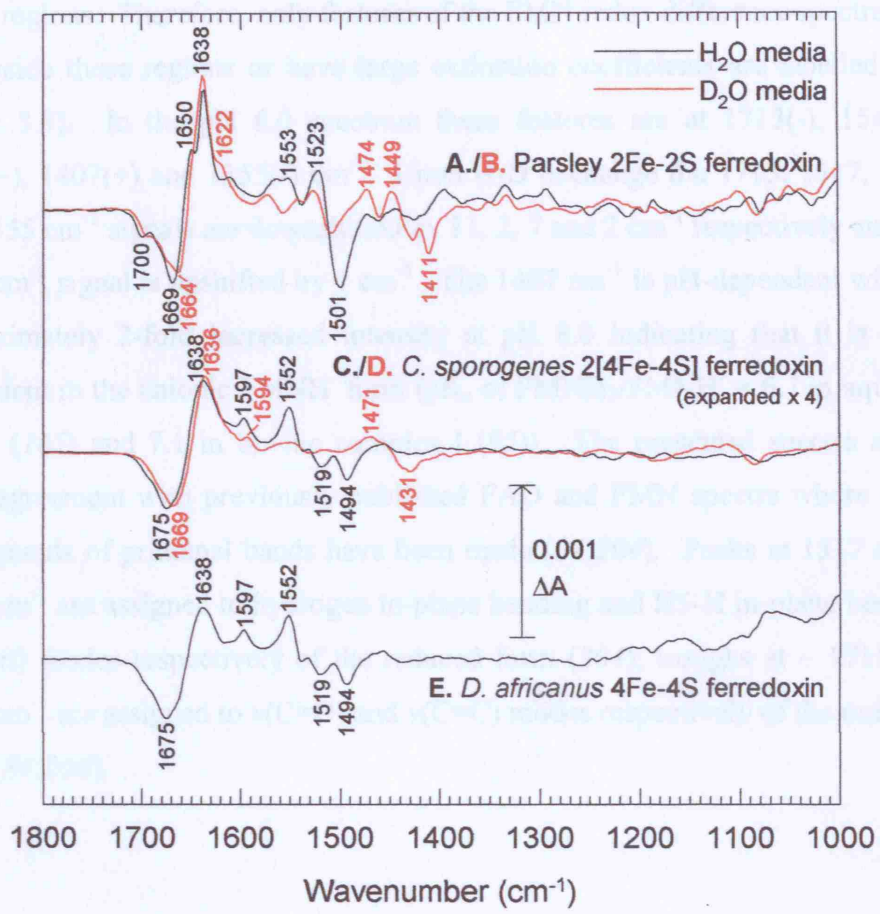

Figure 3.8 Electrochemically-induced redox difference spectra of soluble ferredoxins from Parsley, *C. sporogenes* and *D. africanus*. Ferredoxins were in 0.1 M potassium phosphate and 100 mM potassium chloride at pH/D 8.0. Reducing and oxidising potentials were -500 and 200 mV respectively, 50 μM methyl viologen allowed redox equilibration between electrode and protein for which 8 minutes was allowed. For H-D exchange, samples were washed and concentrated in equivalent D_2O media. Reduced *minus* oxidised and oxidised *minus* reduced spectra (each the average of 1000 interferograms at 4 cm^{-1} resolution) were averaged to produce the spectra shown. Spectra are: 2 mM parsley 2Fe-2S ferredoxin in H_2O (trace A, average of 106 spectra) or D_2O (trace B, average of 54 spectra); 2.5 mM *C. sporogenes* 4Fe-4S ferredoxin in H_2O (trace C, average of 98 spectra) or D_2O (trace D, average of 70 spectra); 0.42 mM *D. africanus* 4Fe-4S ferredoxin in H_2O (trace E, average of 258 spectra).

3.5.2 Flavin mononucleotide

Complex I contains a single non-covalently bound FMN coordinated by the 51 kDa subunit that is thought to accept electrons from NADH via hydride transfer (*90*) (see Chapter 5). The IR spectra of FMN have been described in detail in both H_2O and D_2O (*84;204*). Electrochemically-induced ATR FITR redox difference spectra of FMN in solution at pH/D 6.0 and 8.0 were recorded to aid assignment of signals in the redox difference spectra of complex I to FMN. The redox difference spectra of complex I are dominated by signals in the amide I

and II regions. Therefore, only features of the FMN redox difference spectra that lie outside these regions or have large extinction coefficients are labelled (see Figure 3.9). In the pH 6.0 spectrum these features are at 1713(-), 1547(-), 1517(+), 1407(+) and 1355(-) cm^{-1}. Upon H-D exchange the 1713, 1517, 1407 and 1355 cm^{-1} signals are downshifted by 11, 2, 7 and 2 cm^{-1} respectively and the 1547 cm^{-1} signal is upshifted by 1 cm^{-1}. The 1407 cm^{-1} is pH-dependent with an approximately 2-fold increased intensity at pH 8.0 indicating that it is most prominent in the anionic $FMNH^-$ form (pK_a of $FMNH_2/FMNH^-$ = 6.7 in aqueous media (*165*) and 7.1 in bovine complex I (*95*)). The presented spectra are in good agreement with previously published FAD and FMN spectra where some assignments of principal bands have been made (*84;204*). Peaks at 1517 and ~ 1407 cm^{-1} are assigned to hydrogen in-plane bending and N5-H in-plane bending (in part) modes respectively of the reduced form (*204*); troughs at ~ 1711 and 1547 cm^{-1} are assigned to ν(C=O) and ν(C=C) modes respectively of the oxidised form (*84;204*).

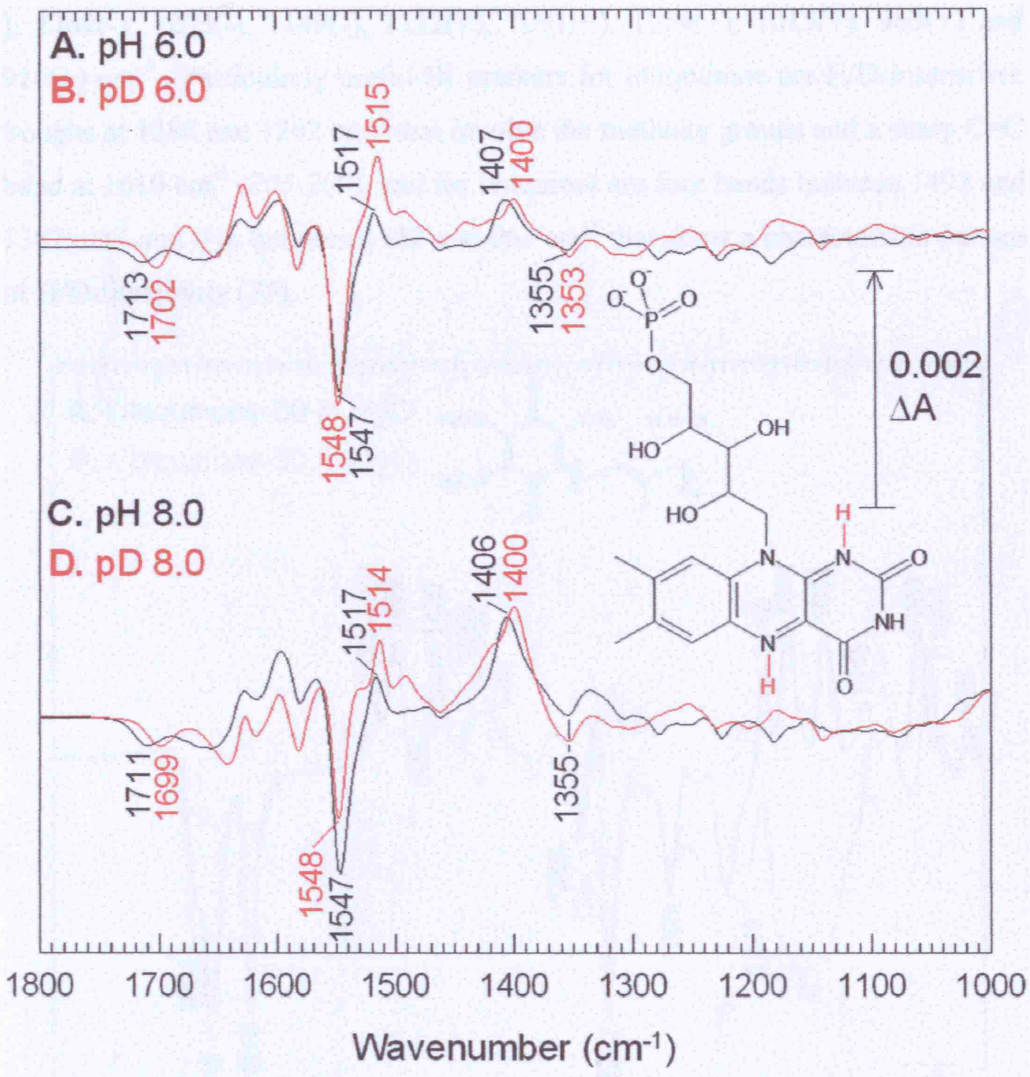

Figure 3.9 Redox difference spectra of FMN at pH 6.0 and 8.0. Reduced *minus* oxidized difference spectra of a solution of 2 mM FMN (E_{m7} = -219 mV) in 20 mM potassium phosphate and 200 mM potassium chloride at pH/D 6.0 and 8.0. Reducing conditions were -550 mV and oxidising conditions were 200 mV and equilibration occurred after 6 minutes. Reproduced from Marshall *et al* (*76*).

3.5.3 Ubiquinone

Biochemical analyses of *Y. lipolytica* complex I preparations have shown that substoichiometric ubiquinone typically remains bound (*148*) and therefore was expected to contribute the complex I difference spectra. The IR redox difference spectra of ubiquinone (*75;205-209*) have been described in detail in both H_2O and D_2O media (see Figure 3.10 - data plotted from (*75*)). Such model spectra provide valuable templates for recognition of ubiquinone bands in difference spectra of complex I. The ubiquinol *minus* ubiquinone spectrum (in H_2O) has features at 1664(-), 1648(-), 1610(-), 1492(+), 1469(+), 1430(+), 1387(+), 1288(-

), 1262(-), 1203(-), 1149(-), 1112(+), 1091(+), 1054(+), 1015(+), 963(+) and 916(+) cm^{-1}. Particularly useful IR markers for ubiquinone are H/D-insensitive troughs at 1288 and 1262 cm^{-1} that involve the methoxy groups and a sharp C=C band at 1610 cm^{-1} (*205-209*), and for ubiquinol are four bands between 1492 and 1387 cm^{-1} and five between 1112 and 963 cm^{-1} that show a characteristic pattern of H/D-sensitivity (*75*).

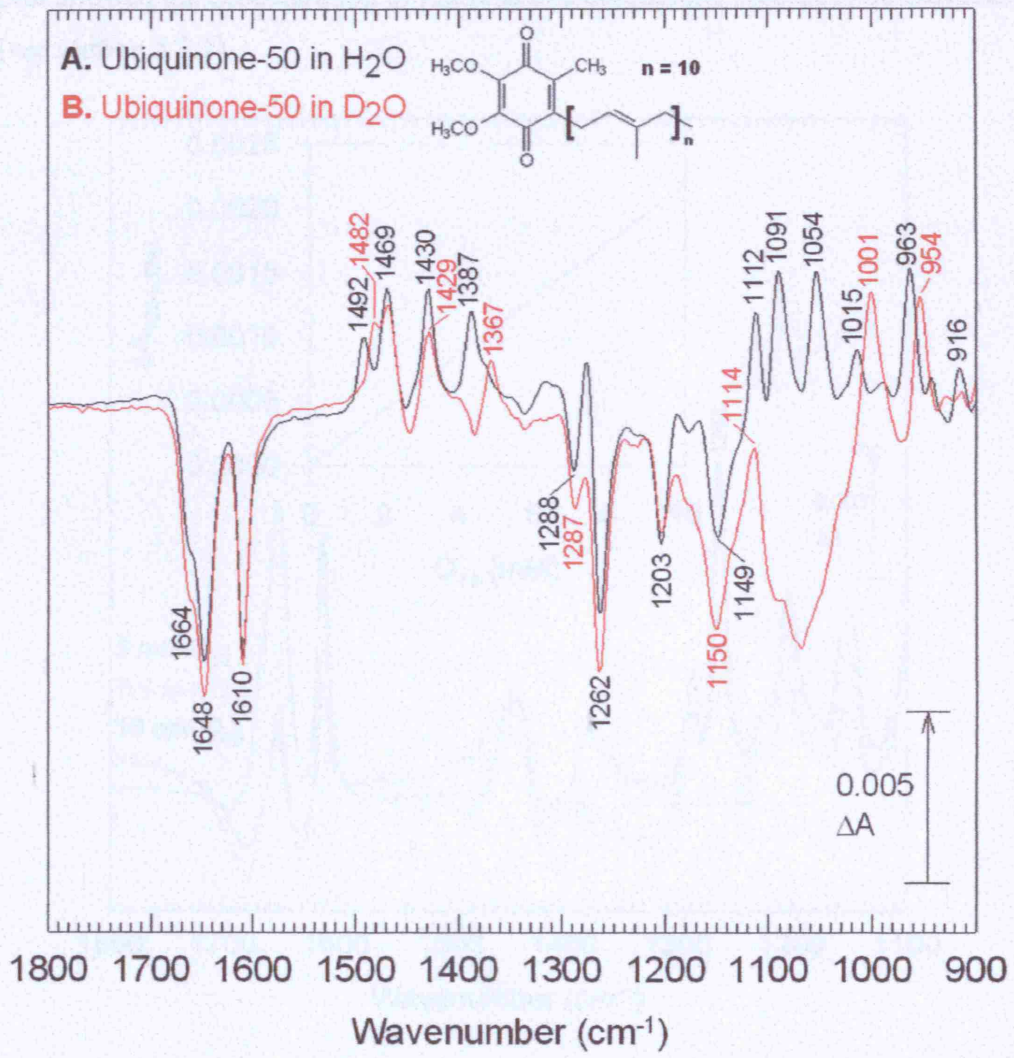

Figure 3.10 Electrochemically-induced redox difference spectra of ubiquinone-50 layer at pH/D 8.0. Several µl of 2 mg/ml ubiquinone-50 in 80% diethyl ether 20% ethanol mixture was applied to the IRE and allowed to evaporate to dryness. The layer was rehydrated with distilled water followed by exchange with 100 mM potassium phosphate, 100 mM potassium chloride pH/D 8.0. Reduction/oxidation was induced by the same electrochemical cell as described in Materials and Methods; addition of 0.5 mM anthraquinone-2,6-disulfonate allowed redox equilibration between the working electrode and the ubiquinone-50 layer. Traces A and B are ubiquinol *minus* ubiquinone in H_2O and D_2O media respectively; each is the average of three 1000 interferogram spectra recorded versus the oxidised background. Data from (*75*).

In order to allow quantitation of redox-active ubiquinone in complex I samples absolute absorbance spectra of solutions of 5, 7.5 and 10 mM *decyl*-ubiquinone in ethanol were measured (see Figure 3.11). The intensity of the band at 1264 cm^{-1}, assigned to a mode involving the methoxy groups, was plotted as $\Delta A_{1264-1241}$ against concentration. Comparison of the intensity of the trough at ~ 1265 cm^{-1} in reduced *minus* oxidised redox difference spectra of complex I with this plot allowed the concentration of redox-active ubiquinone present to be estimated (see section 5.3.2).

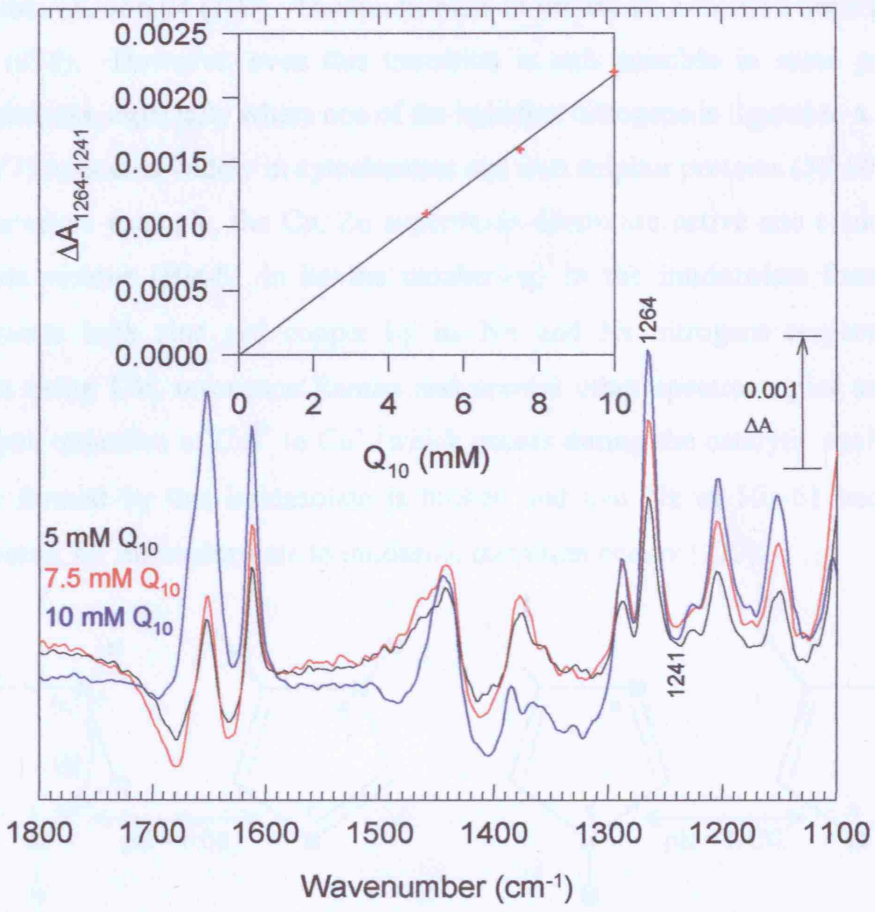

Figure 3.11 ATR FTIR absolute absorbance spectra of *decyl*-ubiquinone. Traces A, B and C arise from 5, 7.5 and 10 mM solutions of *decyl*-ubiquinone in ethanol (ethanol contributions have been subtracted). A plot of $\Delta A_{1264-1241}$ against ubiquinone (Q) concentration (see inset plot) was used to quantify the ubiquinone contribution in difference spectra of complex I.

3.5.4 Histidine

The histidine sidechain has four different protonation states: - imidazolium, Nπ-protonated imidazole, Nτ-protonated imidazole and imidazolate (see Figure 3.12). In aqueous media the two tautomeric imidazole forms are found in equilibrium with each state roughly equally occupied. In proteins one imidazole form can be expected to be favoured by the surrounding protein environment. Transitions of histidine between the imidazole and imidazolium are expected to be important in many enzymological processes on account of the physiologically accessible pK of 6.04 (*100*). The imidazolate to imidazole transition has a pK of 14.37 (*210*). However, even this transition is still possible in some protein environments, especially where one of the histidine nitrogens is ligated to a metal ion (*211*) as occurs widely in cytochromes and iron sulphur proteins (*30;80*). As an alternative example, the Cu, Zn superoxide dismutase active site contains a histidine residue (His-61 in bovine numbering) in the imidazolate form that coordinates both zinc and copper by its Nπ and Nτ nitrogens respectively. Studies using UV, resonance Raman and several other spectroscopies suggest that upon reduction of Cu^{2+} to Cu^{+} (which occurs during the catalytic cycle) the bridge formed by this imidazolate is broken and that Nτ of His-61 becomes protonated, i.e. an imidazolate to imidazole transition occurs (*212*).

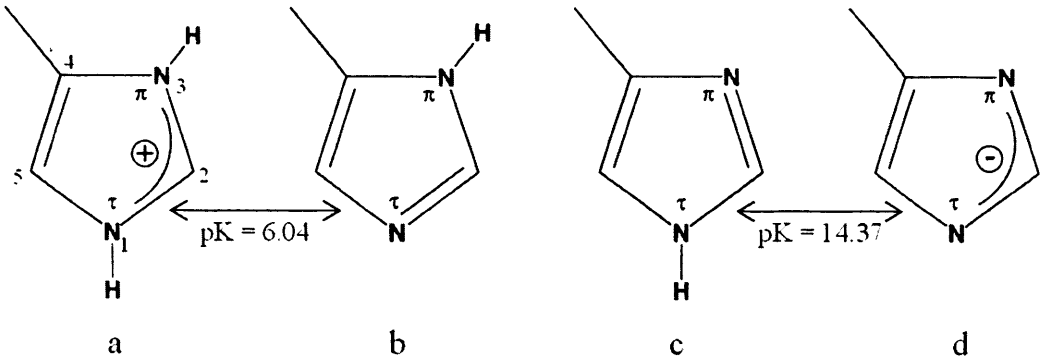

Figure 3.12 Structure diagram of a histidine sidechain: (a) imidazolium form, (b) Nπ-protonated imidazole form, (c) Nτ-protonated imidazole form, (d) imidazolate form. pK for imidazolium form = 6.04 (*100*); pK for imidazolate form = 14.37 (*210*); in aqueous solution Nτ- and Nπ- protonated imidazole forms are in equilibrium and roughly equally occupied. Adapted from (*213*).

The IR absorption characteristics of histidine have recently been determined in detail; the sidechain is particularly amenable to study by IR spectroscopy because each protonation state has differing absorbance characteristics.

Information on band positions and assignments for histidine and/or related materials has been collated by Barth (*214*). Normal mode calculations of the different protonation states of the related 4-methyl-imidazole and its zinc-ligated state have been published by Noguchi *et al* (*211;215*). Additional data, which includes some experimental results from this thesis (see below), have been published by Iwaki *et al* (*30*) and in the review by Rich *et al* (*80*).

Measurements were made to determine the IR signatures arising from protonation state changes of histidine for both imidazolate to imidazole and imidazole to imidazolium transitions in both H_2O and D_2O media (see Figure 3.13). Acquisition of these spectra was complicated by the effect of protonation state on the solubility of histidine: the imidazolate and imidazolium forms of the sidechain carry an overall charge and are highly soluble with respect to the neutral and relatively insoluble imidazole forms. The imidazolium *minus* imidazole difference spectra (Figure 3.13, traces A and B) were induced by cyclic exchange of buffer at pH/D values selected to induce reversible protonation state changes of a proportion of the sidechains of a layer of poly-L-histidine (n = 112) (see Materials and Methods) while leaving a critical proportion in the insoluble imidazole form and thus maintaining layer stability. The imidazole *minus* imidazolate difference spectra (Figure 3.13, traces C and D) were obtained from L-histidine solutions at differing pH/D values chosen to provide a difference in protonation state without saturating the lower pH solution with the less soluble imidazole form. The imidazolium *minus* imidazole difference spectrum recorded in H_2O media has features at 1644(+), 1631(-), 1484(+), 1466(-), 1425(+), 1329(-), 1272(-), 1258(-), 1247(+), 1203(+), 1191(-), 1099(+) and 1085(-) cm^{-1}. The most prominent feature is the peak /trough at 1644/1631 cm^{-1}, although, this is likely to be obscured by amide I changes in a protein difference spectrum. The most useful indicator of the imidazolium-imidazole protonation state change is therefore the peak/trough at 1099/1085 cm^{-1} which occurs in a region of the protein spectra where few other components contribute (with the notable exception of ubiquinone, see Figure 3.10 and Chapter 5). This feature is also present in the spectrum recorded in D_2O media as a peak/trough at 1102/1090 cm^{-1} allowing assignment of protein spectra features to histidine protonation changes based on characteristic band position

and shift on H-D exchange. The imidazole *minus* imidazolate difference spectrum recorded in H_2O media has features at 1573(+), 1545(-), 1490(+), 1451(-), 1403(+), 1323(+), 1262(+) and 1102(-) cm^{-1}. As with the imidazolium *minus* imidazole difference spectrum many of the prominent features can be expected to be obscured by amide I (and II) changes in a protein difference spectrum. However, the troughs at 1451 and 1102 cm^{-1}, which display +1 and 0 cm^{-1} shifts on H-D exchange respectively are useful indicators for detecting the imidazole-imidazolate transition in proteins. Two smaller positive bands at 1323 and 1262 cm^{-1} also provide useful indicators on account of their characteristic H-D exchange sensitivity. Equivalents of these bands have been observed in difference spectra of cytochrome bc_1 complex and have been used to show directly that a key imidazole/imidazolate change of a metal-bound histidine (*216*) occurs in the active site of this enzyme (*30*).

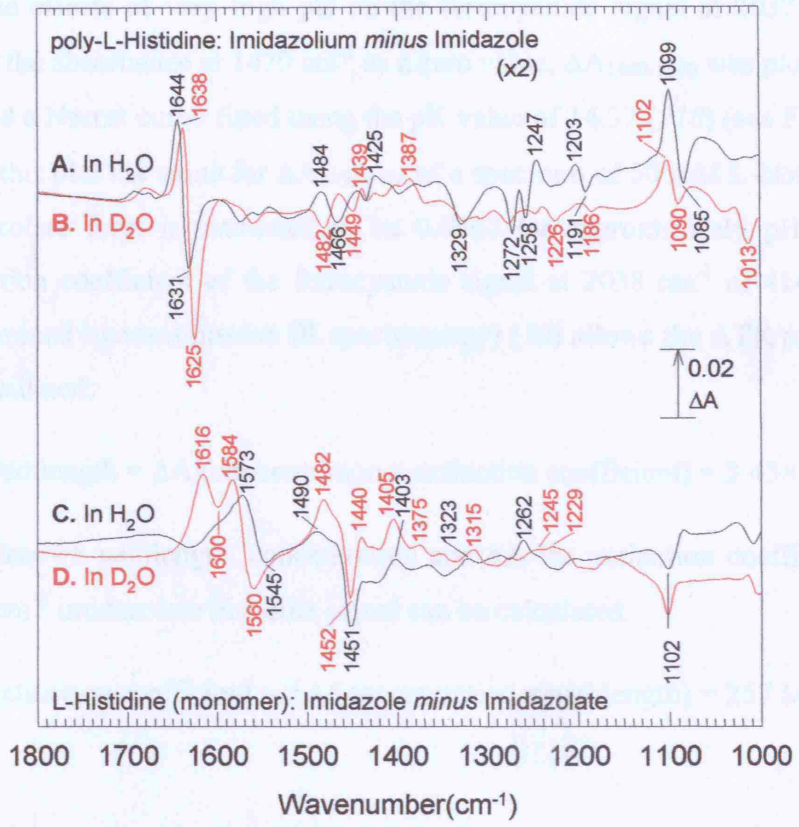

Figure 3.13 Imidazolium *minus* imidazole and imidazole *minus* imidazolate ATR FTIR difference spectra of histidine. Perfusion-induced imidazolium *minus* imidazole difference spectrum in H_2O media (trace A) was recorded by cyclic exchange of 1 mM potassium phosphate, 100 mM potassium chloride at pH 7.0 and 8.0 (pK = 6.04 (*100*)) over a layer of poly-L-histidine (see Materials and Methods). The spectrum is an average of 11 spectra, each of which was an average of 500 interferograms at 4 cm^{-1} resolution. The equivalent difference spectrum in D_2O (trace B) is reproduced from (*80*) where a comparable method was used by M. Iwaki. Imidazole *minus* imidazolate difference spectrum in H_2O (trace C) was obtained by subtracting the absolute spectrum of 500 mM L-histidine in 3.2 mM NaOH at pH 11.5 from the absolute spectrum of 500 mM L-histidine in 1.58 M NaOH at pH 14.2 (solvent contributions were subtracted, each spectrum was the average of 4 spectra, each of which was the average of 500 interferograms at 4 cm^{-1} resolution). The equivalent difference spectrum in D_2O (trace D) is reproduced from (*30*) where a comparable method was used by M. Iwaki. Figure is reproduced with modifications from (*80*).

The imidazole/imidazolate transition of L-histidine was further investigated with the aim of determining an extinction coefficient for the 1451 cm^{-1} imidazolate signal. Absolute absorbance spectra of 50 mM L-histidine, 10 mM potassium ferrocyanide in solutions of NaOH at pH 11.5, 14.6, 14.7, 14.85 and 15.0 were recorded; absolute absorbance spectra at pH 11.4 and 15.0 and a series of difference spectra were plotted (see Figure 3.14). The difference spectra show the increasing intensity of the 1450 cm^{-1} (seen at 1451 cm^{-1} in Figure 3.13) signal

and the effects of very high pH on the ferrocyanide signal at 2037-2039 cm^{-1}. Using the absorbance at 1470 cm^{-1} as a zero value, $\Delta A_{1450\text{-}1470}$ was plotted against pH and a Nernst curve fitted using the pK value of 14.37 (*210*) (see Figure 3.15). From this plot the value for $\Delta A_{1450\text{-}1470}$ of a spectrum of 50 mM L-histidine in the imidazolate form is estimated to be 0.0062 (at approximately pH 17). The extinction coefficient of the ferrocyanide signal at 2038 cm^{-1} of 4140 $M^{-1}.cm^{-1}$ (determined by transmission IR spectroscopy) (*30*) allows the ATR pathlength to be calculated:

$$\text{Pathlength} = \Delta A/(\text{concentration} \times \text{extinction coefficient}) = 3.43\times10^{-4}\text{cm}$$

From known pathlength, concentration and ΔA the extinction coefficient of the 1450 cm^{-1} imidazolate histidine signal can be calculated:

$$\text{Extinction coefficient} = \Delta A/(\text{concentration} \times \text{pathlength}) = 257\ M^{-1}.cm^{-1}$$

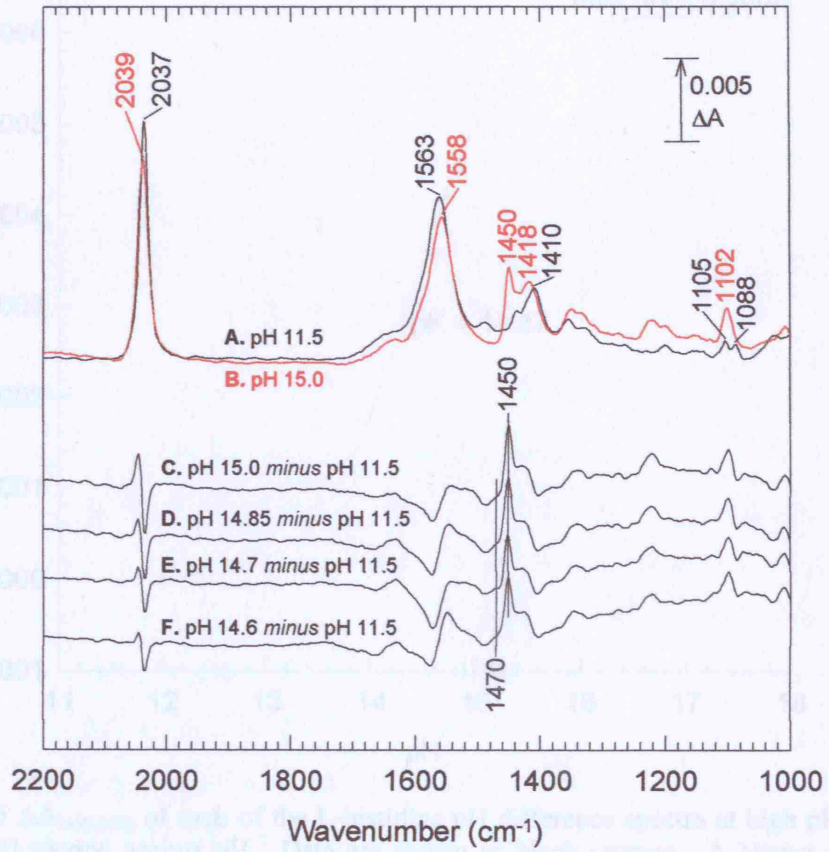

Figure 3.14 ATR FTIR absolute absorbance and pH difference spectra of 50 mM L-histidine, 10 mM potassium ferrocyanide at high pH. Absolute absorbance spectra (traces A and B) were each the average of 4 spectra, each of which was the average of 500 interferograms at 4 cm^{-1} resolution. Difference spectra (traces C, D, E and F) were calculated from spectra that were each the average of 4 spectra, each of which was the average of 500 interferograms at 4 cm^{-1} resolution.

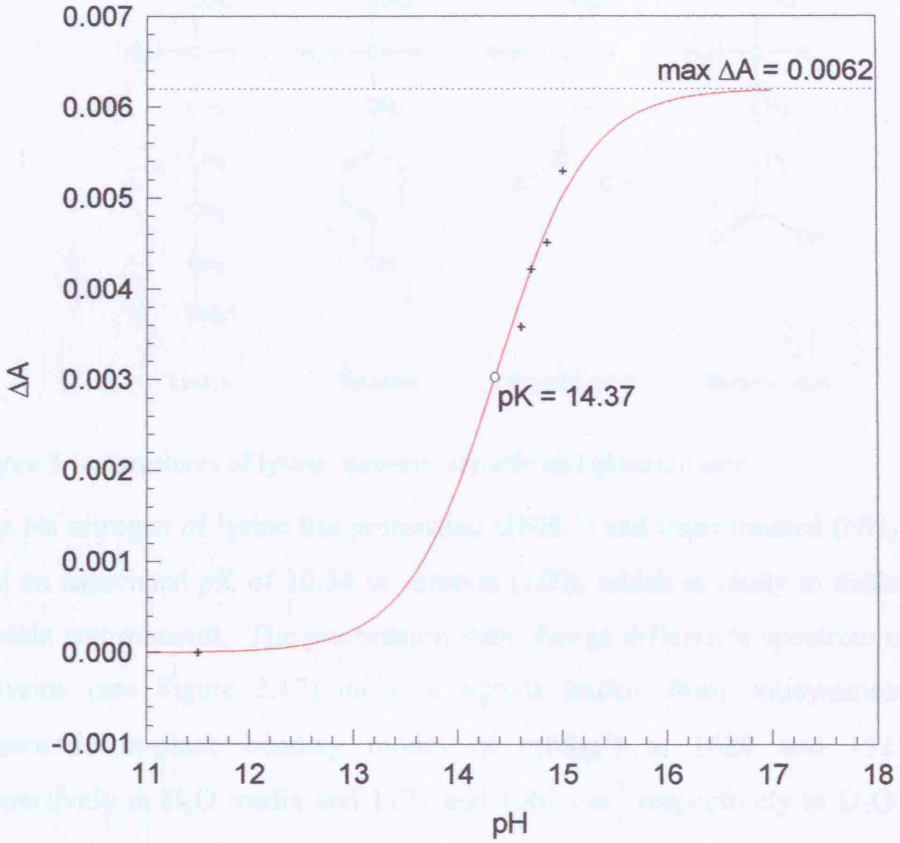

Figure 3.15 $\Delta A_{1450\text{-}1470}$ of each of the L-histidine pH difference spectra at high pH (see Figure 3.14) plotted against pH. Data are shown as black crosses. A Nernst curve, shown as a red line, was fitted to the data using a pK value of 14.37 (*210*) in order to extrapolate a maximum $\Delta A_{1450\text{-}1470}$ of 0.0062 at ~ pH 17.

3.5.5 Lysine, tyrosine, aspartic acid and glutamic acid

Additional protonatable amino acids that may be expected to contribute to the redox difference spectra of cytochrome bc_1 complex and complex I are lysine, tyrosine, aspartic and glutamic acids, the structures of which are shown in Figure 3.16. A large amount of infrared data on these amino acids can be found in the literature. Most useful are reviews by Barth (*214*) and Rich *et al* (*80*). The latter includes protonation state change FTIR difference spectra of these amino acids and these are reproduced in Figure 3.17 to Figure 3.19 and discussed in detail below.

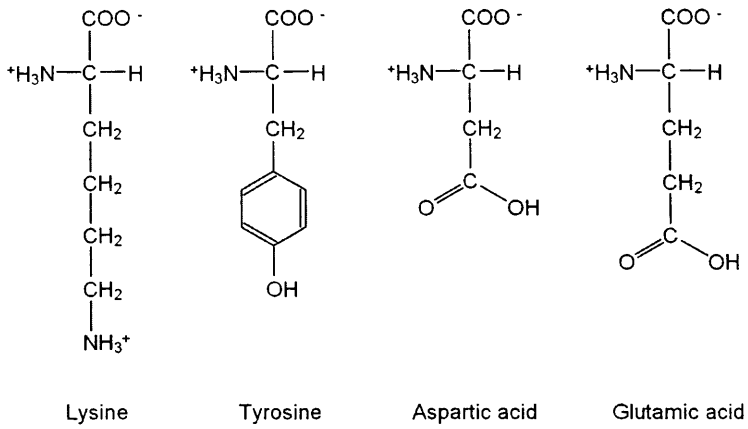

Figure 3.16 Structures of lysine, tyrosine, aspartic and glutamic acid.

The Nε nitrogen of lysine has protonated ε(NH_3^+) and deprotonated (NH_2) states and an associated pK of 10.54 in solution (*100*), which is likely to differ in the protein environment. The protonation state change difference spectrum of poly-L-lysine (see Figure 3.17) includes signals arising from antisymmetric and symmetric in-plane bending modes of ε(NH_3^+) at 1620 and 1521 cm^{-1} respectively in H_2O media and 1171 and 1062 cm^{-1} respectively in D_2O media. It is noted that, in H_2O media, these broad bands are likely to be closer to 1630 and 1526 cm^{-1} (values reported in earlier studies (*214*)) and are distorted in the presented spectra by amide I and II changes manifesting as troughs at 1643 and 1548 cm^{-1}. An additional novel feature in the presented spectra is an H-D insensitive band at 1473 cm^{-1} that is present in the protonated form and absent in the deprotonated form. The 1171 and 1062 cm^{-1} signals in the D_2O spectrum and H-D insensitive 1473 cm^{-1} signal are the most useful for identifying protonation state changes of lysine in protein difference spectra (*80*).

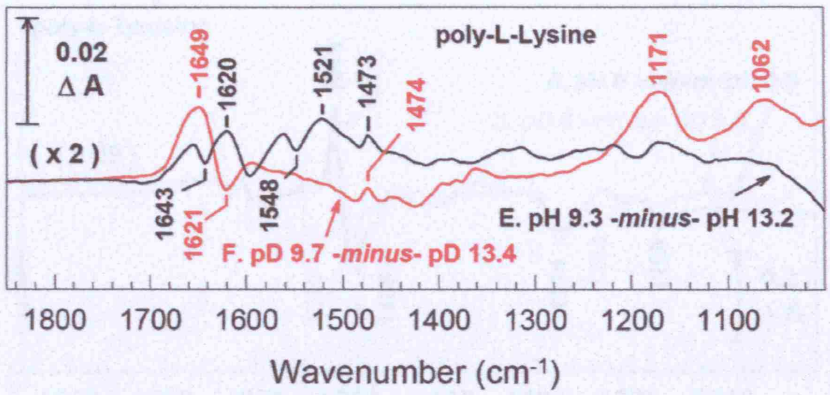

Figure 3.17 pH change-induced protonation state change ATR FTIR difference spectra of poly-L-lysine in H_2O (trace A) and D_2O (trace B) media. Poly-L-lysine was used in order to avoid interference from the $\beta(NH_2)$ amino group. Reproduced from (*80*).

The tyrosine sidechain has a phenolic OH group that undergoes deprotonation with an associated pK of 10.46 in solution (*100*), although this is likely to differ in the protein environment. The tyrosine sidechain is also capable of forming a radical state. Because of the catalytic importance of this sidechain and its informative IR absorption characteristics a great body of IR data is now available on this residue. These data has been collated by Barth (*214*) and collated/expanded by Rich *et al* (*80*) and by Berthomieu on the tyrosine radical IR spectra (*217*). Protonated *minus* deprotonated difference spectra of poly-L-tyrosine in H_2O and D_2O media are shown in Figure 3.18. The 1515 cm^{-1} signal arises from a combination of C-C stretching and C-H in-plane bending ring modes in the protonated state (*214*). Upon deprotonation the band shifts to 1495 cm^{-1} and both signals have characteristic H-D exchange sensitivities. Also useful for identifying tyrosine protonation state change signals are features in the difference spectrum at 1274 and 1169 cm^{-1}. In the absolute IR absorbance spectrum of protonated tyrosine (not shown) a broad peak at 1241 cm^{-1} is assigned to a C-O stretching mode and a peak at 1175 cm^{-1} is assigned to an in-plane bending C-H ring mode (*80;214*). These modes will be affected by deprotonation and these effects are the likely cause of the troughs at 1274 and 1169 cm^{-1} in the protonated *minus* deprotonated difference spectrum. Therefore, the signals at 1515/1495, 1274 and 1169 cm^{-1} are the most useful for identification of tyrosine protonation state changes (*80;214*).

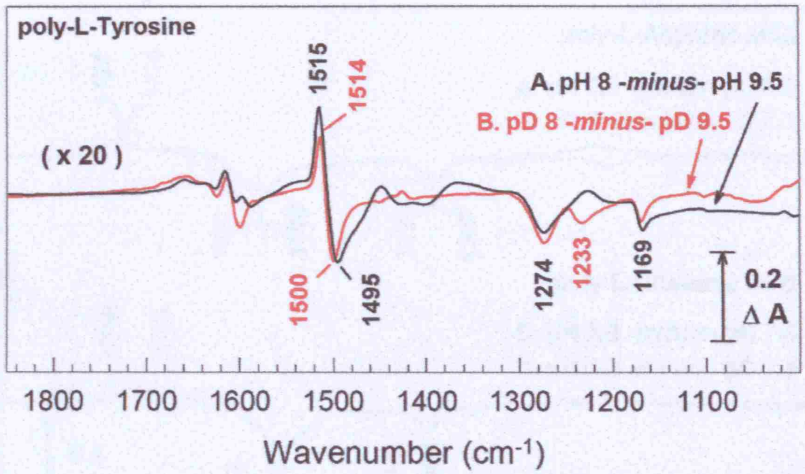

Figure 3.18 pH change-induced protonation state change difference ATR FTIR spectra of poly-L-tyrosine in H2O (trace A) and D2O (trace B) media. Reproduced from (*80*).

The aspartic acid and glutamic acid sidechains, with solution pKs of 3.90 and 4.07 respectively (*100*), are also highly amenable to study by FTIR spectroscopy. Protonated *minus* deprotonated difference spectra of poly-L-aspartic acid and poly-L-glutamic acid in H_2O and D_2O media are reproduced from (*80*) in Figure 3.19. The major signals of the H_2O spectra arise from the loss of symmetric and antisymmetric COO^- stretching modes at 1397 and 1580 cm^{-1}, respectively, in aspartic acid and at 1404 and 1556 cm^{-1}, respectively, in glutamic acid and the gain of the C=O stretching mode of the carboxylic acid which forms a peak within the 1710 - 1790 cm^{-1} region (for both sidechains). The frequency range of the carboxylic acid C=O stretching mode is of great significance because no other side chains have absorbances in this range and therefore, provided vibrational modes from other non-protein components can be ruled out, assignments of this vibration to glutamic/aspartic acid can be considered definitive. In addition, the frequency of the carboxylic acid C=O stretching mode is sensitive to the hydrogen bonding environment of the residue – as hydrogen bond strength increases the frequency of the vibration decreases (*80;218*). Therefore a change in environment of a protonated carboxylic acid residue results in a peak/trough feature within the 1710 - 1790 cm^{-1} region. Further information has also been derived from the separation between the symmetric and antisymmetric COO^- stretching modes which have been used to assess whether the sidechain is acting as a monodentate or bidentate ligand (*219;220*).

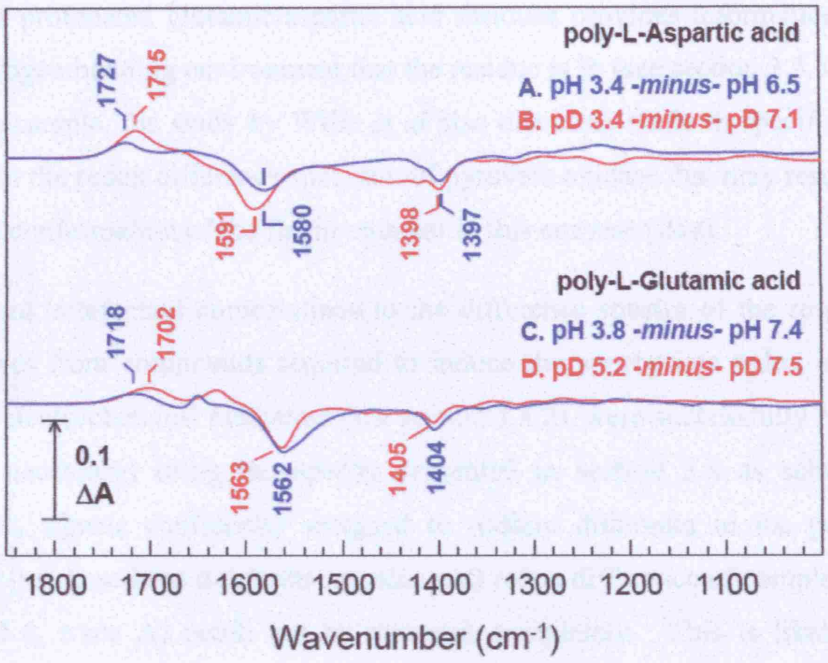

Figure 3.19 pH change-induced protonation state change difference ATR FTIR spectra of poly-L-aspartic acid in H_2O (trace A) and D_2O (trace B) media and poly-L-glutamic acid in H_2O (trace C) and D_2O (trace D) media. Reproduced from (*80*).

3.6 Conclusions

The model compound data presented in this section were used to assist in acquisition and interpretation of the IR spectra of cytochrome bc_1 complex and complex I presented in chapters 4 and 5 respectively. The IR absorption characteristics of the model compounds in solution have been shown by previous studies to be highly comparable to their absorption characteristics when in the protein environment. For example, a study by Wille *et al* showed signals arising from FAD bound in several flavoproteins to be similar in overall shape to those arising from FAD in aqueous solution (*204*). In addition, Iwaki *et al* used model compound data on ubiquinone and histidine to make tentative assignments of signals in the redox difference spectra of bovine cytochrome bc_1 complex to ubiquinone bound in the Q_i-site (*74*) and to make definitive assignments of signals in redox difference spectra of the *Rba. capsulatus* complex to a histidine imidazolate/imidazole transition (*30*). Furthermore, small differences between the frequencies and relative intensities of signals in a model compound spectrum (recorded in aqueous solution) and of signals in a protein spectrum (assigned to that model compound) can provide information about the nature of the protein environment local to the compound. For example, position of the C=O stretching

mode of protonated glutamic/aspartic acid residues provides information about the hydrogen bonding environment that the residue is in (see section 3.5.5). As a further example, the study by Wille *et al* also discusses shifts in specific flavin signals in the redox difference spectrum of pyruvate oxidase that may result from the bent conformation of the flavin cofactor in this enzyme (*204*).

In general, artefactual contributions to the difference spectra of the respiratory complexes from compounds required to induce the appropriate redox changes, such as electrochemical mediators (see section 3.4.2), were successfully removed (where necessary) using the spectra presented in section 3.4 as subtractors. However, signals confidently assigned to sodium dithionite in the perfusion induced (using sodium dithionite as reductant) redox difference of complex I (see Figure 5.6, trace A) could not be removed completely. This is likely to be because the model compound spectrum of sodium dithionite (see Figure 3.7, trace D) arises from very fresh sodium dithionite. The artefactual signals in Figure 5.6, trace A are likely to arise form a mixture of sodium dithionite and the products of its oxidation/decomposition (*221*). For future experimentation this oxidation/decomposition could be monitored by ATR FTIR spectroscopy and a set of high quality model compound spectra could be recorded. A combination of spectra from this set could then be used more effectively to subtract the contributions of sodium dithionite from the complex I difference spectrum.

Chapter 4: Investigation of the Cytochrome bc_1 Complex by Electrochemically-Induced Difference Spectroscopy

4.1 Introduction

Cytochrome bc_1 complex has played an important role in the development of methods for measuring FTIR difference spectra of hydrophobic proteins. The first published redox difference spectra of cytochrome bc_1 complex were measured by Baymann *et al* (*202*) in transmission mode using a spectroelectrochemical cell and detergent solubilised complex from *Rba. capsulatus*. Baymann *et al* measured full redox difference spectra and spectra arising from redox changes of individual components by redox poising, including haem b_L and haem b_H. In addition to signals from amide I and II peptide backbone changes and from haem modes, these spectra were expected to contain signals arising from protonation state changes of groups that are redox-linked to the Fe-S centre, haem b_L and haem b_H (see section 1.1.3.2). Peaks at 1720 cm^{-1} were present in the reduced *minus* oxidised redox difference spectra of both haem b_L and haem b_H (recorded at pH 6.5) and were tentatively assigned to the protonation of glutamic acid(s) and/or aspartic acid(s) (specifically to gain of the C=O stretching mode of the protonated form, see section 3.5.5) upon reduction

of each haem. The appearance of these signals in equivalent spectra recorded at pH 8.7 supported this assignment in the case of haem b_L and allowed the pK of the protonatable group to be estimated as 8.7, which the authors noted to be high for a glutamic/aspartic acid (see section 3.5.5). In the case of the signal associated with haem b_H, additional interpretation was prevented due to the low signal:noise of the haem b_H spectrum recorded at pH 8.7. Candidate glutamic/aspartic acids, from which these signals may arise, were discussed based on the available high resolution structures. Also discussed were signals at 1702/4 cm^{-1}, which were tentatively assigned to either an additional carboxylic C=O stretching mode which is in an unusual environment or a very high frequency amide I vibration (*202*) (signals in this region are discussed further in section 4.5).

This work was furthered by Iwaki *et al* using perfusion-induced ATR FTIR redox difference spectroscopy applied to cytochrome bc_1 complex, from both *Rba. capsulatus* (*75*) and *B. taurus* (*74*), adhered to the IRE as rehydrated films (see section 2.4.3) (*222*). These studies demonstrated that this novel approach was able to produce spectra of higher signal:noise than, but otherwise highly comparable to, equivalent spectra obtained in transmission mode. The versatility of this method was demonstrated by the resolution of signals due to redox changes of haem c_1/Fe-S centre, haem b_L and haem b_H/ubiquinone of the bovine complex by selective reduction (*74*). In addition, signals arising from Fe-S centre and haem c_1, individually, were resolved in the *Rba. capsulatus* complex by use of a mutant in which the midpoint potential of haem c_1 was lowered to 60 mV (*75*). Both of these studies made a range of firm and tentative assignments of features, for example, to amide I and II changes, to haem modes and to changes in amino acid side chains (*74;75*); only those pertaining to the redox-linked protonatable groups of haem b_L and haem b_H, specifically to putative aspartic/glutamic acid residues, are discussed here. The perfusion-induced difference spectra arising from changes associated with the reduction/oxidation of haem b_L and haem b_H, individually, in the bovine complex (*74*) are similar in overall appearance to those in the *Rba. capsulatus* complex (*202*). The 1710 - 1790 cm^{-1} region, where protonation state changes of glutamic acid(s) and/or aspartic acid(s) (or perturbation of these residues in their protonated forms) are

expected to contribute, appears to contain peak/trough features at 1728/1741 cm^{-1} and 1721/1744 cm^{-1} in the haem b_L and haem b_H spectra, respectively. These were tentatively assigned to perturbations and/or protonation or deprotonation of aspartic or glutamic residues close to each haem group (*74*). In addition, based on analysis of available structures the authors suggested Glu-295 and Asp-252 (of cytochrome *b*, *Rba. capsulatus* numbering) as the most likely candidates for haem b_L and haem b_H linked signals, respectively. If signals in the 1710 - 1790 cm^{-1} range of the difference spectra of haem b_L or haem b_H arise from protonation state changes of aspartic/glutamic acid residues, then signals arising from gain/loss of the symmetric and antisymmetric COO^- stretching modes of the deprotonated form might also be expected. Unfortunately these modes absorb in very crowded regions of the spectra (see section 3.5.5), making their definitive identification difficult.

In order to develop this line of work further, electrochemically-induced ATR FTIR redox difference spectroscopy was applied to rehydrated films of bovine cytochrome bc_1 complex using a novel in-house constructed electrochemical cell (see section 2.4.6). The resulting difference spectra for redox changes of all components of the complex and for redox changes associated with haem b_L and haem b_H, individually, are shown to be highly comparable to equivalent spectra obtained using the already-established perfusion method (see Figure 4.2 and Figure 4.3). The use of redox potentiometry in combination with an appropriate redox mediator solution provides greater control of ambient redox potential and ease of use than the perfusion method described above (and in section 2.4.5). In particular, the system can in principle allow full stepwise redox titration of multiple components. Furthermore, the static redox equilibration buffer means that experiments in D_2O media are far more easily and cheaply performed than the perfusion methods that require large volumes of D_2O. At the time these experiments commenced, a facility for acquiring FTIR and UV/visible spectra simultaneously was available for the perfusion method but not for the electrochemical method. Experiments using an early prototype electrochemical cell that included this facility are described in sections 4.4.1 and 4.4.2. However, the reduction in surface area of the working electrode required to accommodate the fibre optic probe was found to result in unacceptably long redox equilibration

times and the prototype was not used for later experiments. Since completion of the experiments described in this thesis, further developments of this technology have resulted in an in-house constructed electrochemical cell which includes a platinum minigrid working electrode and a larger fibre optic probe; these modifications result in higher signal:noise UV/Visible spectra and greatly reduced redox equilibration times.

Section 4.4 describes the application of electrochemically-induced ATR FTIR redox difference spectroscopy to rehydrated films of cytochrome bc_1 complex from *Rba. capsulatus* for the first time. The aim of these experiments was to measure difference spectra arising from redox changes associated with haem b_L and haem b_H, individually, at higher signal:noise than those described above (*202*), in order better to interpret putative glutamic/aspartic acid signals in the 1710 - 1790 cm^{-1} region. In order to test the tentative assignment of protonation state change/perturbation of Glu-295 to the signals within the 1710 cm^{-1} - 1790 cm^{-1} region of the haem b_L spectrum, cytochrome bc_1 complex with a glutamic acid to valine substitution at position 295 in cytochrome *b* (see section 2.1.2) was also analysed. Glu-295 was selected for mutagenesis because it is a component of the highly conserved PEWY motif, close to haem b_L (approximately 9 Å from haem b_L in the stigmatellin bound structure (see Figure 1.6)), and is present in differing orientations in structures with different inhibitors bound (see section 1.1.3.2). In addition to the availability of site directed mutagenesis, use of *Rba. capsulatus* was advantageous because the pH dependencies of each of the B-type haem midpoint potentials suggest a single strongly coupled protonatable group as opposed to the weaker coupling (possibly of several groups) indicated by the bovine B haem midpoint pH dependencies (see section 1.1.3.2).

The experiments described in this chapter were performed after the publication of (*74;75*) and prior to (and contributing to) (*53*), see section 4.5. At the stage of the work reported here, development of the electrochemical cell had progressed to include a prototype which incorporated a fibre optic probe (see section 2.4.6). This allowed the redox states of the B- and C-type haems to be monitored (in real time) during establishment of suitable conditions for reduction/oxidation of haem b_L and haem b_H, individually. In addition, monitoring changes in the UV/Visible spectra recorded simultaneously with FTIR data confirmed the purity of the final

averaged haem b_L and haem b_H spectra. Therefore, both ATR FTIR and UV/visible spectra are presented for wild-type *Rba. capsulatus* cytochrome bc_1 complex.

4.2 IR absorption spectra acquired during preparation of rehydrated films

The process of preparing rehydrated films of cytochrome bc_1 complex that were adhered to the IRE, as described in section 2.4.3, was monitored by IR spectroscopy to assess layer quality and stability. Differences in the absolute absorbance spectra obtained from the bovine and *Rba. capsulatus* complex at each stage of layer preparation were minimal as shown in Figure 4.1. The absorbance spectrum of the ATR-ready aliquot, recorded immediately after sample deposition onto the IRE (trace A), was dominated by the O-H scissoring mode of water at 1638 cm^{-1}. The absorbance spectrum of the dried protein layer, trace B, was dominated by amide I (1651/2 cm^{-1}) and amide II (1540/2 cm^{-1}) protein bands together with a contribution from water underlying the amide I band. Because this contribution from water did not diminish with extended drying time it was concluded that the absorption originates from integral structural waters that are tightly bound to the protein. A band at 1739/8 cm^{-1} can also be seen that is due primarily to the ester bond of lipid (*223*) and can provide a useful means of estimating lipid/protein ratios (see section 1.2.2.3). On several occasions the protein layer was rejected at this stage due to the presence of signals from either excess detergent or polycarbonate; the latter was found to originate from the ultracentrifuge tubes used in ATR-ready sample preparation (see sections 2.4.3 and 3.3.2). The absorbance spectrum obtained after rehydration is shown as trace C; the protein bands decrease in amplitude as the protein layer expands and the water contribution under the amide I envelope increases. In general, it took 60 minutes for the rehydrated film to stabilise to a level sufficient for redox difference spectra to be measured accurately. It was found that rehydrated layers that retained >20% amide II signal ($\Delta A_{1540\text{-}1480\ cm^{-1}}$) on rehydration and had a stable rehydrated $\Delta A_{1540\text{-}1480\ cm^{-1}}$ greater than 0.1 could produce difference spectra of adequate signal/noise ratio.

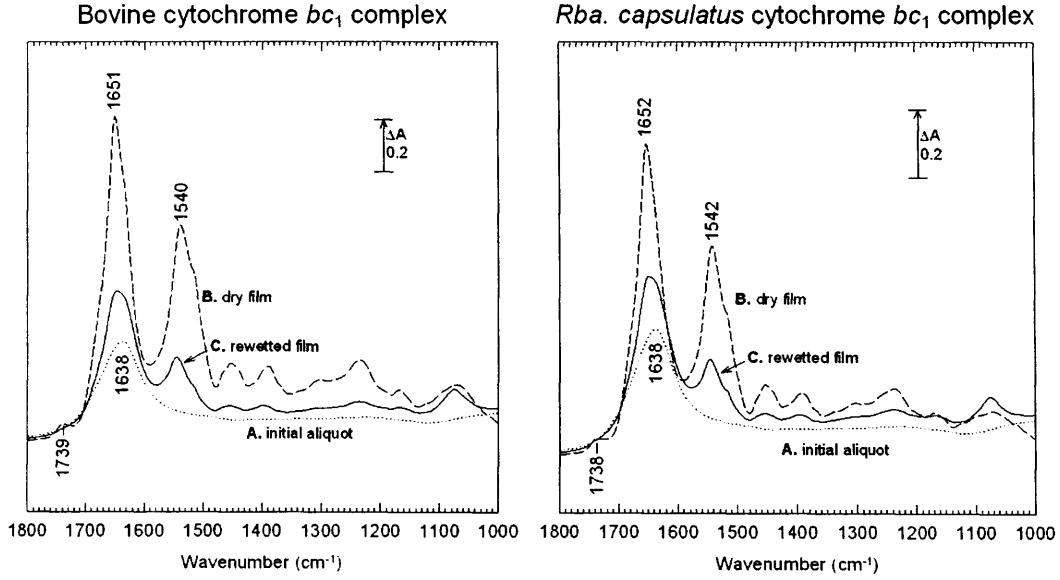

Figure 4.1 ATR FTIR absorption spectra of bovine and *Rba. capsulatus* cytochrome bc_1 complex during rehydrated film preparation from ATR-ready samples. Each spectrum is the average of 500 interferograms recorded against an equivalent background spectrum measured immediately after cleaning and drying the IRE. Trace A was recorded immediately after diluting an ATR-ready sample to 6 μl with water then placing it on the IRE. The absorption spectrum was recorded again after the sample had been dried under a gentle stream of dry air (trace B). A final absorption spectrum was recorded after rehydration with 50 μl 100 mM potassium phosphate, 200 mM potassium chloride pH7.0 (trace C) (see Materials and Methods).

4.3 Comparison of electrochemically- and perfusion-induced ATR FTIR redox difference spectra of bovine cytochrome bc_1 complex

In order to validate use of the newly developed electrochemical cell (see section 2.4.6), electrochemically-induced redox difference ATR FTIR spectra of bovine cytochrome bc_1 complex were measured and compared with equivalent spectra obtained by the already-established perfusion method (reproduced from (*74*)) (see section 2.4.5).

4.3.1 Redox difference spectra of whole complex

Electrochemically-induced ATR FTIR redox difference spectra for reduction and oxidation of all components of a rehydrated film of bovine cytochrome bc_1 complex at pH 7.0 are shown in Figure 4.2. Traces A and B are reduced *minus* oxidised and oxidised *minus* reduced spectra respectively. These spectra are near mirror images of each other confirming the reversibility of the redox-induced changes. A final high quality reduced *minus* oxidised spectrum (trace E) was

obtained by inverting trace B and averaging with trace A (to generate trace C), followed by interactive subtraction of minor contributions from layer swelling/shrinkage, redox mediators and buffer components (trace D) (these adjustments will subsequently be referred to as 'baseline adjustments'). The final spectrum (trace E) exhibits principal features at 1743(-), 1723(+), 1691(-), 1665(+), 1656(-), 1629(+), 1621(-), 1612(+), 1565(-), 1537(+), 1506(-), 1405(+), 1390(-), 1339(+), 1236(+), 1218(+), 1163(+), 1144(-), 1102(-) and 1084(+) cm^{-1}, where (+) and (-) indicate peaks and troughs respectively. The final spectrum (trace E) is in good agreement with the previously-published equivalent perfusion-induced redox difference spectrum (shown as trace F, reproduced from (*74*)) and is of similar amplitude and signal:noise (see section 4.3.3 for discussion).

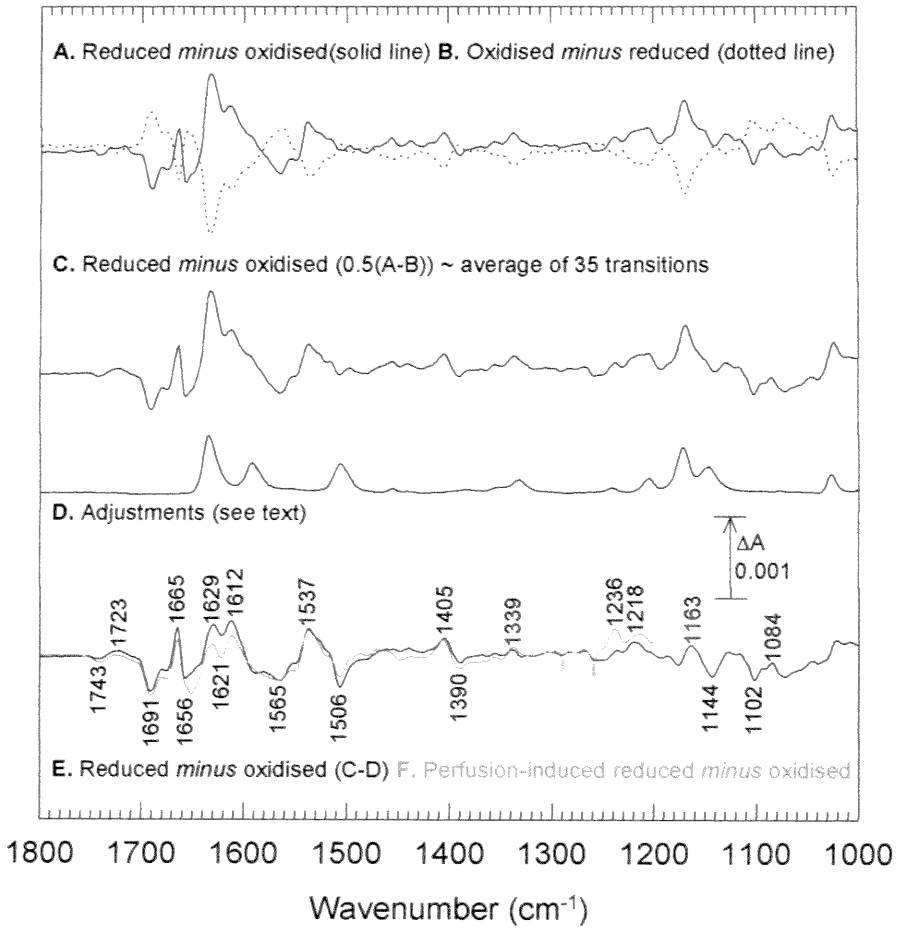

Figure 4.2 Comparison of electrochemically- and perfusion-induced ATR FTIR full redox difference spectra of bovine cytochrome bc_1 complex. Electrochemical reduction conditions were -400 mV applied for 20 minutes and oxidation conditions were 500 mV applied for 15 minutes. Redox mediation between working electrode and protein film was provided by a buffer of 200 mM potassium phosphate, 100 mM potassium chloride, 500 µM potassium ferricyanide, 100 µM benzyl viologen at pH 7; see section 2.4.6. Traces A and B are averages of sample spectra from 17 reduction transitions and 18 oxidation transitions, respectively, with each spectrum consisting of 1000 inferograms. Trace C, obtained by averaging trace A and the inverse of trace B, is equivalent to the average of 35 reduced *minus* oxidised spectra (trace C). The final spectrum, trace E, was obtained by subtracting trace D, a scaled benzyl viologen reduced *minus* oxidised difference spectrum, from trace C. In this experiment it was not necessary to make baseline adjustments for buffer or protein layer swelling/shrinkage contributions. Equivalent perfusion-induced reduced *minus* oxidised difference spectrum (at pH 7.5) was reproduced from (*74*) as trace F for comparison purposes. Peak/trough labelling refers to the electrochemistry data.

4.3.2 Redox difference spectra of haem b_L and b_H

In order to confirm the feasibility of the electrochemical method to obtain electrochemically-induced difference spectra arising from redox changes of haem b_L and haem b_H individually, spectral differences between samples poised at

appropriate ambient potentials were acquired and compared to equivalent perfusion-induced spectra. From the reported E_{m7} values of haem b_L (-25 mV), haem b_H (90 mV), haem c_1 (242 mV) and the Fe-S centre (305 mV) in the bovine complex (see section 1.1.3.2) (*32-34*), and preliminary experiments (data not shown), redox conditions (reduction/oxidation) of -450/-20 mV and 40/200 mV were selected for the for the resolution of haem b_L and haem b_H individually, respectively (see Figure 4.3). The electrochemically-induced reduced *minus* oxidised IR difference spectrum due to haem b_L is plotted as trace A (in black); baseline adjustments were made as described previously. It exhibits principal features at 1742(-), 1702(+), 1691(-), 1683(+), 1675(-), 1664(+), 1647(-), 1630(+), 1614(+), 1557(-), 1540(+), 1522(+), 1497(-), 1406(+), 1336(+), 1265(+), 1230(-), 1205(+), 1169(+), 1141(-), 1129(+), 1109(+), 1092(-), and 1064(-) cm^{-1}. The electrochemically-induced reduced *minus* oxidised IR difference spectrum due to haem b_H is plotted as trace B (in black); baseline adjustments were made as described previously. The final spectrum exhibits principal features at 1740(-), 1688(-), 1674(-), 1665(+), 1654(-), 1636(+), 1617(+), 1583(-), 1553(+), 1521(+), 1510(-), 1486(+), 1413(-), 1404(+), 1364(-), 1331(+), 1303(-), 1276(+), 1245(+), 1225(-), 1214(+), 1180(-), 1160(+), 1116(+), 1101(-) and 1067(-) cm^{-1}. The equivalent perfusion-induced haem b_L and haem b_H difference spectra (reproduced from (*74*)) are shown overlaid in red for comparison purposes. As with the redox difference spectra for all components the haem b_L and haem b_H electrochemically- and perfusion-induced spectra are similar in amplitude, signal:noise and are broadly in agreement; however differences are present in several regions and these are discussed in section 4.3.3.

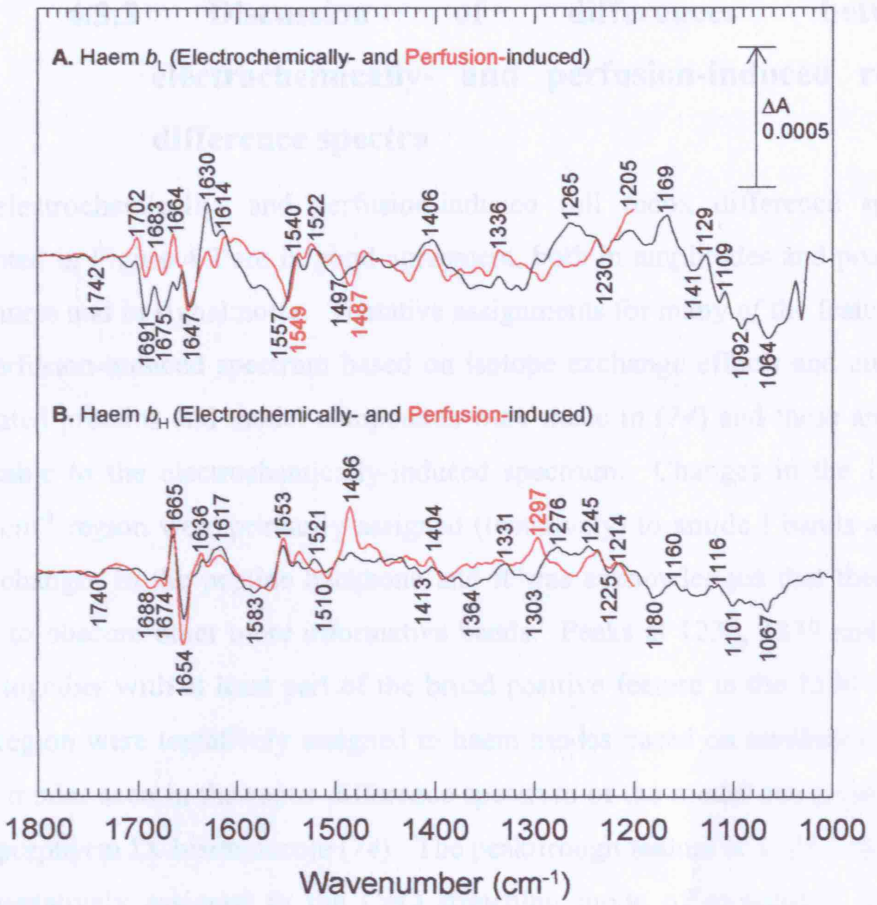

Figure 4.3 Comparison of electrochemically- and perfusion-induced ATR FTIR redox difference spectra of the B-type haems of bovine cytochrome bc_1 complex. Traces A and B are reduced *minus* oxidised difference spectra due to haem b_L and haem b_H respectively. The electrochemically-induced haem b_L difference spectrum (black line) was measured using reducing conditions of -450 mV and oxidising conditions of -20 mV, both applied for 15 minutes. The electrochemically-induced haem b_H difference spectrum (black line) was measured using reducing conditions of 40 mV and oxidising conditions of 200 mV, both applied for 15 minutes. Baseline adjustments (as described previously) were made to final presented haem b_L and b_H spectra which are equivalent to the average of 37 and 26 reduced *minus* oxidised spectra, each consisting of 1000 interferograms, respectively. A solution of 200 mM potassium phosphate, 100 mM potassium chloride, 250 µM hexaammineruthenium chloride, 50 µM anthraquinone-2,6-disulfonate, 50 µM benzyl viologen, 50 µM gallocyanin at pH 7.0 provided buffering and redox mediation. Equivalent perfusion-induced reduced *minus* oxidised difference spectra of haem b_L and haem b_H (acquired by reduction/oxidation with 3 mM sodium dithionite in buffer (50 mM HEPES, 50 mM potassium phosphate, 100 mM potassium chloride 5 µM phenazine methosulfate pH 7.5)/aerobic buffer and 300 µM succinate in buffer/285 µM fumarate 15 µM succinate in buffer, respectively) were reproduced from (*74*) and are overlaid in red for comparison purposes. Peak/trough labelling refers to the electrochemistry data.

4.3.3 Discussion of differences between electrochemically- and perfusion-induced redox difference spectra

The electrochemically- and perfusion-induced full redox difference spectra presented in Figure 4.2 are in good agreement, both in amplitudes and positions of features and in signal:noise. Tentative assignments for many of the features of the perfusion-induced spectrum based on isotope exchange effects and analysis of related proteins and model compounds were made in (*74*) and these are also applicable to the electrochemically-induced spectrum. Changes in the 1700 - 1610 cm^{-1} region were primarily assigned (tentatively) to amide I bands arising from changes in the peptide backbone and it was acknowledged that these are likely to obscure other more informative bands. Peaks at 1236, 1339 and 1405 cm^{-1}, together with at least part of the broad positive feature in the 1550 - 1530 cm^{-1} region were tentatively assigned to haem modes based on similarities with haem modes seen in the redox difference spectrum of the model compound iron protoporphyrin IX-bisimidazole (*74*). The peak/trough feature at 1723/1743 cm^{-1} was tentatively assigned to the C=O stretching mode of protonated aspartic acid(s) and/or glutamic acid(s) (*74*) (see section 3.5.5). Troughs at 1258 and 1289 cm^{-1} in the perfusion-induce spectrum were tentatively assigned to methoxy and/or ring modes of ubiquinone (*74*) (see section 3.5.3). Small troughs at these positions, indicated by arrows in Figure 4.2, are also present in the electrochemically-induced spectrum although it is acknowledged that these signals are only just detectable. Additional tentative assignments are discussed in (*74*).

Electrochemically- and perfusion-induced redox difference spectra from haem b_L and haem b_H, individually, are compared in Figure 4.3. The maximum amplitudes of these spectra are approximately half those of the full redox difference spectra in Figure 4.2, therefore discrepancies between the techniques are likely to be more apparent in this comparison. The overall shapes of the spectra obtained by the two methods are similar with the majority of features being present at similar positions and amplitudes. There are a number of minor differences between the electrochemically- and perfusion-induced difference

spectra of haem b_L. Differences in relative amplitudes of features in the amide I and II regions (1700 - 1590 cm^{-1} and 1570 - 1490 cm^{-1}, respectively) are likely to arise primarily from base line adjustments carried out to remove contributions from shrinking/swelling of the layer in both studies. For example, troughs at 1557 and 1497 cm^{-1} in the electrochemically-induced spectrum appear at 1549 and 1487 cm^{-1} in the perfusion-induced spectrum. The most prominent difference outside the amide I and II regions is the presence of a peak at 1265 cm^{-1} in the electrochemically-induced spectrum that is absent from the perfusion-induced spectrum. This peak does not correspond to any of the model compounds surveyed in Chapter 3 (the very sharp vacuum grease absorption at 1260 cm^{-1} is ruled out by the broad nature of the observed redox signal) and cannot currently be assigned. The amide I and II regions of the haem b_H electrochemically- and perfusion-induced difference spectra are in good agreement. In other regions notable differences include the greater amplitude of the peak at 1485 cm^{-1}, the presence of a peak at 1297 cm^{-1} and the absence of a peak at 1331 cm^{-1} in the perfusion-induced spectrum that are present at reduced amplitude, absent and present, respectively, in the electrochemically-induced spectrum. The peak at 1485 cm^{-1} has been tentatively assigned a C-C ring mode of ubisemiquinone in the Q_i-site (*74*) and it is possible that the semiquinone is stabilised in the reducing conditions used in the perfusion experiment (where the obligatory n=2 couple succinate/fumarate was used to poise potential) and not by those used in the electrochemistry experiment (where complete equilibration of all n=1 states was achieved due to the mediators present). The peaks at 1297 and 1331 cm^{-1}, from the perfusion- and electrochemically-induced spectra, respectively, cannot be assigned at this time.

In conclusion the differences between the electrochemically- and perfusion-induced redox difference spectra presented in Figure 4.2 and Figure 4.3 are considered to be minor and the electrochemical method is considered valid for the analysis of rehydrated films of cytochrome bc_1 complex.

4.4 Investigation of *Rhodobacter capsulatus* cytochrome bc_1 complex by electrochemically-induced redox difference spectroscopy

Electrochemically-induced ATR FTIR redox difference spectroscopy was applied to cytochrome bc_1 complex from *Rba. capsulatus* in order to resolve signals arising from haem b_L and haem b_H, individually. Use of a novel electrochemical cell, which incorporated a fibre optic probe (see section 2.4.6), allowed simultaneous acquisition of FTIR spectra while the redox state of the B- and C-type haems was monitored in real time. This allowed electrochemical conditions suitable for the acquisition of FTIR difference spectra arising solely from redox changes associated with haem b_L and haem b_H, individually, to be determined. Changes in the UV/visible spectra acquired during measurement of FTIR spectra for averaging allowed the purity of the final averaged haem b_L and haem b_H spectra to be confirmed.

4.4.1 UV/Visible redox difference spectra

Electrochemically-induced UV/visible difference spectra of all components of a rehydrated layer of *Rba. capsulatus* cytochrome bc_1 complex adhered to the IRE are shown in Figure 4.4 (see section 2.4.6). Traces A and B are reduced *minus* oxidised and oxidised *minus* reduced spectra respectively. These spectra are near mirror images of each other confirming the reversibility of the induced redox changes. The final spectrum (trace C) is dominated by a peak at 560 nm, characteristic of haem b_H reduction, with a small shoulder at 553 nm, characteristic of haem c_1 reduction. The contribution from reduction of haem b_L, a small peak at 564 nm, would be expected to be obscured by the larger 560 nm peak and the Fe-S centre is not expected to contribute; therefore, this spectrum is consistent with all components of the complex undergoing reduction/oxidation (*74;75*). These spectra were recorded simultaneously with the ATR FTIR difference spectra shown in Figure 4.6 (trace A) and confirm that the spectrum represented the redox transition of all components of the complex.

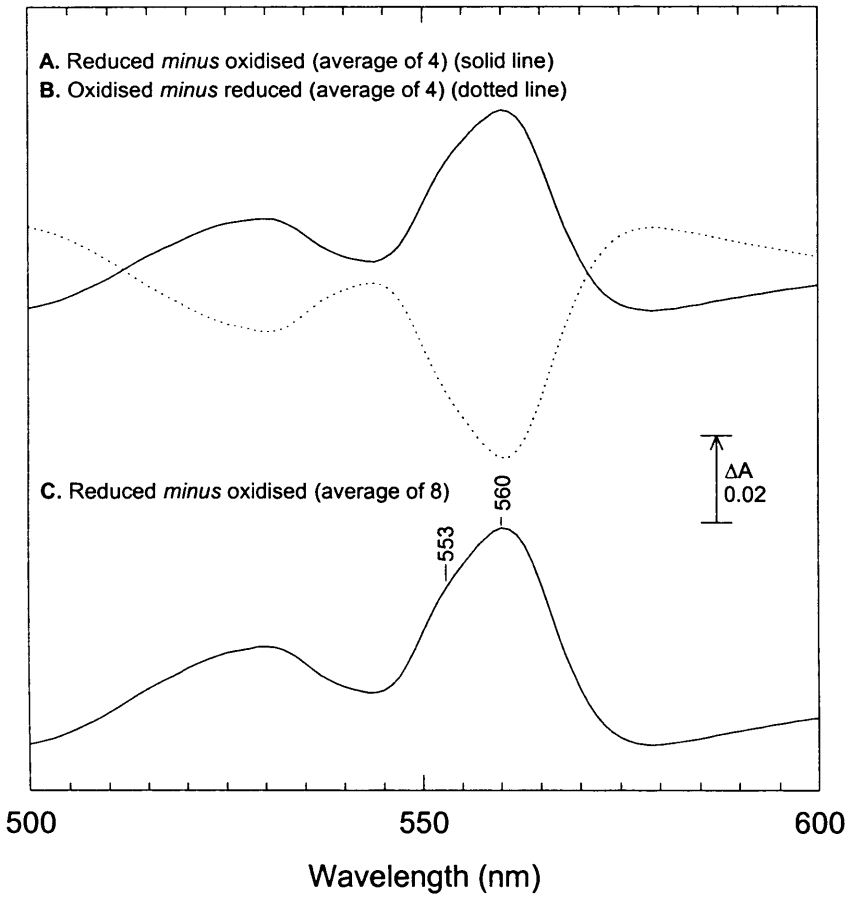

Figure 4.4 Electrochemically-induced UV/visible difference spectra of all components of *Rba. capsulatus* cytochrome bc_1 complex at pH 7.0. Reduction conditions were -450 mV and oxidation conditions were 500 mV, both applied for 25 minutes; buffer/redox mediation solution was as described in Figure 4.2. Traces A and B are averages of sample spectra from 4 reduction transitions and 4 oxidation transitions respectively. The final spectrum, plotted as trace C, was obtained by averaging trace A and the inverse of trace B and is equivalent to the average of 8 reduced *minus* oxidised spectra.

The known midpoint potentials of the *Rba. capsulatus* cytochrome bc_1 complex components: - Fe-S centre E_{m7} = 320 mV, haem c_1 E_{m7} = 320 mV, haem b_L E_{m7} = -140 mV and haem b_H E_{m7} = 40 mV (see section 1.1.3.2) (*31*) and the ability to monitor UV/visible absorbance changes almost in real time allowed selection of appropriate potentials for obtaining UV/visible (and FTIR) difference spectra of the individual B-type haems (see Figure 4.5). The difference spectrum due to reduction/oxidation of both B-type haems together (Figure 4.5, trace B) was dominated by a peak at 561 nm, indicative of reduction/oxidation of haem b_H, without the haem c_1 553 nm shoulder present in the spectrum due to all components (trace A, reproduced from Figure 4.4). The difference spectrum due to haem b_H (trace D) is also dominated by a peak at 561 nm; however, this feature differs in intensity and shape on the high wavelength side from the

feature in trace B. Subtraction of trace D from trace B (trace E) shows this difference more clearly. It consists of a peak at 556 and 567 nm, characteristic of haem b_L reduction/oxidation (*74*), and indicates that trace D is due to changes in haem b_H without contribution from haem b_L. A difference spectrum due to haem b_L is plotted as trace C. Full oxidation of haem b_L was shown to be accompanied by partial oxidation of haem b_H (data not shown) therefore, in order to measure a pure haem b_L spectrum it was necessary only partially to oxidise haem b_L. This explains the difference in magnitude of trace C (shown expanded ×2) and trace E. These spectra were recorded simultaneously with the ATR FTIR difference spectra shown in Figure 4.6 and confirm that trace B (of that figure) consists solely of redox transitions of the two B-type haems and that traces C and D (of that figure) consist solely of redox transition of haem b_L and haem b_H, respectively.

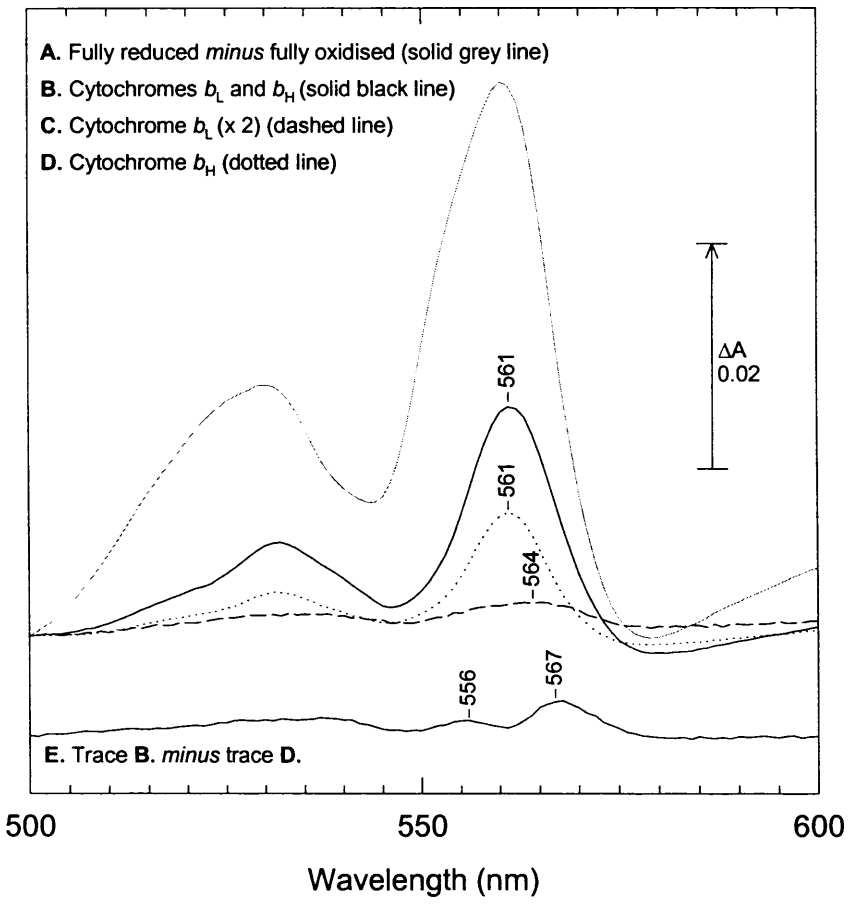

Figure 4.5 Electrochemically-induced UV/visible difference spectra of the B-type haems of *Rba. capsulatus* cytochrome bc_1 complex at pH 7.0. Trace A is reproduced from Figure 4.4 for comparison purposes. Trace B is the difference spectrum due to haems b_L and b_H (combined). It was measured using reducing conditions of -450 mV applied for 10 minutes and oxidising conditions of 190 mV applied for 14 minutes. Buffer/redox mediation solution was as described in Figure 4.3. The final presented spectrum is equivalent to the average of 28 reduced *minus* oxidised spectra. Traces C and D are difference spectra due to haems b_L and b_H respectively. The haem b_L spectrum was measured using reducing conditions of -450 mV and oxidising conditions of -20 mV, both applied for 10 minutes. The haem b_H spectrum was measured using reducing conditions of 40 mV and oxidising conditions of 200 mV, both applied for 20 minutes. The final presented haem b_L and b_H spectra are equivalent to the average of 35 and 31 reduced *minus* oxidised spectra respectively. The difference between traces B and D is plotted as trace E (see text).

4.4.2 IR redox difference spectra

Electrochemically-induced ATR FTIR redox difference spectra of *Rba. capsulatus* cytochrome bc_1 complex were measured concurrently with the UV/visible difference spectra described in section 4.4.1 and are shown in Figure 4.6. The difference spectrum arising from redox changes of all components is shown as trace A and exhibits principal features at 1743(-), 1724(+), 1693(-),

1684(+), 1678(-), 1670(+), 1653(-), 1623(+), 1609(-), 1556(+), 1548(-), 1534(+), 1506(-), 1492(+), 1482(-), 1469(+), 1449(-), 1431(+), 1388(+), 1289(-), 1277(+), 1264(-), 1239(+), 1202(-), 1148(-), 1115(+), 1104(-) and 1088(+) cm^{-1}. It is in good agreement with the previously published equivalent perfusion-induced redox difference spectrum (reproduced from (*75*) and overlaid in red) and shows broad similarities to the electrochemically-induced difference spectrum due to all components of bovine cytochrome bc_1 complex (Figure 4.2), see section 4.5.

Redox-induced ATR FTIR difference spectra arising from redox changes of both B-type haems and of haem b_L and b_H individually were also recorded concurrently with the UV/visible difference spectra shown in Figure 4.5. However, longer timings were necessary for redox equilibration when using the fibre optic enabled electrochemical cell resulting in acquisition of fewer difference spectra for averaging in a given time period and therefore lower signal:noise in the final averaged spectra than in an equivalent spectrum recorded using the electrochemical cell lacking the fibre optic probe (see section 4.5). In order to increase the signal:noise ratio the FTIR spectra arising from redox changes of both B-type haems and of haem b_L and b_H individually were each averaged with data (not shown) acquired from a different protein layer obtained under equivalent conditions using the electrochemical cell lacking the fibre optic probe. Final averaged spectra are shown in Figure 4.6 as traces B, C and D, respectively. The reduced *minus* oxidised IR difference spectrum due to haem b_L, after baseline adjustments, (trace C) exhibits principal features at 1743 (-), 1723(+), 1702(+), 1694(-), 1685(+), 1678(-), 1669(+), 1650(-), 1632(+), 1620(-), 1612(+), 1563(-), 1534(+), 1521(-), 1456(+), 1411(+), 1238(+), 1166(+), 1141(-), 1127(+), 1115(+), 1102(-) cm^{-1}. The reduced *minus* oxidised IR difference spectrum due to haem b_H, after baseline adjustments, (trace D) exhibits principal features at 1740(-), 1653(-), 1624(+), 1612(-), 1563(+), 1487(+), 1470(+), 1451(-), 1431(+), 1387(+), 1328(+), 1311(+), 1289(-), 1274(+), 1263(-), 1204(-), 1126(+), 1114(+), 1104(-) and 1052(+) cm^{-1}. These data are interpreted and discussed in section 4.5.

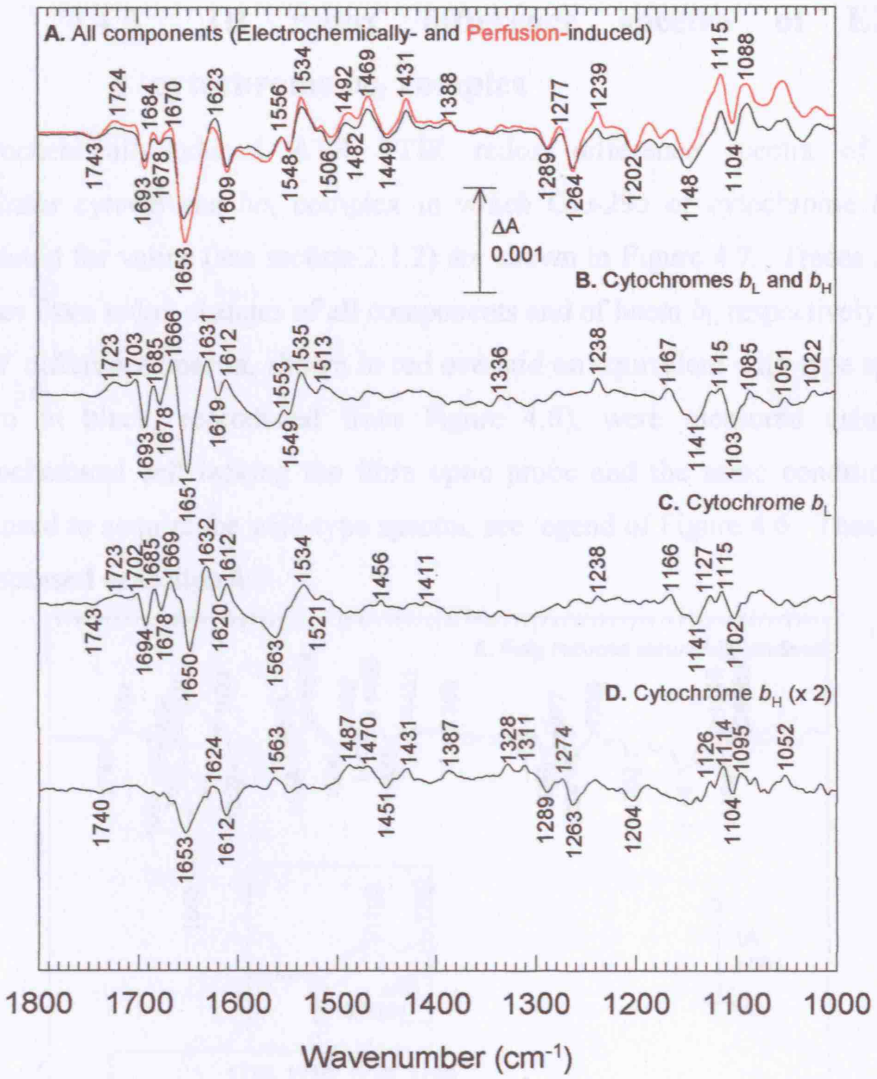

Figure 4.6 Electrochemically-induced ATR FTIR difference spectra of *Rba. capsulatus* cytochrome bc_1 complex at pH 7.0. Trace A is the reduced *minus* oxidised difference spectrum arising from redox changes of all components and is the average of 8 spectra each of which consists of 1000 interferograms. Reduction conditions were -450 mV and oxidation conditions were 500 mV, both applied for 25 minutes; data were recorded synchronously with UV/visible data, see legend of Figure 4.4. See legend of Figure 4.2 for details of the buffer/redox mediation solution. The equivalent perfusion-induced difference spectrum, reproduced from (*75*), is scaled and overlaid in red. Reduced *minus* oxidised difference spectra arising from redox changes of both B-type haems and of haem b_L and b_H are shown as traces B, C and D respectively. Each is the average of spectra recorded concurrently with the UV/visible spectra presented in Figure 4.4 and additional spectra recorded under equivalent conditions using the electrochemical cell lacking the fibre optic probe (see text). Traces B, C and D are the average of 58, 80 and 60 reduced *minus* oxidised difference spectra, each consisting of 1000 interferograms, respectively. See legend of Figure 4.5 for reduction and oxidation conditions and legend of Figure 4.3 for details of buffer/redox mediation solution.

4.4.3 IR redox difference spectra of E295V cytochrome bc_1 complex

Electrochemically-induced ATR FTIR redox difference spectra of *Rba. capsulatus* cytochrome bc_1 complex in which Glu-295 of cytochrome *b* was substituted for valine (see section 2.1.2) are shown in Figure 4.7. Traces A and B arises from redox changes of all components and of haem b_L respectively. The E295V difference spectra, shown in red overlaid on equivalent wild-type spectra (shown in black, reproduced from Figure 4.6), were measured using the electrochemical cell lacking the fibre optic probe and the same conditions as those used to acquire the wild-type spectra, see legend of Figure 4.6. These data are discussed in section 4.5.

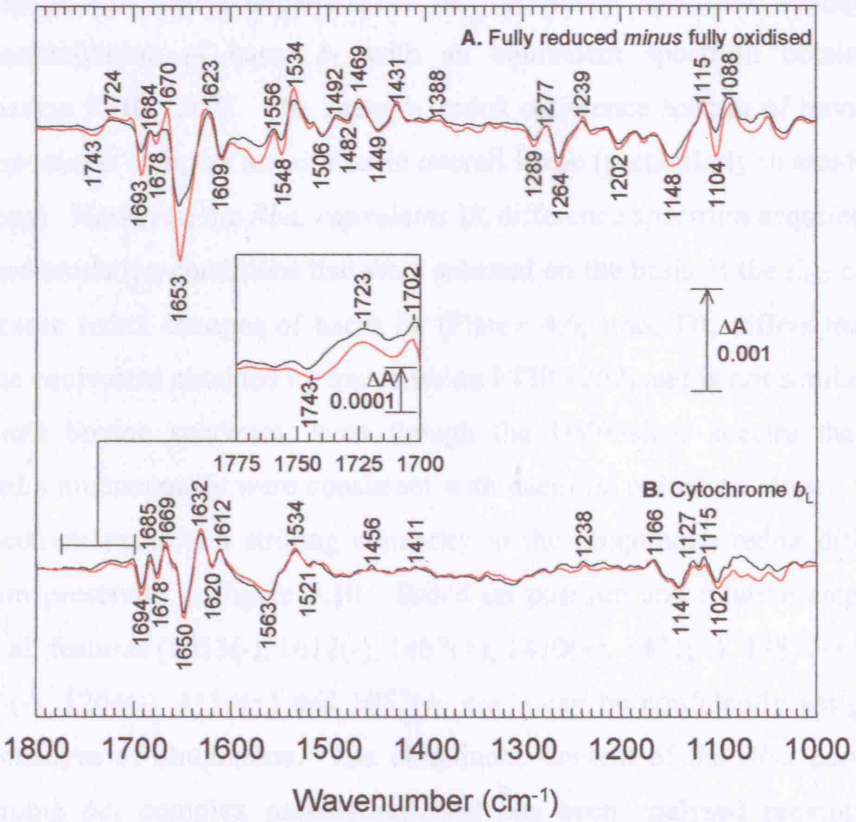

Figure 4.7 Electrochemically-induced ATR FTIR difference spectra of all components and of the haem b_L of *Rba. capsulatus* E295V cytochrome bc_1 complex at pH 7.0. E295V spectra are shown in red and were measured under the same conditions as the wild-type spectra which are reproduced in black from Figure 4.6. Trace A is the average of 144 reduced *minus* oxidised spectra, each consisting of 1000 interferograms, due to redox changes of all components. Trace B is a difference spectrum due to haem b_L and is the average of 46 reduced *minus* oxidised spectra. For redox changes of all components reduction/oxidation conditions were -450/500 mV and for redox changes of haem b_L reduction/oxidation conditions were -450/-20 mV; redox mediation was provided by a buffer of 200 mM potassium phosphate, 100 mM potassium chloride, 500 µM potassium ferricyanide, 100 µM benzyl viologen at pH 7.

4.5 Discussion and conclusions

Electrochemically-induced ATR FTIR difference spectra arising from reduction/oxidation of all components of rehydrated films of bovine cytochrome bc_1 complex have been shown to be highly comparable to equivalent spectra obtained by perfusion-induced ATR FTIR spectroscopy (*74*), as have difference spectra arising from reduction/oxidation of each of the B-type haems individually (see section 4.3.3). These comparisons validate the functionality of the newly developed electrochemical cell and associated protocols. This was further demonstrated (for both the cells with and without the fibre optic probe) by comparison of the full redox difference spectrum of cytochrome bc_1 complex from *Rba. capsulatus* with the equivalent perfusion-induced spectrum from (*75*) (see Figure 4.6) and comparison of the difference spectrum arising from reduction/oxidation of haem b_L with an equivalent spectrum obtained by transmission FTIR (*202*). The haem b_L redox difference spectra of bovine and *Rba. capsulatus* complex are similar in overall shape (particularly in amide I and II regions). However, the *Rba. capsulatus* IR difference spectrum acquired using reduction/oxidation conditions that were selected on the basis of the E_{m7} of haem b_H to cause redox changes of haem b_H (Figure 4.6, trace D), differs markedly from the equivalent obtained by transmission FTIR (*202*) and is not similar to the equivalent bovine spectrum, even though the UV/visible spectra that were recorded simultaneously were consistent with haem b_H reduction alone. Instead this spectrum exhibits a striking similarity to the ubiquinone redox difference spectrum presented in Figure 3.10. Based on position and relative amplitudes almost all features (1653(-), 1612(-), 1487(+), 1470(+), 1431(+), 1387(+), 1289(-), 1263(-), 1204(-), 1114(+) and 1052(+) cm^{-1}) can be confidently assigned to redox changes of ubiquinone. The ubiquinone content of the *Rba. capsulatus* cytochrome bc_1 complex preparation used has been analysed previously by UV/visible spectroscopy and the ubiquinone:cytochrome bc_1 complex ratio was shown to be 6-8:1 (*75*). It would follow that the major contributor to these signals was adventitiously bound ubiquinone. If haem b_H signals underlie the ubiquinone signals they are too small for interpretation. For future experimentation, oxidation conditions could be selected that oxidise haem b_H (E_{m7} = 40 mV) but do not oxidise the majority of ubiquinone (E_{m7} = 110 mV

(solution value) (*100*)) together with reducing conditions that reduce haem b_H without greatly reducing haem b_L (E_{m7} = -140 mV). Or, an attempt could be made to remove the ubiquinone, for example, by washing with detergent while the protein is bound to a column.

Unlike those of haem b_H, the signals arising from reduction/oxidation of haem b_L were successfully resolved in *Rba. capsulatus* using the electrochemical cell and ATR apparatus (see Figure 4.6, trace C). This spectrum is of significantly higher signal:noise than that previously acquired using transmission FTIR by Baymann *et al* (*202*), particularly at lower frequencies where the effective pathlength of the IR beam is extended in ATR mode. The spectrum shares many features with the previously published transmission spectra (*202*) and the perfusion-induced bovine haem b_L difference spectrum (acquired in ATR mode) (*74*), allowing many tentative assignments to be made (see Table 4.1).

Tentative assignments ((*74;202*))	*Rba. capsulatus*		Bovine
	Electrochemically-induced (ATR) Figure 4.6, trace D	Electrochemically-induced (TRANS) (*202*)	Perfusion-induced (ATR) (*74*)
C=O Asp/Glu	**1743(-)**	-	**1741(-)**
C=O Asp/Glu	**1723(+)**	**1720(+)**	**1728(+)**
C=O Haem propionate/Amide I	1702(+)	1704(+)	1701(+)
C=O Haem propionate	1694(-)	1690(-)	1692(-)
C=O Haem propionate	1685(+)	1680(+)	1683(+)
C=O Haem propionate	1678(-)	1674(-)	1675(-)
Amide I	1669(+)	1666(+)	1664(+)
Amide I	-	1652(+)	1656(+)
Amide I	1650(-)	1646(-)	1649(-)
Amide I	1632(+)	1632(+)	1630(+)
Amide I	1620(-)	1618(-)	1622(+)
CαCβ haem vinyl	1612(+)	1608(+)	1612(+)
Amide II	1563(-)	1556(-)	1549(-)
CbCb haem	1534(+)	1532(+)	1537(+)
CbCb haem or Amide II	1521(-)	1518(-)	1525(+)
-	1456(+)	-	-
CaN haem	1411(+)	1400(+)	1407(+)
CαCβ haem vinyl	1141(-)	1140(-)	-

Table 4.1 Comparison of redox difference spectra of haem b_L. Features of redox difference spectra of haem b_L from *Rba. capsulatus*, acquired by electrochemically-induced ATR FTIR spectroscopy (from Figure 4.6, trace D), electrochemically-induced transmission FTIR spectroscopy (from (*202*)) and perfusion-induced ATR FTIR spectroscopy. Tentative assignments for signals to protonation state change of glutamic acid(s) or aspartic acid(s) or to perturbation of one or more such residues in the protonated state are in bold.

In addition to the numerous assignments to amide I and II and various haem modes, a trough/peak feature at ~ 1742/1741 cm^{-1}, which is present in the ATR FTIR haem b_L difference spectra of the *Rba. capsulatus* and bovine complexes, is tentatively assigned to a protonated glutamic acid(s) and/or aspartic acid(s) responding to a change in its environment (or possibly, the redistribution of protons between several carboxylic residues) (*74;202*), see section 3.5.5. The peak (1720 cm^{-1}) of this feature is also present in the transmission mode spectra of *Rba. capsulatus* and it is possible that the trough is also present but obscured by noise (*202*).

An additional smaller peak at ~1702 cm^{-1} may also arise from similar C=O stretching modes (*74;202*), however these modes are not typically expected to absorb below 1710 cm^{-1}. A more likely assignment would be to a high frequency amide I vibrational mode, such as that of a proline, as suggested by Baymann *et al* (*202*) or to a haem propionate (*224*). It has been proposed that a redox linked perturbation of Glu-295 in the protonated form (or protonation state changes of this residue) may contribute to the ~ 1742/1741 cm^{-1} signals (*74*). This was based on the proximity of the residue to haem b_L (see Figure 1.6), that it is highly conserved and that its orientation in high resolution structures has been shown to be dependent on the type of Q_o-site inhibitor bound (*74*) (see section 1.1.3.2). To investigate this proposal further, electrochemically-induced difference spectra arising from reduction/oxidation of all components, and of haem b_L, of E295V *Rba. capsulatus* cytochrome bc_1 complex (see section 2.1.2) were measured (see Figure 4.7). There are no significant differences between the E295V and wild-type full redox and haem b_L difference spectra indicating that Glu-295 is not the source of the signals in the 1710 cm^{-1} - 1790 cm^{-1} region of the haem b_L spectrum and therefore cannot be the redox-linked protonated group of haem b_L. Subsequent to this study an E295H mutant has been analysed in the same manner; the resulting spectra were shown not to differ significantly from wild-type (*53*) confirming the conclusion that Glu-295 is not the source of the signals. If it is assumed that the signals in the 1710 cm^{-1} - 1790 cm^{-1} region arise from a perturbation of a protonated carboxylic acid or a protonation state change of a carboxylic acid, future experiments should investigate alternative candidate glutamic and aspartic acids close to haem b_L and such candidates are detailed in

Figure 4.8A. For example, a good candidate would be Asp-278 because it is close to, and orientated towards, haem b_L (sidechain to haem propionate = 10 Å) and is well conserved.

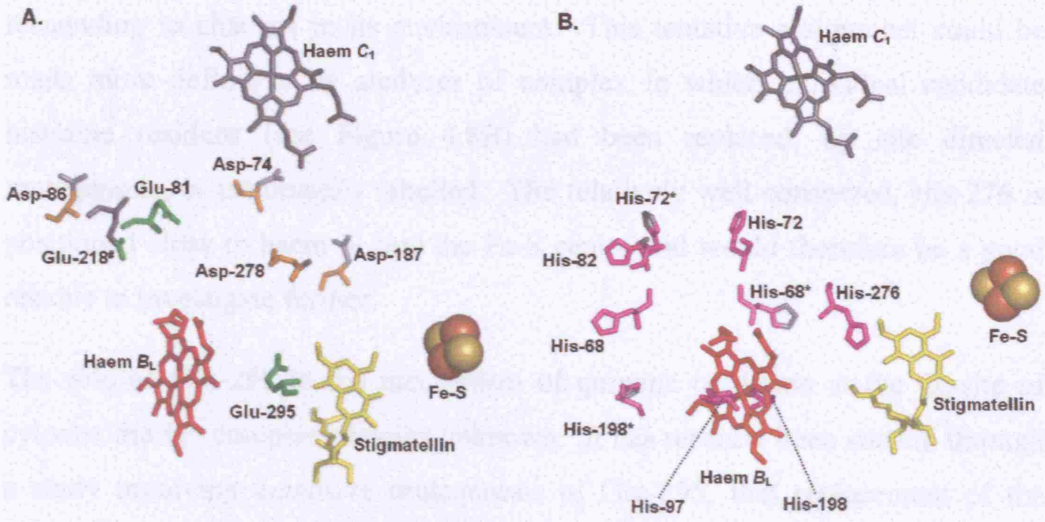

Figure 4.8 Aspartic acid, glutamic acid and histidine residues in the vicinity of haem b_L. Atoms of aspartic acid residues and glutamic acid residues (A) and Histidine residues (B) within 20 Å of the iron of haem b_L in the *Rba. capsulatus* structure (*Rba. capsulatus* numbering) are coloured orange, green and magenta respectively. All residues are of cytochrome *b* except for Glu-218 of cytochrome c_1; His-68*, His-72* and His-198* are of the other cytochrome *b* of the dimeric structure. Figure drawn using PyMOL™ from PDB file 1ZRT.

It is also appropriate to examine the haem b_L difference spectrum for alternative signals that may arise from protonation state changes of a non-glutamic/aspartic acid group. The C=O stretching mode of a haem propionate, in the protonated form, would be expected to absorb between 1700 and 1665 cm^{-1}. The symmetric and antisymmetric COO^- modes would be expected to absorb between 1420 and 1300 cm^{-1} and between 1620 and 1540 cm^{-1} respectively (*224*). Therefore, the peak close to 1700 cm^{-1} in the haem b_L difference spectrum is consistent with the protonation of a haem propionate (or a protonated propionate group responding to a change in environment). This assignment is highly tentative as the feature could also arise from, as discussed above, a glutamic/aspartic acid or an amide I mode. Establishing a more definitive assignment to a propionate would require the analysis of complex in which the haem b_L ring had been isotope labelled, in a similar manner to that used by Mileni *et al* to investigate the role of the ring C propionate of the distal haem in the proposed E-pathway of quinol:fumarate reductase by FTIR (*224*). The haem b_L difference spectrum also contains several

bands in the 1100 cm^{-1} region where protonation state changes of histidine (perturbation of histidine in imidazole/imidazolium forms) are expected to contribute (see section 3.5.4). In the b_L difference spectrum these signals appear as a peak/trough at 1115/1102 cm^{-1} which is consistent with a histidine residue responding to changes in its environment. This tentative assignment could be made more definitive by analyses of complex in which individual candidate histidine residues (see Figure 4.8B) had been replaced, by site directed mutagenesis, or isotopically labelled. The relatively well conserved, His-276 is positioned close to haem b_L and the Fe-S centre and would therefore be a good residue to investigate further.

The role of Glu-295 in the mechanism of quinone oxidation at the Q_o-site of cytochrome bc_1 complex remains unknown. It has recently been shown, through a study involving extensive mutagenesis of Glu-295, that replacement of the residue (with alanine, valine, phenylalanine, histidine, lysine or glutamine) results only in a moderate (between 5 and 50-fold) reduction in hydroquinone oxidation rates. In addition it was shown that replacement of Glu-295 does not effect the midpoint potential pH dependency of haem b_L (or the Fe-S centre) further confirming that Glu-295 is not the strongly redox-linked protonatable group (see section 1.1.3.2). The authors note that the Q_o-site is highly resilient to site directed mutagenesis and suggest that certain residues, most likely including Glu-295, may play vital roles, but that there is a structural redundancy in effect meaning that removal of one of these residues results in the role being performed by another residue(s) (*53*). If this is the case, it is implied that the traditional methods for deducing catalytic site function (i.e. performing site directed mutagenesis to identify key residues, noting their relative positions from a high resolution structure and making deductions from there) will have to be rethought for analysis of the Q_o-site.

Chapter 5: Investigation of Complex I by Redox Difference InfraRed Spectroscopy

5.1 Introduction

As detailed in Chapter 1 (section 1.3), complex I is the least understood of the major respiratory complexes. This is largely due to its great size, high level of complexity, the absence of a complete high resolution structure and a lack of suitable techniques for the study of the reactions of its many redox centres. The non-covalently bound FMN is amenable to study by UV/visible spectroscopy (see section 1.3.8.2). However, the Fe-S centres and ubiquinone all have poor UV/visible signatures. To date, most mechanistic information on the electron-transfer cofactors has come from EPR spectroscopy detection of reduced forms of Fe-S centres and semiquinone forms of ubiquinone and FMN; the conclusions from these studies are detailed in section 1.3.8.1. FTIR spectroscopy provides a useful complementary technique in which all known complex I prosthetic groups, together with protein changes associated with them, can be studied in the whole enzyme at near physiological temperatures. FTIR spectroscopy has recently been applied to *E. coli* complex I and spectral features have been interpreted in terms of large conformational changes of polypeptide (*174*), redox changes of FMN (*84*), redox-linked perturbation of lipid (*225*) and specific redox-linked protonation changes of carboxylic acids (*84;226*) and tyrosine (*173*). These

studies were performed in transmission mode using an ultrathinlayer spectroelectrochemical cell and are described in detail in section 1.3.8.3.

This chapter describes the application of electrochemically-induced ATR FTIR difference spectroscopy to rehydrated films of *Y. lipolytica* and bovine complex I that advance the previous transmission mode FTIR spectroscopic studies of *E. coli* complex I. The results are presented in detail in the following sections but a brief summary is provided below:

Because the study is the first to apply ATR FTIR spectroscopy to complex I from either *Y. lipolytica* or *B. taurus* it was appropriate to survey the features of the fully reduced *minus* fully oxidised redox difference spectrum. Spectra were acquired at pH 6.0 and 8.0 and, to assist interpretation, equivalent spectra after H-D exchange and of globally ^{15}N labelled material were measured for *Y. lipolytica*. Interpretation was further assisted by the model compound measurements described in Chapter 3.

The significance of Fe-S centre N2 is described in Chapter 1, section 1.3.7. Briefly, Fe-S centre N2 is of special interest as its midpoint potential has a redox-linked protonation site (*93*) that may be relevant to the protonmotive mechanism (*96;161*). Furthermore, EPR data have provided strong indications that it can interact magnetically with ubisemiquinone (*144;145*) and so is likely to be the immediate electron donor to substrate ubiquinone. Previous IR studies on *E. coli* complex I have attempted to resolve the redox difference IR spectrum of Fe-S centre N2 using double difference spectroscopy where intact protein samples containing N2 were compared to fragments that had lost centre N2 (*84*). The complications associated with this approach (see section 1.3.8.3) are avoided when investigating complex I from *Y. lipolytica* because in this organism the E_{m7} value of Fe-S centre N2, -140 mV (*99*), is sufficiently separated from those of the other components. This allowed difference spectra arising solely from changes associated with reduction/oxidation of N2 to be recorded directly from the whole complex by using appropriate reduction/oxidation conditions. Equivalent IR difference spectra resulting from N2 associated redox changes were obtained from wild-type and globally ^{15}N labelled material in H_2O and D_2O media, after H-D exchange.

Differences between reduction by electrochemistry and by the substrate NADH were investigated by recording perfusion-induced ATR FTIR difference spectra of bovine

complex I with a view to investigating suggestions that complex I might undergo a conformational change when reduced by natural substrate but not when reduced chemically (*125*). Reversible reduction and oxidation of the complex was induced by buffers containing NADH and NAD^+ respectively. Finally preliminary data were acquired for electrochemically-induced reduction/oxidation of all components of *Y. lipolytica* complex I into which a H226M substitution in the NUCM subunit (homologue of the bovine 49 kDa subunit) had been introduced (see Materials and Methods). This mutant was selected because H226 has been shown to be the redox linked Bohr group of Fe-S centre N2 in *Y. lipolytica* (*101*) (see section 1.3.7).

5.2 Results

5.2.1 IR absorption spectra acquired during preparation of rehydrated films

The process of preparing rehydrated films of complex I that were adhered to the IRE, as described in section 2.4.3, was monitored by IR spectroscopy to assess layer quality and stability. When preparing H-D exchanged material, IR spectroscopy also allowed the extent of H-D exchange to be quantified (see below and section 2.4.4). Differences in the absolute absorbance spectra of bovine and wild-type *Y. lipolytica* complex I at each stage of layer preparation were minimal as shown in Figure 5.1, plots I and II. In addition, these absolute spectra are broadly comparable to those obtained during the preparation of cytochrome bc_1 complex layers (see Chapter 4, Figure 4.1) and the discussion in section 4.2 also applies to plots I and II of Figure 5.1. The absorbance spectrum of the ATR-ready aliquot, recorded immediately after sample deposition onto the IRE (Figure 5.1, plots I and II, trace A) was dominated by the scissoring mode of water centred at 1638 cm^{-1}. The absorbance spectrum of the dried protein layer, trace B, was dominated by amide I (centred at 1650 cm^{-1}) and amide II (centred at 1538/40 cm^{-1}). As with the cytochrome bc_1 complex layer, a water contribution underlying the amide I band in the spectra of the dried complex I layer, which did not diminish with extended drying time, was indicative the presence of integral structural waters that are tightly bound to the protein. The 1740 cm^{-1} band, arising primarily from the ester bond of lipid (*223*) was also present (see section 4.2 and section 1.2.2.3). As was the case with cytochrome bc_1 complex, occasionally the protein layer was rejected at this stage due to the presence of signals from either

excess detergent or polycarbonate; the latter was found to originate from the ultracentrifuge tubes used in ATR-ready sample preparation (sections 2.4.3 and 3.3.2). The absorbance spectrum obtained after rehydration is shown as trace C; the protein bands decrease in amplitude as the protein layer expands and the water contribution under the amide I envelope increases.

The IR absorption spectra obtained during layer preparation of wild-type *Y. lipolytica* complex I after/during H-D exchange (see section 2.4.4) are shown in plot III. Trace A is dominated by the O-D scissoring mode of deuterium oxide at 1205 cm^{-1} and comparison with trace A of plots I, II and VI demonstrates the differing IR absorption properties of deuterium oxide and water (see also section 3.2). H-D exchanged material was dried onto the IRE; during this process the material was exposed to the atmosphere and D-H exchange was able to occur. Trace B, recorded immediately after drying, is therefore the absolute absorbance spectrum of partially H-D exchanged material. The amide I band (centre at 1645 cm^{-1}) predominantly arises from C=O stretching modes and, therefore, the effect of H-D exchange on the band is minor. The observed 5 cm^{-1} downshift is slightly larger than the expected downshift of 1-2 cm^{-1} (*80*); this is likely to be due to the loss of the underlying water contribution. The amide II band arises from ~ 60% N-H bending and ~ 40% C-N stretching modes (*70*) and is therefore much more sensitive to H-D exchange. In trace B the bands at 1540 cm^{-1} and 1440 cm^{-1} result from amide II vibrations of protonated and deuterated peptide bonds respectively. After rehydration with D_2O containing buffer, trace C, the amide II bands arising from vibrational modes of deuterated (1440 cm^{-1}) and protonated (1540 cm^{-1}) peptide increase and decrease in amplitude respectively. This provides a quantitative indicator for extent of H-D exchange within the protein, the final extent of which was estimated to be >90% (see section 2.4.4).

IR spectra obtained during the preparation of rehydrated protein films of globally ^{15}N labelled *Y. lipolytica* complex I are shown in plot IV of Figure 5.1. These spectra only significantly differ from those obtained for the wild-type complex in the position of the amide II envelope in traces B and C. The effect of ^{15}N labelling on amide I, which arises primarily from C=O stretching modes, are minimal as expected. In contrast, the amide II envelope arises from N-H bending and C-N stretching modes (*70*) and is shifted downwards by approximately 20 cm^{-1} on ^{15}N labelling.

In general, it took 60 minutes for the rehydrated film to stabilise to a level sufficient for redox difference spectra to be measured accurately. It was found that rehydrated layers that retained >20% amide II signal (measured as $\Delta A_{1540\text{-}1480\ cm^{-1}}$) on rehydration and had a stable rehydrated amide II signal greater than 0.1 could produce difference spectra of adequate signal/noise ratio.

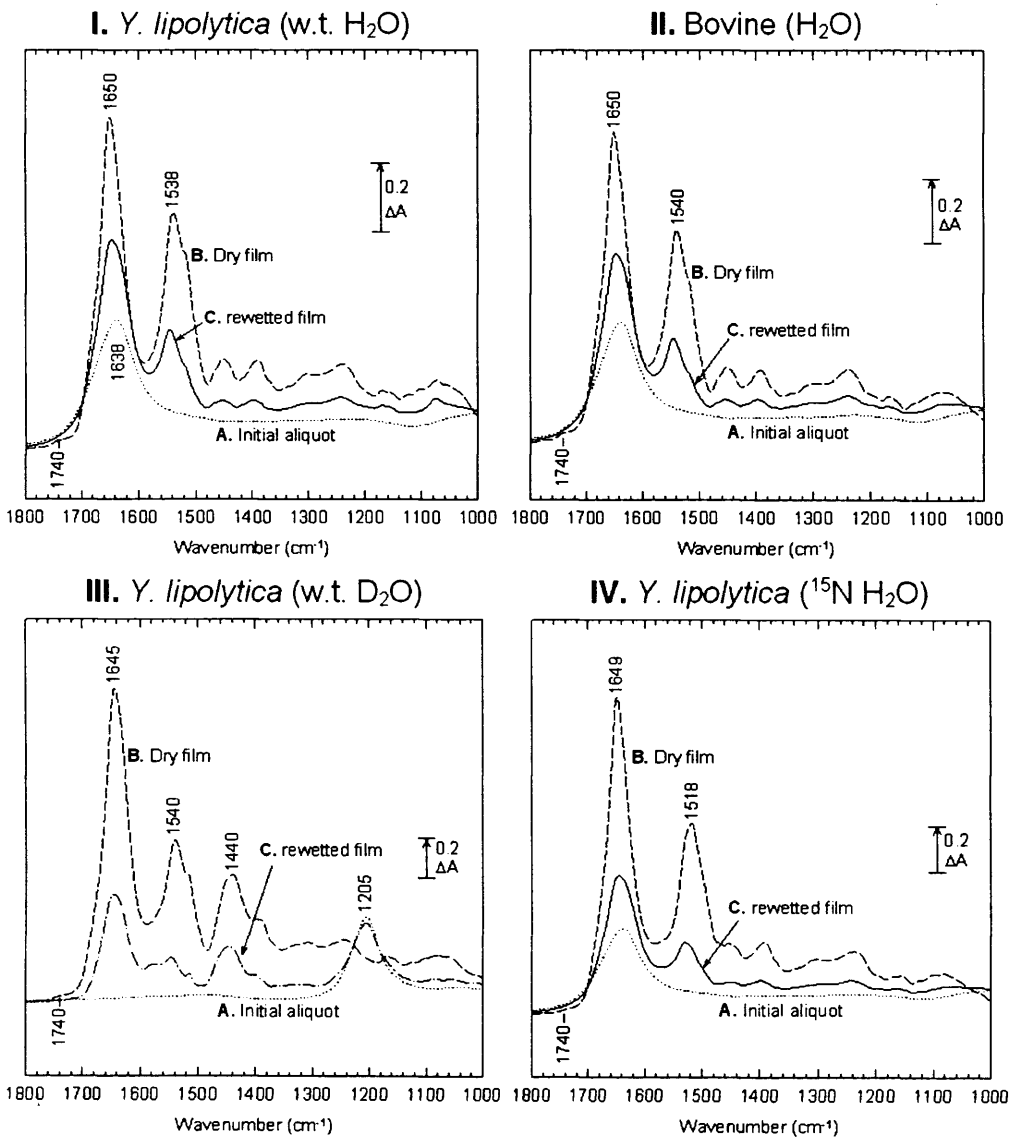

Figure 5.1 ATR FTIR absorption spectra recorded during preparation of rehydrated films of complex I. Plot I is for the wild-type *Y. lipolytica* complex in H_2O media; plot II is for the bovine complex in H_2O media; Plot III is for the wild-type *Y. lipolytica* complex in D_2O media; and Plot IV is for globally ^{15}N labelled *Y. lipolytica* complex in H_2O media (see Materials and Methods). Each spectrum is the average of 500 interferograms recorded against an equivalent background spectrum measured immediately after cleaning and drying the IRE and immediately prior to sample deposition. For H_2O media experiments: trace A was recorded immediately after diluting an ATR-ready sample to 6 μl with water then placing it on the IRE. The absorption spectrum was recorded again after the sample had been dried under a gentle stream of dry air (trace B). A final absorption spectrum was recorded after rehydration with 10 μl 20 mM potassium phosphate, 200 mM potassium chloride at pH 6.0 or 8.0 as appropriate (trace C). D_2O spectra were recorded at the same stages as H_2O spectra except trace C which was recorded 2 hours after sample deposition and after several exchanges of 20 mM potassium phosphate, 200 mM chloride at pD 6.0 or 8.0 within a sealed chamber until H-D exchange was maximal (as determined by amide II signals - see section 2.4.4).

5.2.2 Full redox difference spectra of *Yarrowia lipolytica* complex I

Reduced *minus* oxidised ATR FTIR difference spectra of all components of *Y. lipolytica* complex I at pH 6.0 and 8.0 are shown in Figure 5.2. Traces A and B are reduced *minus* oxidised and oxidised *minus* reduced respectively at pH 6.0. Oxidising and reducing conditions of 425 and -425 mV were selected in order that all known component underwent oxidation/reduction. Preliminary IR data were acquired over approximately ten reduction/oxidation cycles during which the equilibration time was varied to determine the minimum time necessary to achieve the maximum amplitudes of IR difference spectra; timings of 8 minutes for both reduction and oxidation were found to be optimal (data not shown). Traces A and B are nearly mirror images of each other, confirming the reversibility of the induced changes. Averaging trace A with the inverse of trace B yielded trace C, a high quality spectrum equivalent to the average of 140 reduced *minus* oxidised difference spectra. The final spectrum, trace E, was produced by removing contributions from protein layer expansion/contraction, phosphate buffer changes and redox changes of mediators from trace C. An equivalent reduced *minus* oxidised final spectrum at pH 8 is plotted as trace F. The major features of trace E, which is similar to trace F, are 1755(+), 1742(-), 1675(-), 1647(+), 1643(-), 1624(+), 1574(+), 1551(+), 1536(-), 1520(+), 1496(-), 1268(-), 1100(-) and 1090(+) cm^{-1}; where (+) and (-) denote peaks and troughs respectively. A number of overlapping features are also present in the 1470-1370 cm^{-1} region.

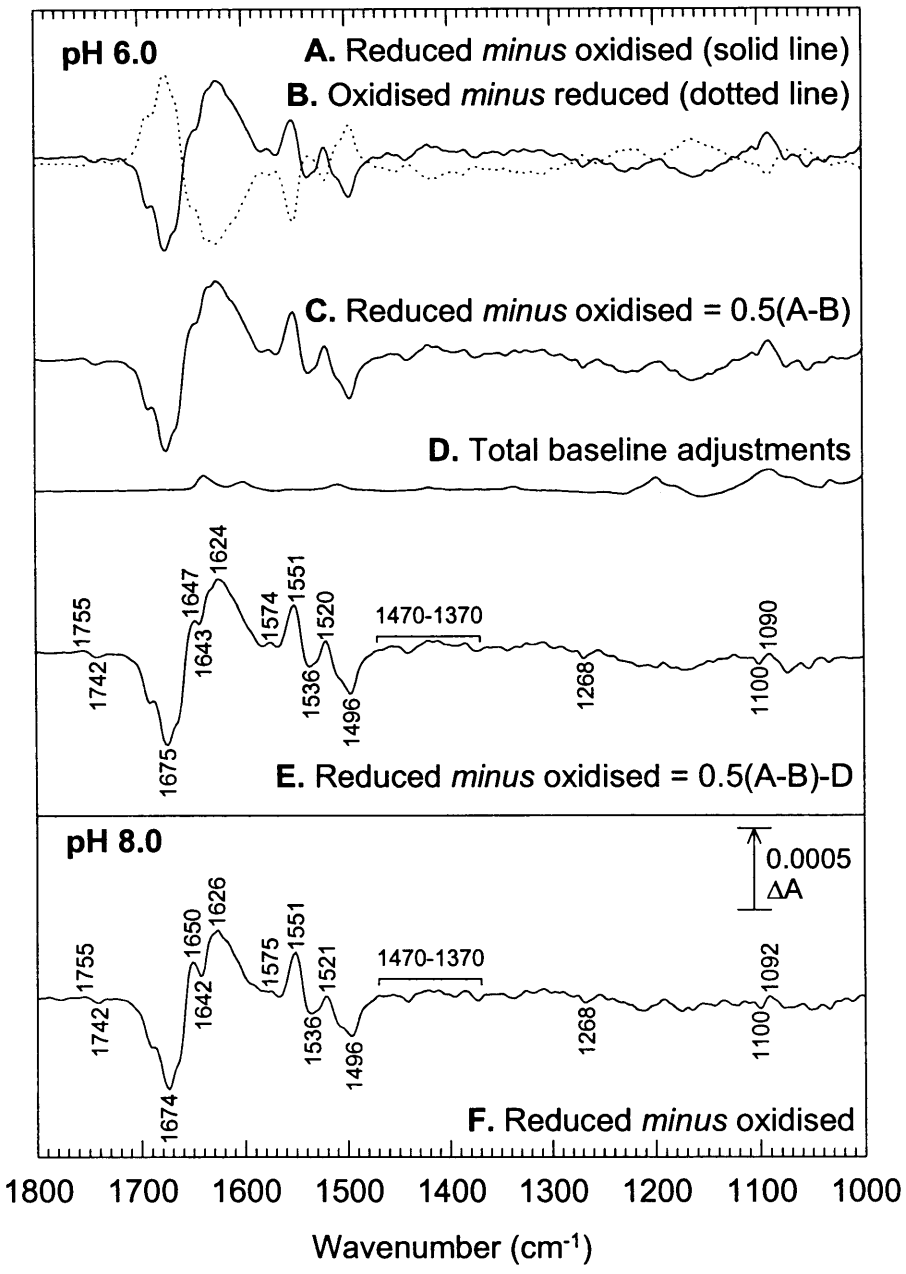

Figure 5.2 Reduced *minus* oxidised electrochemically-induced ATR FTIR difference spectra of all components of *Y. lipolytica* complex I at pH 6.0 and 8.0. Reduction and oxidation conditions were -425 and 425 mV respectively; for each condition 8 minutes was sufficient for redox equilibration. Redox mediation between working electrode and protein film was provided by a buffer of 20 mM potassium phosphate, 200 mM potassium chloride, 1 mM potassium ferricyanide, 100 μM methyl viologen at pH 6.0 or 8.0; see section 2.4.6. Traces A and B are averages of sample spectra from 70 reduction transitions and 70 oxidation transitions respectively at pH 6.0. Trace C, obtained by averaging trace A and the inverse of trace B, is equivalent to the average of 140 reduced *minus* oxidised spectra (trace C). The final spectrum, trace E, was obtained by subtracting contributions from buffer, mediators and protein film expansion/contraction (trace D) from trace C. An equivalent reduced *minus* oxidised spectrum at pH 8.0 is shown as trace F.

5.2.3 Effects of H-D exchange and ^{15}N labelling

Reduced *minus* oxidised difference spectra of all components of *Y. lipolytica* complex I, equivalent to those described in section 5.2.2, were recorded in D_2O media at pD 6.0 and 8.0 after H-D exchange (see section 2.4.4) and are shown in Figure 5.3A. Equivalent reduced *minus* oxidised spectra of globally ^{15}N labelled *Y. lipolytica* complex I at pH 6.0 and 8.0 are shown in Figure 5.3B. In both figures, for comparison purposes, the spectra are overlaid on the spectra of the wild-type complex in H_2O media from Figure 5.2 after normalisation so that the amide I amplitudes were roughly comparable. The differences between these spectra were used to strengthen assignments of bands to amide I/II peptide backbone changes, FMN, and bound ubiquinone, as well as suggesting contributions to spectra from several specific types of amino acids (see section 5.3).

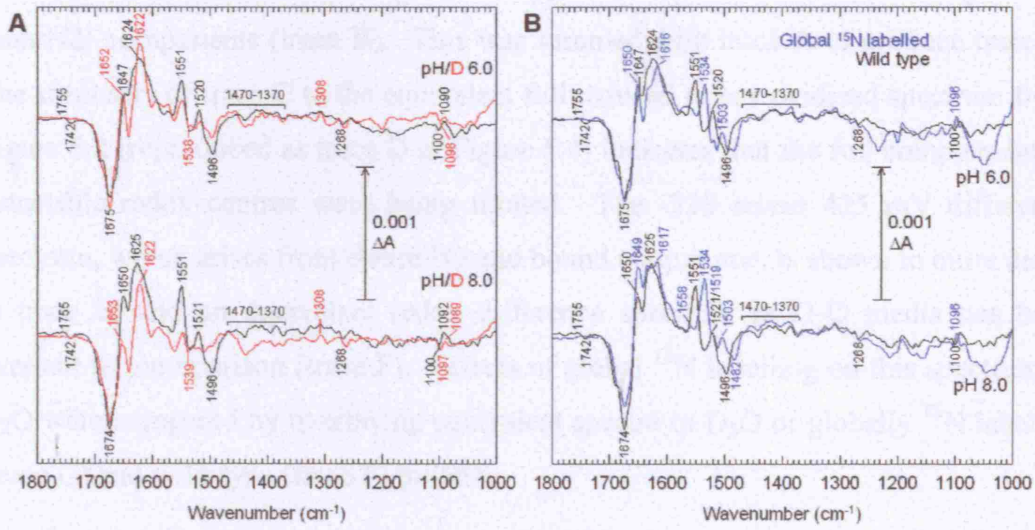

Figure 5.3 Effects of H-D exchange and global ^{15}N labelling on redox difference spectra of *Y. lipolytica* complex I at pH 6.0 and 8.0. A. Reduced *minus* oxidised spectra at pH 6.0 and 8.0 are reproduced from Figure 5.2 with equivalent spectra recorded in D_2O media, after completion of H-D exchange, overlaid in red. The pD 6.0 and 8.0 spectra (for H-D exchanged material) are equivalent to averages of 92 and 66 reduced *minus* oxidised spectra respectively. B. Reduced *minus* oxidised spectra at pH 6.0 and 8.0 are reproduced from Figure 5.2 with equivalent spectra for global ^{15}N labelled complex I overlaid in blue. The pH 6.0 and pH 8.0 spectra (for ^{15}N labelled material) are averages of 104 and 170 reduced *minus* oxidised spectra respectively. All spectra were recorded using reducing conditions of -425 mV and oxidising conditions of 425 mV; see legend of Figure 5.2 and Materials and Methods for details of baseline adjustments and composition of redox mediation buffer.

5.2.4 Resolution of centre N2

The midpoint potential of Fe-S centre N2 of *Y. lipolytica* complex I has been reported to be -140 mV at pH 7.0 (*99*) whereas the midpoint potentials of all other known prosthetic groups are thought to be below -240 mV (see section 1.3.2). Hence, reduced *minus* oxidised difference spectra of *Y. lipolytica* complex I were obtained using -220 mV and 425 mV as reducing and oxidising potentials, respectively (see Figure 5.4, trace A) in order selectively to reduce/oxidise centre N2. Stepwise reduction between -130 and -220 mV confirmed that the species undergoing reduction/oxidation had a midpoint potential close to the expected value and that the potential of -220 mV caused essentially complete reduction with no evidence of change of shape that would indicate that the lower potential Fe-S centres were starting to become reduced. A reduced *minus* oxidised difference spectrum between -425 and -220 mV was also recorded in the same sample in order to reduce the lower potential 'non-N2' components (trace B). This was summed with trace A to produce trace C. The similarity of trace C to the equivalent full reduced *minus* oxidised spectrum from Figure 5.2 (reproduced as trace D in Figure 5.4) indicates that the full complement of detectable redox centres were being titrated. The -220 *minus* 425 mV difference spectrum, which arises from centre N2 and bound ubiquinone, is shown in more detail in trace E, and an equivalent redox difference spectrum in D_2O media has been overlaid for comparison (trace F). Effects of global ^{15}N labelling on this spectrum in D_2O were compared by overlaying equivalent spectra in D_2O of globally ^{15}N labelled (trace G) and wild-type (trace F) proteins.

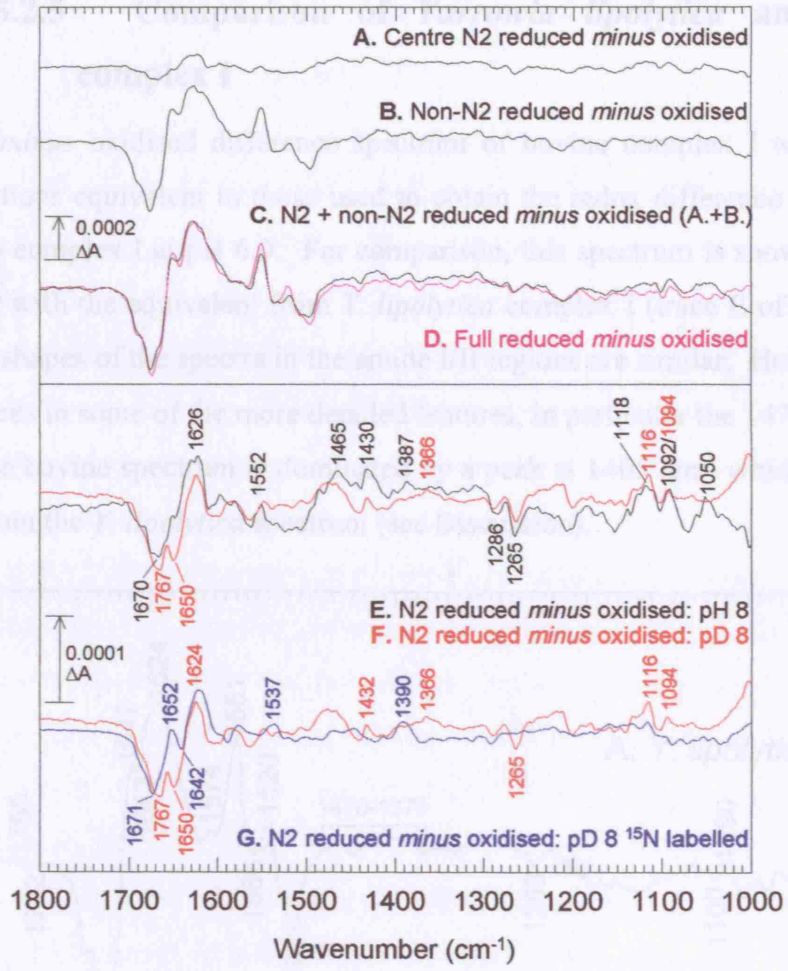

Figure 5.4 Redox difference spectra demonstrating the resolution of Fe-S centre N2 in *Y. lipolytica* complex I by selective redox poising at pH 8.0. Electrochemical conditions of -220 mV (reducing) and 425 mV (oxidising) were used selectively to reduce/oxidise Fe-S centre N2 (E_{m7} = -140 mV (*99*)). The resulting spectrum, equivalent to the average of 51 reduced *minus* oxidised spectra, is plotted as trace A (and reproduced as trace E). As a control, difference spectra were recorded for transitions between -425 mV and -220 mV i.e. reduction/oxidation of all components except N2 (trace B); the sum of traces A and B (trace C) is comparable to a full reduced *minus* oxidised spectrum at pH 8 (trace D, a reproduction of trace F of Figure 5.2). The effects of H-D exchange on the Fe-S centre N2 spectrum are illustrated by comparing trace E, a scaled reproduction of trace A, and trace F, an equivalent spectrum recorded after H-D exchange and in D_2O media. Trace F is equivalent to the average of 60 reduced *minus* oxidised difference spectra. Effects of global ^{15}N labelling combined with H-D exchange are illustrated by comparing trace F with trace G, a Fe-S centre N2 spectrum of ^{15}N labelled material recorded after H-D exchange and in D_2O media. Trace G is equivalent to the average of 147 reduced *minus* oxidised spectra. Redox mediation between working electrode and protein film was provided by a buffer of 20 mM potassium phosphate, 200 mM potassium chloride, 1 mM potassium ferricyanide, 100 µM methyl viologen, 100 µM anthraquinone-2,6-disulfonate at pH/D 6.0 or 8.0; see section 2.4.6.

5.2.5 Comparison of *Yarrowia lipolytica* and bovine complex I

A reduced *minus* oxidised difference spectrum of bovine complex I was recorded under conditions equivalent to those used to obtain the redox difference spectrum of *Y. lipolytica* complex I at pH 6.0. For comparison, this spectrum is shown in Figure 5.5 together with the equivalent from *Y. lipolytica* complex I (trace E of Figure 5.2). The overall shapes of the spectra in the amide I/II regions are similar. However, there are differences in some of the more detailed features, in particular the 1470-1370 cm^{-1} region of the bovine spectrum is dominated by a peak at 1405 cm^{-1} which appears to be absent from the *Y. lipolytica* spectrum (see Discussion).

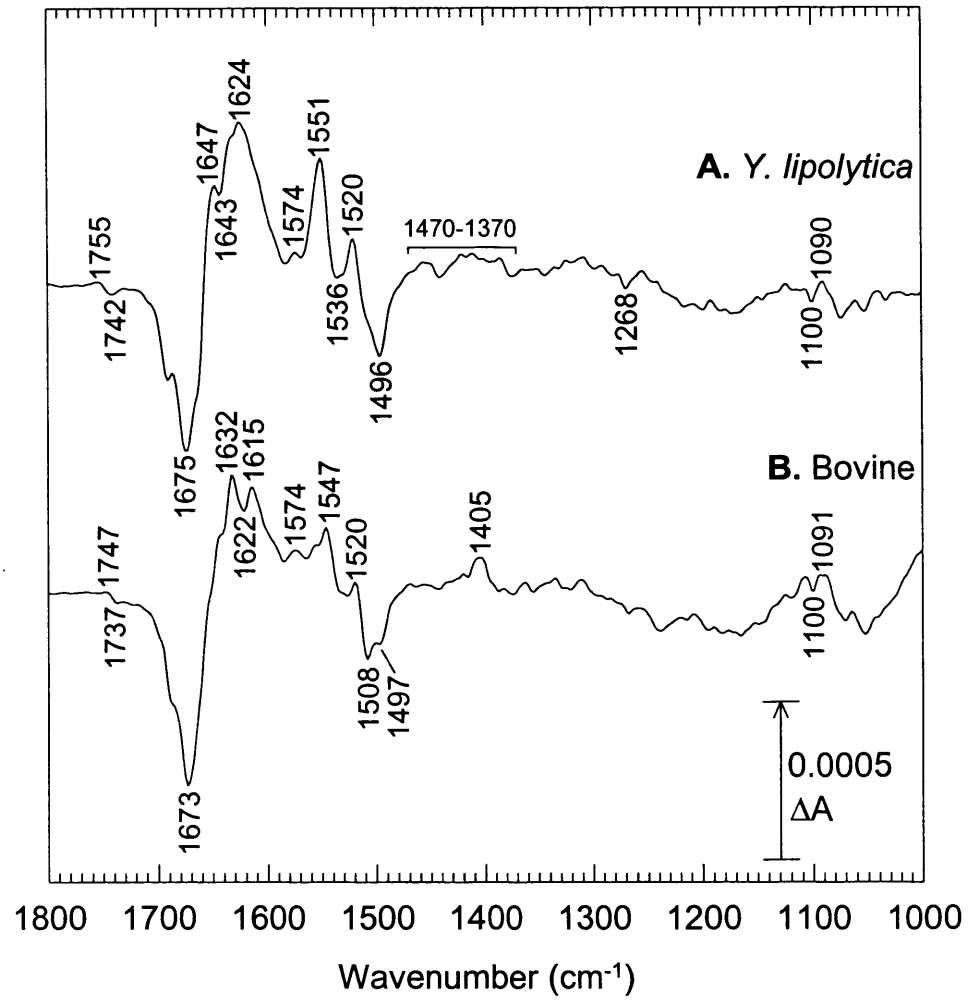

Figure 5.5 Comparison of electrochemically-induced reduced *minus* oxidised difference spectra of bovine and *Y. lipolytica* complex I at pH 6.0. The presented spectrum for bovine complex I is the average of 100 reduced *minus* oxidised difference spectra, each the average of 1000 interferograms; the *Y. lipolytica* difference spectrum is reproduced from Figure 5.2, trace E. Both spectra were acquired using the same experimental conditions (see legend of Figure 5.2 and Materials and Methods).

5.2.6 NADH/NAD^+ perfusion-induced difference spectra of bovine complex I

Spectra recorded to investigate reduction of bovine complex I by perfusion of its substrate, NADH, at pH 8.0 are shown in Figure 5.6. Trace A is a redox difference spectrum obtained by perfusion of sodium dithionite as reductant and NAD^+ as oxidant (see section 2.4.5 and figure legend). It is scaled to the overlaid equivalent electrochemically-induced full redox difference spectrum (trace B) using the amplitude of the average of the absolute absorbance spectra recorded at the beginning and end of each experiment, which were found to correlate with the amplitude of the redox difference spectra. Trace C is a redox difference spectrum obtained by perfusion of NADH as reductant and NAD^+ as oxidant and was generated by averaging data obtained from six separate protein layers (all from the same ATR-ready batch) with data scaled, from the relative amplitudes of the associated absolute absorbance spectra, to trace B (which is reproduced as trace D). Due to the poor stability of sodium dithionite it was not practical to acquire a spectrum of sufficiently high signal:noise to allow direct comparison between reduction by NADH and reduction by sodium dithionite. The poor stability of sodium dithionite also presented challenges in the removal of its contribution to trace A and artefactual signals arising from dithionite and its products are evident in the 1100-1000 cm^{-1} region (see section Figure 3.7).

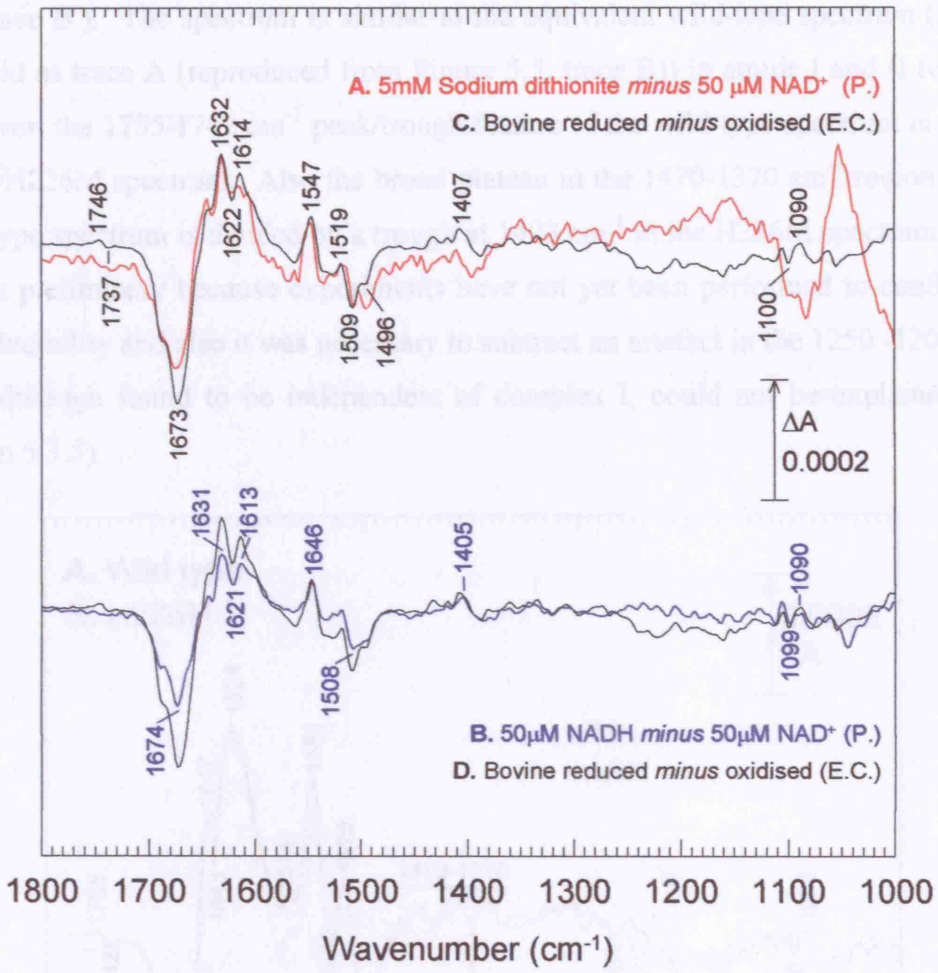

Figure 5.6 Perfusion-induced ATR FTIR redox difference spectra of bovine complex I at pH 8.0. Traces A and B are perfusion-induced reduced *minus* oxidised difference spectra using 5 mM Sodium dithioninte and 50 µM NADH as reductants respectively; for both spectra the oxidant was 50 µM NAD^+. Trace A is the average of three spectra each consisting of 2000 interferograms. Trace B is the average of data obtained from six separate layers and is equivalent to the average of 110 difference spectra each consisting of 1000 interferograms; data were scaled using the average amplitude of absolute absorbance spectra. Trace C (reproduced as D) is an electrochemically-induced redox difference spectrum recorded at pH 8.0 under otherwise equivalent conditions to trace B of Figure 5.5. Traces A and B have been scaled to trace C (and D) by the amplitudes of their associated absolute absorption spectra (see text). Buffer was 50 mM potassium phosphate, 150 mM potassium chloride at pH 8.0 and perfused at 1 ml per minute, 10 minutes were allowed for redox equilibration. See section 2.4.5.

5.2.7 Preliminary electrochemically-induced redox ATR FTIR difference spectrum of H226M *Y. lipolytica* complex I

An electrochemically-induced redox difference spectrum of *Y. lipolytica* complex I in which His-226 of the NUCM subunit (homologue of the bovine 49 kDa subunit) had been replaced by a methionine (see section 2.1.4) was recorded at pH 6.0 (see Figure

5.7, trace B.). The spectrum is similar to the equivalent wild-type spectrum (shown overlaid as trace A (reproduced from Figure 5.5, trace B)) in amide I and II regions. However, the 1755/1742 cm^{-1} peak/trough feature of the wild-type spectrum is absent in the H226M spectrum. Also the broad plateau in the 1470-1370 cm^{-1} region of the wild-type spectrum is divided by a trough at 1403 cm^{-1} in the H226M spectrum. This data is preliminary because experiments have not yet been performed to confirm its reproducibility and also it was necessary to subtract an artefact in the 1250 -1200 cm^{-1} that, although found to be independent of complex I, could not be explained (see section 5.3.5).

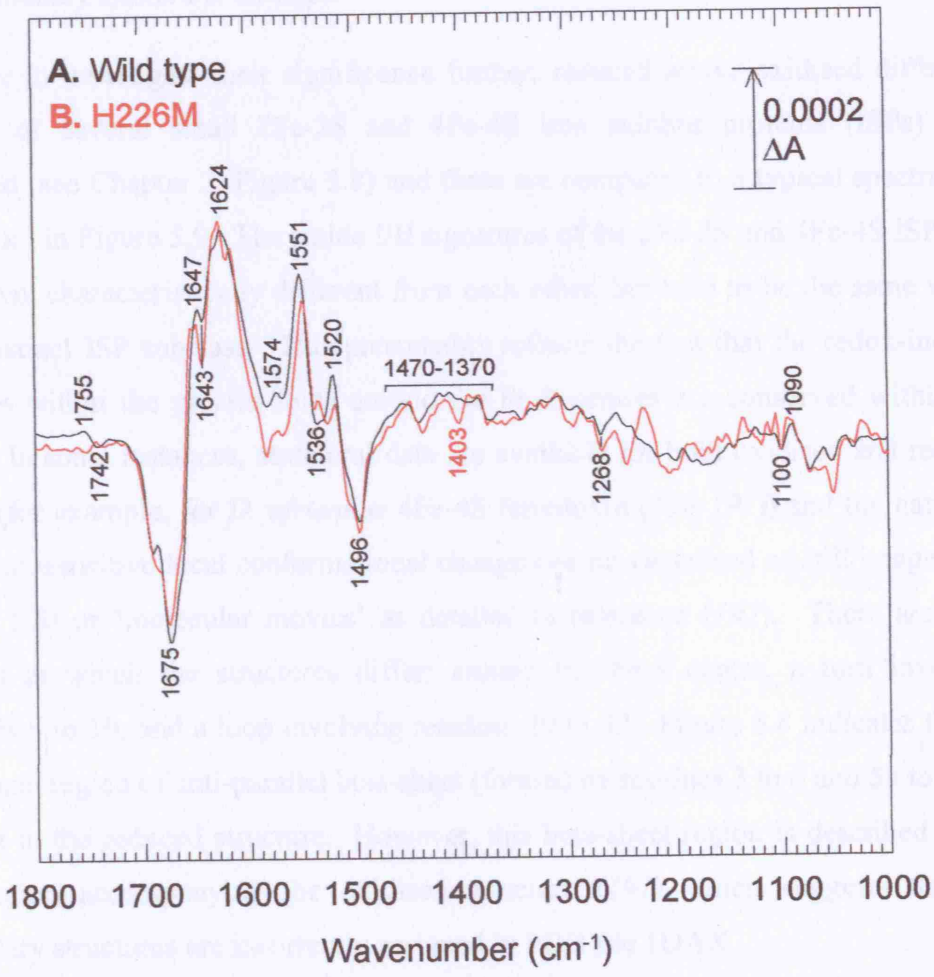

Figure 5.7 Electrochemically-induced ATR FTIR full redox difference spectrum of H226M *Y. lipolytica* complex I at pH 6.0. Trace A is wild-type spectrum reproduced from Figure 5.5 (trace B). Trace B was obtained using equivalent conditions except a reduction potential of -450 mV was used to decrease redox equilibration time, for which 8 minutes and 5 minutes were allowed for reduction and oxidation respectively. Trace B is the average of 20 spectra each of which consisted of 1000 interferograms (see legend of Figure 5.2 and Materials and Methods for redox mediation buffer).

5.3 Discussion and conclusions

5.3.1 Peptide backbone changes and protein stability

The reduced *minus* oxidised difference spectra of complex I are dominated by large changes in the 1700-1590 cm^{-1} and 1570-1490 cm^{-1} regions. These changes are very similar to those found with *E. coli* complex I (*84*) where they were assigned to amide I/II changes that might be associated with large conformational changes of functional significance in relation to protonmotive mechanism (*174*). The effects of H-D exchange and global ^{15}N substitution reported here confirm that they are indeed predominantly amide I/II changes.

In order to investigate their significance further, reduced *minus* oxidised difference spectra of several small 2Fe-2S and 4Fe-4S iron sulphur proteins (ISPs) were recorded (see Chapter 3, Figure 3.8) and these are compared to a typical spectrum of complex I in Figure 5.9. The amide I/II signatures of the 2Fe-2S and 4Fe-4S ISPs are, as shown, characteristically different from each other, but tend to be the same within each distinct ISP subclass. This presumably reflects the fact that the redox-induced changes within the protein folds around the Fe-S centres are conserved within ISP types. In some instances, structural data are available for both oxidised and reduced forms (for example, for *D. africanus* 4Fe-4S ferredoxin (*190;191*)) and the nature of the redox-sensitive local conformational change can be visualised as still images (see Figure 5.8) or 'molecular movies' as detailed in reference (*192*). There are three regions in which the structures differ: around the Fe-S centre, a turn involving residues 8 to 10, and a loop involving residues 29 to 32. Figure 5.8 indicates that an additional region of anti-parallel beta-sheet (formed by residues 3 to 6 and 59 to 62) is present in the reduced structure. However, this beta-sheet region is described in the publication accompanying the oxidised structure (*191*) which suggests that the secondary structures are incorrectly assigned in PDB file 1DAX.

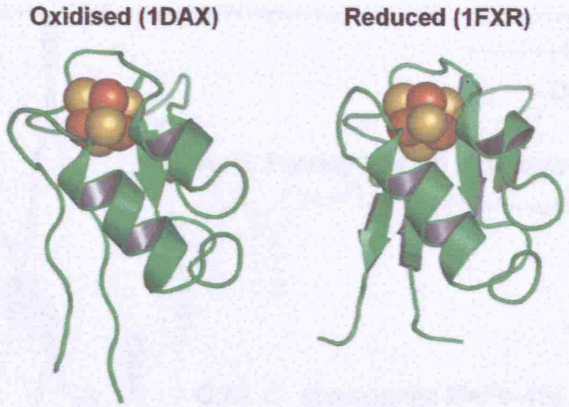

Figure 5.8 *D. africanus* 4Fe-4S ferredoxin structures in reduced and oxidised states. Reduced state was drawn using PDB file 1FXR, obtained by X ray crystallography; oxidised state was drawn using PDB file 1DAX, obtained by NMR. See text for comparison.

The overall shape of the amide I/II region of complex I is remarkably similar to the pattern seen in the small model ISPs both in H_2O and in D_2O, being most similar to that of the 4Fe-4S type, consistent with its complement of 6 4Fe-4S centres and two 2Fe-2S centres. In fact, the magnitudes of the amide I/II changes in the complex I film (which is estimated to contain around 0.25-0.5 mM complex I (see below), thus 1.5-3 mM 4Fe-4S and 0.5-1 mM 2Fe-2S prosthetic groups) were roughly equivalent to the magnitudes obtained from a 2 mM soluble protein. Hence, it is clear that the amide I/II changes in complex I arise primarily from redox-linked changes of local protein folds around the Fe-S centres that tend to be preserved in the ISP subclasses generally. A brief examination of the *T. thermophilus* structure (see section 1.3.5) supports this conclusion, although it is acknowledged that it would be appropriate to carry out a more thorough analysis of the structure in order to provide quantitative data. This conclusion contrasts with the interpretation of similar changes in the redox IR difference spectra of *E. coli* complex I (*174*) where it was suggested that they might indicate more global conformational effects related to the coupling mechanism. However, although the IR data do not support such changes, it should be noted that the IR data do not address whether large domain movements involving only a few residues in the hinge region, or conformational changes in short-lived intermediates, might instead occur.

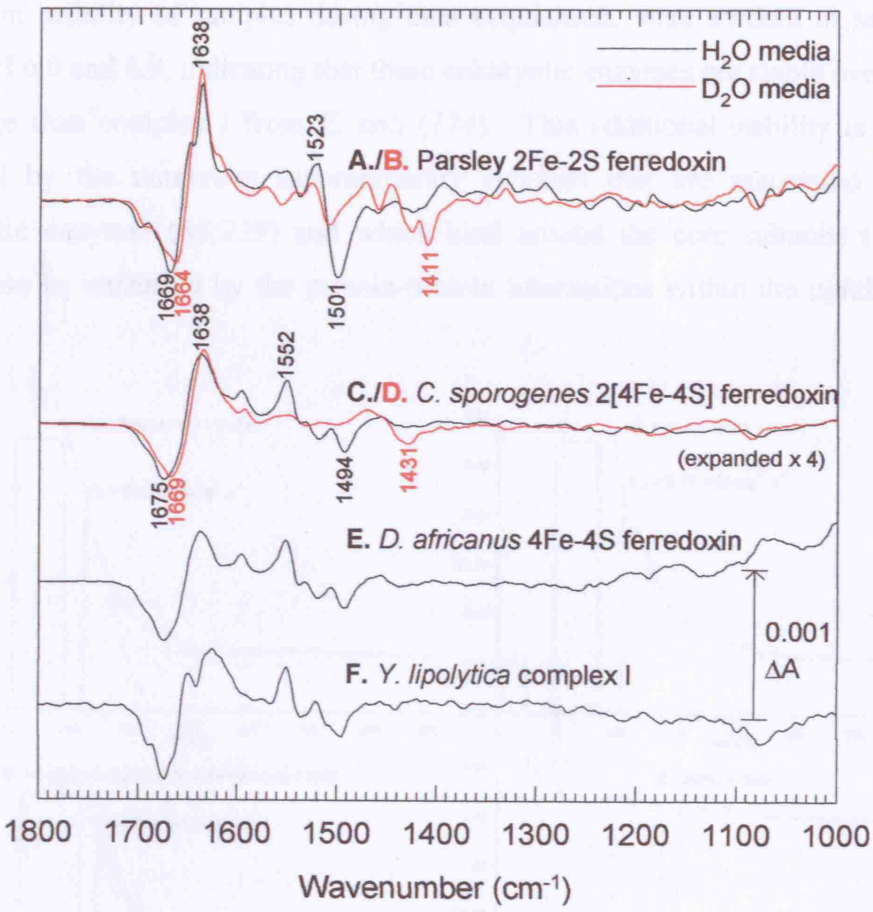

Figure 5.9 Comparison of electrochemically-induced redox difference spectra of ISPs and *Y. lipolytica* complex I at pH 8.0. Traces A-E are reproduced from Figure 3.8; trace F is reproduced from Figure 5.2. See legends of Figure 3.8 and Figure 5.2 for experimental conditions.

The complex I preparations used here require additional lipid in order to observe maximal NADH-*decyl*-ubiquinone oxidoreductase activity (*148*); most probably, lipid is required for rapid exchange of substrate ubiquinone with its binding site. However, the complexes are still likely to be in their native states and display rapid NADH-hexaammineruthenium oxidoreductase activities (*227*) even without lipid supplementation and this activity remained in samples that had undergone a drying/rehydration cycle (see Figure 5.10). Furthermore, the redox centres in the protein film could be reduced by NADH (see Figure 5.6 and below). Hence, it may be concluded that the complex I samples are in a native state, although it would be of interest in future to extend the studies to preparations in which their NADH-*decyl*-ubiquinone oxidoreductase activities have been reactivated (*184;228*). No large differences in redox difference spectra, apart from some variation in the magnitude of a presumed carboxylic acid change around 1740 cm^{-1} (see below), nor differences in

long term stability of samples during data acquisition, were evident in samples at either pH 6.0 and 8.0, indicating that these eukaryotic enzymes are stable over a larger pH range than complex I from *E. coli* (*174*). This additional stability is probably provided by the numerous supernumerary subunits that are associated with the eukaryotic enzymes (*88;229*) and which bind around the core subunits (*109*) and might also be enhanced by the protein-protein interactions within the tightly packed layer.

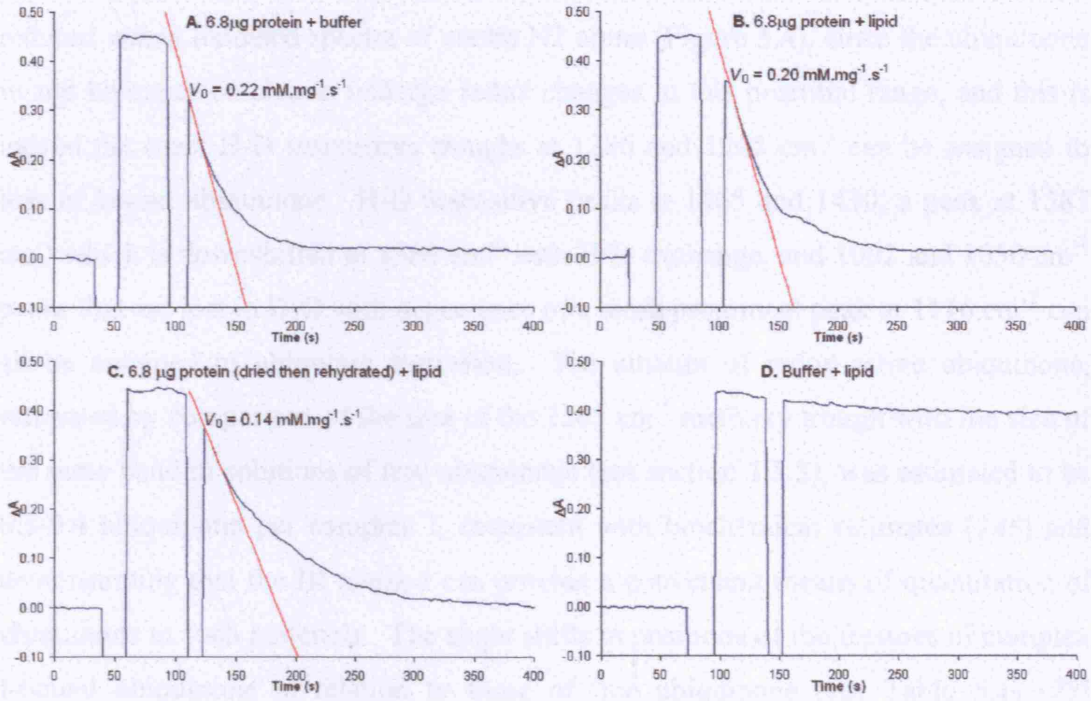

Figure 5.10 Initial NADH oxidation rates of *Y. lipolytica* complex I. Trace A is oxidation of NADH by 6.8 µg complex I in buffer. Trace B is equivalent for protein treated with lipid as described in materials and methods section 2.1.5. Trace C is equivalent to trace B except that the protein was dried to the round bottomed glass flask then resuspended prior to the assay. Trace D is a control spectrum and shows negligible NADH oxidation by lipid and buffer (see section 2.1.5 for experimental conditions).

5.3.2 Changes associated with ubiquinone

Fe-S modes are not expected to contribute at frequencies above 800 cm^{-1} and, therefore, all changes should arise from protein, FMN, ubiquinone and, possibly, as-yet unrecognised redox groups. The redox IR spectra of model ubiquinone (*75;205-209*) have been described in detail in both H_2O and D_2O media as shown in Chapter 3, Figure 3.10. Biochemical analyses of the complex I preparations have shown that substoichiometric ubiquinone typically remains bound to the *Y. lipolytica* complex I preparations (*148*). Particularly useful IR markers for ubiquinone are H-D insensitive

troughs at 1288 and 1262 cm^{-1} that involve the methoxy groups and a sharp C=C band at 1610 cm^{-1} (*205-209*) and, for ubiquinol, four bands between 1492 and 1387 cm^{-1} and five between 1112 and 963 cm^{-1} that show a characteristic pattern of H-D sensitivity (*75*). Some indications of the strongest of the methoxy-related bands of ubiquinone are evident in the full redox spectra of wild-type *Y. lipolytica* complex I as a 1268 cm^{-1} trough (see Figure 5.2). This signal is also present in the preliminary full redox difference spectrum of H226M *Y. lipolytica* complex I presented in Figure 5.7. Ubiquinone-related bands of *Y. lipolytica* should become much more evident in the reduced *minus* oxidised spectra of centre N2 alone (Figure 5.4), since the ubiquinone would be expected also to undergo redox changes in this potential range, and this is indeed the case: H-D insensitive troughs at 1286 and 1265 cm^{-1} can be assigned to loss of bound ubiquinone. H-D insensitive peaks at 1465 and 1430, a peak at 1387 cm^{-1} which is downshifted to 1366 cm^{-1} with H-D exchange, and 1092 and 1050 cm^{-1} peaks that are lost in D_2O with appearance of a more prominent peak at 1116 cm^{-1} can all be assigned to ubiquinol formation. The amount of redox-active ubiquinone, estimated by comparison of the size of the 1265 cm^{-1} methoxy trough with the size of the same band in solutions of free ubiquinone (see section 3.5.3), was estimated to be 0.2-0.4 ubiquinone per complex I, consistent with biochemical estimates (*148*) and demonstrating that the IR method can provide a convenient means of quantitation of ubiquinone in such materials. The slight shifts in positions of the features of complex I-bound ubiquinone in relation to those of free ubiquinone (see Table 5.1) (*75*) indicate that it is bound in a specific site rather than being non-specifically associated (*230*). Its substoichiometry strongly suggests that it is the substrate Q-site that is partially occupied rather than indicating a very tightly-bound form, the possibility of which is ruled out by these data. The level of occupancy by ubiquinone appears to be somewhat variable in different preparations. For example, the redox difference spectrum of the bovine complex I sample (Figure 5.5) shows a much weaker ubiquinone signature, indicating a lower retained ubiquinone content in this preparation. In addition, the signature ubiquinone redox bands are virtually absent from the ^{15}N labelled *Y. lipolytica* complex I sample due to a particularly low retained level of ubiquinone in this sample. Such variable levels of ubiquinone in substrate Q-sites (and of retained lipid) are not uncommon in purified preparations of many membrane-derived Q-reactive redox enzymes.

Assignment	Unbound model UQ-50	UQ bound in *Y.l* complex I
Ubiquinol	1469 cm^{-1}	1465 cm^{-1}
Ubiquinol	1430 cm^{-1}	1430 cm^{-1}
Ubiquinol	1387 cm^{-1}	1387 cm^{-1}
Ubiquinol (D)	1367 cm^{-1}	1366 cm^{-1}
Ubiquinone	1288 cm^{-1}	1286 cm^{-1}
Ubiquinone	1262 cm^{-1}	1265 cm^{-1}
Ubiquinol	1112 cm^{-1}	1118 cm^{-1}

Table 5.1 Comparison of ubiquinone/ol signals from model compound spectrum with from the centre N2 redox difference spectrum. Positions of signals arising from formation of ubiquinol and loss of ubiquinone in electrochemically-induced reduced *minus* oxidised difference spectra of model compound ubiquinone-50 are taken Figure 3.10 and compared with those from the *Y. lipolytica* complex I (centre N2 spectra) (see Figure 5.4, trace E/F). (D) indicates the signal was present in the spectra recorded in D_2O media.

5.3.3 Changes associated with FMN

The redox IR spectra of FMN (*84;204*) have been described in detail in both H_2O and D_2O media. Some further details of FMN redox IR spectra at pH/pD 6.0 and 8.0 are shown in Figure 3.9 and are consistent with published spectra where some assignments of principal bands have been made (*84*). The most prominent features are a large trough at ~ 1547 cm^{-1} (assigned to a ν(C=C) mode of FMN (*84*)) and H-D exchange-sensitive peaks at ~ 1517 (assigned to hydrogen in-plane bending) and ~ 1406 cm^{-1} (assigned in part to N5-H in-plane bending (*204*)). The 1406 cm^{-1} band is increased in intensity relative to other bands at pH 8.0, indicating that it is most prominent in the anionic $FMNH^-$ form (pKa of $FMNH_2/FMNH^-$ = 6.7 in aqueous media (*165*) and 7.1 in bovine complex 1 (*95*)). *Y. lipolytica* complex I spectra in H_2O media (Figure 5.2) exhibit several overlapping bands in the 1470-1370 cm^{-1} region that arise in large part from ubiquinol (see above). The model FMN data (see Figure 3.9) predict peaks at 1406 cm^{-1} for reduced protein-bound FMN with intensities in the range of $0.5\text{-}1\times10^{-4}$ and $1\text{-}2\times10^{-4}$ ΔA at pH 6.0 and 8.0, respectively, and this will sit between the 1430 and 1387 cm^{-1} peaks of ubiquinol (*75*), giving rise to the rather flat, broad overlapping peaks in this region in the spectra of Figure 5.2 and Figure 5.3. In contrast, a distinct 1405 cm^{-1} peak of reduced FMN is evident in the bovine spectrum (Figure 5.5) of roughly the expected intensity, presumably in its $FMNH_2$ form at pH 6.0 since its pK is 7.1 (*95*). In preliminary data obtained from

H226M *Y. lipolytica* the 1470-1370 cm^{-1} region includes a distinct trough at 1403 cm^{-1}. Excluding the improbable imidazole to imidazolate histidine transition (for which other indicators, for example a peak at 1451 cm^{-1} are absent) (see Figure 3.13, trace C) a histidine contribution is not expected to contribute directly in this region. It would therefore seem more likely that this feature arises from the absence of the 1405 cm^{-1} peak of reduced flavin signal. The preliminary data obtained from the H226M mutant is discussed further in section 5.3.5.

The largest band of free FMN, the ν(C=C) 1547 cm^{-1} trough, whose ΔA from the model spectra is expected to be $2\text{-}3\times10^{-4}$, is obscured by the very large amide II changes of the Fe-S centres. After H-D exchange, which shifts the majority of the amide II changes away from this region, the full reduced *minus* oxidised *Y. lipolytica* spectra do have a small trough at 1538 cm^{-1} (see Figure 5.3A) that likely arises from this H-D exchange-insensitive ν(C=C) mode of the bound FMN. Hellwig et al (*84*) have previously assigned a band at 1548 cm^{-1} in redox difference spectra of the NADH dehydrogenase fragment of *E. coli* complex I primarily to FMN. Comparison with the redox spectra of model ISPs (Figure 5.9), however, strongly suggests that this arises predominately from the flanking amide II changes of polypeptide around the Fe-S centres. In this same work, an indistinct shoulder at 1710 cm^{-1} was also suggested to arise at least in part from an equivalent of the 1713 cm^{-1} carbonyl band of free FMN, although it was noted that a lack of H-D sensitivity made this assignment questionable, and a band close to 1400 cm^{-1} was assigned to an amino acid carboxylate group rather than to reduced FMN (*84*). In the spectra reported here, there is no clear 1710 cm^{-1} band that could reasonably be attributed to this FMN carbonyl group, which in any case is expected to be of low intensity and likely to be obscured by the strong amide I changes associated with redox changes of the Fe-S centres. Hence, in summary, the 1406 cm^{-1} band of reduced FMN seems to be the best IR marker band, at least for eukaryotic complex I, even though in full redox difference spectra it can be obscured by overlapping ubiquinol bands.

5.3.4 IR characteristics associated with reduction/oxidation of centre N2

The ability selectively to reduce centre N2 and bound ubiquinone at the reducing potential used here of -220 mV is consistent with their higher midpoint potentials

relative to the other Fe-S and FMN cofactors. The centre N2 redox IR spectra are dominated by amide I/II changes, and these again closely resemble those seen in small soluble 4Fe-4S proteins (see Figure 5.4 and Figure 5.9), indicating that centre N2 retains characteristics of the 4Fe-4S class despite its unusual ligation by consecutive cysteine residues (*90*). Furthermore, because only a single Fe-S is reduced, the bands arising from the substoichiometric bound ubiquinone and ubiquinol that are more weakly evident in the full redox spectra are now much more prominent, as discussed above.

Of particular interest in relation to the possible coupling mechanism is the nature of the protonation site that is redox-linked to centre N2 (*143*). In previous work on *E. coli* complex I, it was reported that reduction of centre N2 at pH 6.0 was associated with deprotonation of a carboxylic amino acid (*84*) together with protonation of two tyrosine groups (*173*). These tyrosines were suggested by site-directed mutagenesis to be Tyr-114 and Tyr-139 on the NuoB (PSST) subunit. Their equivalents on the *T. thermophilus* Nqo6 subunit are Trp-96, which is located ~ 19 Å from N2, and Tyr-121, which is located ~ 15 Å from N2, respectively (Figure 5.11). Clearly, such unusual protonation chemistry or such long distances might be expected to play a major role in the proton/electron coupling mechanism of complex I. However, the 1755/1742 cm^{-1} carboxylic acid feature seen in the full redox spectra of eukaryotic complex I (see Figure 5.2 and Figure 5.5) appears to be associated only with the lower potential 'non-N2' components in experiments such as those in Figure 5.4, and the redox spectra of centre N2 show no clear evidence for equivalent redox-linked protonation changes of either tyrosines or carboxylic acids in the eukaryotic protein. This is particularly clear in centre N2 redox spectra in D_2O and after ^{15}N labelling (traces F and G, Figure 5.4); although there is a peak at 1552 cm^{-1} that could conceivably arise from carboxylate formation on reduction, its sensitivity to H-D exchange and to ^{15}N labelling rules this out and strongly suggests that it is instead an amide II feature. Similarly, there are no ^{15}N-insensitive bands in the 1500 cm^{-1} region that would indicate tyrosine changes. As a result, it is concluded that protonation changes of carboxylic acids or tyrosine are not linked to centre N2 redox changes in eukaryotic complex I. Nevertheless, equivalents of Tyr-114 and Tyr-139 are conserved in both the *Y. lipolytica* and bovine (Tyr-114 is replaced by Trp-96 in *T. thermophilus*) PSST subunits so some consideration of the possible origin of the very

different behaviours is desirable. In the case of *E. coli* centre N2, its midpoint potential is reported to be -210 mV at pH 7.0, a value very close to the isopotential group of N1b, N3, N4 and N5 (E_{m7} -280 to -240 mV). As a result, the data on centre N2 in (*84*) could not be obtained by selective reduction and instead it was necessary to subtract the IR redox difference spectrum of the soluble dehydrogenase fragment (consisting of NuoE, NuoF and NuoG, see section 1.3.4) from the IR redox spectrum of the intact complex. This fragment was thought to contain all Fe-S centres except centre N2 and therefore signals in the double difference spectra were thought likely to arise from changes associated with reduction/oxidation of centre N2. However, it is now known that this fragment also lacks Fe-S centres N6a and N6b (*92;160*) and there is a possibility that signals in the double difference spectrum could also be associated with redox changes of a novel chromophore of unknown chemical structure (*160;173*). Also, it is not possible to confirm that the conformation of the protein in the dehydrogenase fragment, particularly in the region of interface between the dehydrogenase and connecting fragments, is identical to its conformation in the whole complex. In contrast, centre N2 in *Y. lipolytica* complex I, like the bovine enzyme (*96*), has a midpoint potential (E_{m7} = -140 mV (*99*)) that is high enough above the other Fe-S centres (E_{m7} -250 mV or below (*96*)) that it could be resolved directly in the intact complex by selective reduction without a need to compare different protein preparations. Given the very different redox midpoint potentials of the *E. coli* and eukaryotic centres N2, it is conceivable that their redox-linked chemistry is also very different. However, it is also feasible that the *E. coli* complex I fragment that has lost centre N2 has major alterations to other parts of the protein structure that behave differently in the fragment compared to the intact enzyme and this could give rise to the additional signals that appear to be associated with centre N2 in the *E. coli* complex I.

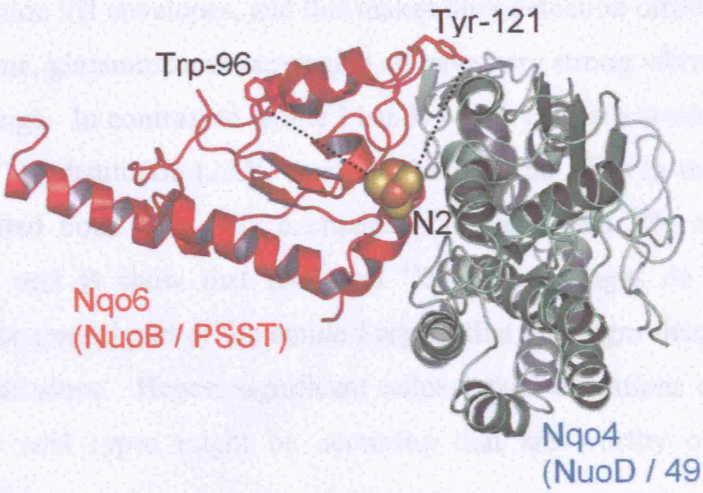

Figure 5.11 Detail of N2 environment in *T. thermophilus*. Nqo6 and Nqo4 are shown in red and pale blue respectively. The sidechains of Trp-96 and Tyr-121 of Nqo6 are located 19 and 15 Å away from N2 (edge-to-edge) respectively. Orientation is such that the peripheral domain would extend out of the page and the membrane domain would extend to the left.

Hence, the nature of the redox-linked protonation site of centre N2 remains unclear, though the present work argues strongly against the involvement of a network of tyrosines/carboxylic acid changes (*84;173*). The H-D exchange and ^{15}N substitution effects on the amide I envelope raise the possibility that a lysine or arginine could provide the site. In addition, the signals in the 1100 cm^{-1} region in Figure 5.4 may not be fully accounted for by the hydroxyl-related bands of ubiquinol in this region (for example, a positive band at 1116 cm^{-1} is present in the ^{15}N substituted sample of trace G, Figure 5.4 even although the ubiquinone content is very low), and this raises the alternative possibility that the redox reaction of centre N2 might be associated with histidine protonation changes. This would be consistent with other data that have implicated His-226 as the redox-linked protonation group (*101*). Such possibilities are discussed further in section 5.3.5; including discussion of the preliminary full redox difference spectrum of *Y. lipolytica* H226M complex I (see section 2.1.4).

5.3.5 Amino acid sidechain

Besides the protonation site that is redox-linked to centre N2, additional band changes arising from environmental, redox or protonation state changes of specific types of amino acid residues are expected to contribute to the full redox difference spectra. Some possible assignments may be suggested by comparisons with IR databases of amino acid vibrational spectra ((*77;80;214;231;232*) and references therein) - see Chapter 1. The principal bands of several amino acids tend to occur at frequencies

within the amide I/II envelopes, and this makes their detection difficult. For example, lysine, arginine, glutamine and asparagine all have very strong vibrations in the 1690-1620 cm^{-1} range. In contrast to amide I bands which are very weakly downshifted in D_2O or by ^{15}N substitution (*233*), bands of these amino acids in this region are very strongly shifted both with H-D exchange (*214*) and with ^{15}N substitution (*234*). Figure 5.3A and B show that H-D and $^{14}N/^{15}N$ exchanges do cause significant changes in the central part of the amide I region that are larger than might arise from amide I bands alone. Hence, significant redox-linked alterations of one or more of these amino acid types might be occurring that are worthy of further specific investigations.

Easier to assign are bands of amino acids that occur in less congested regions of the spectra. One such signal that is consistently evident in the full reduced *minus* oxidised spectra (Figure 5.2, Figure 5.3 and Figure 5.5) is a peak/trough close to 1090/1100 cm^{-1}. Protein bands in this region result from changes in environment or protonation state of histidine (*211;213;215*). The trough is only slightly downshifted in D_2O but changes dramatically with ^{15}N labelling to give predominantly a 1096 cm^{-1} peak. This behaviour is consistent with the protonation to the imidazolium form of a neutral histidine that is protonated in the Nπ position (see section 3.5.4) (*211;213*). His-226 (*Y. lipolytica* numbering) has been shown to be the redox Bohr group of centre N2 (*101*). Analysis of the *T. thermophilus* structure shows it is located with 4 Å of N2 orientated such that Nτ is proximal to the cluster and Nπ facing away from the cluster (see Figure 5.12). In addition the next closest conserved histidine residue, His-63, is approximately 14 Å from N2. This makes His-226 a good candidate for the source of the signals discussed above (i.e. that may arise from a protonation of a Nπ nitrogen of a histidine residue upon reduction of N2). In order to investigate this possibility preliminary data were acquired for the reduction/oxidation of all components of H226M *Y. lipolytica* complex I (see section 2.1.4 and 5.2.7 and Figure 5.7). The presented full redox difference spectrum is broadly comparable to the wild-type spectrum (overlaid). The trough/peak feature at 1100/1090 cm^{-1} appears to present in both spectra and therefore the data do not support the assignment of that feature to protonation state change of His-226. As detailed in section 5.2.7 the presented data is preliminary and further analysis of the mutant is required, including

resolution of signals associated with redox changes of Fe-S centre N2, in order to make a definitive statement.

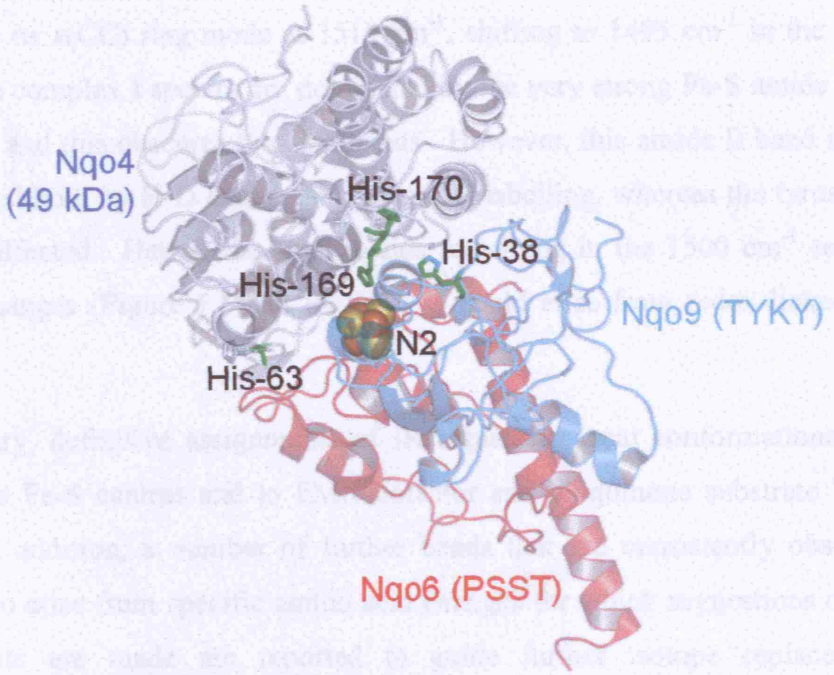

Figure 5.12 Histidine residues located within 15 Å of Fe-S centre N2 in *T. thermophilus* structure. His-169 and His-63 (*T. thermophilus* numbering, equivalent to His-226 and His-253, respectively, in *Y. lipolytica*) are well conserved while His-38 and His-170 are poorly conserved.

A second signal that is consistently evident is a trough/peak at 1742/1755 cm^{-1} (1737/1747 cm^{-1} in bovine). These frequencies are characteristic of a protonated aspartic or glutamic acid residue whose environment is perturbed by one or more redox centres (*214*). However, although consistently present, its size relative to other bands has proved to be variable within a factor of 2-3, with its size in Figure 5.2 data being at the higher end of the range. In addition, although H-D exchange causes its loss, possibly due to the expected downshift where it might become obscured by the amide I envelope edge, it also appears to be lost in the ^{15}N substituted samples, a substitution that should not affect carboxylic acid vibrations. Furthermore these bands appear to absent from the preliminary H226M *Y. lipolytica* redox difference spectrum (see Figure 5.7). Hence, further investigations are required to determine whether this band arises from a carboxylic acid, from the ester bond of a bound lipid (*223*) or from an as-yet unknown functional moiety.

A significant body of data is available on tyrosine, tyrosinate and the related *p*-cresol in H_2O and D_2O (*214*), and on specific isotope effects both for model compounds (*235;236*) and tyrosine in proteins (*173;236;237*). The most prominent band of tyrosine is its ν(CC) ring mode at 1515 cm^{-1}, shifting to 1495 cm^{-1} in the tyrosinate form. The complex I spectra are dominated by the very strong Fe-S amide II peak at 1520 cm^{-1} and this obscures tyrosine bands. However, this amide II band is strongly downshifted both by H-D exchange and by ^{15}N labelling, whereas the tyrosine bands are little affected. Hence, the small bands remaining in the 1500 cm^{-1} region after these exchanges (Figure 5.3 and Figure 5.4) could arise from redox-linked tyrosine changes.

In summary, definitive assignments of IR signals to local conformational changes around the Fe-S centres and to FMN cofactor and ubiquinone substrate have been made. In addition, a number of further bands that are consistently observed that should also arise from specific amino acid changes for which suggestions of possible assignments are made are reported to guide further isotope replacement and mutagenesis investigations.

Chapter 6: Conclusions and Prospects

This thesis describes the use of a novel in-house constructed electrochemical cell that functions to induce precise and reproducible changes in samples allowing simultaneous acquisition of ATR FTIR spectra with the option of recording UV/visible spectra concurrently. This system can be fully-automated and applied to hydrophilic proteins in solution or hydrophobic proteins as rehydrated films adhered to the IRE. Provided an appropriate electrochemical mediator compound is available, proteins can be poised at any potential and, by using an appropriate combination of mediators, almost any redox transition can be performed. This methodology has developed to the point where information at the atomic level is now available from large complicated proteins.

In this study the electrochemical technique and associated protocols were applied to rehydrated films of cytochrome bc_1 complex and complex I of the respiratory chain. In early experiments, redox difference spectra arising from reduction/oxidation of all components, and from reduction/oxidation of haem b_H and haem b_L individually, of bovine cytochrome bc_1 complex were measured and shown to be comparable to previously published equivalent spectra obtained using the well established perfusion method (*74*) thus confirming the validity of the electrochemical method. The method was then applied to cytochrome bc_1 complex from *Rba. capsulatus* to investigate the

protonation state changes redox-linked to haem b_L. Signals characteristic of a perturbation of a protonated aspartic acid(s) and/or glutamic acid(s), or possibly the redistribution of protons between several carboxylic residues were identified and tentatively assigned to Glu-295 (*Rba. capsulatus* numbering) of the highly conserved PEWY motif (on cytochrome *b*). However, acquisition and analysis of the redox difference spectrum of haem b_L of an E295V mutant of the complex ruled this residue out. For the origin of this signal to be established, further site directed mutagenesis is required and, based on its proximity to haem b_L and orientation, the well conserved Asp-278 is suggested as the next residue for scrutiny. These experiments also identified a signal that may arise from a protonation state change/perturbation (of protonated form) of a haem propionate(s) and signals that may arise from perturbation of a histidine residue(s) which require further investigation.

The electrochemical technique was also applied to rehydrated layers of complex I from *Y. lipolytica* and *B. taurus*. In order to assist in interpreting the *Y. lipolytica* data equivalent spectra were recorded in D_2O media and of globally ^{15}N labelled material; in addition, signals arising from Fe-S centre N2 were resolved by redox poising. Signals assigned to protein backbone changes are shown to arise from changes local to the Fe-S centres and not, as has previously been suggested (*174*), from large scale conformational changes of functional significance in relation to protonmotive mechanism. A signal characteristic of the reduced form of FMN was present in the bovine full redox difference spectrum. The absence of this signal in the equivalent *Y. lipolytica* spectrum was attributed to the presence of flanking signals assigned to ubiquinol; as is consistent with the differing quinone content of the two preparations. Analysis of the bound ubiquinone and ubiquinol signals present in the centre N2 difference spectrum allowed the ubiquinone content to be estimated at 0.2 - 0.4 Q per complex I, a value that is in good agreement with biochemical estimates (*148*). The Fe-S centre N2 redox difference spectra also contained signals that may arise from the centre N2 redox-linked protonation group. The presented data rules out the previously suggested involvement of a carboxylic amino acid (*84*) and tyrosine groups (*173*) and instead supports the possible involvement of a lysine, arginine or histidine residue. Future directions for the analysis of complex I include the definitive identification of the Fe-S centre N2 redox-linked protonation group. Until a complete

high resolution structure is available candidate residues for site directed mutagenesis will continue to be selected partially through homology modelling (*102*).

Also presented is a body of model compound data that was recorded to assist in the acquisition and interpretation of the spectra of the respiratory complexes. The acquisition of model compound data is vital for the analysis of the complex difference spectra of proteins, yet is also highly time consuming. However, the amount of model compound data in the literature is slowly increasing all the time. In addition, very recent developments in computational techniques, such as DFT calculations, have begun to make progress in the modelling of model compound IR absorbance characteristics *in silico*. Once these techniques are perfected the process of interpreting protein IR difference spectra will be greatly enhanced both in speed and the amount of information available. Therefore, further work should not only include new experiments but also re-analysis of existing data, such as that presented in this thesis.

References

1. Mitchell, P. (1961) Coupling of phosphorylation to electron and proton transfer by a chemi-osmotic type of mechanism, *Nature 191*, 144-148.

2. Stryer, L. (1995) *Biochemistry* W. H. Freeman & Co, New York.

3. Schägger, H. (2001) Respiratory chain supercomplexes, *IUBMB Life 52*, 119-128.

4. Nicholls, D. G. (1982) *Bioenergetics: An Introduction to the Chemiosmotic Theory* Academic Press, London.

5. Rich, P. R. (2003) The molecular machinery of Keilin's respiratory chain, *Biochem. Soc. Trans. 31*, 1095-1105.

6. Grigorieff, N. (1998) Three-dimensional structure of bovine NADH:ubiquinone oxidoreductase (complex I) at 22 Å in ice, *J. Mol. Biol. 277*, 1033-1046.

7. Hägerhäll, C. and Hederstedt, L. (1996) A structural model for the membrane-integral domain of succinate:quinone oxidoreductases, *FEBS Lett. 389*, 25-31.

8. Sun, F., Huo, X., Zhai, Y., Wang, A., Xu, J., Su, D., Bartlam, M., and Rao, Z. (2005) Crystal structure of mitochondrial respiratory membrane protein complex II, *Cell 121*, 1043-1057.

9. Hagerhall, C. (1997) Succinate: quinone oxidoreductases Variations on a conserved theme, *Biochim. Biophys. Acta 1320*, 107-141.

10. Yankovskaya, V., Horsefield, R., Törnroth, S., Luna-Chavez, C., Myoshi, H., Léger, C., Byrne, B., Ceccini, G., and Iwata, S. (2003) Architecture of succinate dehydrogenase and reactive oxygen species generation, *Science 299*, 700-704.

11. Page, C. C., Moser, C. C., Chen, X., and Dutton, P. L. (1999) Natural engineering principles of electron tunnelling in biological oxidation-reduction, *Nature 402*, 47-52.

12. Nakamura, K., Yamaki, M., Sarada, M., Nakayama, S., Vibat, C. R. T., Gennis, R. B., Nakayashiki, T., Inokuchi, H., Kojima, S., and Kita, K. (1996) Two hydrophobic subunits are essential for the heme b ligation and functional assembly of complex II (succinate-ubiquinone oxidoreductase) from *Escherichia coli*, *J. Biol. Chem. 271*, 521-527.

13. Nihei, C., Nakayashiki, T., Nakamura, K., Inokuchi, H., Gennis, R. B., Kojima, S., and Kita, K. (2001) Abortive assembly of succinate-ubiquinone reductase (complex II) in a ferrochelatase-deficient mutant of *Escherichia coli*, *Mol. Genet. Genomics 265*, 394-404.

14. Matsson, M., Tolstoy, D., Aasa, R., and Hederstedt, L. (2000) The distal heme center in *Bacillus subtilis* succinate:quinone reductase is crucial for electron transfer to menaquinone, *Biochemistry 39*, 8617-8624.

15. Gennis, R. B. and Stewart, V. (1996) Respiration, in *Escherichia coli and Salmonella: Cellular and Molecular Biology* (Neidhardt, F. C., Ed.) 2 ed., pp 217-261, ASM Press, Washington, DC.

16. Baysal, B. E., Ferrell, R. E., Willett-Brozick, J. E., Lawrence, E. C., Myssiorek, D., Bosch, A., van der Mey, A., Taschner, P. E., Rubinstein, W. S., Myers, E. N., Richard III, C. W., Cornelisse, C. J., Devilee, P., and Devlin, B. (2000) Mutations in SDHD, a mitochondrial complex II gene, in hereditary paraganglioma, *Science 287*, 848-851.

17. Iverson, T. M., Luna-Chavaz, C., Cecchini, G., and Rees, D. C. (1999) Structure of the *Escherichia coli* fumarate reductase respiratory complex, *Science 284*, 1961-1966.

18. Lancaster, C. R. D., Kröger, A., Auer, M., and Michel, H. (1999) Structure of fumarate reductase from *Wolinella succinogenes* at 2.2 A resolution., *Nature 402*, 377-385.

19. Hederstedt, L. (2003) Complex II is complex too, *Science 299*, 671-672.

20. Pereira, M. M. and Teixeira, M. (2003) Is a Q-cycle-like mechanism operative in dihaemic succinate:quinone and quinol:fumarate oxidoreductases?, *FEBS Lett. 543*, 1-4.

21. Pankhurst, K. L., Mowat, C. G., Rothery, E. L., Hudson, J. M., Jones, A. K., Miles, C. S., Walkinshaw, M. D., Armstrong, F. A., Reid, G. A., and Chapman, S. K. (2006) A proton delivery pathway in the soluble fumarate reductase from *Shewanella frigidimarina*, *J. Biol. Chem. 281*, 20589-20597.

22. Gao, X., Wen, X., Esser, L., Quinn, B., Yu, L., Yu, C.-A., and Xia, D. (2003) Structural basis for the quinone reduction in the bc_1 complex: A comparative analysis of crystal structures of mitochondrial cytochrome bc_1 with bound substrate and inhibitors at the Q_i site, *Biochemistry 42*, 9067-9080.

23. Zhang, Z., Huang, L., Shulmeister, V. M., Chi, Y.-I., Kim, K. K., Hung, L.-W., Crofts, A. R., Berry, E. A., and Kim, S.-H. (1998) Electron transfer by domain movement in cytochrome bc_1, *Nature 392*, 677-684.

24. Lange, C., Nett, J. H., Trumpower, B. L., and Hunte, C. (2001) Specific roles of protein-phospholipid interactions in the yeast cytochrome bc_1 complex structure, *EMBO J. 20*, 6591-6600.

25. Berry, E. A., Huang, L.-S., Saechao, L. K., Pon, N. G., Valkova-Valchanova, M., and Daldal, F. (2004) X-ray structure of *Rhodobacter capsulatus* cytochrome bc_1: comparison with its mitochondrial and chloroplast counterparts, *Photosynth. Res. 81*, 251-275.

26. Lange, C. and Hunte, C. (2002) Crystal structure of the yeast cytochrome bc_1 complex with its bound substrate cytochrome *c*, *Proc. Natl. Acad. Sci. USA 99*, 2800-2805.

27. Huang, L.-S., Cobessi, D., Tung, E. Y., and Berry, E. A. (2005) Binding of the respiratory chain inhibitor antimycin to the mitochondrial bc_1 complex: A new crystal structure reveals an altered intramolecular hydrogen-bonding pattern, *J. Mol. Biol. 351*, 573-597.

28. Mitchell, P. (1976) Possible molecular mechanisms of the protonmotive function of cytochrome systems, *J. Theor. Biol. 62*, 327-367.

29. Zu, Y., Fee, J. A., and Hirst, J. (2001) Complete thermodynamic characterization of reduction and protonation of the bc_1-type Rieske [2Fe-2S] center of *Thermus thermophilus*, *J. Am. Chem. Soc. 123*, 9906-9907.

30. Iwaki, M., Yakovlev, G., Hirst, J., Osyczka, A., Dutton, P. L., Marshall, D., and Rich, P. R. (2005) Direct observation of redox-linked histidine protonation changes in the iron-sulfur protein of cytochrome bc_1 complex by ATR-FTIR spectroscopy, *Biochemistry 44*, 4230-4237.

31. Osyczka, A., Moser, C. C., Daldal, F., and Dutton, P. L. (2004) Reversible redox energy coupling in electron transfer chains, *Nature 427*, 607-612.

32. Rich, P. R., Jeal, A. E., Madgwick, S. A., and Moody, A. J. (1990) Inhibitor effects on the redox-linked protonations of the *b* haems of the mitochondrial bc_1 complex, *Biochim. Biophys. Acta 1018*, 29-40.

33. Rich, P. R. (1983) Electron transfer through the isolated mitochondrial cytochrome *b*-c_1 complex, *Biochim. Biophys. Acta 722*, 271-280.

34. Link, T. A., Hagen, W. R., Pierik, A. J., Assmann, C., and von Jagow, G. (1992) Determination of the redox properties of the Rieske [2Fe-2S] cluster of bovine heart bc_1 complex by direct electrochemistry of a water-soluble fragment, *Eur. J. Biochem. 208*, 685-691.

35. Zhang, L., Tai, C.-H., Yu, L., and Yu, C.-A. (2000) pH-induced intramolecular electron transfer between the iron-sulphur protein and cytochrome c_1 in bovine cytochrome bc_1 complex, *J. Biol. Chem. 275*, 7656-7661.

36. Ding, H., Robertson, D. E., Daldal, F., and Dutton, P. L. (1992) Cytochrome bc_1 complex [2Fe-2S] cluster and its interaction with ubiquinone and ubihydroquinone at the Q_o site: A double-occupancy Q_o site model, *Biochemistry 31*, 3144-3158.

37. Bartoschek, S., Johansson, M., Geierstanger, B. H., Okun, J. G., Lancaster, C. R. D., Humpfer, E., Yu, L., Yu, C.-A., Griesinger, C., and Brandt, U. (2001) Three molecules of ubiquinone bind specifically to mitochondrial cytochrome bc_1 complex, *J. Biol. Chem. 276*, 35231-35234.

38. Brandt, U., Schägger, H., and von Jagow, G. (1988) Characterisation of binding of the methoxyacrylate inhibitors to mitochondrial cytochrome *c* reductase, *Eur. J. Biochem. 173*, 499-506.

39. Crofts, A. R., Hong, S. J., Ugulava, N., Barquera, B., Gennis, R., Guergova-Kuras, M., and Berry, E. A. (1999) Pathways for proton release during ubihydroquinone oxidation by the bc_1 complex, *Proc. Natl. Acad. Sci. USA 96*, 10021-10026.

40. Crofts, A. R. (2005) The bc_1 complex: what is there left to argue about?, in *Biophysical and Structural Aspects of Bioenergetics* (Wikström, M., Ed.) pp 123-155, The Royal Society of Chemistry, Cambridge, U.K.

41. Jünemann, S., Heathcote, P., and Rich, P. R. (1998) On the mechanism of quinol oxidation in the bc_1 complex, *J. Biol. Chem. 273*, 21603-21607.

42. Crofts, A. R., Guergova-Kuras, M., Huang, L.-S., Kuras, R., Zhang, Z., and Berry, E. A. (1999) Mechanism of ubiquinol oxidation by the bc_1 complex: Role of the iron sulfur protein and its mobility, *Biochemistry 38*, 15791-15806.

43. Crofts, A. R., Hong, S., Zhang, Z., and Berry, E. A. (1999) Physiochemical aspects of the movement of the Rieske iron sulfur protein during quinol oxidation by the bc_1 complex from mitochondria and photosynthetic bacteria, *Biochemistry 38*, 15827-15839.

44. Crofts, A. R., Barquera, B., Gennis, R. B., Kuras, R., Guergova-Kuras, M., and Berry, E. A. (1999) Mechanism of ubiquinol oxidation by the bc_1 complex: Different domains of the quinol binding pocket and their role in the mechanism and binding of inhibitors, *Biochemistry 38*, 15807-15826.

45. Brandt, U. (1996) Bifurcated ubihydroquinone-oxidation in the cytochrome bc_1 complex by proton-gated charge-transfer, *FEBS Lett. 387*, 1-6.

46. Brandt, U. (1998) The chemistry and mechanics of ubihydroquinone oxidation at center P (Q_o) of the cytochrome bc_1 complex, *Biochim. Biophys. Acta 1365*, 261-268.

47. Link, T. A. (1997) The role of the 'Rieske' iron sulfur protein in the hydroquinone oxidation (Q_P) site of the cytochrome bc_1 complex, *FEBS Lett. 412*, 257-264.

48. Trumpower, B. L. and Gennis, R. B. (1994) Energy transduction by cytochrome complexes in mitochondrial and bacterial respiration: The enzymology of coupling electron transfer reactions to transmembrane proton translocation, *Annu. Rev. Biochem. 63*, 675-716.

49. Snyder, C. H., Gutiérrez-Circlos, E.-B., and Trumpower, B. L. (2000) Evidence for a concerted mechanism of ubiquinol oxidation by the cytochrome bc_1 complex, *J. Biol. Chem. 275*, 13535-13541.

50. Iwata, S., Lee, J. W., Okada, K., Lee, J. K., Iwata, M., Rasmussen, B., Link, T. A., Ramaswamy, S., and Jap, B. K. (1998) Complete structure of the 11-subunit bovine mitochondrial bc_1 complex, *Science 281*, 64-71.

51. Hunte, C., Koepke, J., Lange, C., Rossmanith, T., and Michel, H. (2000) Structure at 2.3 Å resolution of the cytochrome bc_1 complex from the yeast *Saccharomyces cerevisiae* co-crystallized with antibody Fv fragment, *Structure 8*, 669-684.

52. Palsdottir, H., Lojero, C. G., Trumpower, B. L., and Hunte, C. (2003) Structure of the yeast cytochrome bc_1 complex with a hydroxyquinone anion Q_0 site inhibitor bound, *J. Biol. Chem. 278*, 31303-31311.

53. Osyczka, A., Zhang, H., Mathé, C., Rich, P. R., Moser, C. C., and Dutton, P. L. (2006) Role of the PEWY glutamate in hydroquinone-quinone oxidation-reduction catalysis in the Q_o site of cytochrome bc_1, *Biochemistry 45*, 10492-10503.

54. Iwata, S., Ostermeier, C., Ludwig, B., and Michel, H. (1995) Structure at 2.8 Å resolution of cytochrome *c* oxidase from *Paracoccus denitrificans*, *Nature 376*, 660-669.

55. Tsukihara, T., Aoyama, H., Yamashita, E., Tomizaki, T., Yamaguchi, H., Shinzawa-Itoh, K., Nakashima, R., Yaono, R., and Yoshikawa, S. (1996) The whole structure of the 13-subunit oxidized cytochrome *c* oxidase at 2.8 Å, *Science 272*, 1136-1144.

56. Ostermeier, C., Harrenga, A., Ermler, U., and Michel, H. (1997) Structure at 2.7 Å resolution of the *Paracoccus denitrificans* two-subunit cytochrome *c* oxidase complexed with an antibody F_v fragment, *Proc. Natl. Acad. Sci. USA 94*, 10547-10553.

57. Svensson-Ek, M., Abramson, J., Larsson, G., Törnroth, S., Brzezinski, P., and Iwata, S. (2002) The X-ray crystal structures of wild-type and EQ(I-286) mutant cytochrome *c* oxidases from *Rhodobacter sphaeroides*, *J. Mol. Biol. 321*, 329-339.

58. Lin, J., Pan, L.-P., and Chan, S. I. (1993) The subunit location of magnesium in cytochrome *c* oxidase, *J. Biol. Chem. 268*, 22210-22214.

59. Yoshikawa, S., Muramoto, K., Shinzawa-Itoh, K., Aoyama, H., Tsukihara, T., Ogura, T., Shimokata, K., Katayama, Y., and Shimada, H. (2006) Reaction mechanism of bovine cytochrome *c* oxidase, *Biochim. Biophys. Acta 1757*, 395-400.

60. Wolf, D. E., Hoffman, C. H., Trenner, N. R., Arison, B. H., Shunk, C. H., Linn, B. O., McPherson, J. F., and Folkers, K. (1958) Coenzyme Q. I. Structure studies on the coenzyme Q group, *J. Am. Chem. Soc. 80*, 4752-4753.

61. Gordillo, G. J. and Schiffrin, D. J. (2000) The electrochemistry of ubiquinone-10 in a phospholipid model membrane, *Faraday Discuss. 116*, 89-107.

62. Fisher, N. and Rich, P. R. (2000) A motif for quinone binding sites in respiratory and photosynthetic systems, *J. Mol. Biol. 296*, 1153-1162.

63. Bushnell, G. W., Louie, G. V., and Brayer, G. D. (1990) High resolution three-dimensional structure of horse heart cytochrome *c*, *J. Mol. Biol. 214*, 585-595.

64. Liu, X., Kim, C.-N., Yang, J., Jemmerson, R., and Wang, X. (1996) Induction of apoptotic program in cell-free extracts: requirement for dATP and cytochrome c, *Cell 86*, 147-157.

65. Fillingame, R. H., Angevine, C. M., and Dmitriev, O. Y. (2003) Mechanics of coupling proton movements to *c*-ring rotation in ATP synthase, *FEBS Lett. 555*, 29-34.

66. Bouguer, P. (1729) *Essai d'optique sur la gradation de la lumière* Claude Jombert, Paris.

67. Keilin, D. (1925) On cytochrome, a respiratory pigment, common to animals, yeast, and higher plants, *Proc. Roy. Soc. Lond. B 98*, 312-339.

68. Keilin, D. (1966) *The history of cell respiration and cytochrome* Cambridge University Press, Cambridge.

69. (1968) *Biological Oxidations* Interscience Publishers, New York.

70. Stuart, B. (2004) *Infrared Spectroscopy: Fundamentals and Applications* John Wiley & Sons, Chicester.

71. Günzler, H. and Gremlich, H.-U. (2002) *IR Spectroscopy: An Introduction* Wiley-VCH, Weinheim, Germany.

72. Goormaghtigh, E., Raussens, V., and Ruysschaert, J.-M. (1999) Attenuated total reflection infrared spectroscopy of proteins and lipids in biological membranes, *Biochim. Biophys. Acta 1422*, 105-185.

73. Stuart, B. (1997) *Biological Applications of Infrared Spectroscopy* John Wiley & Sons, Chicester.

74. Iwaki, M., Giotta, L., Akinsiku, A. O., Schägger, H., Fisher, N., Breton, J., and Rich, P. R. (2003) Redox-induced transitions in bovine cytochrome bc_1 complex studied by perfusion-induced ATR-FTIR spectroscopy, *Biochemistry 42*, 11109-11119.

75. Iwaki, M., Osyczka, A., Moser, C. C., Dutton, P. L., and Rich, P. R. (2004) ATR-FTIR spectroscopy studies of iron-sulfur protein and cytochrome c_1 in the *Rhodobacter capsulatus* cytochrome bc_1 complex, *Biochemistry 43*, 9477-9486.

76. Marshall, D., Fisher, N., Grigic, L., Zickermann, V., Brandt, U., Shannon, R. J., Hirst, J., Lawrence, R., and Rich, P. R. (2006) ATR-FTIR redox difference spectroscopy of *Yarrowia lipolytica* and bovine complex I, *Biochemistry 45*, 5458-5467.

77. Barth, A. and Zscherp, C. (2002) What vibrations tell us about proteins, *Q. Rev. Biophys. 35*, 369-430.

78. Byler, D. M. and Susi, H. (1986) Examination of the secondary structure of proteins by deconvolved FTIR spectra, *Biopolymers 25*, 469-487.

79. Goormaghtigh, E., Cabiaux, V., and Ruysschaert, J.-M. (1990) Secondary structure and dosage of soluble and membrane proteins by attenuated total reflection Fourier-transform infrared spectroscopy on hydrated films, *Eur. J. Biochem. 193*, 409-420.

80. Rich, P. R. and Iwaki, M. (2005) Infrared protein spectroscopy as a tool to study protonation reactions within proteins, in *Biophysical and Structural Aspects of Bioenergetics* (Wikström, M., Ed.) pp 314-333, The Royal Society of Chemistry, Cambridge, U.K.

81. Ingledew, W. J. and Rich, P. R. (2005) A study of the horseradish peroxidase catalytic site by FTIR spectroscopy, *Biochem. Soc. Trans. 33*, 886-889.

82. Iwaki, M. and Rich, P. R. (2004) Direct detection of formate ligation in cytochrome *c* oxidase by ATR-FTIR spectroscopy, *J. Am. Chem. Soc. 126*, 2386-2389.

83. Iwaki, M., Puustinen, A., Wikström, M., and Rich, P. R. (2004) ATR-FTIR spectroscopy and isotope labelling of the P_M intermediate of *Paracoccus denitrificans* cytochrome *c* oxidase, *Biochemistry 43*, 14370-14378.

84. Hellwig, P., Scheide, D., Bungert, S., Mäntele, W., and Friedrich, T. (2000) FT-IR spectroscopic characterization of NADH:ubiquinone oxidoreductase (complex I) from *Esherichia coli*: oxidation of FeS cluster N2 is coupled with

the protonation of an aspartate or glutamate side chain, *Biochemistry 39*, 10884-10891.

85. Sonar, S., Liu, X.-M., Lee, C.-P., Coleman, M., He, Y.-W., Pelletier, S., Herzfeld, J., RajBhandry, U. L., and Rothschild, K. J. (1995) Site-directed isotope labelling and FT-IR spectroscopy: The Tyr 185/Pro 186 peptide bond of bacteriorhodopsin is perturbed during the primary photoreaction, *J. Am. Chem. Soc. 117*, 11614-11615.

86. Nagano, T., Liu, J.-G., Naruta, Y., Ikoma, T., Tero-Kubota, S., and Kitagawa, T. (2006) Characterization of the phenoxyl radical in model complexes for the Cu_B site of cytochrome *c* oxidase: steady-state and transient absorption measurements, UV resonance Raman spectroscopy, EPR spectroscopy, and DFT calculations for M-BIAIP, *J. Am. Chem. Soc. 128*, 14560-14570.

87. Friedrich, T. (1998) The NADH:ubiquinone oxidoreductase (complex I) from *Escherichia coli*, *Biochim. Biophys. Acta 1364*, 134-146.

88. Hirst, J., Carroll, J., Fearnley, I. M., Shannon, R. J., and Walker, J. E. (2003) The nuclear encoded subunits of complex I from bovine heart mitochondria, *Biochim. Biophys. Acta 1604*, 135-150.

89. Carroll, J., Fearnley, I. M., Shannon, R. J., Hirst, J., and Walker, J. E. (2003) Analysis of the subunit composition of complex I from bovine heart mitochondria, *Molecular and Cellular Proteomics 2*, 117-126.

90. Sazanov, L. A. and Hinchliffe, P. (2006) Structure of the hydrophilic domain of respiratory complex I from *Thermus thermophilus*, *Science 311*, 1430-1436.

91. Weidner, U., Geier, S., Ptock, A., Friedrich, T., Leif, H., and Weiss, H. (1993) The gene locus of the proton-translocating NADH:ubiquinone oxidoreductase in *Escherichia coli*. Organization of the 14 genes and relationship between the derived proteins and subunits of mitochondrial complex I, *J. Mol. Biol. 233*, 109-122.

92. Rasmussen, T., Weiss, H., Kintscher, L., Brors, B., Scheide, D., and Friedrich, T. (2001) Identification of two tetranuclear FeS clusters on the ferredoxin-type subunit of NADH:ubiquinone oxidoreductase (complex I), *Biochemistry 40*, 6124-6131.

93. Ingledew, W. J. and Ohnishi, T. (1980) An analysis of some thermodynamic properties of iron-sulphur centres in site I of mitochondria, *Biochem. J. 186*, 111-117.

94. Nakamaru-Ogiso, E., Yano, T., Yagi, T., and Ohnishi, T. (2005) Characterization of the iron-sulfur cluster N7 (N1c) in the subunit NuoG of the proton-translocating NADH-ubiquinone oxidoreductase from *Escherichia coli*, *J. Biol. Chem. 280*, 301-307.

95. Sled, V. D., Rudnitzky, N. I., Hatefi, Y., and Ohnishi, T. (1994) Thermodynamic analysis of flavin in mitochondrial NADH: ubiquinone oxidoreductase (complex I), *Biochemistry 33*, 10069-10075.

96. Ohnishi, T. (1998) Iron-sulfur clusters/semiquinones in complex I, *Biochim. Biophys. Acta 1364*, 186-206.

97. Meinhardt, S. W., Wang, D.-C., Hon-nami, K., Yagi, T., Oshima, T., and Ohnishi, T. (1990) Studies on the NADH-menaquinone oxidoreductase segment of the respiratory chain in *Thermus thermophilus* HB-8, *J. Biol. Chem. 265*, 1360-1368.

98. Leif, H., Sled, V. D., Ohnishi, T., Weiss, H., and Friedrich, T. (1995) Isolation and characterization of the proton-translocating NADH:ubiquinone oxidoreductase from *Escherichia coli*, *Eur. J. Biochem. 230*, 538-548.

99. Garofano, A., Zwicker, K., Kerscher, S., Okun, P., and Brandt, U. (2003) Two aspartic residues in the PSST-homologous NUKM subunit of complex I from *Yarrowia lipolytica* are essential for catalytic activity, *J. Biol. Chem. 278*, 42435-42440.

100. Dawson, R. M. C., Elliott, D. C., Elliott, W. H., and Jones, K. M. (1986) *Data for biochemical research* Oxford Science Publications, Oxford.

101. Zwicker, K., Galkin, A., Dröse, S., Grgic, L., Kerscher, S., and Brandt, U. (2006) The redox-Bohr group associated with iron-sulfur cluster N2 of complex I, *J. Biol. Chem. 281*, 23013-23017.

102. Brandt, U., Abdrakhmanova, V., Zickermann, V., Dröse, S., Zwicker, K., and Kerscher, S. (2005) Structure-function relationships in mitochondrial complex I of the strictly aerobic yeast *Yarrowia lipolytica*, *Biochem. Soc. Trans. 33*, 840-844.

103. Friedrich, T. and Weiss, H. (1997) Modular evolution of the respiratory NADH:ubiquinone oxidoreductase and the origin of its modules, *J. Theor. Biol. 187*, 529-540.

104. Fearnley, I. M. and Walker, J. E. (1992) Conservation of sequences of subunits of mitochondrial complex I and their relationships with other proteins, *Biochim. Biophys. Acta 1140*, 105-134.

105. Yamaguchi, M., Belogrudov, G. I., Matsuno-Yagi, A., and Hatefi, Y. (2000) The multiple nicotinamide nucleotide-binding subunits of bovine heart mitochondrial NADH:ubiquinone oxidoreductase (complex I), *Eur. J. Biochem. 267*, 329-336.

106. Runswick, M. J., Fearnley, I. M., Skehel, J. M., and Walker, J. E. (1991) Presence of an acyl carrier protein in NADH:ubiquinone oxidoreductase from bovine heart mitochondria, *FEBS Lett. 286*, 121-124.

107. Fearnley, I. M., Carroll, J., Shannon, R. J., Runswick, M. J., Walker, J. E., and Hirst, J. (2001) GRIM-19, a cell death regulatory gene product, is a subunit of bovine mitochondrial NADH:Ubiquinone oxidoreductase (complex I), *J. Biol. Chem. 276*, 38345-38348.

108. Huang, G., Chen, Y., Lu, H., and Cao, X. (2006) Coupling mitochondrial respiratory chain to cell death: an essential role of mitochondiral complex I in the interferon-β and retinoic acid-induced cancer cell death, *Cell Death Differ.*

109. Friedrich, T., Steinmüller, K., and Weiss, H. (1995) The proton-pumping respiratory complex I of bacteria and mitochondria and its homologue in chloroplasts, *FEBS Lett. 367*, 107-111.

110. Friedrich, T. and Scheide, D. (2000) The respiratory complex I of bacteria, archaea and eukarya and its module common with membrane-bound multisubunit hydrogenases, *FEBS Lett. 479*, 1-5.

111. Brandt, U. (2006) Energy converting NADH:quinone oxidoreductase (complex I), *Annu. Rev. Biochem. 75*, 69-92.

112. Tran-Betcke, A., Warnecke, U., Böcker, C., Zaborosch, C., and Friedrich, B. (1990) Cloning and nucleotide sequences of the genes for the subunits of NAD-reducing hydrogenase of *Alcaligenes eutrophus* H16, *J. Bacteriol. 172*, 2920-2929.

113. Böhm, R., Sauter, M., and Böck, A. (1990) Nucleotide sequence and expression of an operon in Escherichia coli coding for formate hydrogenlyase components, *Mol. Microbiol. 4*, 231-243.

114. Albracht, S. P. J. (1993) Intimate relationships of the large and the small subunits of all nickel hydrogenases with two nuclear-encoded subunits of mitochondrial NADH:ubiquinone oxidoreductase, *Biochim. Biophys. Acta 1144*, 221-224.

115. Kashani-Poor, N., Zwicker, K., Kerscher, S., and Brandt, U. (2001) A central role for the 49-kDa subunit within the catalytic core of mitochondrial complex I, *J. Biol. Chem. 276*, 24082-24087.

116. Kerscher, S., Kashani-Poor, N., Zwicker, K., Zickermann, V., and Brandt, U. (2001) Exploring the catalytic core of complex I by *Yarrowia lipolytica* yeast genetics, *J. Bioenerg. Biomemb. 33*, 187-195.

117. Sazanov, L. A., Peak-Chow, S. Y., Fearnley, I. M., and Walker, J. E. (2000) Resolution of the membrane domain of bovine complex I into subcomplexes: implications for the structural organization of the enzyme, *Biochemistry 39*, 7229-7235.

118. Ragan, C. I., Galante, Y. M., and Hatefi, Y. (1982) Purification of three iron-sulphur proteins from the iron-protein fragment of mitochondrial NADH-ubiquinone oxidoreductase, *Biochemistry 21*, 2518-2824.

119. Sazanov, L. A. and Walker, J. E. (2000) Cryo-electron crystallography of two sub-complexes of bovine complex I reveals the relationship between the membrane and peripheral arms, *J. Mol. Biol 302*, 455-464.

120. Finel, M., Skehel, J. M., Albracht, S. P. J., Fearnley, I. M., and Walker, J. E. (1992) Resolution of NADH:ubiquinone oxidoreductase from bovine heart

mitochondria into two subcomplexes, one of which contains the redox centers of the enzyme, *Biochemistry 31*, 11425-11434.

121. Hinchliffe, P. and Sazanov, L. A. (2005) Organization of iron-sulfur clusters in respiratory complex I, *Science 309*, 771-774.

122. Guenebaut, V., Schlitt, A., Weiss, H., Leonard, K., and Friedrich, T. (1998) Consistent structure between bacterial and mitochondrial NADH:Ubiquinone oxidoreductase (complex I), *J. Mol. Biol. 276*, 105-112.

123. Böttcher, B., Scheide, D., Hesterberg, M., Nagel-Steger, L., and Friedrich, T. (2002) A novel, enzymatically active conformation of the NADH:ubiquinne oxidoreductase (complex I), *J. Biol. Chem. 277*, 17970-17977.

124. Sazanov, L. A., Carroll, J., Holt, P., Toime, L., and Fearnley, I. M. (2003) A role for native lipids in the stabilization and two-dimensional crystallization of the *Escherichia coli* NADH-ubiquinone oxidoreductase (complex I), *J. Biol. Chem. 278*, 19483-19491.

125. Mamedova, A. A., Holt, P. J., Carroll, J., and Sazanov, L. A. (2004) Substrate-induced conformational change in bacterial complex I, *J. Biol. Chem. 279*, 23830-23836.

126. Peng, G., Fritzsch, G., Zickermann, V., Schägger, H., Mentele, R., Lottspeich, F., Bostina, M., Radermacher, M., Huber, R., Stetter, K. O., and Michel, H. (2003) Isolation, characterization and electron microscopic single particle analysis of the NADH:ubiquinone oxidoreductase (complex I) from the hyperthermophilic eubacterium *Aquifex aeolicus*, *Biochemistry 42*, 3032-3039.

127. Guénebaut, V., Vincentelli, R., Mills, D., Weiss, H., and Leonard, K. (1997) Three-dimensional structure of NADH-dehydrogenase from *Neurospora crassa* by electron microscopy and conical tilt reconstruction, *J. Mol. Biol. 265*, 409-418.

128. Djafarzadeh, R., Kerscher, S., Zwicker, K., Radermacher, M., Lindahl, M., Schagger, H., and Brandt, U. (2000) Biophysical and structural characterization of proton-translocating NADH-dehydrogenase (complex I) from the strictly aerobic yeast *Yarrowia lipolytica*, *Biochim. Biophys. Acta 1459*, 230-238.

129. Zickermann, V., Bostina, M., Hunter, C., Ruiz, T., Radermacher, M., and Brandt, U. (2003) Functional implications from an unexpected position of the 49-kDa subunit of NADH: ubiquinone oxidoreductase, *J. Biol. Chem. 278*, 29072-29078.

130. Radermacher, M., Ruiz, T., Clason, T., Benjamin, S., Brandt, U., and Zickermann, V. (2006) The three-dimensional structure of complex I from *Yarrowia lipolytica*: a highly dynamic enzyme, *J. Struct. Biol. 154*, 269-279.

131. Dudkina, N. V., Holger, E., Wilko, K., Boekema, E. J., and Braun, H.-P. (2005) Structure of a mitochondrial supercomplex formed by respiratory-chain complexes I and III, *Proc. Natl. Acad. Sci. USA 102*, 3225-3229.

132. Grigorieff, N. (1999) Structure of the respiratory NADH:ubiquinone oxidoreductase, *Curr. Opin. Struct. Biol. 9*, 476-483.

133. Friedrich, T. and Böttcher, B. (2004) The gross structure of the respiratory complex I: a Lego system, *Biochim. Biophys. Acta 1608*, 1-9.

134. Yagi, T. and Matsuno-Yagi, A. (2003) The proton-translocating NADH-quinone oxidoreductase in the respiratory chain: the secret unlocked, *Biochemistry 42*, 2266-2274.

135. Leonard, K., Haiker, H., and Weiss, H. (1987) Three-dimensional structure of NADH: ubiquinone reductase (complex 1) from Neurospora mitochondria determined by electron microscopy of membrane crystals, *J. Mol. Biol. 194*, 277.

136. Hofhaus, G., Weiss, H., and Leonard, K. (1991) Electron microscopic analysis of the peripheral and membrane parts of mitochondrial NADH dehydrogenase (complex I), *J. Mol. Biol. 221*, 1027-1043.

137. Patel, S. D. and Ragan, C. I. (1988) Structural studies on mitochondrial NADH dehydrogenase using chemical cross-linking, *Biochem. J. 256*, 521-528.

138. Yamaguchi, M. and Hatefi, Y. (1993) Mitochondrial NADH:ubiquinone oxidoreductase (complex I): Proximity of the subunits of the flavoprotein and the iron-sulfur protein subcomplexes, *Biochemistry 32*, 1935-1939.

139. Di Bernardo, S., Yano, T., and Yagi, T. (2000) Exploring the membrane domain of the reduced nicotinamide adenine dinucleotide-quinone oxidoreductase of *Paracoccus denitrificans*: characterization of the NQO7 subunit, *Biochemistry 39*, 9411-9418.

140. Kao, M.-C., Di Bernardo, S., Matsuno-Yagi, A., and Yagi, T. (2003) Characterization and topology of the membrane domain Nqo10 subunit of the proton-translocating NADH-quinone oxidoreductase of *Paracoccus denitrificans*, *Biochemistry 42*, 4534-4543.

141. Kao, M.-C., Di Bernardo, S., Matsuno-Yagi, A., and Yagi, T. (2002) Characterization of the membrane domain Nqo11 subunit of the proton-translocating NADH-quinone oxidoreductase of *Paracoccus denitrificans*, *Biochemistry 41*, 4377-4384.

142. Roth, R. and Hägerhäll, C. (2001) Transmembrane orientation and topology of the NADH:quinone oxidoreductase putative quinone binding subunit NuoH, *Biochim. Biophys. Acta 1504*, 352-362.

143. Hirst, J. (2005) Energy transduction by respiratory complex I - an evaluation of current knowledge, *Biochem. Soc. Trans. 33*, 525-529.

144. Magnitsky, S., Toulokhonova, L., Yano, T., Sled, V. D., Hagerhall, C., Grivennikova, V. G., Burbaev, D. S., Vinogradov, A. D., and Ohnishi, T. (2002) EPR characterization of ubisemiquinone and iron-sulfur cluster N2,

central components of the energy coupling in the NADH-ubiquinone oxidoreductase (complex I) in situ, *J. Bioenerg. Biomemb. 34*, 193-208.

145. Yano, T., Dunham, W. R., and Ohnishi, T. (2005) Characterization of the ΔμH+-sensitive ubisemiquinone species (SQNf) and the interaction with cluster N2: New insight into the energy-coupled electron transfer in complex I, *Biochemistry 44*, 1744-1754.

146. Wikström, M. (1984) Two protons are pumped from the mitochondrial matrix per electron transferred between NADH and ubiquinone, *FEBS Lett. 169*, 300-304.

147. Galkin, A. S., Grivennikova, V. G., and Vinogradov, A. D. (1999) $H^+/2e^-$ stoichiometry in NADH-quinone reductase reactions catalyzed by bovine heart submitochondrial particles, *FEBS Lett. 451*, 157-161.

148. Dröse, S., Zwicker, K., and Brandt, U. (2002) Full recovery of the NADH:ubiquinone activity of complex I (NADH:ubiquinone oxidoreductase) from *Yarrowia lipolytica* by the addition of phospholipids, *Biochim. Biophys. Acta 1556*, 65-72.

149. Kurki, S., Zickermann, V., Kervinen, M., Hassinen, I., and Finel, M. (2000) Mutagenesis of three conserved Glu residues in a bacterial homologue of the ND1 subunit of complex I affects ubiquinone reduction kinetics but not inhibition by dicyclohexylcarbodiimide, *Biochemistry 39*, 13496-13592.

150. Earley, F. G. P., Patel, S. D., Ragan, C. I., and Attardi, G. (1987) Photolabelling of a mitochondrially encoded subunit of NADH dehydrogenase with [3H]dihydrorotenone, *FEBS Lett. 219*, 108-113.

151. Darrouzet, E., Issartel, J.-P., Lunardi, J., and Dupuis, A. (1998) The 49-kDa subunit of NADH-ubiquinone oxidoreductase (complex I) is involved in the binding of piericidin and rotenone, two quinone-related inhibitors, *FEBS Lett. 431*, 34-38.

152. Gong, X., Xie, T., Yu, L., Hesterberg, M., Scheide, D., Friedrich, T., and Yu, C.-A. (2003) The ubiquinone-binding site in NADH:Ubiquinone oxidoreductase from *Escherichia coli* , *J. Biol. Chem. 278*, 25731-25737.

153. de Vries, D. D., Went, L. N., Bruyn, G. W., Scholte, H. R., Hofstra, R. M. W., Bolhuis, P. A., and van Oost, B. A. (1996) Genetic and biochemical impairment of mitochondrial complex I activity in a family with Leber hereditary optic neuropathy and hereditary spastic dystonia, *Am. J. Hum. Genet. 58*, 703-711.

154. Ohshima, M., Miyoshi, H., Sakamoto, K., Takegami, K., Iwata, J., Kuwabara, K., Iwamura, H., and Yagi, T. (1998) Characterization of the ubiquinone reduction site of mitochondrial complex I using bulky synthetic ubiquinones, *Biochemistry 37*, 6436-6445.

155. Degli Esposti, M. (1998) Inhibitors of NADH-ubiquinone reductase: an overview, *Biochim. Biophys. Acta 1364*, 222-235.

156. Okun, J. G., Lümmen, P., and Brandt, U. (1999) Three classes of inhibitors share a common binding domain in mitochondrial complex I (NADH:ubiquinone oxidoreductase), *J. Biol. Chem. 274*, 2625-2630.

157. Krebs, W., Steuber, J., Gemperli, A. C., and Dimroth, P. (1999) Na^+ translocation by the NADH:ubiquinone oxidoreductase (complex I) from *Klebsiella pneumoniae*, *Mol. Microbiol. 33*, 590-598.

158. Steuber, J., Schmid, C., Rufibach, M., and Dimroth, P. (2000) Na^+ translocation by complex 1 (NADH: quinone oxidoreductase) of *Escherichia coli*, *Mol. Microbiol. 35*, 428-434.

159. Dutton, P. L., Moser, C. C., Sled, V. D., Daldal, F., and Ohnishi, T. (1998) A reductant-induced oxidation mechanism for complex I, *Biochim. Biophys. Acta 1364*, 245-257.

160. Friedrich, T., Brors, B., Hellwig, P., Kintscher, L., Rasmussen, T., Scheide, D., Schulte, U., Mäntele, W., and Weiss, H. (2000) Characterization of two novel redox groups in the respiratory NADH:ubiquinone oxidoreductase (complex I), *Biochim. Biophys. Acta 1459*, 305-309.

161. Brandt, U. (1997) Proton-translocation by membrane-bound NADH:ubiquinone-oxidoreductase (complex I) through redox-gated ligand conduction, *Biochim. Biophys. Acta 1318*, 79-91.

162. Hirst, J. (2005) Current knowledge about the mechanism of energy transduction by respiratory complex I, in *Biophysical and Structural Aspects of Bioenergetics* (Wikström, M., Ed.) pp 185-200, The Royal Society of Chemistry, Cambridge, U.K.

163. Belogrudov, G. and Hatefi, Y. (1994) Catalytic sector of complex I (NADH:ubiquinone oxidoreductase): Subunit stoichiometry and substrate-induced conformation changes, *Biochemistry 33*, 4571-4576.

164. Friedrich, T. (2001) Complex I: a chimaera of a redox and conformation-driven proton pump?, *J. Bioenerg. Biomemb. 33*, 169-177.

165. Clark, W. M. (1960) *Oxidation-reduction potentials of organic systems* Bailliere, Tindall & Cox, Ltd., London.

166. Beinert, H. and Sands, R. H. (1960) Studies on mitochondria and submitochondrial particles by paramagnetic resonance (EPR) spectroscopy, *Biochem. Biophys. Res. Commun. 3*, 41-45.

167. Ohnishi, T. (1975) Thermodynamic and EPR characterization of iron-sulfur centers in the NADH-ubiquinone segment of the mitochondrial respiratory chain in pigeon heart, *Biochim. Biophys. Acta 387*, 475-490.

168. Albracht, S. J. P., Dooijewaard, G., Leeuwerik, F. J., and van Swol, B. (1977) EPR signals of NADH: Q oxidoreductase shape and intensity, *Biochim. Biophys. Acta 459*, 300-317.

169. Yano, T., Sklar, J., Nakamaru-Ogiso, E., Takahashi, Y., Yagi, T., and Ohnishi, T. (2003) Characterization of cluster N5 as a fast-relaxing [4Fe-4S] cluster in the Nqo3 subunit of the proton-translocating NADH-ubiquinone oxidoreductase from *Paracoccus denitrificans*, *J. Biol. Chem. 278*, 15514-15522.

170. Yano, T., Sled, V. D., Ohnishi, T., and Yagi, T. (1996) Expression and characterization of the flavoprotein subcomplex composed of 50-kDa (NQO1) and 25-kDa (NQO2) subunits of the proton-translocating NADH-quinone oxidoreductase of *Paracoccus denitrificans*, *J. Biol. Chem. 271*, 5907-5913.

171. Vinogradov, A. D., Sled, V. D., Burbaev, D. S., Grivennikova, V. G., Moroz, I. A., and Ohnishi, T. (1995) Energy-dependent complex I-associated ubisemiquinones in submitochondrial particles, *FEBS Lett. 370*, 83-87.

172. Ghisla, S. (1980) Fluorescence and optical characteristics of reduced flavins and flavoproteins, *Meth. Enzymol. 66*, 360-373.

173. Flemming, D., Hellwig, P., and Friedrich, T. (2003) Involvement of tyrosines 114 and 139 of subunit NuoB in the proton pathway around cluster N2 in *Escherichia coli* NADH:ubiquinone oxidoreductase, *J. Biol. Chem. 278*, 3055-3062.

174. Hellwig, P., Stolpe, S., and Friedrich, T. (2004) Fourier transform infrared spectroscopic study on the conformational reorganization in *Escherichia coli* complex I due to redox-driven proton translocation, *Biopolymers 74*, 69-72.

175. Venyaminov, S. Y. and Kalnin, N. N. (1990) Quantitative IR spectrophotometry of peptide compounds in water (H2O) solutions. Amide II absorption bands of polypeptides and fibrous proteins in a-,b-, and random coil conformations, *Biopolymers 30*, 1259-1271.

176. Hartzell, C. R., Beinert, H., van Gelder, B. F., and King, T. E. (1978) Preparation of cytochrome oxidase from beef heart, *Meth. Enzymol. 53*, 54-66.

177. Berden, J. A. and Slater, E. C. (1970) The reaction of antimycin with a cytochrome b preparation active in reconstitution of the respiratory chain, *Biochim. Biophys. Acta 216*, 237-249.

178. Moody, A. J., Cooper, C. E., and Rich, P. R. (1991) Characterisation of 'fast' and 'slow' forms of bovine heart cytochrome-*c* oxidase, *Biochim. Biophys. Acta 1059*, 189-207.

179. Robertson, D. E., Ding, H., Chelminski, P. R., Slaughter, C., Hsu, J., Moomaw, C., Tokito, M., Daldal, F., and Dutton, P. L. (1993) Hydroubiquinone-cytochrome c_2 oxidoreductase from *Rhodobacter capsulatus*: Definition of a minimal, functional isolated preparation, *Biochemistry 32*, 1310-1317.

180. Ljungdahl, P. O., Pennoyer, J. D., Robertson, D. E., and Trumpower, B. L. (1987) Purification of highly active cytochrome bc1 complexes from phylogenetically diverse species by a single chromatographic procedure, *Biochim. Biophys. Acta 891*, 227-241.

181. Andrews, K. M., Crofts, A. R., and Gennis, R. B. (1990) Large-scale purification and characterization of a highly active four-subunit cytochrome bc_1 complex from *Rhodobacter sphaeroides*, *Biochemistry 29*, 2645-2651.

182. Atta-Asafo-Adjei, E. and Daldal, F. (1991) Size of the amino acid side chain at position 158 of cytochrome *b* is critical for an active cytochrome bc_1 complex and for photosynthetic growth of *Rhodobacter capsulatus*, *Proc. Natl. Acad. Sci. USA 88*, 492-496.

183. Valkova-Valchanova, M. B., Saribas, A. S., Gibney, B. R., Dutton, P. L., and Daldal, F. (1998) Isolation and characterization of a two-subunit cytochrome b-c_1 subcomplex from *Rhodobacter capsulatus* and reconstitution of its ubihydroquinone oxidation (Q_o) site with purified Fe-S protein subunit, *Biochemistry 37*, 16242-16251.

184. Sharpley, M. S., Shannon, R. J., Draghi, F., and Hirst, J. (2005) Interactions between phospholipids and NADH:ubiquinone oxidoreductase (complex I) from bovine mitochondria, *Biochemistry 45*, 241-248.

185. Walker, J. E., Skehel, J. M., and Buchanan, S. K. (1995) Structural analysis of NADH : ubiquinone oxidoreductase from bovine heart mitochondria, *Meth. Enzymol. 260*, 14-34.

186. Kashani-Poor, N., Kerscher, S., Zickermann, V., and Brandt, U. (2001) Efficient large scale purification of his-tagged proton translocating NADH:ubiquinone oxidoreductase (complex I) from the strictly aerobic yeast *Yarrowia lipolytica*, *Biochim. Biophys. Acta 1504*, 363-370.

187. Kerscher, S. J., Okun, J. G., and Brandt, U. (1999) A single external enzyme confers alternative NADH:ubiquinone oxidoreductase activity in *Yarrowia lipolytica*, *J. Cell Sci. 112*, 2347-2354.

188. Grgic, L., Zwicker, K., Kashani-Poor, N., Kerscher, S., and Brandt, U. (2004) Functional significance of conserved histidines and arginines in the 49-kDa subunit of mitochondrial complex I, *J. Biol. Chem. 279*, 21193-21199.

189. (1962) *Data for biochemical research* Oxford at Clarendon Press, Oxford.

190. Sery, A., Housset, D., Serre, L., Bonicel, J., Hatchikian, C., Frey, M., and Roth, M. (1994) Crystal structure of the ferredoxin I from *Desulfovibrio africanus* at 2.3 Å resolution, *Biochemistry 33*, 15408-15417.

191. Davy, S. D., Osborne, M. J., and Moore, G. R. (1998) Determination of the structure of oxidised *Desulfovibrio africanus* ferredoxin I by ^{1}H NMR spectroscopy and comparison of its solution structure with its crystal structure, *J. Mol. Biol. 277*, 683-706.

192. Echols, N., Milburn, D., and Gerstein, M. (2003) MolMovDB: analysis and visualization of conformational change and structural flexibility, *Nucleic Acids Res. 31*, 478-482.

193. Moss, D. A. and Bendall, D. S. (1984) Cyclic electron transport in chloroplasts. The Q-cycle and the site of action of antimycin, *Biochim. Biophys. Acta 767*, 389-395.

194. Hatchikian, C., Jones, H. E., and Bruschi, M. (1979) Isolation and characterization of a rubredoxin and two ferredoxins from *Desulfovibrio africanus*, *Biochim. Biophys. Acta 548*, 471-483.

195. Payne, M. J., Woods, L. F., Gibbs, P., and Cammack, R. (1990) Electron paramagnetic resonance spectroscopic investigation of the inhibition of the phosphoroclastic system of *Clostridium sporogenes* by nitrite, *J. Gen. Microbiol. 136*, 2067-2076.

196. Mayhew, S. G. (1999) The effects of pH and semiquinone formation on the oxidation-reduction potentials of flavin mononucleotide: A reappraisal, *FEBS Lett. 265*, 698-702.

197. Schellenberg, K. A. and Hellerman, L. (1958) Oxidation of reduced diphosphopyridine nucleotide, *J. Biol. Chem. 231*, 547-556.

198. Glasoe, P. K. and Long, F. A. (1960) Use of glass electrodes to measure acidities in deuterium oxide, *J. Phys. Chem. 64*, 188-190.

199. Rath, P., DeGrip, W. J., and Rothschild, K. J. (1998) Photoactivation of rhodopsin causes an increased hydrogen-deuterium exchange of buried peptide groups, *Biophys. J. 74*, 192-198.

200. Mayo, D. W., Miller, F. A., and Hannah, R. W. (2004) *Course notes on the interpretation of infrared and raman spectra* Wiley-Interscience, Hoboken, New Jersey.

201. Klähn, M., Mathias, G., Kötting, C., Nonella, M., Schlitter, J., Gerwert, K., and Tavan, P. (2004) IR spectra of phosphate ions in aqueous solution: predictions of a DFT/MM approach compared with observations, *J. Phys. Chem. A 108*, 6186-6194.

202. Baymann, F., Robertson, D. E., Dutton, P. L., and Mäntele, W. (1999) Electrochemical and spectroscopic investigations of the cytochrome bc_1 complex from *Rhodobacter capsulatus*, *Biochemistry 38*, 13188-13199.

203. Iwaki, M., Cotton, N. P. J., Quirk, P. G., Rich, P. R., and Jackson, J. B. (2006) Molecular recognition between protein and nicotinamide dinucleotide in intact, proton-translocating transhydrogenase studied by ATR-FTIR, *J. Am. Chem. Soc. 128*, 2621-2629.

204. Wille, G., Ritter, M., Friedemann, R., Mäntele, W., and Hübner, G. (2003) Redox-triggered FTIR difference spectra of FAD in aqueous solution and bound to flavoproteins, *Biochemistry 42*, 14814-14821.

205. Burie, J.-R., Boussac, A., Boullais, C., Berger, G., Mattioli, T., Mioskowski, C., Nabedryk, E., and Breton, J. (1995) FTIR spectroscopy of UV-generated quinone radicals: Evidence for an intramolecular hydrogen atom transfer in ubiquinone, naphthoquinone, and plastoquinone, *J. Phys. Chem. 99*, 4059-4070.

206. Bauscher, M., Nabedryk, E., Bagley, K., Breton, J., and Mäntele, W. (1990) Investigation of models for photosynthetic electron acceptors: Infrared spectroelectrochemistry of ubiquinone and its anions, *FEBS Lett. 261*, 191-195.

207. Bauscher, M. and Mäntele, W. (1992) Electrochemical and infrared-spectroscopic characterization of redox reactions of p-quinones, *J. Phys. Chem. 96*, 11101-11108.

208. Hellwig, P., Mogi, T., Tomson, F. L., Gennis, R. B., Iwata, J., Miyoshi, H., and Mäntele, W. (1999) Vibrational modes of ubiquinone in cytochrome bo_3 from *Escherichia coli* identified by Fourier transform infrared difference spectroscopy and specific ^{13}C labelling, *Biochemistry 38*, 14683-14689.

209. Ritter, M., Anderka, O., Ludwig, B., Mäntele, W., and Hellwig, P. (2003) Electrochemical and FTIR spectroscopic characterization of the cytochrome bc_1 complex from *Paracoccus denitrificans*: Evidence for protonation reactions coupled to quinone binding, *Biochemistry 42*, 12391-12399.

210. Yagil, G. (1967) The proton dissociation constant of pyrrole, indole and related compounds, *Tetrahedron 23*, 2855-2861.

211. Hasegawa, K., Ono, T.-A., and Noguchi, T. (2000) Vibrational spectra and Ab Initio DFT calculations of 4-methylimidazole and its different protonation forms: Infrared and Raman markers of the protonation state of a histidine side chain, *J. Phys. Chem. B 104*, 4253-4265.

212. Wang, D., Zhao, X., Vargek, M., and Spiro, T. G. (2000) Metal-bound histidine modes in UV resonance Raman spectra of Cu,Zn superoxide dismutase, *J. Am. Chem. Soc. 122*, 2193-2199.

213. Noguchi, T., Inoue, Y., and Tang, X.-S. (1999) Structure of a histidine ligand in the photosynthetic oxygen-evolving complex as studied by light-induced Fourier transform infrared difference spectroscopy, *Biochemistry 38*, 10187-10195.

214. Barth, A. (2000) The infrared absorption of amino acid side chains, *Prog. Biophys. Mol. Biol. 74*, 141-173.

215. Hasegawa, K., Ono, T.-A., and Noguchi, T. (2002) Ab initio density functional theory calculations and vibrational analysis of zinc-bound 4-methylimidazole as a model of a histidine ligand in metalloenzymes, *J. Phys. Chem. A 106*, 3377-3390.

216. Rich, P. R. (2004) The quinone chemistry of *bc* complexes, *Biochim. Biophys. Acta 1658*, 165-171.

217. Berthomieu, C. and Hienerwadel, R. (2005) Vibrational spectroscopy to study the properties of redox-active tyrosines in photosystem II and other proteins, *Biochim. Biophys. Acta 1707*, 51-66.

218. Nie, B., Stutzman, J., and Xie, A. (2005) A vibrational spectral marker for probing the hydrogen-bonding status of protonated Asp and Glu residues, *Biophys. J. 88*, 2833-2847.

219. Gibson, D. H., Ding, Y., Miller, R. L., Sleadd, B. A., Mashuta, M. S., and Richardson, J. F. (1999) Synthesis and characterization of ruthenium, rhenium and titanium formate, acetate and fluoroacetate complexes. Correlation of IR spectral propertied and bonding types, *Polyhedron 18*, 1189-1200.

220. Noguchi, T., Ono, T.-A., and Inoue, Y. (1995) Direct detection of a carboxylate bridge between Mn and Ca2+ in the photosynthetic oxygen-evolving center by means of Fourier transform infrared spectroscopy, *Biochim. Biophys. Acta 1228*, 189-200.

221. Mayhew, S. G. (1978) The redox potential of dithionite and SO_2^- from equilibrium reactions with flavodoxins, methyl viologen and hydrogen plus hydrogenase, *Eur. J. Biochem. 85*, 535-547.

222. Akinsiku, A. O. (2001) Ubiquinone binding sites of mitochondrial bc_1 complex, Ph.D. Thesis, University of London.

223. DeGrip, W. J., Gray, D., Gillespie, J., Bovee, P. H. M., Van den Berg, E. M. M., Lugtenberg, J., and Rothschild, K. J. (1988) Photoexcitation of rhodopsin: conformation changes in the chromophore, protein and associated lipids as determined by FTIR difference spectroscopy, *Photobiochem. Photobiophys. 48*, 497-504.

224. Mileni, M., Hass, A. H., Mantele, W., Simon, J., and Lancaster, C. R. D. (2005) Probing heme propionate involvement in transmenbrane proton transfer coupled to electron transfer in dihemic quinol:fumarate reductase by ^{13}C-labeling and FTIR difference spectroscopy, *Biochemistry 44*, 16718-16728.

225. Hielsher, R., Wenz, T., Stolpe, S., Hunte, C., Friedrich, T., and Hellwig, P. (2005) Monitoring redox dependent contribution of lipids in FTIR difference spectra of complex I from *E. coli*, *Biopolymers 82*, 291-294.

226. Flemming, D., Hellwig, P., Lepper, S., Kloer, D. P., and Friedrich, T. (2006) Catalytic importance of acidic amino acids on subunit nuoB of the *Escherichia coli* NADH:ubiquinone oxidoreductase (complex I), *J. Biol. Chem. 281*, 24781-24789.

227. Dröse, S., Galkin, A., and Brandt, U. (2005) Proton pumping by complex I (NADH:ubiquinone oxidoreductase) from *Yarrowia lipolytica* reconstituted into proteoliposomes, *Biochim. Biophys. Acta 1710*, 87-95.

228. Nakashima, Y., Shinzawa-Itoh, K., Watanabe, K., Naoki, K., Hano, N., and Yoshikawa, S. (2002) Steady-state kinetics of NADH:coenzyme Q

oxidoreductase isolated from bovine heart mitochondria, *J. Bioenerg. Biomemb. 34*, 11-19.

229. Carroll, J., Shannon, R. J., Fearnley, I. M., Walker, J. E., and Hirst, J. (2002) Definition of the nuclear encoded protein composition of bovine heart mitochondrial complex I, *J. Biol. Chem. 277*, 50311-50317.

230. Breton, J., Burie, J.-R., Berthomieu, C., Berger, G., and Nabedryk, E. (1994) The binding sites of quinones in photosynthetic bacterial reaction centers investigated by light-induced FTIR difference spectroscopy: Assignment of the Q_A vibrations in *Rhodobacter sphaeroides* using ^{18}O- or ^{13}C-labeled ubiquinone and vitamin K_1, *Biochemistry 33*, 4953-4965.

231. Venyaminov, S. Y. and Kalnin, N. N. (1990) Quantitative IR spectrophotometry of peptide compounds in water (H_2O) solutions. I. Spectral parameters of amino acid residue absorption bands, *Biopolymers 30*, 1243-1257.

232. Wolpert, M. and Hellwig, P. (2006) Infrared spectra and molar absorption coefficients of the 20 alpha amino acids in aqueous solutions in the spectral range from 1800 to 500cm^{-1}, *Spectrochim. Acta A 64*, 987-1001.

233. Haris, P. I., Robillard, G. T., van Dijk, A. A., and Chapman, D. (1992) Potential of ^{13}C and ^{15}N labeling for studying protein-protein interactions using Fourier transform infrared spectroscopy, *Biochemistry 31*, 6279-6284.

234. Xiao, Y., Hutson, M. S., Belenky, M., Herzfeld, J., and Braiman, M. S. (2004) Role of arginine-82 in fast proton release during the bacteriorhodopsin photocycle: a time-resolved FT-IR study of purple membranes containing ^{15}N labeled arginine, *Biochemistry 43*, 12809-12818.

235. Berthomieu, C., Boullais, C., Neumann, J.-M., and Boussac, A. (1998) Effect of ^{13}C, ^{18}O- and ^{2}H-labeling on the infrared modes of UV-induced phenoxyl radicals, *Biochim. Biophys. Acta 1365*, 112-116.

236. Hienerwadel, R., Boussac, A., Breton, J., and Berthomieu, C. (1997) Fourier transform infrared difference spectroscopy of photosystem II tyrosine D using site-directed mutagenesis and specific isotope labeling, *Biochemistry 36*, 14712-14723.

237. Hellwig, P., Pfitzner, U., Behr, J., Rost, B., Pesavento, P., Donk, W. v., Gennis, R. B., Michel, H., Ludwig, B., and Mäntele, W. (2002) Vibrational modes of tyrosine in cytochrome *c* oxidase from *Paracoccus denitrificans*: FTIR and electrochemical studies on Tyr-D4-labeled and on Tyr280His and Tyr35Phe mutant enzymes, *Biochemistry 41*, 9116-9125.

Appendix I (publications)